

DTIC FILE COPY

AD-A215 422



DTIC
 ELECTE
 DEC 14 1989
 S B D

ENHANCED TRACKING OF BALLISTIC
 TARGETS USING FORWARD LOOKING
 INFRARED MEASUREMENTS WITH
 ACTIVE TARGET ILLUMINATION

Thesis
 Claude W. Eden
 Captain, USAF

DEPARTMENT OF THE AIR FORCE
 AIR UNIVERSITY

AIR FORCE INSTITUTE OF TECHNOLOGY

Wright-Patterson Air Force Base, Ohio

DISTRIBUTION STATEMENT A
 Approved for public release;
 Distribution Unlimited

89 12 14 035

AFIT/GE/ENG/89D-11

ENHANCED TRACKING OF BALLISTIC
TARGETS USING FORWARD LOOKING
INFRARED MEASUREMENTS WITH
ACTIVE TARGET ILLUMINATION

Thesis
Claude W. Eden
Captain, USAF
AFIT/GE/ENG/89D-11

DTIC
ELECTE
DEC 14 1989
S B D

Approved for public release; distribution unlimited

AFIT/GE/ENG/89D-11

ENHANCED TRACKING OF BALLISTIC TARGETS
USING FORWARD LOOKING INFRARED MEASUREMENTS
WITH ACTIVE TARGET ILLUMINATION

THESIS

Presented to the Faculty of the School of Engineering
of the Air Force Institute of Technology

Air University

In Partial Fulfillment of the
Requirements for the Degree of
Master of Science in Electrical Engineering

Claude W. Eden, B.S.E.E.

Captain, USAF

December 1989

Approved for public release; distribution unlimited

Preface

This study is the latest step in a continuing a line of research begun more than ten years ago. This work has continued the development of an algorithm for tracking airborne targets using measurements from an array of infrared detector elements. Until now, the research has only been concerned with passively acquired measurements. This thesis effort expands this by considering the addition of actively acquired measurements, i.e, measurements of laser light reflected from the target. [Handwritten marks]

In any Masters degree program, the shape of the thesis work bears the imprint of the thesis advisor as heavily as the imprint of the student. This is especially true in this thesis. Any success associated with this work is due in large part to Dr. Peter Maybeck. His guidance and partnership in this research effort was instrumental in my completion of this work. Additionally, I would like to thank Lt Col Zdzislaw Lewantowicz and Capt Randall Paschall for their review and comments on this research. Thanks also go to Kristen Larsen and Richard Norris for their assistance in dealing with software problems.

Accession For	
NTIS GRA&I	<input checked="" type="checkbox"/>
DTIC TAB	<input type="checkbox"/>
Unannounced	<input type="checkbox"/>
Justification	
By	
Distribution/	
Availability Codes	
Dist	Avail and/or Special
A-1	

Table of Contents

	Page
Preface	ii
List of Figures	vii
List of Tables	ix
List of Symbols	x
Abstract	xiv
1. Introduction	1
1.1 Background	1
1.2 Summary of Previous AFIT Research	4
1.3 Objectives	12
1.3.1 Observability Analysis	13
1.3.2 Active Illumination Modelling	14
1.3.3 FLIR Filter	15
1.3.4 Single-State Filter Performance	15
1.4 Thesis Overview	16
2. Truth Model	17
2.1 Introduction	17
2.2 Dynamics Model	18
2.2.1 Target Dynamic States	21
2.2.2 The Atmospheric States	24
2.2.3 Bending/Vibration States	27
2.3 Simulation Space	30
2.3.1 Coordinate Frames	30
2.3.2 Target Model	32
2.3.3 Target Image Projection onto the FLIR Plane	38
2.3.4 Velocity Projection onto the FLIR Plane	40
2.4 Measurement Models	43
2.4.1 Infrared Measurement Model	43
2.4.2 Laser Reflection Measurement Model	48
2.5 Summary	53

	Page
3. Filter Models	54
3.1 Introduction	54
3.2 FLIR Filter	54
3.2.1 Dynamics Model	54
3.2.2 Measurement Model	60
3.2.2.1 Template Generation	61
3.2.2.2 Enhanced Correlation "Pseudo-Measurements"	65
3.3 Center of Mass Offset Filter	67
3.3.1 Dynamics Model	68
3.3.2 Measurement Model	70
3.4 Summary	70
4. Tracking Algorithm and Performance Evaluation Tools	72
4.1 Introduction	72
4.2 Tracking Algorithm Overview	72
4.3 Field-of-View Rotation	74
4.4 Truth Model Parameters	79
4.5 Filter Paramters	81
4.6 Tracking Algorithm Statistics	82
4.7 Performance Plots	83
4.7.1 Plot Designation Codes	91
4.8 Summary	93
5. Performance Analysis	94
5.1 Introduction	94
5.2 Filter Observability Study	94
5.3 Filter Tuning Process	98

	Page
5.4 Mass Center Offset Filter Sensitivity Study	104
5.5 Mass Center Offset Filter Robustness Study	108
5.6 Pixel Constant Study	111
5.7 Offset Distance Study	113
5.8 Summary	115
6. Conclusions and Recommendations	117
6.1 Introduction	117
6.2 Conclusions	117
6.2.1 Six-State Filter Tuning	117
6.2.2 Offset Filter Sensitivity Study	118
6.2.3 Offset Filter Robustness Study	118
6.2.4 Pixel Proportionality Constant Study	119
6.2.5 Offset Distance Study	119
6.3 Recommendations	120
6.3.1 Six-State Filter Modeling and Tuning	120
6.3.2 Illumination Modeling Improvement	121
6.3.3 Different Initial Filter Parameters	122
6.3.4 Pixel Proportionality Constant Filter Tuning	122
6.3.5 Mass Center Error Reslution	123
Appendix A. Mass Center Measurement Simulation	124
Appendix B. Plots for Six-State Filter Tuning	131
Appendix C. Plots for Sensitivity Study	172
Appendix D. Plots for Robustness Study	182

	Page
Appendix E. Plots for Pixel Constant Study	201
Appendix F. Plots for Offset Distance Study	211
Bibliography	218
Vita	220

List of Figures

Figure	Page
2.1 The FLIR Plane	33
2.2 The Target Frame	34
2.3 Gaussian Intensity Function Distributions	35
2.4 Hotspot Dispersion on FLIR Plane	37
2.5 Target Image Projection Geometry	39
2.6 Inertial Velocity FLIR Plane Projection Geometry	42
2.7 FLIR Image Intensity Function for the Difference Between Two Gaussian Intensity Functions	45
2.8 Center of Mass Measurement Geometry	51
3.1 Enhanced Correlator/Linear Measurement Model Data Processing Algorithm	62
3.2 Physical Representation of Estimated Filter State	69
4.1 Tracking Algorithm	73
4.2 Data Processing Algorithm for Diagonally Rotated Field-of-View	76
4.3 Example of Actual vs. Filter Computed RMS Error Performance Plot (Plot #1)	85
4.4 Example of Position Error at time t_i Performance Plot (Plot #3)	86
4.5 Example of Centroid Position Error at time t_i Performance Plot (Plot #4)	87
4.6 Example of Centroid Position Error at time t_i Performance Plot (Plot #5)	88

Figure	Page
4.7 Example of Offset Actual vs. Filter Computed RMS Error Performance Plot (Plot #11)	89
4.8 Example of Offset Error at time t_1 Performance Plot (Plot #13)	90
A.1 Laser Beam Simulation	125
A.2 Reflection Simulation	125
A.3 Center of Mass Measurement Simulation	127

List of Tables

Table	Page
5.1 Tuning Run Parameters	100
5.2 Run 1 Temporally Averaged Statistics	100
5.3 Run 2 Temporally Averaged Statistics	101
5.4 Run 3 Temporally Averaged Statistics	103
5.5 Run 4 Temporally Averaged Statistics	104
5.6 Sensitivity Study Time Averaged Statistics	107
5.7 Robustness Study Time Averaged Statistics	109
5.8 Pixel Constant Study Time Averaged Statistics	112
5.9 Offset Distance Study Time Averaged Statistics	115

List of Symbols

Symbol	Page
A_p	46
AR	38
$b_{j\hat{x}}(t_i)$	46
$B_T(t)$	18
B_{Td}	19
CM	14
DRFOV	75
EKF	4
$F(t)$	65
F_f	56
$F_T(t)$	18
FLIR	1
FOV	2
G_f	56
$G(J_x, J_y)$	65
$g(x, \nu)$	65
$g(x, \nu) \cdot l(x, \nu)$	66
H_f	67
\mathbf{A}	63
i_1	46
i_2	46
i_{max}	43
\hat{x}_n	24

Symbol	Page
K_b	27
k_p	22
$L_{offset}(t_i)$	52
$L'(f_x, f_y)$	66
$l(x, y)$	66
$Length_{Actual}$	49
$Length_{FIR}$	49
LOS	21
MAP	8
MMAF	7
$n_{jk}(t_i)$	46
$P_{cm offset}$	70
'ppu'	31
'pu'	31
Q_f	19
$Q_{f,i}$	20
r	38
R_f	67
RRFOV	10
t_i	58
t_i'	58
$u_f(t)$	18
$u_{f,i}$	19
'w'	31

Symbol	Page
u_{LOS}	38
u_x	55
u_y	55
$w_{cm\ offset}$	68
w_{da}	21
w_{db}	21
w_f	56
$w_T(t)$	18
w_{Td}	19
x_a	21
x_b	21
x_a	17
x_b	17
x_c	17
$x_{cm\ offset}$	68
x_d	21
x_f	56
$x_T(t)$	18
y_t	17
y_a	17
y_b	17
y_c	17
y_t	17
$z_{cm\ offset}$	70

Symbol	Page
$\angle_{jk}(t_i)$	46
α	31
β	31
$\dot{\alpha}'$	22
$\dot{\beta}'$	22
δt	22
Φ_T	19
γ	38
Θ_f	75
Θ_T	38
σ_b	30
$\sigma_{\rho\nu}$	38
$\sigma_{\rho\nu 0}$	38
$\sigma_{\nu 0}$	38
σ_ν	38
$\bar{\sigma}_a$	57
$\bar{\sigma}_x$	57
$\bar{\sigma}_y$	57
τ_a	56
τ_x	56
τ_y	56
ω_b	30
ω_{nb}	27
ξ_b	27

Abstract

This thesis is the latest extension of a line of research begun over ten years ago. The purpose of this research has been to develop an algorithm to track airborne targets (aircraft and/or ballistic missiles) using forward looking infrared (FLIR) measurements, as a means of aiming a high energy laser.

This research deviates from past research in considering the use of actively acquired measurements. Past research has concentrated on the use of passively acquired measurements, i.e. measurements of the target's thermal intensity functions (hotspots) from an array of infrared detector elements. This research considered illumination of the target by a low power laser. The measurement of the reflected laser light would then give information about the hardbody location, and presumably an aiming point for the high power laser.

Specifically, this thesis investigated a ballistic missile in boost phase of flight. Measurements of the missile exhaust plume thermal intensity from an array of infrared detector elements were used by an enhanced correlator/linear Kalman filter to produce estimates of the FLIR image centroid location and velocity. These estimates were then used to simulate the aiming of a low power laser at the missile hardbody. The "pseudo-measurement" output of

an optical sensor receiving the reflections from the missile hardbody was then used by a second Kalman filter to estimate the location of the missile mass center.

This thesis effort involved sensitivity and robustness studies of the measurement noise variance in the filter which estimates the missile mass center. These studies indicated the filter's relative insensitivity to changes in the measurement noise variance; this parameter only affected the transient time for the filter to reach the steady state value of the mass center location. Other parameter studies were conducted involving the distance between the missile mass center and the exhaust plume intensity center, and the infrared sensor element resolution size. The first study indicated decreased filter performance in locating the mass center with increased distance. The results from the second study were inconclusive and require further work.

ENHANCED TRACKING OF BALLISTIC TARGETS USING
FORWARD LOOKING INFRARED MEASUREMENTS
WITH ACTIVE TARGET ILLUMINATION

1. Introduction

With the advent of the Strategic Defense Initiative (SDI), research into the use of the high energy laser as a weapon has intensified. The laser's ability to concentrate energy in a small area makes it especially attractive for use against airborne targets (aircraft and/or ballistic missiles). Any system using a high energy laser must have the capabilities of autonomously tracking targets and accurately pointing the laser at those targets. It is the requirement for autonomous tracking that motivates this line of research.

1.1 Background

The Air Force Weapons Laboratory (AFWL) at Kirtland Air Force Base, New Mexico, is presently engaged in research involving the use of high energy lasers against airborne targets. In the system now under development, targets are passively detected using a forward looking infrared (FLIR) sensor, consisting of a 300 x 500 pixel array of detectors.

Each pixel, or picture element, detects infrared energy over an area 15 microradians (azimuth) by 15 microradians (elevation) square [14]. For this and previous work [13,14], a subset of this array consisting of an 8 x 8 array of pixels is used to process infrared energy for target tracking. This subarray of pixels is defined as the tracking field of view (FOV) [13,14].

In the system under consideration, the laser and FLIR sensor share a common optical aperture. The tracking algorithm uses the incoming FLIR data to determine a position offset between the target position and the current center of the FOV. A controller then zeros these offsets to keep the center of the sensor FOV on the target. Because of the shared aperture, centering the sensor FOV on the target also insures the laser is pointing at the target.

In earlier research, the tracking function was accomplished via a standard correlation algorithm. This algorithm compares the current target FLIR image with target image data from the previous sample period. The correlation between past and present image data is used to generate the relative target position offsets, since a translation of the target image in the FLIR sensor plane is assumed to represent a spatial translation of the actual target. This algorithm has the advantages of relative real-time implementation ease, and of having relatively good tracking performance against a wide range of targets, particularly

spatially distributed ones. However, the use of a correlation algorithm does have some associated disadvantages.

First, an inherent time lag exists. This lag is due to the time required for computation of target image correlation as well as the lag associated with physical pointing of the tracker at the target. Second, the correlation algorithm is unable to distinguish between image spatial translation due to target dynamics and image translation due to other factors such as atmospheric jitter [10] and platform bending/vibration [4]. Finally, the correlation algorithm is unable to take advantage of information on target characteristics, such as size or shape, which may be known a priori or could be estimated in real time.

To overcome these disadvantages, Kalman filtering methodology has been incorporated into the tracking algorithm for the purposes of estimation and control [1-5,11-18]. By modeling the effects of target dynamics, atmospheric jitter, and platform bending/vibration, and including them in the filter dynamics model, enhanced estimates of target position can be produced. These estimates can then be propagated forward to produce a position estimate at some future time for use in laser pointing and target tracking, thereby providing performance potential superior to that accomplishable by a simple correlation algorithm.

1.2 Summary of Previous AFIT Research

Since 1978, The Air Force Institute Of Technology (AFIT) has had a continuing line of research investigating the use of Kalman filtering techniques in the AFWL high energy laser pointing and tracking system. This research has produced numerous theses and papers. Previous theses [4,13,14] have summarized that body of work. That summary is included here with modifications.

The first study, begun in 1978 by Mercier [10], compared an extended Kalman filter (EKF) with a standard correlator tracker. The targets were represented as point sources of infrared energy, and the FLIR sensor image was modeled as a Gaussian bivariate distribution with circular equal-intensity contours. The four-state filter maintained estimates of target position and atmospheric jitter states in each of two FLIR plane coordinate directions. Both position and jitter states were modeled as first order, zero-mean, Gauss-Markov processes. For that effort, FLIR measurement noise was modeled as consisting of background clutter and internal sensor noise (thermal noise and dark current). The measurement noise was also considered to be temporally and spatially uncorrelated. The results showed the EKF's ability to outperform the standard correlator in tracking long-range benign trajectory targets by about an order of magnitude in rms tracking error.

Harnly and Jensen [2] expanded Mercier's work by examining target scenarios under less restrictive assumptions. Target velocity and acceleration states were added to the filter in order to handle less benign target trajectories, and the FLIR plane target image was modeled with elliptical rather than circular equal-intensity contours. Adaptive estimation of parameters associated with the target shape function was utilized to provide desired performance. The measurement noise model was also modified to allow for spatially correlated background noise. Adaptive estimation of filter dynamics driving noise was also incorporated into the tracking algorithm. The results indicated the filter's increased ability to track targets over a wider range of maneuver scenarios.

The research conducted by Mercier, and Harnly and Jensen had been based on the assumption that the target image intensity function was known a priori to be composed of a single hot spot and well modeled as a bivariate Gaussian function. Singletary [16] and Rogers [15] pursued a line of research which made no such assumption. The algorithms developed used exponential smoothing of centered target images, as an approximation to finite memory averaging, to produce an estimate of the target image intensity shape function, or template. This shape function was then used directly in the measurement model of an Kalman filter. These algorithms were then tested using target scenarios in

which targets were represented as multiple hot spots, and the results indicated performance comparable to that of filters used previously on single hot-spot targets, in which only parameters in an assumed bivariate Gaussian intensity had to be identified rather than an entire intensity function.

Rogers also investigated an enhanced correlation tracker which had "pseudo-measurements" as an output. The enhancement was due to the current target FLIR image being correlated with the intensity template described in the previous paragraph, rather than with the previous image data. The "pseudo-measurements" produced were position offsets between the target FLIR image and the center of the FLIR FOV in each of the two FLIR plane coordinate directions. These offsets were then used as measurements provided to a Kalman filter. The preprocessing of the FLIR data by the enhanced correlator algorithm allowed the use of a linear Kalman filter instead of the previously used EKF. This reduced the computational loading when compared to the previously used EKF. Performance was generally comparable in terms of rms tracking errors, with the correlator-linear Kalman filter having lower mean tracking errors but higher standard deviations than the EKF.

Kozemchak [3] and Millner [11] continued the algorithm development with investigations of both the EKF and Roger's enhanced correlator/linear Kalman filter, using more

realistic target trajectories. Both Gauss-Markov and constant turn-rate models were considered for acceleration representation within the filter. Because of the goal of attempting to maintain tracking lock on harshly maneuvering targets, the scheme used by Harnly and Jensen [2] for adaptively estimating filter driving noise was also implemented. Both filtering schemes exhibited good tracking performance for target maneuvers up to five g's. However, the abrupt onset of harsh maneuvers led to serious performance degradation.

In attempting to solve the problem of tracking harshly maneuvering targets, Flynn [1] proposed the use of a multiple model adaptive filter (MMAF). Suizu [17], following up on Flynn's research, implemented a bank of two elemental Kalman filters. One filter was tuned for benign target maneuvers and accepted measurements from a narrow (8 x 8 pixel) FLIR FOV. The second filter was tuned for dynamic target maneuvers and used measurements from a wide (24 x 24 pixel) FLIR FOV. Using a Bayesian probabilistic weighted average of the elemental filter outputs [7:129-136], the MMAF tracker was able to maintain lock on targets whose dynamics ranged from benign to 20-g pull-up maneuvers at 20 kilometers. The elemental filters were implemented using both the EKF and the enhanced correlator/linear Kalman filter. Performance results were comparable, with the correlator/linear Kalman filter having smaller mean errors

and larger standard deviations than the EKF, as seen in earlier work of Rogers.

Loving [5] expanded Suizu's MMAF implementation by adding a third elemental filter to the MMAF structure. This filter was tuned for intermediate target dynamics and used measurements from a narrow (8×8 pixel) FLIR FOV. Loving also compared a Maximum A Posteriori (MAP) MMAF scheme to the Bayesian MMAF structure previously used. The MAP structure differs from the Bayesian structure in using only the estimates from the elemental filter with the highest probabilistic weight, rather than a weighted sum of elemental filter outputs as in the Bayesian MMAF. The addition of the third filter enhanced the MMAF tracking performance. No significant difference in performance was found between the Bayesian and MAP MMAF algorithms.

Netzer [12] continued further research into the three-filter Bayesian MMAF algorithm. After examining the steady state bias errors produced in the more benign of the two FLIR plane directions when the target made a 20-g turn, he determined the need to investigate an MMAF structure with elemental filters tuned for target maneuvers predominantly in either azimuth or elevation. This segregation of maneuver direction into different elemental filters allows the MMAF algorithm to distinguish maneuvers in these two directions. This enables the tracker to expand the FOV in the critical direction on a harshly maneuvering target. The

tracker can then maintain lock on a maneuvering target in the critical direction while still producing accurate estimates in the direction of benign maneuvers. Netzer also recommended the use of a constant turn rate process for modeling acceleration at close ranges.

Tobin [18] further expanded the research into MMAFs using Netzer's recommendations. He added two elemental filters, tuned for maneuvers in azimuth and elevation, to the three-filter bank. A comparison between constant turn rate and Gauss-Markov processes as acceleration models in the elemental filters was also made. Although the results indicated smaller steady state errors for the constant turn-rate model, the Gauss-Markov model filters had consistently better transient error performance. The performance analysis of the five-filter-bank MMAF indicated the tracker's ability to maintain target lock during a jink in elevation while still producing superior tracking performance in the azimuth direction over an MMAF without any directionally tuned elemental filters. This was a preliminary feasibility study, with an eventual goal of using an arbitrary direction for maneuver acceleration, as opposed to strictly azimuth or elevation.

Leeney [4] continued the MMAF investigation by adding states to the truth model to account for bending/vibration effects in a large space structure. Although bending/vibration states were not added to the filter model, the

elemental filters were retuned using the updated truth model. The retuned MMAF tracker exhibited satisfactory tracking performance against targets undergoing dynamic (10-g) maneuvers, provided that the values given to the parameters associated with the bending/vibration effects are on the order to be expected. Leeney also examined the use of a higher sampling rate (50 Hertz versus 30 Hertz), but found the additional computational burden outweighed the performance increase. A preliminary investigation into the use of a rotating rectangular (24 x 8 pixels) field of view (RRFOV), in which the elongated side of the FOV would be aligned with the estimated acceleration direction, was done. The rationale was to replace the two rectangular FOV elemental filters of Tobin's research with a single filter. The initial investigation revealed that acceleration state estimates were too noisy for accurately estimating the maneuver direction; the more precise velocity estimates were used instead, with the long side of the rectangular FOV being aligned perpendicular to the velocity vector. Leeney's preliminary work did indicate enough promise with this idea for further exploration

Norton [13] implemented the RRFOV in his research. In addition, he also considered the effect of filter dynamics driving noise strength versus FOV size on filter performance. His results showed that choice of a larger dynamics driving noise strength in the direction of maneuver was more

important than increased FOV size in improving filter performance. By using an 8 x 8 pixel rotating FOV (instead of an 8 x 24 pixel rectangular FOV) in combination with larger values of dynamics driving noise in the direction of maneuver, an improvement in performance was achieved. Norton also investigated a means to rotate the dynamics driving noise strength "Q" matrix mathematically so that the larger "Q" values stayed aligned with the acceleration direction. A scheme for simulating the physical rotation of the FLIR sensor plane to keep one axis aligned with the acceleration vector was also investigated. Preliminary results from implementation of these various schemes into an MMAF algorithm were encouraging.

Most recently, Rizzo [14] used Norton's results to investigate a ballistic missile tracking scenario. Interested in "pogo" phenomenon, where the missile exhaust plume oscillates along the missile hardbody longitudinal axis, he modeled this as a second order process. Two parameters, natural frequency and oscillation amplitude, were studied, and elemental filters from a four-filter bank were tuned for different combinations of these two parameters. A comparison between a rotating FOV and a diagonal rotating FOV, in which the maneuver direction was aligned with the FOV diagonal rather than one of the FLIR plane axes, was also made. The results indicated superior tracking performance using the diagonal rotating FOV.

For his research, Rizzo used Norton's eight-state elemental filters as benchmarks for comparison. These filters were then augmented to ten states by the addition of two states associated with "pogo" effects. Both the eight and ten-state filters were then tuned against Norton's 12-state truth model, which was increased to 14 states by the addition of the same 2 "pogo" states. After tuning both sets of filters, Rizzo observed the performance of the eight-state filters to be superior to that of the ten-state filters. Since the ten-state filters had knowledge of the "pogo" effects which were also included in the truth model, and should have outperformed the eight-state filters which had no knowledge of the "pogo" effects, a preliminary stochastic observability analysis [6:243] was conducted to determine possible causes for this anomaly. The analysis revealed that target velocity and acceleration states were almost unobservable for the specific class of missile targets he was considering. Recommendations for future work included reducing the order of the filter models, and remodeling the velocity states as first order Gauss-Markov processes. Because of the performance anomalies discovered, Rizzo did not implement an MMAF structure.

1.3 Objectives

Previous research at AFIT has been directed toward the goal of producing an autonomous tracker. The progression of

past research shows a clear trend toward development of an algorithm that tracks aircraft and ballistic missiles under increasingly realistic conditions. These efforts have concentrated on tracking targets using only passively acquired infrared measurements. Unfortunately, by doing so, the filter has no information with which to estimate the missile hardbody location, as separated from the exhaust plume high intensity peak. This thesis effort will consider using actively acquired measurements as well, in order to help resolve the hardbody itself.

Specifically, the scenario investigated will consist of tracking a ballistic missile in boost phase through the atmosphere. The ground sensors will consist of a FLIR sensor detecting exhaust heat and an additional optical sensor that detects the returns from a low power laser illuminating the missile hardbody. By observing the laser returns, some additional information to help discern the missile hardbody from the exhaust plume is provided to the filter. The specific objectives of this thesis effort are outlined below.

1.3.1 Observability Analysis. Based on Rizzo's recommendations [14], a stochastic observability analysis [6:243] will be conducted. Because of the observability-like problem encountered by Rizzo, Norton's eight-state filter [13] will be used for this study. The analysis will indicate

which states are least observable, and thus the candidates for elimination in an order reduction effort to address this issue. Rizzo [14:7-4] indicated target acceleration and perhaps velocity as the two most likely candidates. Once the appropriate reduced order filter has been determined, it will be used as the benchmark filter for this investigation.

1.3.2 Active Illumination Modelling. In the scenario considered for this thesis effort, illumination of the missile hardbody is accomplished by sweeping a low power laser up and down the estimated missile velocity vector, starting from the estimated centroid of intensity. The dithering of the laser would illuminate all or some part of the missile hardbody. By viewing the speckle or other properties of the return signal, there should be some indication of the line defining the boundary between the hardbody and the spatial region outside the hardbody. For this preliminary work, a modelling of the physical process of target illumination by a laser will not be attempted. This effort will instead concentrate on specifying the form of the measurement data presented to the filter from this process.

The rationale for using laser illumination is to provide information to the filter about the location of the missile center of mass (CM) relative to the FLIR plane intensity image centroid. The measurement form used in this thesis

would present this as a measurement of the CM offset from the image centroid along the estimated velocity vector. A separate single state filter will be used to estimate the offset distance, based on this measurement.

1.3.3 FLIR Filter. The reduced order filter from Section 1.3.1 will be established as the basic filter used for all investigations in this research. Before beginning any of the parameter studies involving the single-state filter, the reduced order filter will be tuned using Norton's twelve-state truth model. The truth model will be changed to reflect a ballistic missile target, rather than the highly dynamic aircraft target used by Norton.

1.3.4 Single-State Filter Performance. Once the filter from Section 1.3.3 has been tuned for best tracking performance, a series of parametric studies involving the single-state filter will be performed. A sensitivity study will be conducted first to determine the effect of changing the laser reflection measurement noise level on the single-state filter's performance. For this sensitivity study, the filter will be correctly informed of the changes made in the "real world" tracking scenario. Once the sensitivity study has been completed, a robustness study involving reflection measurement noise level will be performed, in which the filter will not be informed of changes in the "real world". A series of parameter studies, involving variation of FLIR

sensor sensitivity, and separation distance of image centroid from missile CM, will complete the analysis.

1.4 Thesis Overview

This chapter has reviewed past research and enumerated the objectives for this thesis effort. Chapter 2 considers the truth model and develops the simulation model used in this and past investigations. Chapter 3 presents the detailed filter development. Chapter 4 develops the complete algorithm used in this research and discusses the manner in which the results of the analyses will be presented. The results of the performance analyses follow in Chapter 5. The final chapter summarizes the conclusions and makes recommendations for future study.

2. Truth Model

2.1 Introduction

A truth model is the result of an attempt to describe the behavior of real world phenomena of interest in an accurate mathematical form. In many cases, the complete description of true system behavior may require an infinite dimensional state space model. The number of truth model states must, of necessity, be finite dimensional, capturing enough of the dominant characteristics of system behavior for an accurate representation, while at the same time not becoming too large to be computationally unmanageable. In a simulation, such as the one used in this thesis effort, the truth model provides the basis for depicting the true "real world" dynamic behavior of a system. The truth model becomes the standard against which the performance of the Kalman filter is evaluated.

For this thesis, the true dynamics of the apparent target image in the FLIR plane are due to the summed effects of true target motion, atmospheric jitter, and hardware vibration/bending. The dynamics are represented as changes in the FLIR plane x and y coordinates (i.e., azimuth and elevation) of the target intensity image. The position of the target image at any one time is given by:

$$x_c = x_t + x_a + x_b \quad (2-1)$$

$$y_c = y_t + y_a + y_b \quad (2-2)$$

where

x_c, y_c = image centroid coordinates

x_t, y_t = component of x_c, y_c due to actual target dynamics

x_a, y_a = component of x_c, y_c due to atmospheric jitter

x_b, y_b = component of x_c, y_c due to mechanical bending/
vibration of hardware

This chapter will describe the state space structure of this truth model. The twelve-state dynamics model necessary to account for the terms in Equations (2-1) and (2-2) will be developed first, followed by the appropriate measurement model. The chapter will then discuss the simulation space used in this thesis effort. This discussion will include descriptions of the coordinate frames, target models, and derivations of all the measurement simulations.

2.2 Dynamics Model

The twelve-state dynamics model used for the truth model consists of a two-state target dynamics model, a six-state atmospheric jitter model, and a four-state mechanical vibration/bending model. This model is represented by the following first order linear, stochastic differential equation:

$$\dot{\mathbf{x}}(t) = \mathbf{F}_T \mathbf{x}_T(t) + \mathbf{B}_T \mathbf{u}_T(t) + \mathbf{w}_T(t) \quad (2-3)$$

where:

\mathbf{F}_T = 12 x 12 time-invariant truth model system
plant matrix

\mathbf{B}_T = 12 x 2 time invariant truth model

input distribution matrix

$\mathbf{x}_T(t)$ = 12-dimensional truth model state vector

$\mathbf{u}_T(t)$ = 2-dimensional truth model input state vector

$\mathbf{w}_T(t)$ = 12-dimensional zero mean, white, Gaussian
noise vector with autocorrelation function:

$$E[\mathbf{w}_T(t)\mathbf{w}_T^T(t+\tau)] = \mathbf{Q}_T\delta(\tau). \quad (2-4)$$

The equivalent discrete-time model [6] corresponding to Equation (2-3) is of the form:

$$\mathbf{x}_T(t_{i-1}) = \Phi_T(t_{i-1}, t_i)\mathbf{x}_T(t_i) + \mathbf{B}_{Td}\mathbf{u}_{Td}(t_i) + \mathbf{w}_{Td}(t_i) \quad (2-5)$$

where the state transition matrix $\Phi_T(t_{i-1}, t_i)$ is determined by solving the differential equation [6:40-41]:

$$\frac{d\Phi_T(t, t_i)}{dt} = \mathbf{F}_T\Phi_T(t, t_i) \quad (2-6)$$

using the initial condition: $\Phi_T(t_i, t_i) = \mathbf{I}$

The discrete-time input distribution matrix in Equation (2-5) is:

$$\mathbf{B}_{Td} = \int_{t_i}^{t_{i-1}} \Phi_T(t_{i-1}, \tau)\mathbf{B}_T d\tau \quad (2-7)$$

Finally, the vector quantities in Equation (2-5) are:

$\mathbf{x}_T(t_i)$ = 12-dimensional discrete-time truth model
state vector

$\mathbf{u}_{Td}(t_i)$ = 2-dimensional discrete-time input vector

$\mathbf{w}_{Td}(t_i)$ = 12-dimensional discrete time, zero mean
white Gaussian noise vector with covariance:

$$Q_{Td} = \int_{t_i}^{t_{i+1}} \Phi_T(t_{i+1}, \tau) Q_T \Phi_T^T(t_{i+1}, \tau) d\tau \quad (2-8)$$

where Q_T is defined in Equation (2-4).

As previously mentioned, the truth model consists of a target dynamics position state, three atmospheric jitter shaping filter [10] states, and two mechanical bending states, in both x and y FLIR plane directions. In augmented form, the truth model state vector becomes:

$$\mathbf{x}_T = \begin{bmatrix} \mathbf{x}_d \\ \mathbf{x}_a \\ \mathbf{x}_b \end{bmatrix} \quad (2-9)$$

The discrete time truth model state transition matrix is:

$$\Phi_T = \begin{bmatrix} \Phi_d_{(2 \times 2)} & \mathbf{0}_{(2 \times 6)} & \mathbf{0}_{(2 \times 4)} \\ \mathbf{0}_{(6 \times 2)} & \Phi_a_{(6 \times 6)} & \mathbf{0}_{(6 \times 4)} \\ \mathbf{0}_{(4 \times 2)} & \mathbf{0}_{(4 \times 6)} & \Phi_b_{(4 \times 4)} \end{bmatrix} \quad (2-10)$$

and the discrete-time truth model distribution matrix is:

$$B_{Td} = \begin{bmatrix} B_{dt}_{(2 \times 2)} \\ \mathbf{0}_{(6 \times 2)} \\ \mathbf{0}_{(4 \times 2)} \end{bmatrix} \quad (2-11)$$

and the discrete-time truth model white Gaussian noise process is given by:

$$\mathbf{w}_{Td} = \begin{bmatrix} \mathbf{0}_{(2 \times 1)} \\ \mathbf{w}_{da}_{(6 \times 1)} \\ \mathbf{w}_{db}_{(4 \times 1)} \end{bmatrix} \quad (2-12)$$

where:

x_d = 2-dimensional target dynamics state vector

x_a = 6-dimensional atmospheric jitter state vector

x_b = 4-dimensional bending/vibration state vector

$w_{da}(t_i)$ = 6-dimensional discrete time, white Gaussian
noise related to atmospheric states

$w_{db}(t_i)$ = 4-dimensional discrete-time, white Gaussian
noise related to bending states

After examining Equations (2-5) and (2-9) to (2-12), the truth model state dynamics representation is observed to be composed of three totally independent partitions. This allows the dynamics, jitter, and bending models to be developed separately. The next subsections details the development of these three models.

2.2.1 Target Dynamic States. For this and previous thesis efforts [1-5,10-18], target dynamics are modelled as they occur in the FLIR plane. The FLIR image plane is modelled as being coincident with the array of FLIR sensor elements, and perpendicular to the sensor-target line-of-sight (LOS) vector. Since the sensor-to-target range is large, the azimuth and elevation displacements from the FLIR image plane origin are directly proportional to "pseudo" azimuth and elevation angles. These "pseudo" angles, α' and β' , as well as the FLIR plane, are developed in Section 2.3.4.

To convert the "pseudo" angle measurement units of microradians to the displacement distances in pixels, a pixel proportionality constant is used. This constant represents the angular FOV of a single picture element, or pixel. Continuing with Rizzo's work [14], a value on the order of 15 microradians/pixel was initially used in this thesis work.

Using the assumptions that the azimuth and elevation rates remain essentially constant over any sample period, the discrete target dynamics model is:

$$x_t(t_{i+1}) = x_t(t_i) + \frac{(\dot{\alpha}')(\Delta t)}{k_p} \quad (2-13)$$

$$y_t(t_{i+1}) = y_t(t_i) - \frac{(\dot{\beta}')(\Delta t)}{k_p} \quad (2-14)$$

where:

$\dot{\alpha}'(t_i) = \frac{d\alpha'}{dt}$, measured in micro-radians/second and constant over the time interval $[t_i, t_{i+1}]$

$\dot{\beta}'(t_i) = \frac{d\beta'}{dt}$, measured in micro-radians/second and constant over the time interval $[t_i, t_{i+1}]$

Δt = sample time interval $t_{i+1} - t_i$

k_p = pixel proportionality constant,

15 micro-radians/pixel

Note the minus sign in Equation (2-14). This is due to the difference in the y axis orientations between the FLIR plane coordinate frame and the inertial coordinate frame. These

coordinate frames are shown in Figure 2.1 and developed in Section 2.3.1.

Arranging these equations in state space form yields:

$$\begin{bmatrix} x_t(t_{i-1}) \\ y_t(t_{i-1}) \end{bmatrix} = \begin{bmatrix} 1 & 0 \\ 0 & 1 \end{bmatrix} \begin{bmatrix} x_t(t_i) \\ y_t(t_i) \end{bmatrix} + \begin{bmatrix} \frac{\Delta t}{k_p} & 0 \\ 0 & -\frac{\Delta t}{k_p} \end{bmatrix} \begin{bmatrix} \dot{\alpha}'(t_i) \\ \dot{\beta}'(t_i) \end{bmatrix} \quad (2-15)$$

Using the matrices of Equation (2-15) and the block form of the overall truth model, the upper left hand block of Equation (2-10) is:

$$\Phi_d \text{ }_{2 \times 2} = \begin{bmatrix} 1 & 0 \\ 0 & 1 \end{bmatrix} \quad (2-16)$$

and the upper block of Equation (2-11) is:

$$\mathbf{B}_{Td} = \begin{bmatrix} \frac{\Delta t}{k_p} & 0 \\ 0 & -\frac{\Delta t}{k_p} \end{bmatrix} \quad (2-17)$$

and the deterministic input vector in Equation (2-5) is:

$$\mathbf{u}_{Td}(t_i) = \begin{bmatrix} \dot{\alpha}'(t_i) \\ \dot{\beta}'(t_i) \end{bmatrix} \quad (2-18)$$

The truth model missile trajectory simulation is a continuation of that used by Rizzo [14]. The underlying dynamics model [14:3-10] is that of a point mass influenced by a thrust force and a gravitational force, with all other external forces assumed negligible.

The formulation of the truth model target dynamics states in deterministic state space form such as Equation (2-15) has some advantages. First, although the truth model trajectory could have been stored as FLIR plane position coordinates for each sample time in the simulation, rather than inputting the angular rate inputs to produce such a position time history, the present form is more flexible in supporting a wide variety of missile trajectories. For instance, if a stochastic, rather than deterministic, dynamics model is desired, this can be implemented easily by the addition of a noise term to Equation (2-15).

2.2.2 The Atmospheric States. Using power spectral density characteristics, it can be shown that the atmospheric jitter phenomena can be approximated by the output of a third-order shaping filter driven by white Gaussian noise [10]. The Laplace domain representation of the shaping filter transfer function is given by [10:12]:

$$\frac{x_a(s)}{w_a(s)} = \frac{K_a AB^2}{(s+A)(s+B)^2} \quad (2-19)$$

where:

x_a = atmospheric jitter position in one direction of the FLIR image plane, the output of the shaping filter defined in Equation (2-19)

w_a = zero mean, unit strength, white Gaussian noise

K_a = gain, adjusted for desired jitter RMS value

A = break frequency, 14.14 rad/sec [10]

B = break frequency, 659.5 rad/sec [10]

The inverse Laplace transform of Equation (2-19) is a third-order, linear differential equation. This can be expressed as three coupled, first order, linear differential equations in state space form. The atmospheric jitter effects can be modeled identically in both the x and y directions. The augmented six-state truth model for atmospheric jitter expressed in Jordan canonical form is [10]:

$$\dot{\mathbf{x}}_a(t) = \mathbf{F}_a \mathbf{x}_a(t) + \mathbf{G}_a \mathbf{w}_a(t) \quad (2-20)$$

where:

$\mathbf{x}_a(t)$ = 6-dimensional state vector

\mathbf{F}_a = 6 x 6 time-invariant plant matrix

$\mathbf{w}_a(t)$ = 2-dimensional, zero mean, white Gaussian noise process with unit strength and independent components, described as:

$$E[\mathbf{w}_a(t)] = \mathbf{0}$$

$$E[\mathbf{w}_a(t) \mathbf{w}_a^T(t+\tau)] = \mathbf{Q}_a \delta(\tau) = \begin{bmatrix} 1 & 0 \\ 0 & 1 \end{bmatrix} \delta(\tau)$$

The six atmospheric states in the state vector correspond to the low frequency pole and the higher frequency double pole in the x and y FLIR plane directions. The atmospheric plant matrix is defined in Jordan Canonical form as [10:13]:

$$\mathbf{F}_a = \begin{bmatrix} -A & 0 & 0 & 0 & 0 & 0 \\ 0 & -B & 1 & 0 & 0 & 0 \\ 0 & 0 & -B & 0 & 0 & 0 \\ 0 & 0 & 0 & -A & 0 & 0 \\ 0 & 0 & 0 & 0 & -B & 1 \\ 0 & 0 & 0 & 0 & 0 & -B \end{bmatrix} \quad (2-21)$$

and the noise distribution matrix is [10:13-14]:

$$\mathbf{G}_\alpha = \begin{bmatrix} G_1 & 0 \\ G_2 & 0 \\ G_3 & 0 \\ 0 & G_1 \\ 0 & G_2 \\ 0 & G_3 \end{bmatrix} \quad (2-22)$$

where:

$$G_1 = \frac{K_\alpha AB^2}{(A-B)^2}$$

$$G_2 = -G_1$$

$$G_3 = \frac{K_\alpha AB^2}{(A-B)}$$

The equivalent discrete-time model associated with Equation (2-20) is the atmospheric jitter partition of Equation (2-5) and is given by:

$$\mathbf{x}_\alpha(t_{i-1}) = \Phi_\alpha(t_{i-1}, t_i) \mathbf{x}_\alpha(t_i) + \mathbf{w}_{d\alpha}(t_i) \quad (2-23)$$

Mercier [10] showed that the state transition matrix derived from the time-invariant plant matrix of Equation (2-20) is:

$$\Phi_\alpha(\Delta t) = \begin{bmatrix} \Phi_{\alpha 11} & 0 & 0 & 0 & 0 & 0 \\ 0 & \Phi_{\alpha 22} & \Phi_{\alpha 23} & 0 & 0 & 0 \\ 0 & 0 & \Phi_{\alpha 33} & 0 & 0 & 0 \\ 0 & 0 & 0 & \Phi_{\alpha 44} & 0 & 0 \\ 0 & 0 & 0 & 0 & \Phi_{\alpha 55} & \Phi_{\alpha 56} \\ 0 & 0 & 0 & 0 & 0 & \Phi_{\alpha 66} \end{bmatrix} \quad (2-24)$$

where:

$$\phi_{a11} = \phi_{a44} = \exp(-A\Delta t)$$

$$\phi_{a22} = \phi_{a55} = \exp(-B\Delta t)$$

$$\phi_{a23} = \phi_{a56} = \Delta t \exp(-B\Delta t)$$

$$\phi_{a33} = \phi_{a66} = \exp(-B\Delta t)$$

The six-dimensional, zero mean, discrete-time, white, Gaussian noise $\mathbf{w}_{da}(t_i)$ has statistics defined as:

$$E[\mathbf{w}_{da}(t_i)] = \mathbf{0} \quad (2-25a)$$

$$E[\mathbf{w}_{da}(t_i)\mathbf{w}_{da}^T(t_i)] = \mathbf{Q}_{da} = \int_{t_i}^{t_{i+1}} \Phi_a(t_{i+1}, \tau) \mathbf{G}_a \mathbf{Q}_a \mathbf{G}_a^T \Phi_a^T(t_i, \tau) d\tau \quad (2-25b)$$

2.2.3 Bending/Vibration States. Leeney [4] recently added mechanical bending states to the truth model. These states were added to account for vibrational effects in the FLIR data that occur when the sensor is mounted on a moving non-rigid platform. Based on AFWL-conducted tests, Leeney concluded that bending effects in both the x and y FLIR directions could be represented by a second order shaping filter, driven by white Gaussian noise. The Laplace domain transfer function of this shaping filter is represented by [5:33]:

$$\frac{x_b(s)}{w_b(s)} = \frac{K_b \omega_{nb}^2}{s^2 + 2\zeta_b \omega_{nb} s + \omega_{nb}^2} \quad (2-26)$$

where:

x_b = shaping filter output, the FLIR plane positional offset due to bending/vibration

w_b = zero mean, unit strength, white Gaussian noise
with an autocorrelation of:

$$E[w_b(t)w_b(t+\tau)] = Q_b\delta(t-\tau); Q_b = 1$$

K_b = gain adjustment to achieve desired root mean
square (RMS) bending output; $K_b^2 = 5 \times 10^{-13}$

(Note: K_b^2 is given here because the strength of the
bending white noise is expressed in terms of this
parameter, rather than K_b)

ζ_b = damping coefficient, = 0.15

ω_{nb} = undamped natural bending frequency, π rad/sec

Leeney [4:35] determined that the x and y directions could
be treated independently and augmented them together to form
a four-state model. The linear stochastic differential
equation describing the bending/vibration effects is:

$$\dot{x}_b(t) = F_b x_b(t) + G_b w_b(t) \quad (2-27)$$

where:

$x_b(t)$ = 4-dimensional state vector

F_b = 4 x 4 time-invariant plant matrix

$w_b(t)$ = 2-dimensional, zero mean, white Gaussian
noise process with independent components of

unit strength, $Q_b = \begin{bmatrix} 1 & 0 \\ 0 & 1 \end{bmatrix}$

G_b = 4 x 2 noise distribution matrix

The bending plant matrix is defined as [4:142]:

$$F_b = \begin{bmatrix} 0 & 1 & 0 & 0 \\ -\omega_{nb}^2 & -2\zeta_b \omega_{nb} & 0 & 0 \\ 0 & 0 & 0 & 1 \\ 0 & 0 & -\omega_{nb}^2 & -2\zeta_b \omega_{nb} \end{bmatrix} \quad (2-28)$$

and the noise distribution matrix is [4:142]:

$$G_b = \begin{bmatrix} 0 & 0 \\ \omega_{nb}^2 k_p & 0 \\ 0 & 0 \\ 0 & \omega_{nb}^2 k_p \end{bmatrix} \quad (2-29)$$

(Note that k_p is the pixel proportionality constant)

The equivalent discrete-time model for Equation (2-27) is of the form:

$$x_b(t_{i+1}) = \Phi_b(t_{i+1}, t_i) x_b(t_i) + w_{db}(t_i) \quad (2-30)$$

where:

$$\Phi_b(\Delta t) = \begin{bmatrix} \phi_{b1} & \phi_{b2} & 0 & 0 \\ \phi_{b3} & \phi_{b4} & 0 & 0 \\ 0 & 0 & \phi_{b1} & \phi_{b2} \\ 0 & 0 & \phi_{b3} & \phi_{b4} \end{bmatrix} \quad (2-31)$$

and

$$\phi_{b1} = \exp(-\sigma_b \Delta t) \left[\cos(\omega_b \Delta t) + \frac{\sigma_b}{\omega_b} \sin(\omega_b \Delta t) \right]$$

$$\phi_{b2} = \exp(-\sigma_b \Delta t) \left[\frac{1}{\omega_b} \sin(\omega_b \Delta t) \right]$$

$$\phi_{b3} = \exp(-\sigma_b \Delta t) \left[-1 - \left(\frac{\sigma_b}{\omega_b} \right)^2 \right] \sin(\omega_b \Delta t)$$

$$\phi_{b4} = \exp(-\sigma_b \Delta t) \left[\cos(\omega_b \Delta t) - \frac{\sigma_b}{\omega_b} \sin(\omega_b \Delta t) \right]$$

$$\Delta t = \text{sample time interval } [t_{i+1} - t_i]$$

σ_b = real part of the root of the characteristic equation in Equation (2-26)

ω_b = imaginary part of the root of the characteristic equation in Equation (2-26)

The four-dimensional, zero mean, white Gaussian noise process of Equation (2-30) has an equivalent, discrete-time representation with statistics given by:

$$E[\mathbf{w}_{db}(t_i)] = \mathbf{0} \quad (2-32)$$

$$E[\mathbf{w}_{db}(t_i)\mathbf{w}_{db}^T(t_i)] = \mathbf{Q}_{db} = \int_{t_i}^{t_{i+1}} \Phi_b(t_{i+1}, \tau) \mathbf{G}_b \mathbf{Q}_b \mathbf{G}_b^T \Phi_b^T(t_{i+1}, \tau) d\tau \quad (2-33)$$

2.3 Simulation Space

In order to simulate the operation of a FLIR sensor accurately, a "simulation space" has been developed for use on a digital computer. This simulation space has two purposes. First, the representation of a realistic target trajectory through three-dimensional space can be achieved. Second, the simulation space provides the means of mathematically translating the target infrared image and velocity vector in three-dimensional space onto the two-dimensional FLIR image plane. These translations will be discussed in this section. However, the coordinate frames which provide the basis for these transformations will be presented first.

2.3.1 Coordinate Frames. The following coordinate frames are used in the simulation of the operation of the FLIR sensor on a digital computer [14:3:23-24]:

Inertial Frame:

Origin: location of the FLIR sensor

Axes: e_x - due north, tangent to the earth's surface,
defines zero azimuth

e_y - inertial "up" with respect to flat earth
approximation

e_z - vector completing right-hand coordinate set,
defines 90: azimuth

Note: The azimuth angle (α) is measured eastward from e_x .
The elevation angle (β) is measured "up" from the
horizontal plane defined by e_x and e_z .

Target Frame:

Origin: center of mass of the target

Axes: e_v - along the true velocity vector

$e_{\rho v}$ - out the right side of the target,
perpendicular to e_v

$e_{\rho\rho v}$ - vector completing the right-hand
coordinate set

Note: 'v' - along the velocity vector

' ρv ' - perpendicular to the velocity vector

' $\rho\rho v$ ' - perpendicular to both of the above

$\alpha - \beta - r$ Frame:

Origin: center of mass of the target

Axes: e_r - coincident with the true sensor-to-target
LOS vector.

e_α, e_β - define a plane perpendicular to e_r ,
rotated from inertial e_x and e_y by the
azimuth angle (α) and elevation angle (β).

FLIR Image Plane:

This is the FLIR image plane defined by the e_α and e_β unit vectors. Because of small angle approximations, the "pseudo" azimuth and elevation angles, α' and β' as shown in Figure 2.1, measured with respect to the FLIR LOS vector, are linearly proportional to the x and y cartesian coordinates on the FLIR plane. The x and y coordinates are distances, in pixels, from the center of the FLIR FOV. Observing the FLIR plane from the inertial origin, x is positive to the right and y is positive down. This convention is used to maintain a right-handed coordinate system. The inertial and target frames, as well as the FLIR image plane, are illustrated in Figures 2.1. and 2.2. Note that, for interpreting the projections in Figure 2.2, the e_y direction is not necessarily in the FLIR image plane; this will be developed further in Section 2.3.3.

2.3.2 Target Model The basic target model used for this and previous theses [14] is a planform with two intensity functions. The spatial relationship between the two intensity functions is shown in Figure 2.3. The displacement of the two Gaussian intensity function centroids along

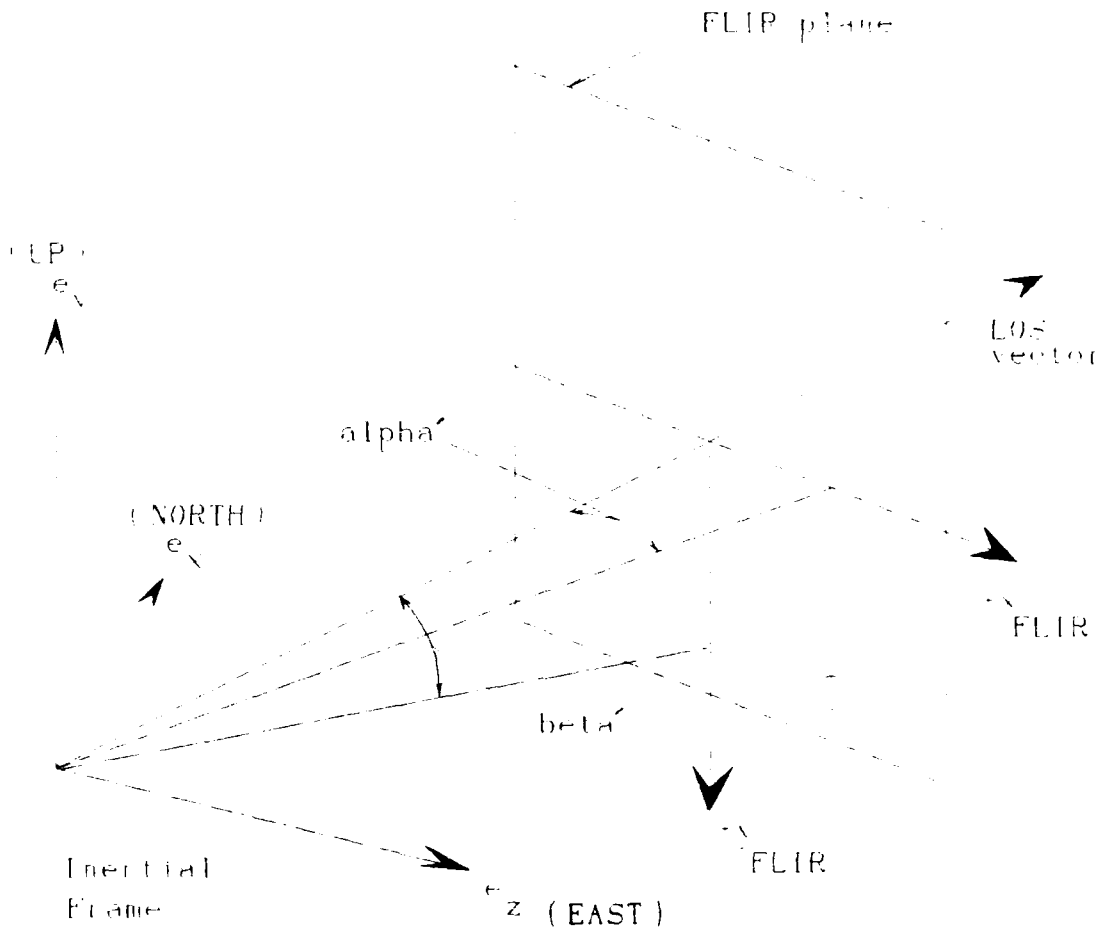


Figure 2.1 The FLIR Plane

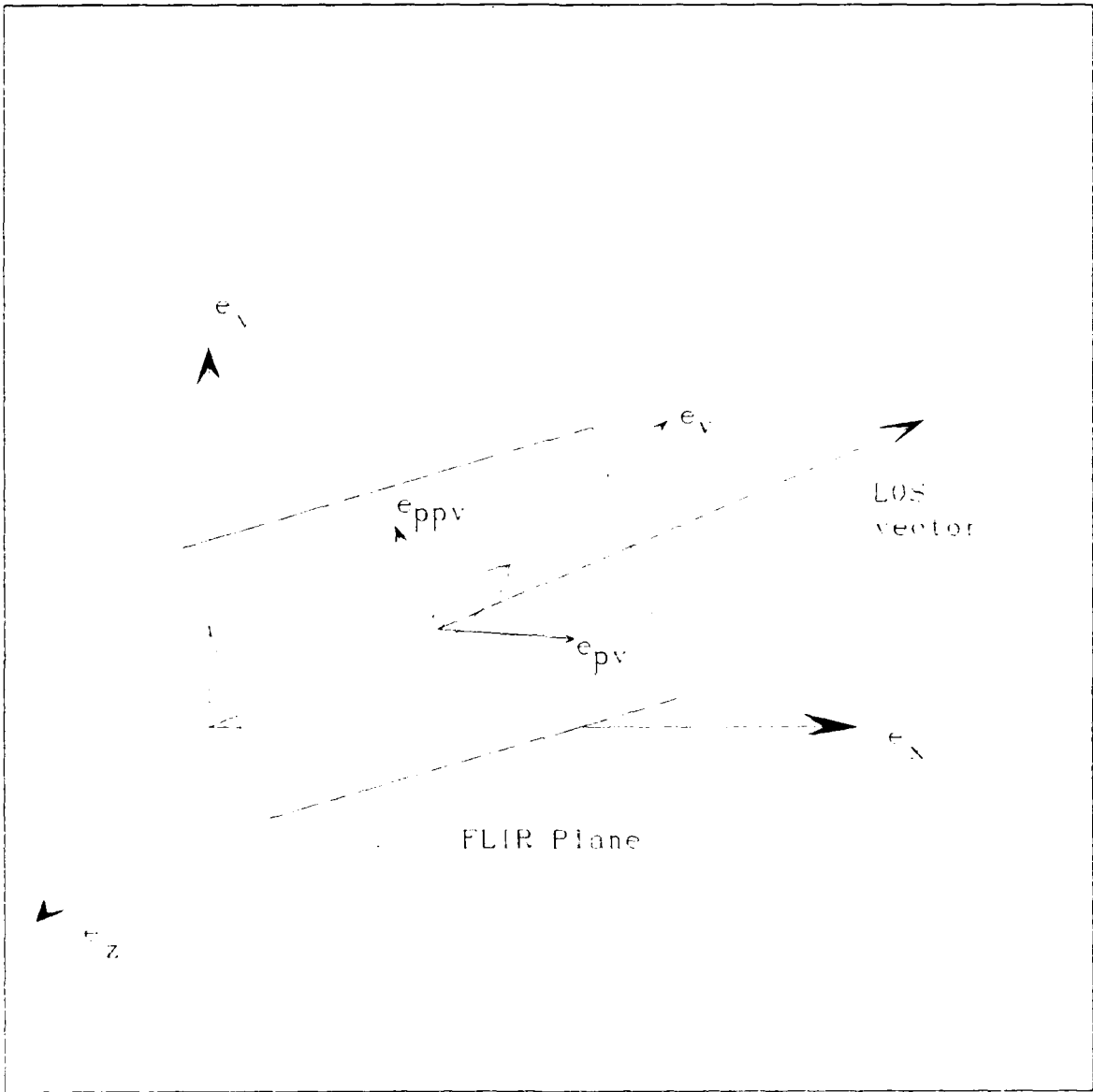


Figure 2.2 The Target Frame

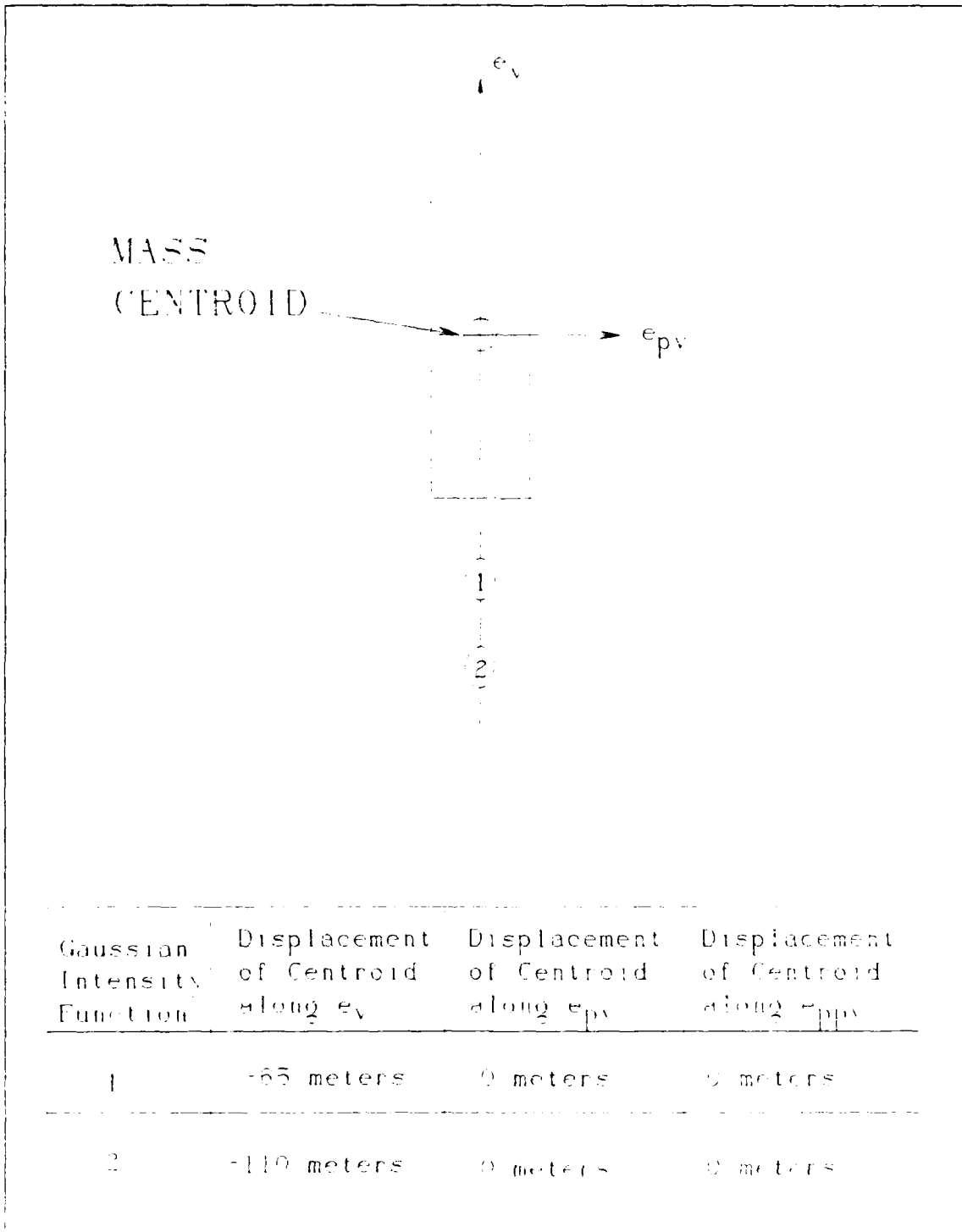


Figure 2.3 Gaussian Intensity Function Distributions

the e_y axis was based on the assumption that the dispersion of the exhaust plume in the e_x direction is approximately 20 times the radius of the missile [14]. The centroid of the first intensity function is located 65 meters behind the center of mass of the missile. This distance was chosen to simulate the composite centroid of the exhaust plume being close to the missile exhaust nozzle, using the assumption that the distance from the missile center of mass to the end of the missile is 20 meters. The second intensity function is located 110 meters from the center of mass. The relationship between the missile center of mass and the centers of these intensity functions remain fixed in the target frame during a simulation, and is indicated in Figure 2.3. As was previously indicated in Section 2.2.1, any external forces acting on the missile other than thrust and gravitational forces are assumed negligible. Therefore, sideslip angle and angle of attack are considered to be zero. These simplifications allow the semi-major axes of the elliptical constant-intensity contours of each of the infrared intensity functions to be aligned with the target's velocity vector, as illustrated in Figure 2.4. As noted in previous thesis efforts [12], this yields a simplification of the simulation space geometry while retaining the essential features of the trajectory simulation necessary for the performance analysis of the tracker.

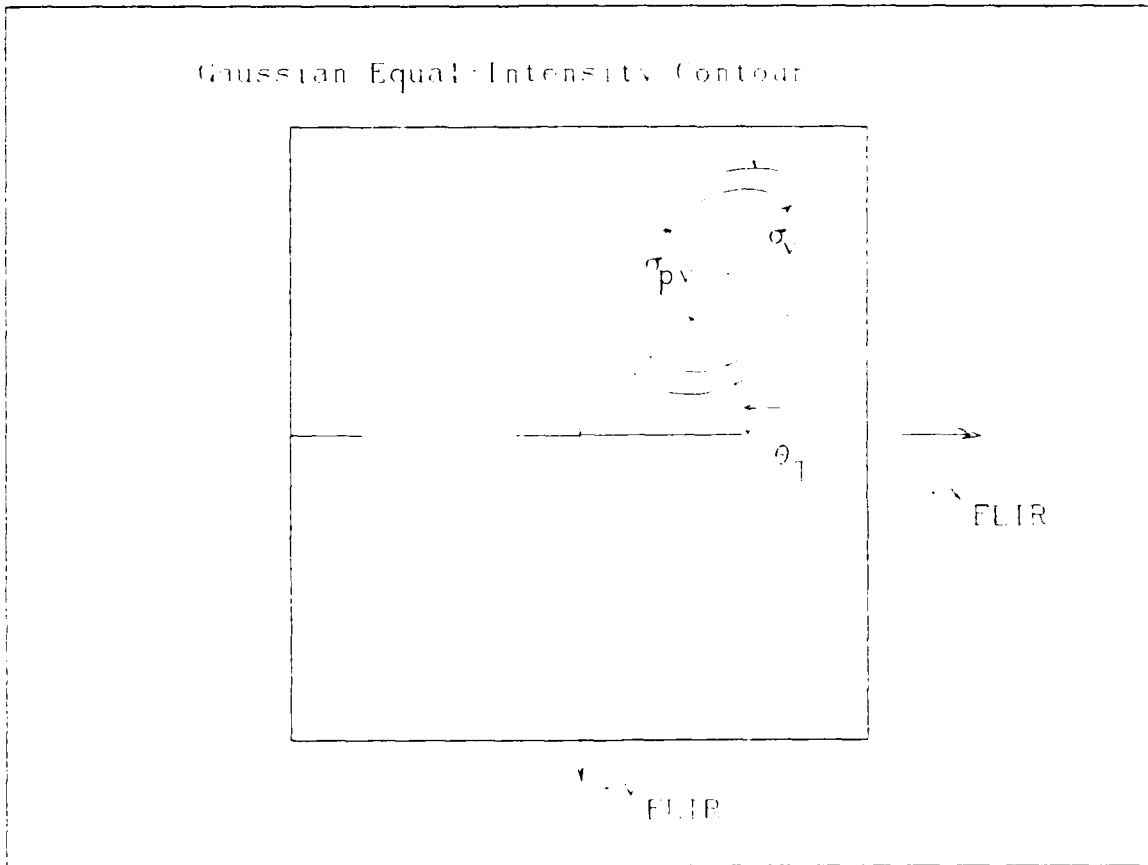


Figure 2-4 Hotspot Dispersion Ellipsoid on FLIR Plane

2.3.3. Target Image Projection onto the FLIR Plane.

During the simulation, as the target propagates through three-dimensional inertial space, the output of the FLIR detector elements in the array is simulated by projecting the target's two intensity functions onto the FLIR plane. In this and previous research [13,14], each of the intensity functions remains fixed with respect to the target frame, while the locations of the intensity functions in the FLIR frame change as the target's orientation relative to the sensor also changes. For simplicity, the location of each of the intensity functions (hotspots) is initialized in the target frame as a displacement from the missile center of mass (Figure 2.3). To orient the intensity functions in the FLIR coordinate frame, they are rotated by the target orientation angle θ_T (Figure 2.4).

Consider the geometry of Figure 2.5. This figure shows the geometrical relationship between the current target image and a "reference target" image in the FLIR plane (Figure 2.3 or 2.4). The reference image is oriented to correspond to the largest apparent planform at a given range. Using Figures 2.4 and 2.5, the current single hot-spot image is defined as [5:37]:

$$\sigma_{\rho v} = \sigma_{\rho v 0} \begin{pmatrix} r \\ r \end{pmatrix} \quad (2-34)$$

$$\begin{aligned} \sigma_v &= \begin{pmatrix} r \\ r \end{pmatrix} (\sigma_{\rho v 0} + (\sigma_{v 0} - \sigma_{\rho v 0}) \cos \gamma) \\ &= \sigma_{\rho v} \left(1 + \frac{v}{u} \cos (AR-1) \right) \end{aligned} \quad (2-35)$$

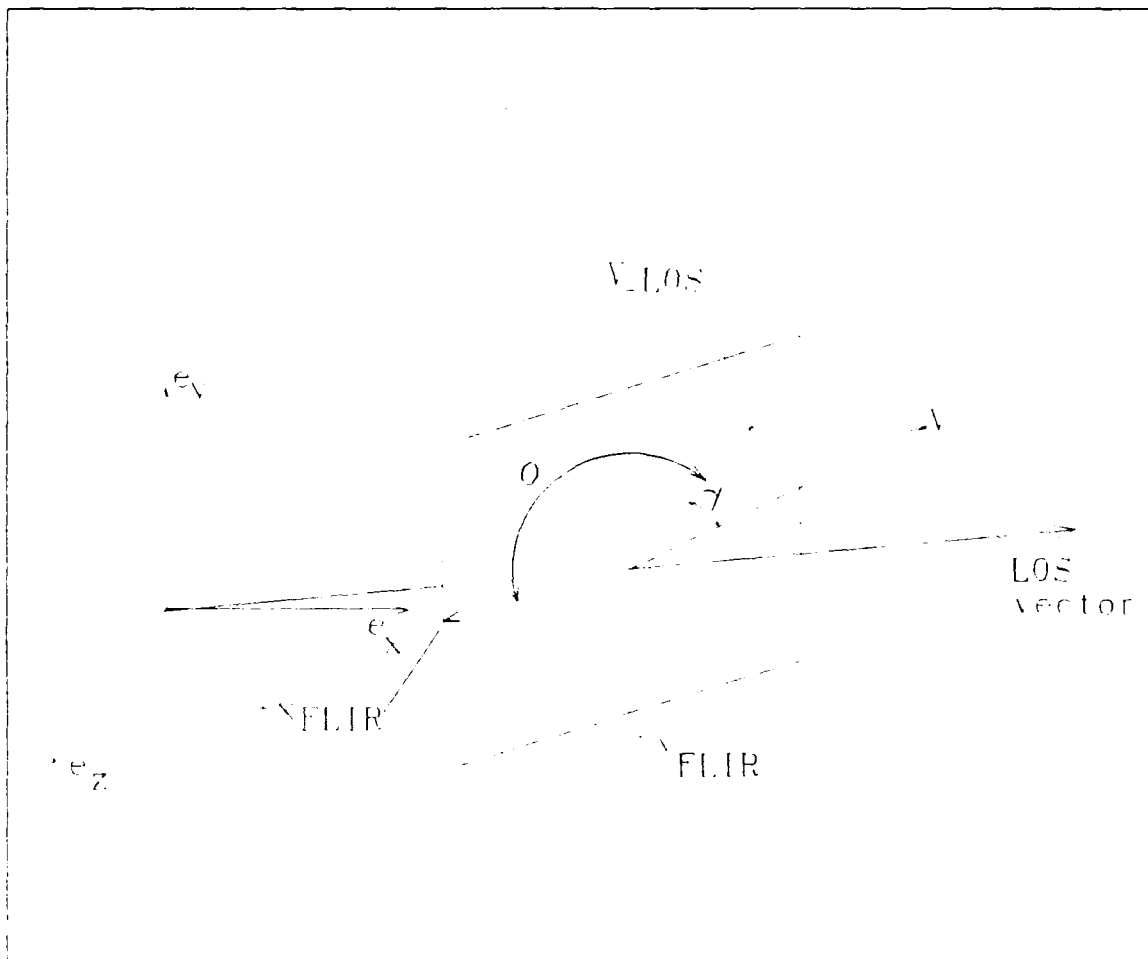


Figure 2.5 Target Image Projection Geometry

where:

$\sigma_{\nu 0}, \sigma_{\rho \nu 0}$ = the initial dispersion of the target
intensity function along e_{ν} and $e_{\rho \nu}$ in the
target frame of the reference image

$\sigma_{\nu}, \sigma_{\rho \nu}$ = the current dispersions of the target image

r_0 = initial sensor-to-target range of the
reference image

r = current sensor-to-target range

\mathbf{v} = target inertial velocity vector

v = magnitude of \mathbf{v}

$\mathbf{v}_{\perp LOS}$ = projection of \mathbf{v} onto the FLIR plane;

the component of \mathbf{v} perpendicular to the
LOS vector

$v_{\perp LOS}$ = magnitude of $\mathbf{v}_{\perp LOS}$; $v_{\perp LOS} = \sqrt{\dot{\alpha}^2 + \dot{\beta}^2}$

γ = angle between \mathbf{v} and the FLIR plane

$AR = \frac{\sigma_{\nu 0}}{\sigma_{\rho \nu 0}}$: aspect ratio of the reference image

Equations (2-34) and (2-35) define the dispersion along the principle axes of the intensity function's constant-intensity ellipses as seen by the FLIR sensor (Figure 2.4). Such a description is accomplished for each of the two intensity functions of Figure 2.3.

2.3.4. Velocity Projection onto the FLIR Plane.

The deterministic input vector, $\mathbf{u}_{Td}(t_i) = [\dot{\alpha}'(t_i) \ \dot{\beta}'(t_i)]^T$ in Equation (2-5), is the projection of the target's inertial

velocity vector onto the FLIR image plane. Harnly and Jensen [2] demonstrated that this projection is based on the geometry illustrated in Figure 2.6. From Figure 2.6, it can be seen that:

$$\alpha(t) = \arctan \left[\frac{z(t)}{x(t)} \right] \quad (2-36)$$

Taking the time derivative of Equation (2-36) and using the fact that the sensor-to-target range is large so that $\dot{\alpha}(t) = \dot{\alpha}'(t)$ yields:

$$\dot{\alpha}'(t) = \dot{\alpha}(t) = \frac{x(t)v_z(t) - z(t)v_x(t)}{x^2(t) + z^2(t)} \quad (2-37)$$

where:

v_x, v_z = components of the target's inertial velocity
in the e_x and e_z directions

In a similar development:

$$\beta(t) = \arctan \left[\frac{y(t)}{r_h(t)} \right] \quad (2-38)$$

$$\dot{\beta}'(t) = \dot{\beta}(t) = \frac{r_h(t)v_y(t) - y(t)\dot{r}_h(t)}{r_h^2(t)} \quad (2-39)$$

where:

$$\dot{r}_h(t) = \frac{x(t)v_x(t) + z(t)v_z(t)}{r_h(t)}$$

v_y = component of the target's inertial velocity in
the e_y direction

Equations (2-37) and (2-39) define the deterministic input vector $u_{T_d}(t_i)$ in the truth model dynamics difference equation, Equation (2-5).

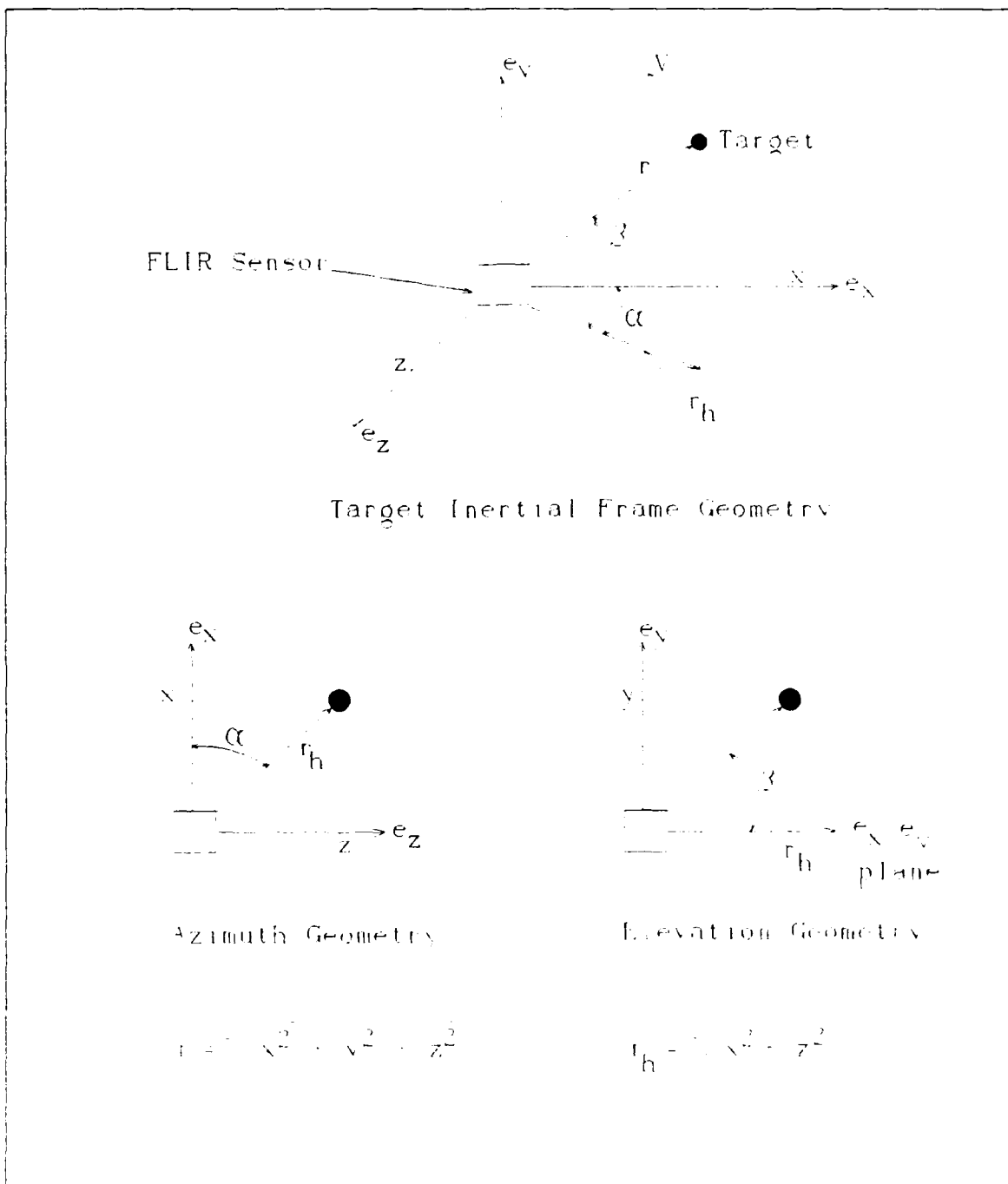


Figure 2.5 Inertial Velocity FLIR Plane Projection Geometry

2.4 Measurement Models

The realistic modelling of measurements of real-world phenomena is an important feature of any simulation. This section of the chapter will describe the method for simulating the measurement output from each infrared detector element in the FLIR array which has been used in previous efforts, as well as in this effort. The method for simulating the output from an optical sensor which receives low power laser light reflected from the missile, as developed for this thesis effort, will also be discussed.

2.4.1 Infrared Measurement Model Information on the target is obtained by measuring the average intensity of the infrared energy received by each detector element in the FLIR array. The target's apparent infrared image or "intensity function" on the pixel array of detectors is the collective sum of effects due to target exhaust plume infrared radiation, background noise, and sensor noise.

Consider the energy radiated from a target with a single intensity function. The infrared intensity function on the FLIR image plane can be modelled as a bivariate Gaussian distribution with elliptical constant intensity contours [2]. This bivariate Gaussian intensity function is given by the following equation [13]:

$$I[x, y, x_{peak}(t), y_{peak}(t)] = I_{max} \exp\{-0.5[\Delta x \Delta y] \mathbf{P}^{-1} [\Delta x \Delta y]^T\} \quad (2-40)$$

where:

$$\Delta x = (x - x_{peak}) \cos \theta_T + (y - y_{peak}) \sin \theta_T$$

$$\Delta y = (y - y_{peak}) \cos \theta_T - (x - x_{peak}) \sin \theta_T$$

θ_T = target orientation angle between the projection of the velocity vector onto the FLIR plane and the FLIR plane x axis; See Figures 2.5 & 2.7

x, y = reference coordinate axes on the FLIR plane

x_{peak}, y_{peak} = coordinates of the peak intensity of the single Gaussian intensity function

I_{max} = maximum intensity of the function

P = 2 x 2 target dispersion matrix whose eigenvalues (σ_u and $\sigma_{\rho u}$) define the dispersion of the elliptical constant intensity contours (along the velocity vector and perpendicular to the velocity vector) in the FLIR plane (see Section 2.3.3)

The composite FLIR plane image intensity function, represented as the difference between two individual intensity functions for a missile exhaust plume, is shown in Figure 2.7. To form the characteristic crescent shape of a missile plume, the rear individual intensity function is subtracted from the forward intensity function. Since the intensity value from an FLIR sensor element cannot be nega-

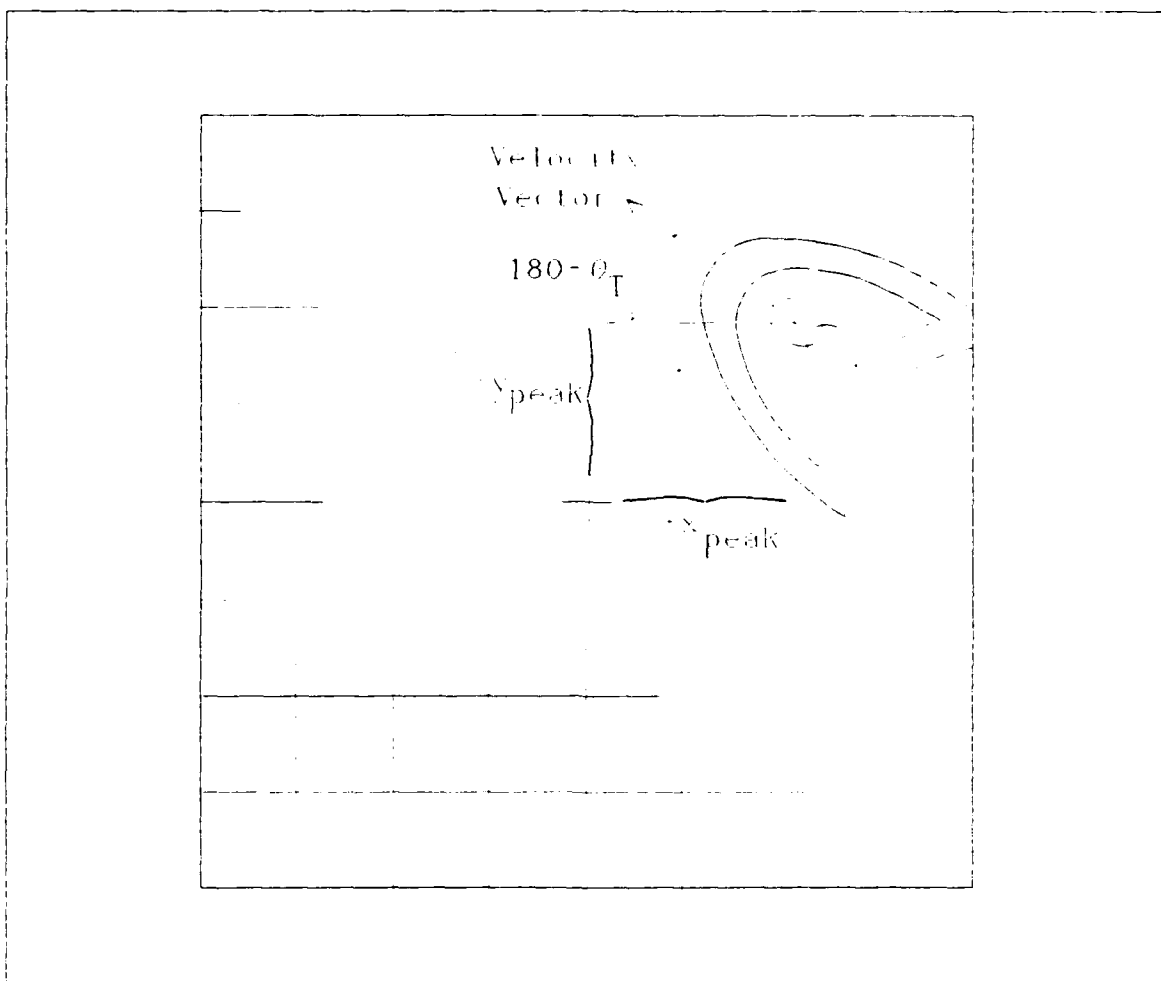


Figure 2.7 FLIR Image Plane Intensity Function for the Difference Between Two Gaussian Intensity Functions

tive, the simulation software sets any calculated negative intensity values to zero.

The intensity measurement produced by each sensor pixel is the average infrared energy intensity on that pixel. This intensity is the sum of the target's intensity function, spatially correlated background noise, and FLIR sensor noise. The output of the sensor pixel in the j^{th} row and k^{th} column of the array at time t_i is [14]:

$$z_{jk}(t_i) = \frac{1}{A_p} \int_{pixel_{jk}} \{ I_1[x, y, x_{peak_1}(t_i), y_{peak_1}(t_i)] - I_2[x, y, x_{peak_2}(t_i), y_{peak_2}(t_i)] \} dx dy + n_{jk}(t_i) + b_{jk}(t_i) \quad (2-41)$$

where:

$z_{jk}(t_i)$ = output of pixel jk , average intensity on that pixel

A_p = area of one pixel

I_1, I_2 = intensity function of the first and second Gaussian intensity function (see Figures 2.3 and 2.7)

x, y = coordinates of any point within pixel jk

x_{peak_1}, y_{peak_1} = coordinates of maximum intensity of the first Gaussian intensity point

x_{peak_2}, y_{peak_2} = coordinates of maximum intensity of the second Gaussian intensity point

$n_{jk}(t_i)$ = effect of internal FLIR sensor noise on pixel jk

$b_{jk}(t_i)$ = effect of spatially correlated background noise
on pixel jk

The sensor error $n_{jk}(t_i)$ is the result of thermal noise and dark current in the infrared detectors. This error is assumed to be both temporally and spatially uncorrelated [14].

The background noise $b_{jk}(t_i)$ is represented as a spatially correlated noise with radial symmetry, whose correlation decays exponentially. Harnly and Jensen [2] used a correlation distance of approximately two pixels in the FLIR plane, and simulated this by maintaining non-zero correlation coefficients between each pixel and its nearest two neighbors in all directions.

By concatenating all 64 values of b_{jk} (corresponding to an 8 x 8 pixel field of view) into a 64-dimensional vector $\mathbf{b}(t_i)$, the spatially correlated background noise is modelled as [14]:

$$\mathbf{b}(t_i) = \sqrt{\mathbf{R}} \mathbf{b}'(t_i) \quad (2-42)$$

where:

\mathbf{R} = 64 x 64 correlation matrix of the discrete,
zero mean, white Gaussian vector noise process $\mathbf{b}(t_i)$

$\mathbf{b}'(t_i)$ = 64-dimensional, discrete, zero-mean, white
Gaussian vector noise process with the
correlation matrix \mathbf{I}_{64} .

$\sqrt{\mathbf{R}}$ = Cholesky square root

A detailed development of this spatially correlated noise process as well as the FLIR sensor noise process can be found in the work of Harnly and Jensen [2]. It is mentioned here only for completeness in describing the truth model. The actual parameters used for the sensor error and the background noise will be detailed in Chapter 4.

2.4.2 Laser Reflection Measurement Model For this initial effort, no attempt was made to model the physical phenomena involved with laser light reflected from the missile hardbody being received by an optical sensor. Since the purpose of reflected laser light would be to provide information on the location of the missile center of mass, an attempt was made to model the information about the center of mass which would be derived from reflected laser light.

The scenario for development of the missile center of mass measurement is a continuation of that used by Rizzo [14]. A ballistic missile in boost phase is tracked using measurements from the FLIR sensor. The "pseudo" measurements derived from the FLIR sensor measurements and enhanced correlator are input to a Kalman filter, which provides position and velocity estimates of the infrared image centroid of the exhaust plume. The enhanced correlator will be described in Chapter 4. These estimates are then used to aim a low power laser along the filter estimated velocity

vector from the estimated center of intensity. Any reflections received from the missile provide information about the missile center of mass. By observing the characteristics of the return signal from the laser being swept along the velocity vector, one can anticipate getting an indication of when the laser passes the interface between the hardbody and just background, at both ends of the missile hardbody. Since the image intensity centroid position and velocity estimates are in terms of FLIR plane variables, a decision was made to simulate the mass center measurement in the FLIR plane also. With this decision, the problem of simulation then becomes a problem involving plane geometry.

The first phase of the simulation involves the projection of the three-dimensional missile hardbody onto the two-dimensional FLIR plane. For simplification, a rectangle was chosen to represent the shape of the missile hardbody projection. With the assumption that the longitudinal axis of the missile hardbody is aligned with the velocity vector, the geometry for projection of the missile's three-dimensional length onto the FLIR plane is shown in Figure 2.5.

The geometry is described by:

$$\text{Length}_{FLIR} = \cos \gamma \text{ Length}_{Actual} \quad (2-43)$$

where:

Length_{FLIR} = FLIR plane projection of missile length

γ = angle between \mathbf{v} and the FLIR plane (radians)

Length_{Actual} = true missile length in pixels

Since the missile is cylindrical, the projection of the missile diameter onto the FLIR plane is equal to the missile diameter. Once the projection of the missile's dimensions onto the FLIR plane is accomplished, the rectangle representing the missile is located on the FLIR plane by offsetting the rectangle's center from the truth model image centroid along the FLIR plane truth model velocity vector. The offset distance was chosen by using the intensity function displacements in Figure 2.3.

The next step in the simulation involves the determination of the missile center of mass measurement. This is accomplished geometrically. The path along which the laser would be dithered is represented by a rectangle (a rectangle rather than a line was used to account for the laser beam width). If the laser hits the missile, some form of reflection is obtained. This reflection is geometrically simulated by having the two rectangles overlap as shown in Figure 2.8a. The coordinates of this overlap area are determined by finding the intersections of the line segments representing the sides of the rectangles. These intersection points, as shown in Figure 2.8b, (representing the corners of some enclosed area) are used to determine the centroid of the area of intersection (and presumably reflection). Once the center of mass measurements coordinates have been calculated, the offset distance from the filter estimated image centroid is determined. In the simulation, if the combina-

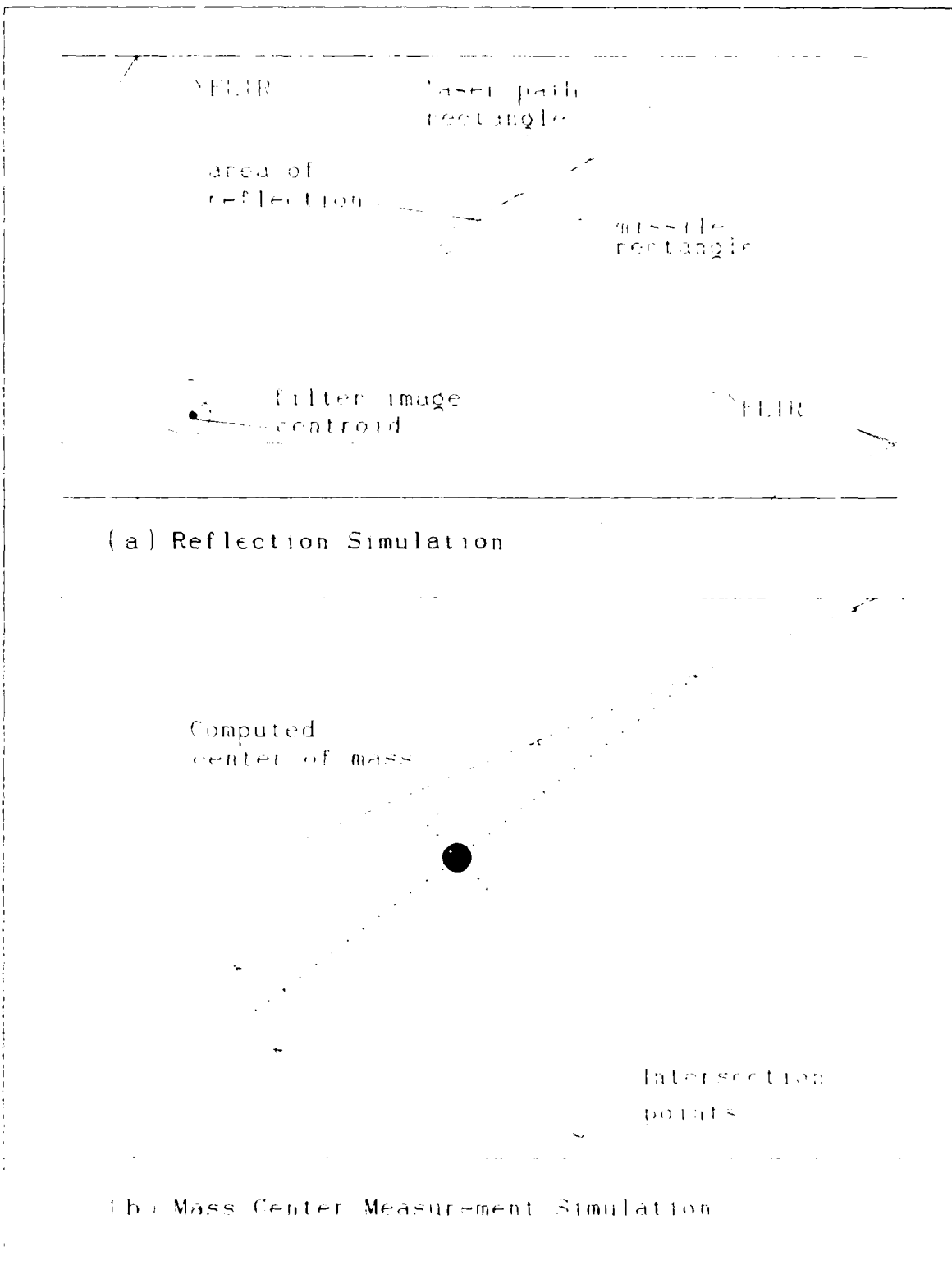


Figure 2.8 Center of Mass Measurement Geometry

tion of estimated intensity centroid position and estimated velocity vector orientation is not accurate enough to cause the two rectangles to overlap, then no "reflection" occurs, and no measurement update occurs in the filter. In this case, the filter simply propagates the estimate until a reflection does occur. A complete development of the geometrical simulation of the mass center measurement is detailed in Appendix A.

The offset measurement which is available for filter use is modeled by adding measurement noise. The output of the sensor at time t_i is:

$$z(t_i) = L_{offset}(t_i) + v(t_i) \quad (2-44)$$

where:

$z(t_i)$ = sensor output at time (t_i)

$L_{offset}(t_i)$ = offset of center of mass from filter estimated FLIR image centroid along the filter-estimated velocity direction in the FLIR plane

$v(t_i)$ = discrete, zero mean, white Gaussian measurement noise with statistics $E\{v(t_i)\} = 0$,
 $E\{v(t_i)v(t_j)\} = R(t_i), \quad i=j, \quad 0 \text{ otherwise}$

The simulated measurement developed in this section will be related to the linear filter measurement model in Chapter 3. The parameters used for the measurement noise strength will be discussed in Chapter 5.

2.5 Summary

This chapter has developed the truth model dynamic system as the augmentation of a deterministic target trajectory component, a stochastic component due to atmospheric jitter, and a stochastic component due to mechanical bending/vibration. In order to simulate the operation of a tracker on a computer, a simulation space with various coordinate frames and a target model was developed. Finally, a measurement model for the output of the infrared detectors in the FLIR array and a model for the output of the optical sensor receiving returns from the reflected laser light were developed.

3. Filter Models

3.1 Introduction

This chapter presents the filter models used in this thesis effort. Section 3.2 develops the six-state filter, based on FLIR measurements, which consists of target dynamic states and atmospheric jitter states. Section 3.3 develops the single state filter, based on the processing of low-power laser returns, which estimates the offset distance between the image centroid and the missile center of mass. The measurement models used in each of the filters are also developed.

3.2 FLIR Filter

The filter initially used at the beginning of this thesis was based on the eight-state benchmark filter used by Rizzo [14]. Based on the results of the observability analyses (see Chapter 5), the target acceleration states were deleted from the filter. For the remainder of this thesis work, a six-state linear Kalman filter was used to provide state estimates for the FLIR image position and velocity, as well as estimates of atmospheric jitter.

3.2.1 Dynamics Model. Previous AFIT research has considered two different models for representing target dynamics. The first model represents target acceleration as

a zero mean, first-order Gauss-Markov process; the second describes acceleration using a constant turn-rate model. With the deletion of acceleration states from the previously used eight-state filter, a new representation for target velocity was needed. A decision was made [8,14] to represent target velocity as a zero mean, first-order Gauss-Markov process. This is because time-correlated physical states such as position, velocity, and acceleration can often be well represented by an exponentially time-correlated first-order Gauss-Markov process. The state vector for the six-state Kalman filter used in this research is defined as:

$$\begin{bmatrix} x_1 \\ x_2 \\ x_3 \\ x_4 \\ x_5 \\ x_6 \end{bmatrix} = \begin{bmatrix} x_t \\ y_t \\ v_x \\ v_y \\ x_a \\ y_a \end{bmatrix} \quad (3-1)$$

where the states are:

$x_t = x$ (i.e., azimuth) component of FLIR image centroid position due to target dynamics

$y_t = y$ (i.e., elevation) component of FLIR image centroid position due to target dynamics

$v_x = x$ component of FLIR image velocity

$v_y = y$ component of FLIR image velocity

$x_a = x$ component of atmospheric jitter

$y_a = y$ component of atmospheric jitter

Each element in Equation (3-1) is coordinatized in the FLIR plane. Note that the atmospheric jitter model has been reduced from the six-state form in the truth model (see Section 2.2.2) to the two-state model seen here. The effect of the higher frequency double pole was negligible [13] and was disregarded to reduce the filter order. Also note the omission of any bending/vibration states. Leeney [4] tested the omission of bending states from a similar filter, and found no significant degradation in filter performance. The filter model is described by the following time-invariant, linear stochastic differential equation:

$$\dot{\mathbf{x}}_f(t) = \mathbf{F}_f \mathbf{x}_f(t) + \mathbf{G}_f \mathbf{w}_f(t) \quad (3-2)$$

where:

$\mathbf{x}_f(t)$ = six-state filter state vector of Equation (3-1)

\mathbf{F}_f = time-invariant system plant matrix

\mathbf{G}_f = time-invariant noise distribution matrix

$\mathbf{w}_f(t)$ = zero mean, white Gaussian noise vector of strength \mathbf{Q}_f

and

$$\mathbf{F}_f = \begin{bmatrix} 0 & 0 & 0 & 0 & 0 & 0 \\ 0 & 0 & 0 & 1 & 0 & 0 \\ 0 & 0 & -\frac{1}{\tau_x} & 0 & 0 & 0 \\ 0 & 0 & 0 & -\frac{1}{\tau_v} & 0 & 0 \\ 0 & 0 & 0 & 0 & -\frac{1}{\tau_a} & 0 \\ 0 & 0 & 0 & 0 & 0 & -\frac{1}{\tau_a} \end{bmatrix} \quad (3-3)$$

and

$$G_f = \begin{bmatrix} 0 & 0 & 0 & 0 \\ 0 & 0 & 0 & 0 \\ 1 & 0 & 0 & 0 \\ 0 & 1 & 0 & 0 \\ 0 & 0 & 1 & 0 \\ 0 & 0 & 0 & 1 \end{bmatrix} \quad (3-4)$$

with

$$Q_f = \begin{bmatrix} \frac{2\sigma_x^2}{\tau_x} & 0 & 0 & 0 \\ 0 & \frac{2\sigma_y^2}{\tau_y} & 0 & 0 \\ 0 & 0 & \frac{2\sigma_a^2}{\tau_a} & 0 \\ 0 & 0 & 0 & \frac{2\sigma_a^2}{\tau_a} \end{bmatrix} \quad (3-5)$$

where:

τ_x, τ_y = correlation times for the target x and y velocities

τ_a = correlation time for the atmospheric jitter position process

σ_x^2, σ_y^2 = variance and mean-squared value for the target x and y velocities

σ_a^2 - variance and mean-squared value for the atmospheric jitter position process

The parameters used for the filter correlation times and variances will be described in Chapter 5.

The filter state estimate and error covariance matrix are propagated forward over a sample period using the following equations [6:171-172]:

$$\hat{\mathbf{x}}_f(t_{i-1}^-) = \Phi_f(\Delta t) \hat{\mathbf{x}}_f(t_i^-) \quad (3-6)$$

$$\mathbf{P}_f(t_{i-1}^-) = \Phi_f(\Delta t) \mathbf{P}_f(t_i^-) \Phi_f^T(\Delta t) + \mathbf{Q}_{df} \quad (3-7)$$

where:

$\hat{\mathbf{x}}_f(t_i)$ = filter estimate of 6-dimensional state vector

$\mathbf{P}_f(t_i)$ = filter covariance matrix (6x6)

(t_i^-) = time instant before FLIR measurement is incorporated into the estimate at time t_i

(t_i^+) = time instant after FLIR measurement is incorporated into the estimate at time t_i

$\Phi_f(\Delta t)$ = time invariant state transition matrix for propagation over the sample period: $\Delta t = t_{i-1} - t_i$

and \mathbf{Q}_{df} is defined as:

$$\mathbf{Q}_{df} = \int_{t_i}^{t_{i+1}} \Phi_f(t_{i+1}, \tau) \mathbf{G}_f \mathbf{Q}_f \mathbf{G}_f^T \Phi_f^T(t_{i+1}, \tau) d\tau \quad (3-8)$$

with

$$\Phi_f(\Delta t) = \begin{bmatrix} 1 & 0 & \phi_{13} & 0 & 0 & 0 \\ 0 & 1 & 0 & \phi_{24} & 0 & 0 \\ 0 & 0 & \phi_{33} & 0 & 0 & 0 \\ 0 & 0 & 0 & \phi_{44} & 0 & 0 \\ 0 & 0 & 0 & 0 & \phi_{55} & 0 \\ 0 & 0 & 0 & 0 & 0 & \phi_{66} \end{bmatrix} \quad (3-9)$$

where:

$$\phi_{13} = \tau_x (1 - \exp(-\frac{\Delta t}{\tau_x}))$$

$$\phi_{24} = \tau_y (1 - \exp(-\frac{\Delta t}{\tau_y}))$$

$$\phi_{33} = \exp(-\frac{\Delta t}{\tau_x})$$

$$\phi_{44} = \exp\left(-\frac{\Delta t}{\tau_y}\right)$$

$$\phi_{55} = \phi_{66} = \exp\left(-\frac{\Delta t}{\tau_a}\right)$$

and

$$Q_{df} = \begin{bmatrix} q_{df11} & 0 & q_{df13} & 0 & 0 & 0 \\ 0 & q_{df22} & 0 & q_{df24} & 0 & 0 \\ q_{df31} & 0 & q_{df33} & 0 & 0 & 0 \\ 0 & q_{df42} & 0 & q_{df44} & 0 & 0 \\ 0 & 0 & 0 & 0 & q_{df55} & 0 \\ 0 & 0 & 0 & 0 & 0 & q_{df66} \end{bmatrix} \quad (3-10)$$

where:

$$q_{df11} = 2\sigma_x^2\tau_x\left[\Delta t - 2\tau_x(1 - \exp(-\frac{\Delta t}{\tau_x})) + \frac{\tau_x}{2}(1 - \exp(-\frac{2\Delta t}{\tau_x}))\right]$$

$$q_{df22} = 2\sigma_y^2\tau_y\left[\Delta t - 2\tau_y(1 - \exp(-\frac{\Delta t}{\tau_y})) + \frac{\tau_y}{2}(1 - \exp(-\frac{2\Delta t}{\tau_y}))\right]$$

$$q_{df13} = 2\sigma_x^2\left[2\tau_x(1 - \exp(-\frac{\Delta t}{\tau_x})) - \frac{\tau_x}{2}(1 - \exp(-\frac{2\Delta t}{\tau_x}))\right]$$

$$q_{df24} = 2\sigma_y^2\left[2\tau_y(1 - \exp(-\frac{\Delta t}{\tau_y})) - \frac{\tau_y}{2}(1 - \exp(-\frac{2\Delta t}{\tau_y}))\right]$$

$$q_{df31} = q_{df13}$$

$$q_{df33} = \sigma_x^2(1 - \exp(-\frac{2\Delta t}{\tau_x}))$$

$$q_{df42} = q_{df24}$$

$$q_{df44} = \sigma_y^2(1 - \exp(-\frac{2\Delta t}{\tau_y}))$$

$$q_{df55} = q_{df66} = \sigma_a^2(1 - \exp(-\frac{2\Delta t}{\tau_a}))$$

The pointing controller used for this and previous studies is idealized. Physical implementation considerations, such as servo lag and inertia, are neglected. Netzer [12] demonstrated that any errors generated by the use of an

idealized controller are small and are interpreted by the Kalman filter as atmospheric jitter. Following the filter propagation cycle, the estimates $\hat{x}_1(t_{i-1})$ and $\hat{x}_2(t_{i-1})$ are used to generate control signals to point the FLIR sensor optical centerline at the target.

3.2.2 Measurement Model. As an alternative to the 64-dimensional, non-linear measurement model of Equation (2-41), Rogers [15] developed an enhanced correlation algorithm to provide two "measurements" of centroid offsets in the FLIR plane to a linear Kalman filter measurement model. The correlation algorithm enhancement occurs in several ways [18].

First, the current FLIR data frame is correlated with a template (an estimate of the target's intensity function), instead of being correlated with the previous FLIR data frame. This template will be developed in Section 3.2.2.1. Second, instead of outputting the peak of the correlation function, the enhanced correlator outputs the center of mass of that portion of the correlation function that is greater than some predetermined lower bound, a technique known as "thresholding". Therefore, the enhanced correlator does not suffer the problem of distinguishing global peaks from local peaks, as do many conventional "peak-finding" correlation algorithms. Third, by using the enhanced correlation algorithm, the FLIR/laser pointing commands are generated via

the Kalman filter propagation cycle rather than as the "raw measurement" output of a standard correlation algorithm. Finally, the Kalman filter state estimate is used to center the template, so that the offsets seen in the enhanced correlator algorithm should be smaller than in the conventional correlator. This increases the amount of "overlap" between the actual FLIR data and the stored template, thus improving performance.

The outputs of the enhanced correlator are the two FLIR plane x and y offsets of Equations (2-1) and (2-2). It is these enhanced or "pseudo-measurements", rather than the raw FLIR data, which are used in the linear Kalman filter measurement update cycle. An overview of the enhanced correlation process is presented next. For a more detailed development, see Rogers [15].

3.2.2.1 Template Generation. The template described in this section is part of an overall data processing algorithm, shown in Figure 3.1. The following discussion of the template refers to the "Form Smoothed Template" block in Figure 3.1.

The template (an estimate of the target's intensity function) is generated by averaging the N most recent centered intensity functions observed by the FLIR sensor. The intensity functions are centered on the FLIR plane by use of the "shifting" property of the Fourier transform, since the frequency domain is where the correlation is being

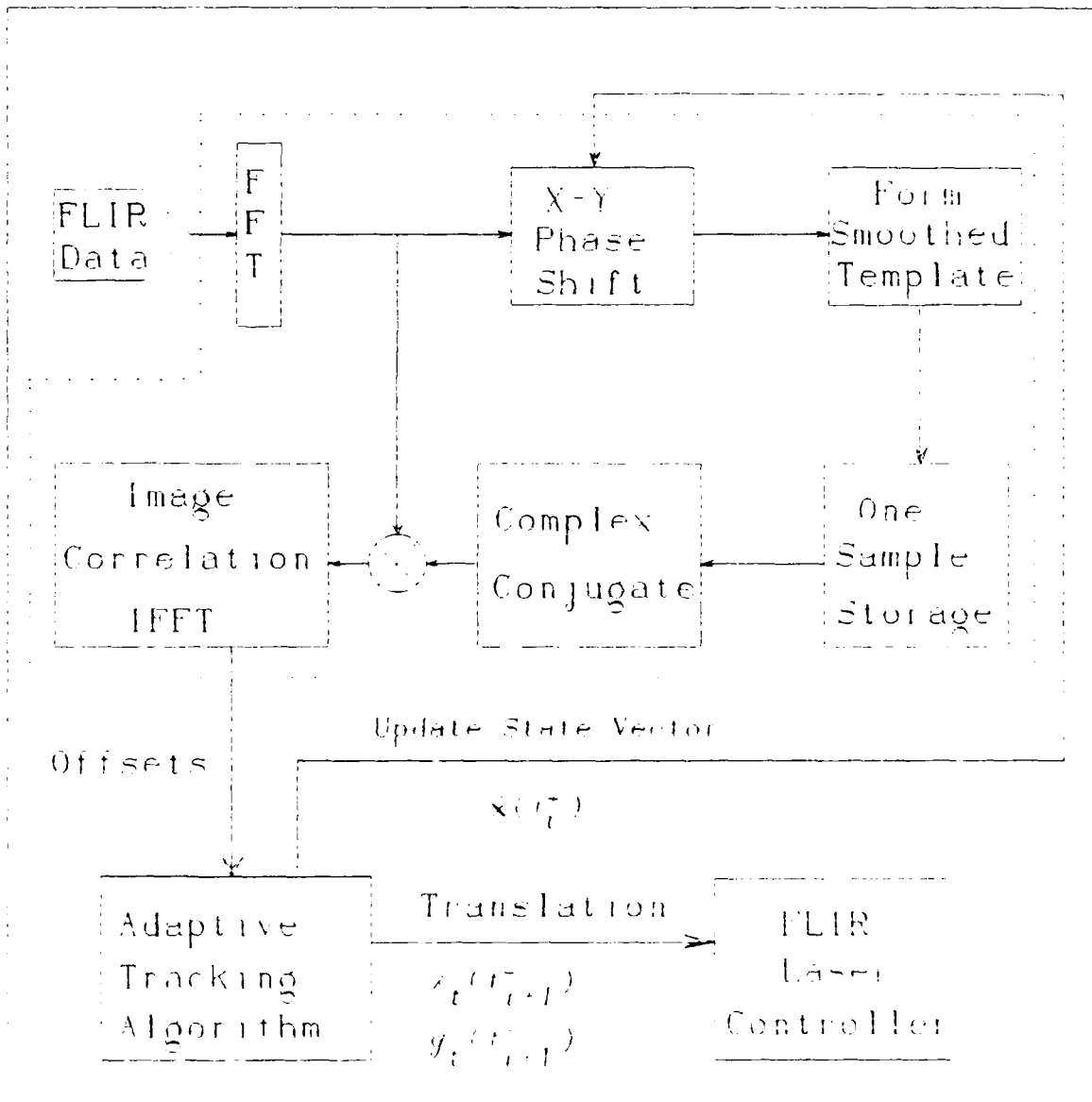


Figure 3.1 Enhanced Correlator Linear Measurement Model Data Processing Algorithm

determined. The value of the memory size N is determined by the dynamics of the target intensity function, with more dynamically changing functions requiring smaller values of N.

For online filter applications, the use of true finite memory filtering techniques causes difficulties with constraints on computer memory. To avoid these difficulties, "exponential smoothing" was used to approximate the averaging. The properties of exponential smoothing are very similar to finite memory filtering [7], but with the advantage of only requiring storage for the FLIR data from the previous sample instead of N previous samples. The exponential smoothing algorithm maintains the template by the use of the following equation:

$$\hat{I}(t_i) = \gamma I(t_i) + (1-\gamma)\hat{I}(t_{i-1}) \quad (3-11)$$

where:

$\hat{I}(t_i)$ = "smoothed estimate" (template) of target's
intensity function

$I(t_i)$ = "raw" intensity function from the current FLIR
data frame

γ = smoothing constant; $0 < \gamma \leq 1$

The smoothing constant's value is comparable to the value selected for N. Larger smoothing constant values emphasize the current FLIR data and correspond to small values of N.

Based on previous studies [3,5,11,13,14,17], a value of 0.1 will be used for the smoothing constant.

Figure 3.1 details the structure of the overall enhanced correlation/linear measurement model data processing algorithm. This structure deals with an algorithm which uses data from a non-rotated FLIR field of view. For this thesis work, the algorithm was modified to use a diagonally rotated FLIR field of view. That modification will be presented in Chapter 4. When the incoming FLIR data is received, a transformation to the Fourier domain by a fast Fourier transform is done. The FLIR image data is then centered in the FLIR plane by use of the shifting property of the Fourier transform. The filter computed shift is equal to:

$$x_{\text{shift}}(t_i) = \hat{x}_t(t_i) + \hat{x}_a(t_i) \quad (3-12)$$

$$y_{\text{shift}}(t_i) = \hat{y}_t(t_i) + \hat{y}_a(t_i) \quad (3-13)$$

where \hat{x}_t , \hat{x}_a , \hat{y}_t , and \hat{y}_a are the estimates of the states defined in Equation (3-1).

There are several reasons for performing a Fourier transformation on the FLIR data. First is that the correlation described in Section 3.2.2.2 is readily done in the Fourier domain. The second is that this form of the algorithm allows for implementation of optical processing [15].

The shifts of Equations (3-12) and (3-13) (the "X-Y Phase Shift" block of Figure 3.1) are performed using the shifting property of Fourier transforms. This property allows translation shifts in the spatial domain to be accomplished by performing a linear phase shift in the Fourier domain [15]. The phase shift is expressed as:

$$F\{g(x-x_{\text{shift}}, y-y_{\text{shift}})\} = G(f_x, f_y) \exp\{-j2\pi(f_x x_{\text{shift}} + f_y y_{\text{shift}})\} \quad (3-14)$$

where:

$g(x, y)$ = 2-dimensional spatial data array

$F\{\cdot\}$ = Fourier transform operator

$G(f_x, f_y) = F\{g(x, y)\}$

After centering, the data is incorporated into the template using the exponential smoothing technique of Equation (3-11). It is this template which is now stored and used for correlation with the next FLIR data frame to produce the "pseudo-measurement" used by the filter.

3.2.2.2 Enhanced Correlation "Pseudo-Measurements".

The template, as developed in the previous section, serves as the filter's best estimate of the shape of the target intensity function prior to receiving a new FLIR data frame. The correlation of the incoming FLIR data with the template provides the position offset of the target intensity function from the center of the field of view. This cross-correlation, performed in the Fourier domain space, is computed

by taking the inverse fast Fourier transform of the following equation [15]:

$$F\{g(x,y) \cdot l(x,y)\} = G(f_x, f_y) L^*(f_x, f_y) \quad (3-15)$$

where:

$F\{\cdot\}$ = Fourier transform operator

$g(x,y) \cdot l(x,y)$ = cross correlation of $g(x,y)$ and $l(x,y)$

$g(x,y)$ = measured target intensity function

$l(x,y)$ = expected target intensity function (template)

$$G(f_x, f_y) = F\{g(x,y)\}$$

$L^*(f_x, f_y)$ = complex conjugate of $F\{l(x,y)\}$

After the inverse fast Fourier transformation has been done, the values of the correlation function $g(x,y) \cdot l(x,y)$ are modified so that any value in the correlation function less than 0.3 [14] of the function's maximum value is set to zero. This "thresholding" technique is used to eliminate false peaks in the correlation function that occur due to noise and other effects. As indicated in Figure 3.1, the output of the inverse fast Fourier transform is the offset of the "thresholded" FLIR intensity function from the center of the FLIR field of view. This offset is assumed to be the result of the summed effects of target dynamics, atmospheric jitter, and measurement noise. Expressed in terms of the filter states of Equation (3-1), the offset measurement in pixels is:

$$X_{offset} = X_t + X_a + X_{jt} \quad (3-16)$$

$$Y_{offset} = Y_t + Y_a + Y_{jt} \quad (3-17)$$

These two measurements can then be represented in state space form as:

$$\mathbf{z}(t_i) = \mathbf{H}_f \mathbf{x}_f(t_i) + \mathbf{v}_f(t_i) \quad (3-18)$$

where:

$$\mathbf{z}(t_i) = [x_{offset}, v_{offset}]^T$$

$\mathbf{x}_f(t_i)$ = state vector of Equation (3-1)

\mathbf{H}_f = 2x6 measurement matrix

$\mathbf{v}_f(t_i)$ = 2-dimensional, discrete-time, zero-mean, white Gaussian measurement noise of covariance \mathbf{R}_f

The measurement matrix, \mathbf{H}_f , is

$$\mathbf{H}_f = \begin{bmatrix} 1 & 0 & 0 & 0 & 1 & 0 \\ 0 & 1 & 0 & 0 & 0 & 1 \end{bmatrix} \quad (3-19)$$

and the covariance matrix \mathbf{R}_f is [9,15]:

$$\mathbf{R}_f = \begin{bmatrix} 0.00363 & 0 \\ 0 & 0.00598 \end{bmatrix} \quad (3-20)$$

The measurement vector and measurement distribution matrix are then used in the linear Kalman filter update equations. It is assumed the reader already has a knowledge of linear Kalman filter theory, so the equations will not be repeated here.

3.3 Center of Mass Offset Filter

The main thrust of this thesis work is to consider the use of additional measurements to aid in determination of

the missile hardbody location. The purpose of the second filter developed in this effort is to estimate the offset distance between the filter image intensity centroid estimate and the missile hardbody center of mass. The decision [8] was made to orient the offset distance angularly using the filter estimated FLIR plane image centroid velocity vector. This decision was based on the desire to use any information already available to aid in determining the missile center of mass location. The six-state filter already provides estimates of the FLIR image velocity, and this should be reflective of the missile hardbody velocity vector. Figure 3.2 shows the physical representation of the filter's estimate of the offset distance.

3.3.1 Dynamics Model. For this effort, the offset between the filter FLIR image centroid and the missile center of mass was represented as a bias. The decision was made [8] to represent this offset bias using a model of an integrator driven by white Gaussian noise (actually pseudo-noise for filter tuning: an undriven integrator yields a bias as an output). The single state representation of the linear, time-invariant, stochastic differential equation is:

$$\dot{x}_{cm\ offset}(t) = w_{cm\ offset}(t) \quad (3-21)$$

where:

$x_{cm\ offset}(t)$ = state representing offset distance between
missile cm and FLIR image centroid

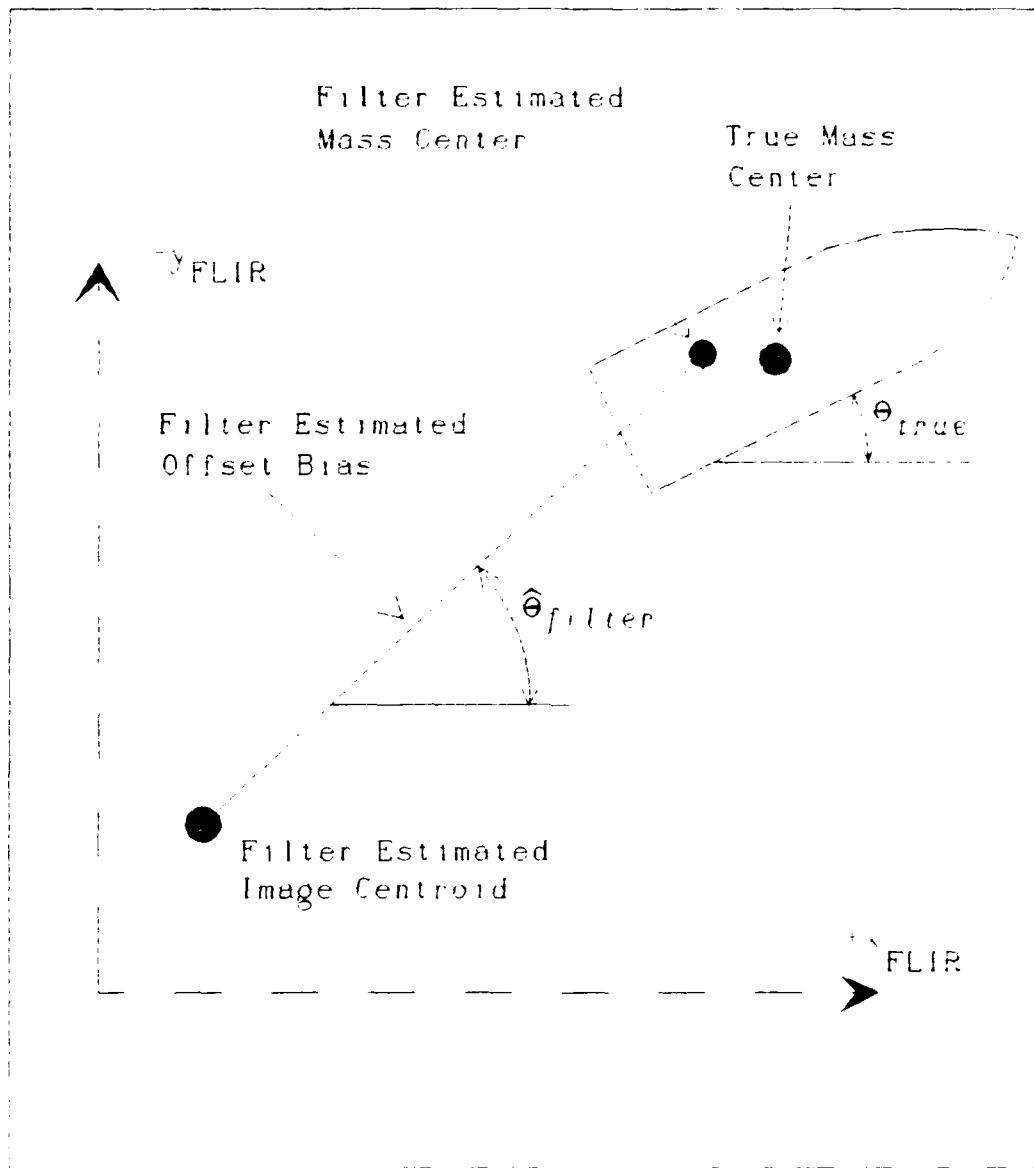


Figure 3.2 Physical Representation of Estimated Filter State

$w_{cm\ offset}(t)$ = zero mean, white Gaussian noise with strength Q

The scalar representation of the filter propagation Equations (3-6) and (3-7) are:

$$\hat{x}_{cm\ offset}(t_{i-1}) = \hat{x}_{cm\ offset}(t_i^-) \quad (3-22)$$

$$P_{cm\ offset}(t_{i-1}) = P_{cm\ offset}(t_i^-) + Q_{d\ cm\ offset} \quad (3-23)$$

3.3.2 Measurement Model.

One of the reasons for the method in which the center of mass offset measurement simulation was developed in Chapter 2 was to preserve linearity in the filter equations. Other formulations (such as separately estimating the x and y components of the bias) were considered, but involved non-linear measurement models. The use of a single state, representing the magnitude of the bias, allowed a linear filter formulation to be used. This allows the scalar measurement model to be expressed as:

$$z_{cm\ offset}(t_i) = x_{cm\ offset}(t_i) + v_{cm\ offset}(t_i) \quad (3-24)$$

where:

$z_{cm\ offset}(t_i)$ = the mass center offset measurement
at time t_i

$v_{cm\ offset}(t_i)$ = discrete-time, zero mean, white Gaussian
measurement noise with variance $R_{cm\ offset}$

3.4 Summary

This chapter has presented models upon which the two Kalman filters used in this thesis effort are based. The

six-state filter includes models to estimate target dynamics and atmospheric jitter. The measurement model included the development of "pseudo-measurements", which are created by correlating the current FLIR data frame with a template representing the target's expected infrared intensity function shape. The second single state filter provides estimates of the offset of the missile hardbody center of mass from the six-state filter estimated FLIR image centroid. The offset was modeled as bias, the output of an undriven integrator, and the white driving noise was added to allow for filter tuning. The offset distance is oriented using the six-state estimate of the FLIR plane FLIR image velocity vector. The measurement model for this filter presented the measurement as a direct representation of the offset state plus measurement noise.

4. Tracking Algorithm and Performance Evaluation Tools

4.1 Introduction

The purpose of this chapter is to present an overall description of the tracking algorithm used in this thesis effort. Modifications to the material presented in Chapter 3 to accommodate a diagonally rotated FLIR field-of-view will be presented. The truth model and filter model parameters used in this work will also be detailed. Finally, the evaluation tools for measuring filter performance will also be shown.

4.2 Tracking Algorithm Overview

The main objective of this thesis research is to develop an algorithm which can accurately track the center of mass of a ballistic missile (in boost phase) using both passively (FLIR) and actively (low power laser reflection off missile hardbody) acquired measurements. This involves development of two separate filters and of the simulation of the actively acquired measurement.

Figure 4.1 details the overall algorithm. The raw FLIR measurement is input into the enhanced correlator data-processing algorithm. This algorithm is contained within the dotted lines of Figure 3.1 in the previous chapter. After the "pseudo-measurements" are produced, they become linear measurements entered into the six-state linear Kalman

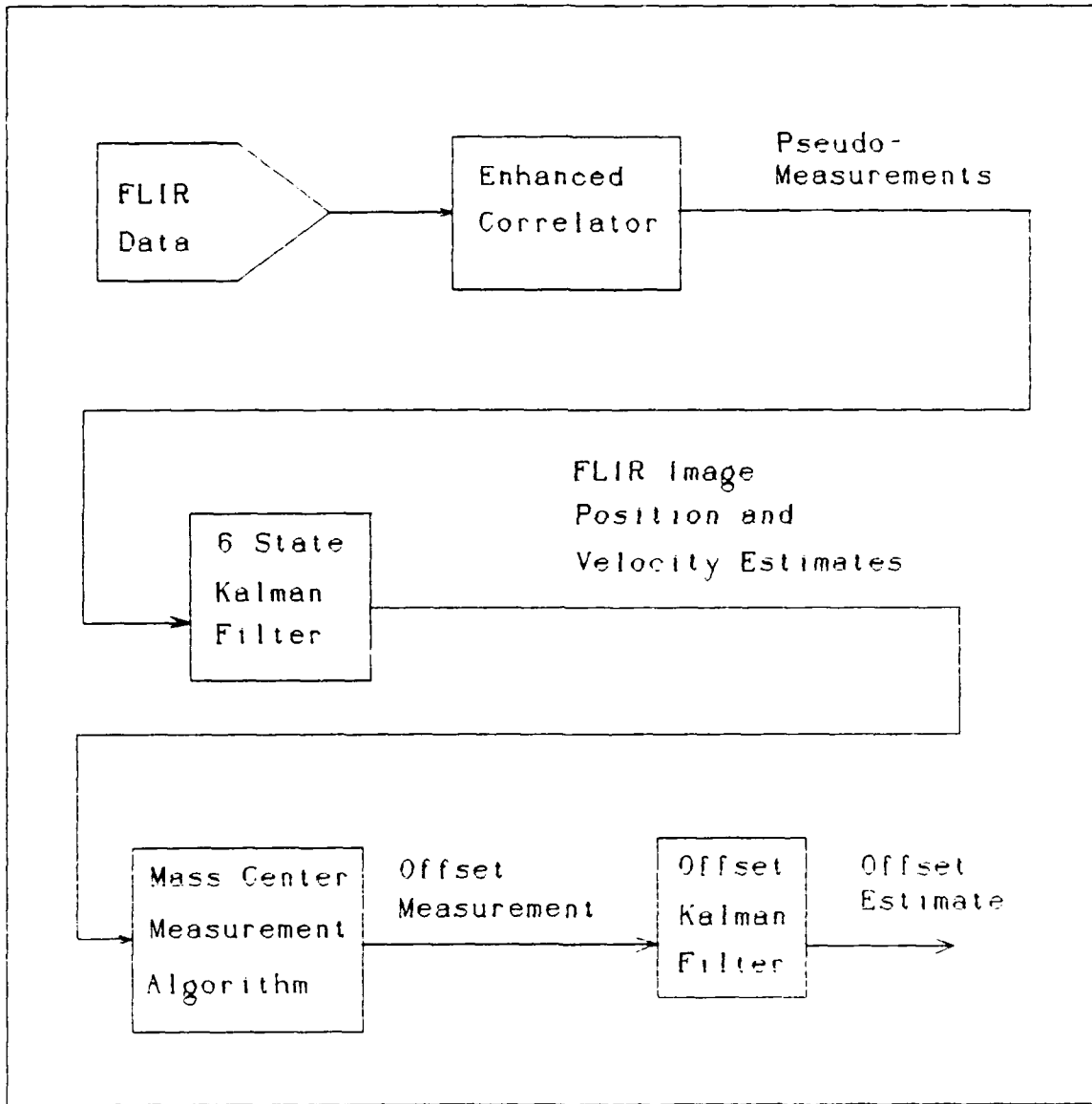


Figure 4.1 Tracking Algorithm

filter. The filter produces estimates of the FLIR plane FLIR image centroid position and velocity vector. These estimates are used by the mass enter measurement algorithm to produce a "pseudo-measurement" representing the output of an optical sensor receiving reflected laser light from the missile hardbody as the laser is swept up and down the velocity vector direction from the estimated centroid location. This output, in the form of an offset distance, is then used by a second filter to produce an estimate of the target center of mass position. This estimate would then be the primary means of aiming a high energy laser at the missile hardbody.

4.3 Field-of-View Rotation

In field-of-view rotation schemes, the FLIR sensor field of view is rotated so that the target's filter-estimated FLIR plane velocity vector is aligned with one of the FLIR plane axes or with some other appropriate direction in the FLIR plane. The idea, first investigated by Leeney [4], was an attempt to maintain lock on highly dynamic targets that could "jink" in either of the two FLIR plane directions. Norton [13] extended Leeney's preliminary work by examining the use of a rotating field-of-view in an MMAF scheme. Most recently, Rizzo [14] investigated the performance of identical filters with different FOV rotation schemes. He compared non-rotating, rotating (aligning the principal axis of

the field-of-view with the estimated velocity vector), and diagonally rotating (aligning the diagonal of the field-of-view with that estimated velocity vector) fields of view. The filter using the diagonally rotated field-of-view (DRFOV) had the lowest mean tracking error and standard deviation. Based on Rizzo's [14] work, it was decided to use a DRFOV in conjunction with the six-state filter.

As previously mentioned in Chapter 3, the use of a rotating field of view causes some modifications to be made to the data processing algorithm of Figure 3.1 of the previous chapter. These modifications are shown in Figure 4.2 with the addition of the "rotate" blocks. These modifications will be described briefly here; for a complete development see Rizzo [14].

The basis for the rotating FOV is the filter estimated target FLIR plane velocity vector orientation. This is given by:

$$\hat{\theta}_f = \arctan \left[\frac{-\hat{v}_y}{\hat{v}_x} \right] \quad (4-1)$$

where $\hat{\theta}_f$ is shown in Figure 3.2

Note that the terms in Equation (4-1) are the third and fourth states in the six-state filter defined in Equation (3-1). This allows the filter to provide the orientation control directly to the FLIR sensor for on-line application.

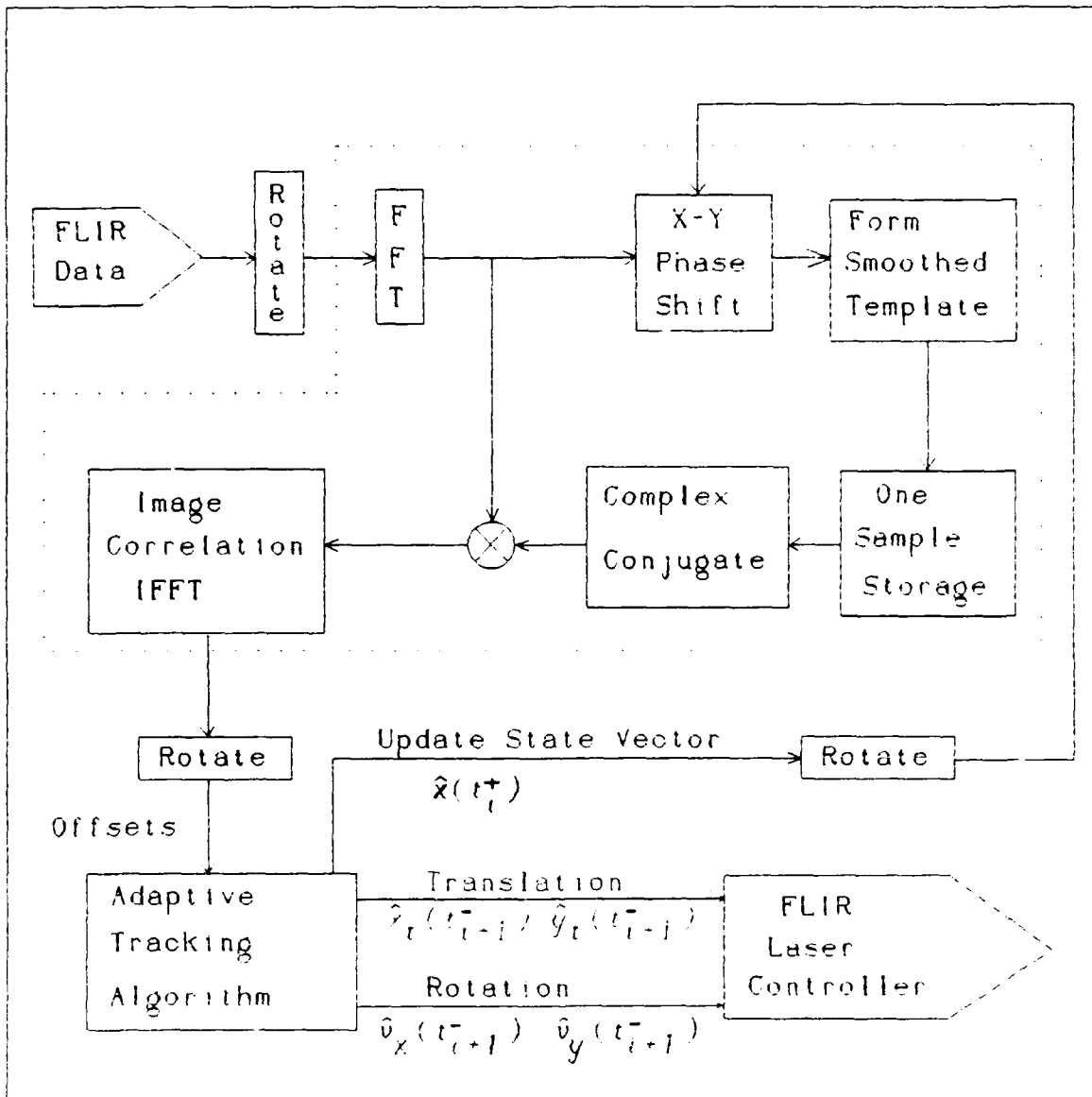


Figure 4.2. Data Processing Algorithm For Diagonally Rotated Field-of View

The negative sign in the numerator of Equation (4-1) keeps the orientation angle positive in the counterclockwise direction from the FLIR plane x axis when viewed from the inertial frame origin. This also allows a direct comparison with the truth model velocity orientation angle, facilitating the calculation of the error statistics.

To simulate the physical rotation of the FLIR sensor, the incoming FLIR data is rotated before entering the data processing algorithm of Figure 4.2. This is simulated by performing a negative rotation, based on the positive orientation angle, on the location and orientation of the individual Gaussian intensity functions described in Section 2.4.1. This corresponds to a positive rotation of the FOV and aligns the FOV with the positive orientation angle. Mathematically, this is done by first rotating the intensity function peaks defined by Equation (2-40) using the following rotational transformation matrix, first produced by Norton [13]:

$$\begin{bmatrix} x'_{peak} \\ y'_{peak} \end{bmatrix} = \begin{bmatrix} \cos \hat{\theta}_f & -\sin \hat{\theta}_f \\ \sin \hat{\theta}_f & \cos \hat{\theta}_f \end{bmatrix} \begin{bmatrix} x_{peak} \\ y_{peak} \end{bmatrix} \quad (4-2)$$

Note here that the primed variables are in the rotated coordinate system. The intensity function of Equation (2-40) (refer to Figure 2.4) then becomes:

$$I[x', y', x'_{peak}(t), y'_{peak}(t)] = I_{max} \exp\{-0.5[\Delta x' \Delta y'] \cdot \mathbf{P}[\Delta x' \Delta y']^T\} \quad (4-3)$$

where:

$$\Delta x' = (x' - x'_{peak}) \cos \Delta \theta + (y' - y'_{peak}) \sin \Delta \theta$$

$$\Delta y' = (y' - y'_{peak}) \cos \Delta \theta - (x' - x'_{peak}) \sin \Delta \theta$$

$\Delta \theta$ = difference between the truth model velocity orientation angle and the filter computed orientation angle, i.e. $\Delta \theta = \theta_T - \hat{\theta}_f$

x' , y' = rotated coordinates from the original FLIR coordinate frame via Equation (4-2)

Once the incoming FLIR data has been rotated, the data processing algorithm generates the template in the same manner as was done in Figure 3.1.

Recall that the incoming data was centered in the FLIR plane via the shifting of Equations (3-12) and (3-13). However, these shifts were computed in the unrotated filter coordinate system, while the current FLIR data image is in a rotated frame. To implement the algorithm properly, the translational shift is accomplished in the rotated frame by the transformation:

$$\begin{bmatrix} x'_{shift} \\ y'_{shift} \end{bmatrix} = \begin{bmatrix} \cos \hat{\theta}_f & -\sin \hat{\theta}_f \\ \sin \hat{\theta}_f & \cos \hat{\theta}_f \end{bmatrix} \begin{bmatrix} x_{shift} \\ y_{shift} \end{bmatrix} \quad (4-4)$$

where x_{shift} and y_{shift} are given in Equations (3-12) and (3-13).

This transformation is accomplished by the "rotate" block following the tracking algorithm block. With this

transformation, both the current image data and the template are in the same coordinate frame.

The final modification to the algorithm occurs with the "rotate" block after the "IFFT" block. The outputs of the IFFT block are the linear offsets between the current image data and the centered template. However, these offsets are in a rotated frame, while the states in the filter are in the original unrotated frame. To insure compatibility, the offsets are rotated back into the original frame by the transformation:

$$\begin{bmatrix} z_1 \\ z_2 \end{bmatrix} = \begin{bmatrix} \cos \hat{\theta}_f & \sin \hat{\theta}_f \\ -\sin \hat{\theta}_f & \cos \hat{\theta}_f \end{bmatrix} \begin{bmatrix} z_1' \\ z_2' \end{bmatrix} \quad (4-5)$$

where the primed and unprimed coordinates are in the unrotated and rotated coordinate systems, respectively.

4.4 Truth Model Parameters

Since the scenario used for this thesis was a continuation of that used by Rizzo, the truth model parameters are the same. The rationale for the choice of these parameters is fully detailed by Rizzo [14]; it will not be repeated here. For the nominal ballistic missile trajectory studied, the initial conditions for the target inertial frame (see Section 2.3.1) position and velocity vectors are:

$$e_x = 20,000 \text{ meters}$$

$$e_y = 100,000 \text{ meters}$$

$$e_z = 2,000,000 \text{ meters}$$

$$v_x = -2500 \frac{\text{meters}}{\text{second}}$$

$$v_y = 4330 \frac{\text{meters}}{\text{second}}$$

$$v_z = 0 \frac{\text{meters}}{\text{second}}$$

The maximum intensity value for each of the intensity functions of Equation (2-40) is 20 intensity units. The RMS value of v_{jk} , which is the sum of spatially correlated background noise (b_{jk}) and FLIR sensor noise (n_{jk}) in Equation (2-41), is one. This yields a signal-to-noise ratio of twenty, which is typical of many tracking scenarios [18].

In his investigation of plume "pogo" effects, Rizzo [14] desired to have the exhaust plume in the FLIR plane contained within a 5 x 5 pixel window. This value was chosen so that the maximum plume "pogo" oscillation would "fit" within an 8 x 8 pixel FOV. To represent the reference ellipsoid hotspot dispersion of Figure 2.4, the hotspot dispersion along the e_{pv} direction of the target frame (Equation 2-35) was chosen to be 1 pixel, and the dispersion in the e_x direction as 1.5 pixels. The pixel proportionality constant was initially continued from Rizzo's value of 1.5 micro-radians/pixel. Although the "pogo" phenomenon was not considered in this research, the desire to keep the missile hardbody center of mass and the missile plume centroid in

the same 8 x 8 pixel FOV prompted the continued use of the same values to describe the hotspot dispersion.

The variance and mean squared value for the atmospheric jitter, in both x and y directions, was continued from previous theses [13,14,18] as 0.2 pixels². The truth model bending/vibration parameters are in Section 2.2.3.

4.5 Filter Parameters

For the first analysis of the problem involving use of actively acquired measurements, it was decided to concentrate solely on the problem of tracking, rather than acquisition and tracking. Therefore, in the simulation used for this research, the six-state filter is initialized with zero errors in the position and velocity at time t=0. The atmospheric jitter states are also initialized to zero. The initial state covariance matrix is identical to that used by Rizzo, for states which are common to both filters. With this condition, the matrix becomes:

$$P(t) = \begin{bmatrix} 10 & 0 & 0 & 0 & 0 & 0 \\ 0 & 10 & 0 & 0 & 0 & 0 \\ 0 & 0 & 2000 & 0 & 0 & 0 \\ 0 & 0 & 0 & 2000 & 0 & 0 \\ 0 & 0 & 0 & 0 & 0.2 & 0 \\ 0 & 0 & 0 & 0 & 0 & 0.2 \end{bmatrix} \quad (4-6)$$

For the initial conditions on the single state filter, both the state and the covariance were set to zero. It must be noted that using these initial values will have a significant effect on the initial transient performance of the filter. The values for the dynamics and measurement noise strength were the subjects of analysis in both filters, and these will be discussed in Chapter 5.

4.6 Tracking Algorithm Statistics

The performance of the tracking algorithm is evaluated using Monte-Carlo simulation techniques [6]. Previous research has shown that ten Monte-Carlo runs demonstrate sufficient convergence to the actual statistics obtained from an infinite number of runs [17,18]. Based on these previous efforts, ten Monte-Carlo runs were used to analyze tracker performance in this research.

The sample mean errors of the tracking algorithm's estimates are calculated as [17]:

$$\bar{E}_s(t_i) = \frac{1}{N} \sum_{n=1}^N [s_{Tn}(t_i) - \hat{s}_{fn}(t_i)] \quad (4-7)$$

where:

$\bar{E}_s(t_i)$ = sample mean error of state estimate at time t_i
averaged over N runs

$\hat{s}_{fn}(t_i)$ = state estimate at time t_i during simulation n

$s_{Tn}(t_i)$ = truth model state value at time t_i during
simulation n

N = number of Monte-Carlo runs

The sample variance of the error is given by:

$$\sigma_s^2 = \frac{1}{N-1} \sum_{n=1}^N ([s_{Tn}(t_i) - \hat{s}_{fn}(t_i)]^2) - \frac{N}{N-1} \bar{E}_s(t_i) \quad (4-8)$$

These two statistics are calculated for the target x and y positions and velocities due to dynamics, and the FLIR image centroid x and y coordinates. The performance of the filter in estimating the centroid location, as well as velocity is of primary importance in generating the mass center offset measurement used by the single state filter. The same error statistics are also calculated for the offset estimate. All the error statistics are in units of pixels, and calculated for both before and after measurement update.

For further simplification, the above statistics are temporally averaged over the seven second simulation. These temporal averages, when used in conjunction with the plotted time histories of the error statistics, provide some indication of trends during the simulation.

4.7 Performance Plots

Thirteen plots are used to assess filter performance in this study. The first ten plots are used to describe the performance of the six-state filter. They are:

1. True x position rms error vs. filter-computed x position rms error
2. True y position rms error vs. filter-computed y position rms error

3. Mean \ddot{x} target position error \pm one σ at all time t_i
4. Mean \ddot{y} target position error \pm one σ at all time t_i
5. Mean \dot{x} target position error \pm one σ at all time t_i
6. Mean \dot{y} target position error \pm one σ at all time t_i
7. Mean x centroid position error \pm one σ at all time t_i
8. Mean y centroid position error \pm one σ at all time t_i
9. Mean \dot{x} centroid position error \pm one σ at all time t_i
10. Mean \dot{y} centroid position error \pm one σ at all time t_i

Examples of plots 1, 3, 7, 9, 11, and 13 are shown in Figures 4.3 through 4.8. The first two plots indicate the adequacy of the filter tuning by direct comparison of the actual true rms error vs. the filter computed rms error. Note that in Figure 4.3, the constant graph is the filter computed error and the graph with the peaks and valleys represents the actual error. The degree of overlap between the two graphs indicates how well the filter is tuned against the truth model. Plots 3 through 6 indicate how the tuning is affecting the filter's ability to estimate the portion of the image position due strictly to target dynamics. Plots 7 through 10 provide primary tracking performance information, since the location of the image centroid is used in the determination of the hardbody center of mass. Plots 11-13 assess the performance of the filter which estimates the offset distance between the FLIR image

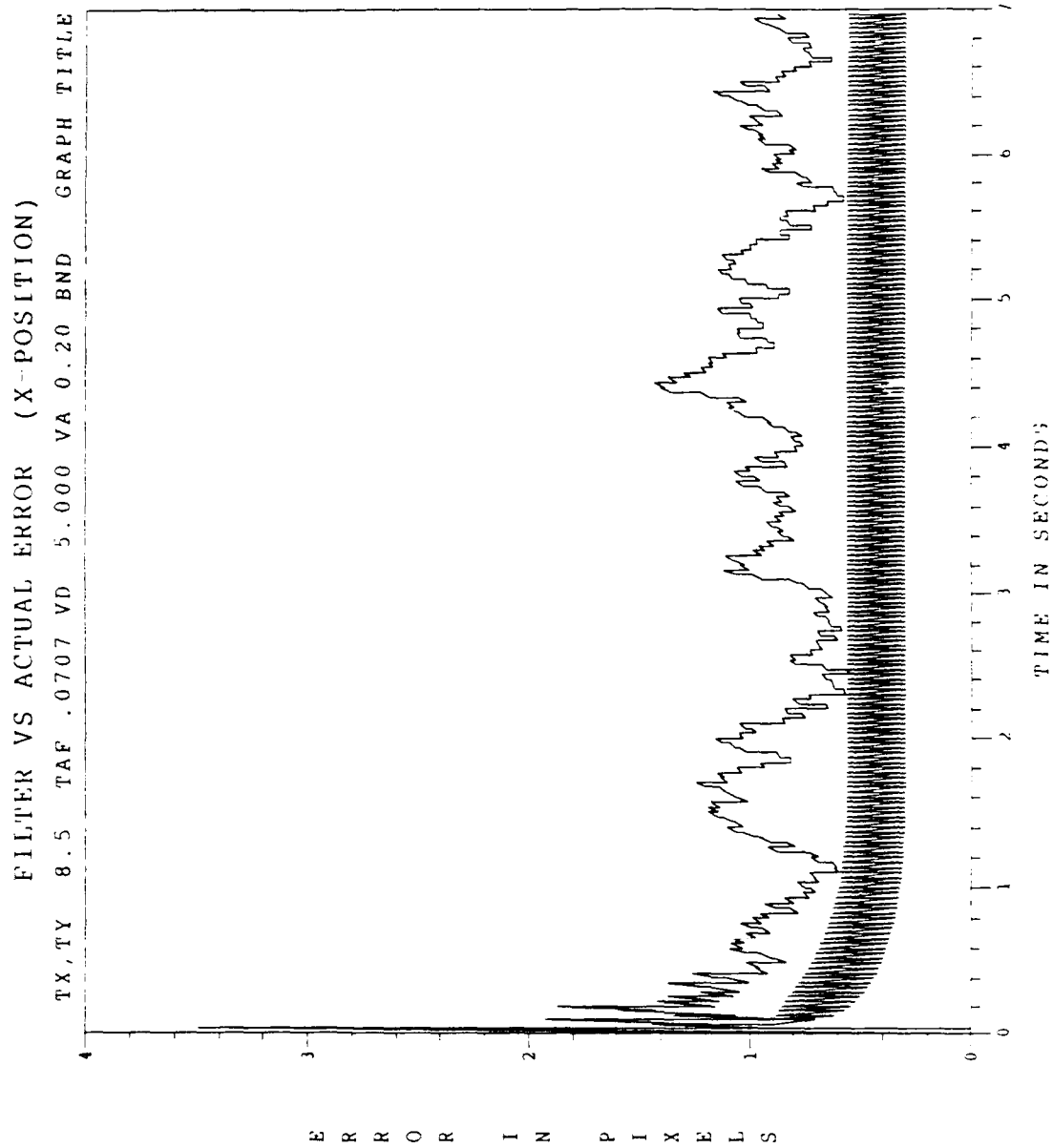


Figure 4.3 Example of Actual vs. Filter Computed RMS Error Performance Plot (Plot #1)

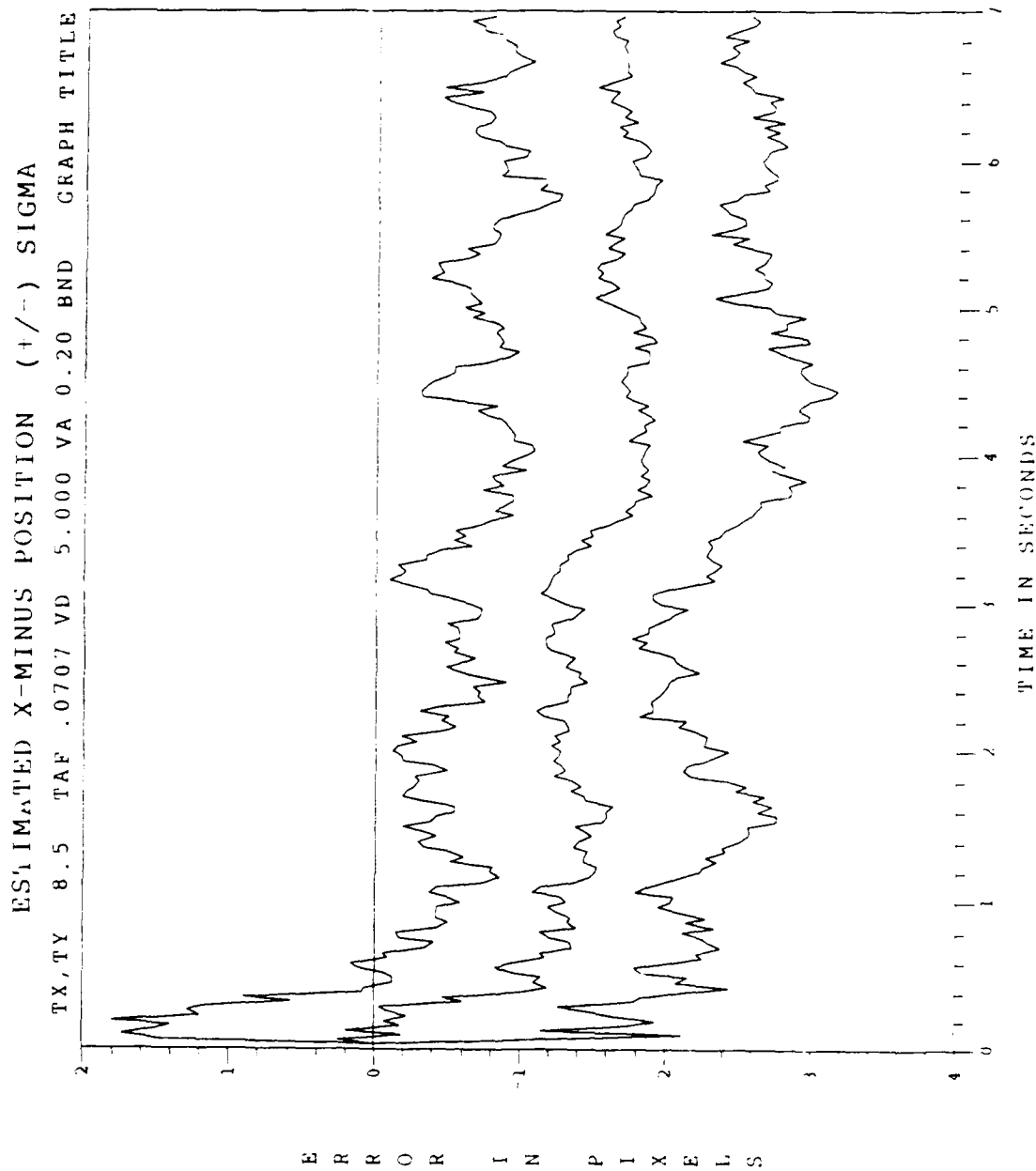


Figure 4.4 Example of Position Error at time t
Performance Plot (Plot #3)

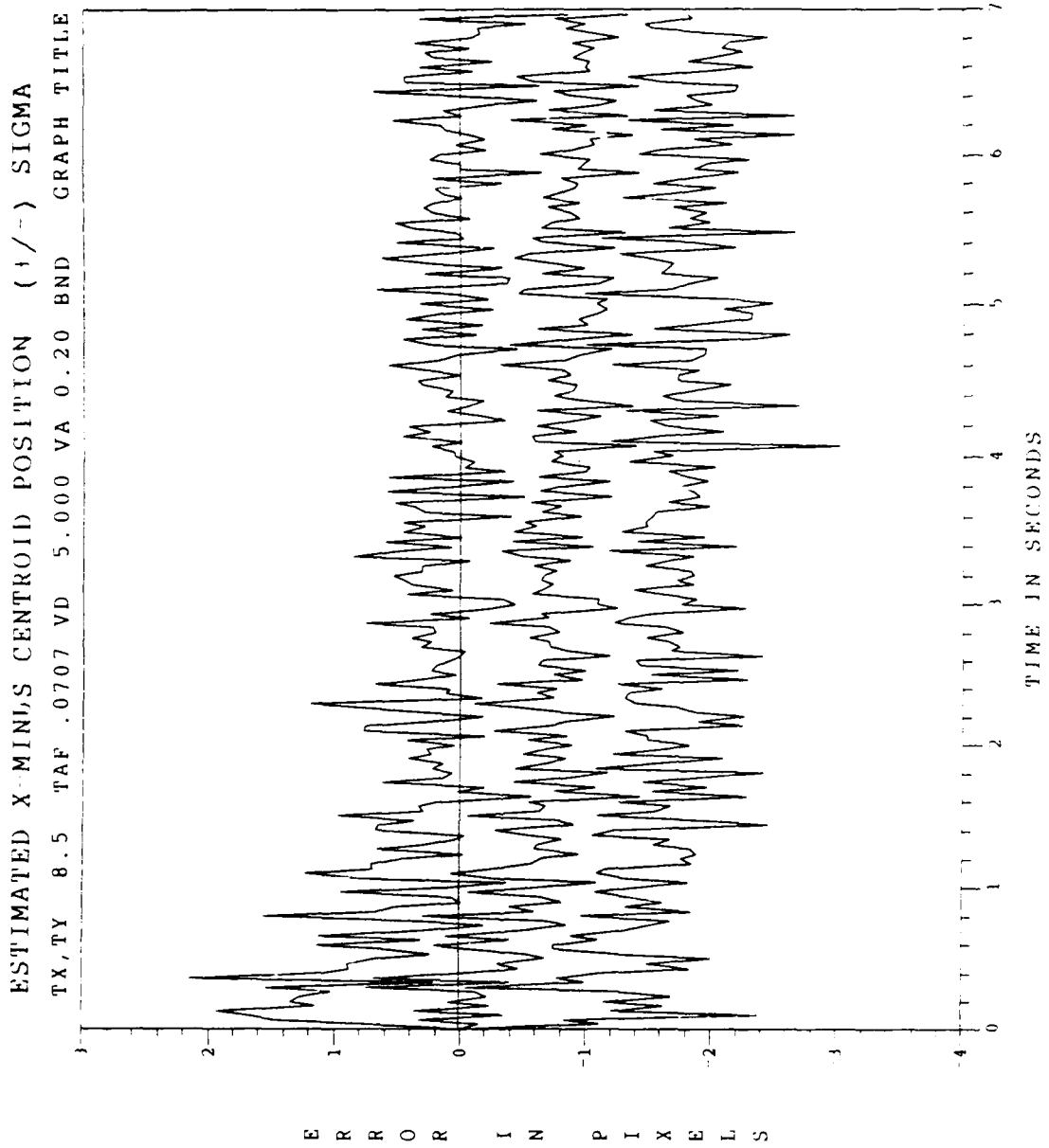


Figure 4.5 Example of Centroid Position Error at time t_1
 Performance Plot (Plot #7)

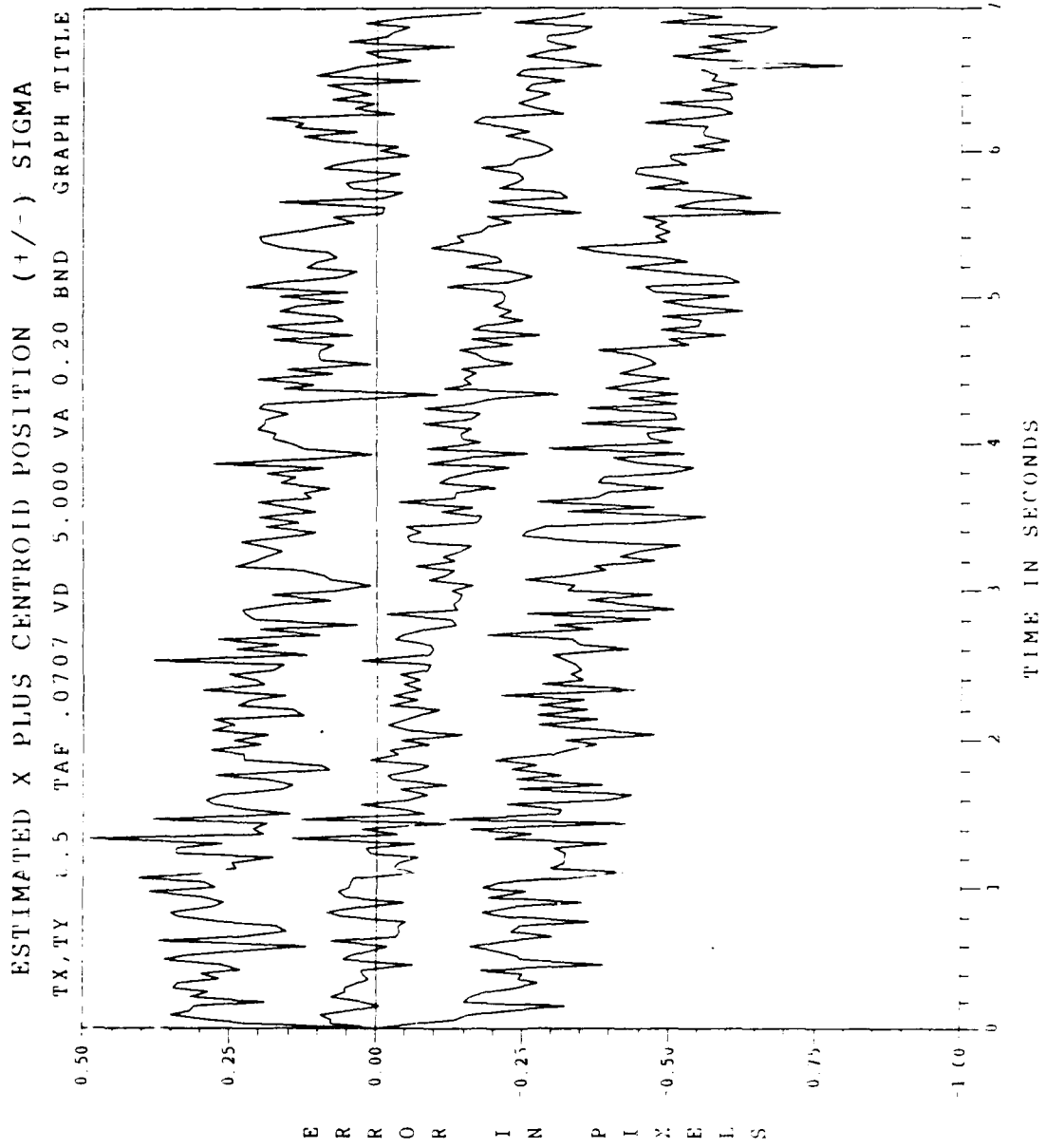


Figure 4.6 Example of Centroid Position Error at time t_i
Performance Plot (Plot #9)

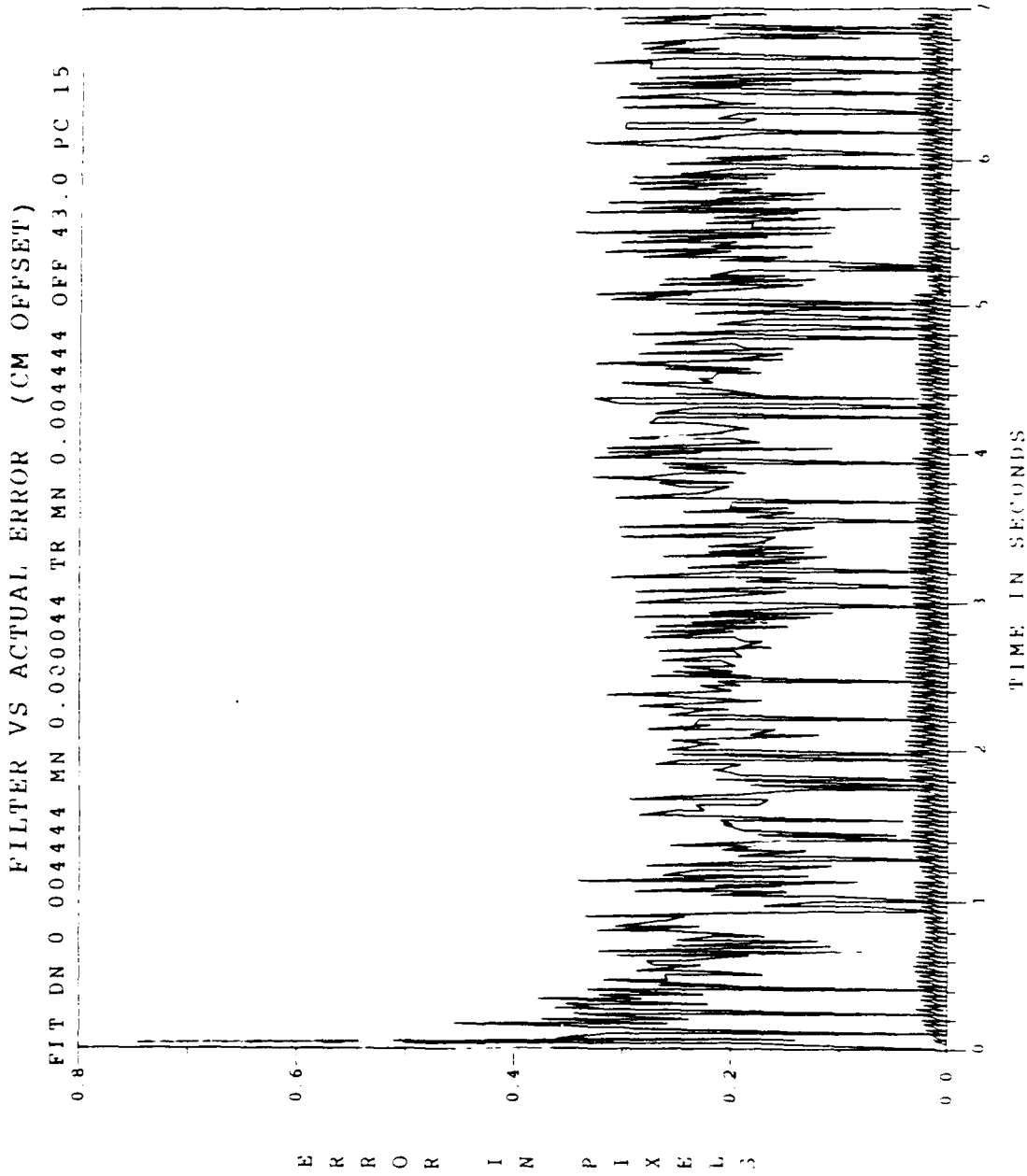


Figure 4.7 Example of Offset Actual vs. Filter RMS Error Performance Plot (Plot #11)

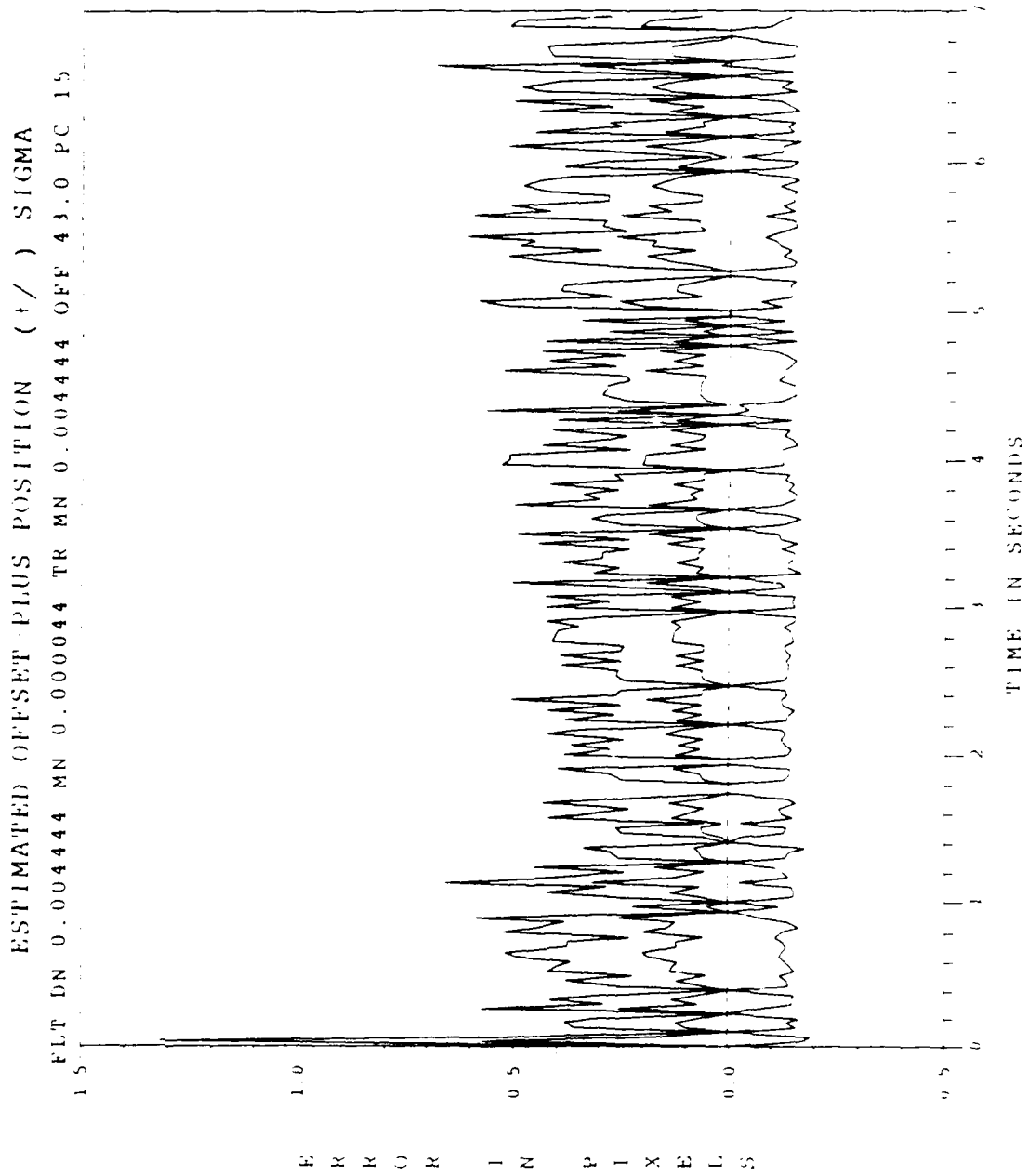


Figure 4.9 Example of Offset Error at time t
 Performance Plot (Plot #13)

centroid and the missile hardbody center of mass. The error for this filter is determined in two steps. First, the filter estimated location of the center of mass is computed using the filter estimated offset length, the estimated velocity vector orientation angle, and the estimated image centroid location. The error is then calculated as the difference between the estimated center of mass and the truth model center of mass. As previously mentioned in Section 2.4.2, there may be sample times in the simulation when no measurement occurs. In this case, the last filter estimate based on a measurement update is used for error computation until the next measurement update occurs. The filter error plots are:

11. True offset rms error vs filter offset rms error
12. Mean offset error, \pm one σ , at all time t_i
13. Mean offset error, \pm one σ , at all time t_i^*

Similar to plots 1 and 2, plot 11 indicates the adequacy of filter tuning. Plots 11 and 12 are the primary indicators of filter performance, indicating the filter's ability to locate the missile center of mass.

4.7.1 Plot Designation Codes. The first ten plots have four fields in the graph label. The first field, labeled "TX, TY", indicates the correlation time constant (in seconds) used for the velocity model in the x and y

directions. The second field, labeled "TAF", is the time constant (in seconds) used for the atmospheric jitter model, and is equal in both x and y directions. The third field, labeled "VD", is the variance of the discrete driving noise for the velocity states in pixels²/seconds², and is assumed equal in both the x and y directions. The fourth field, "VA", is the variance of the driving noise associated with the atmospheric jitter, and is also assumed equal in both the x and y directions. It also has units of pixels²/seconds². The last field, "BND", simply indicates the inclusion of bending states in the truth model.

For the three plots associated with the offset filter, there are five fields in the graph label. The first, "FLT DN", indicates the variance of the filter discrete-time dynamics driving noise, in pixels². The next field, "MN", indicates the variance of the filter measurement noise, also in pixels². The third field, "TR MN", indicates the measurement noise variance in the truth model generation of the offset measurement used by the filter. The fourth field, "OFF", is the true offset distance, in meters, between the missile center of mass and the truth model image centroid. The last field, "PC", indicates the pixel proportionality constant, in micro-radians/pixel. The values given to these parameters will be discussed in Chapter 5.

4.8 Summary

This chapter has presented the overall tracking algorithm used in this research by combining the results of Chapters 2 and 3. An overall view of the algorithm was presented, along with modifications to the algorithm caused by the inclusion of a diagonally rotated FLIR field of view. The truth model and filter parameters used in this research were then detailed. Finally, the statistical tools used for the filter performance evaluation were shown.

5. Performance Analysis

5.1 Introduction

This chapter presents the results of the evaluation of the performance characteristics of the algorithms discussed in Chapter 4. Section 5.2 details the observability analysis conducted to determine the states which were used in the six-state filter. Section 5.3 then presents the analysis of the tuning process for that filter. Once tuning of the six-state filter was accomplished, a parameter study involving the single state filter for estimating the mass-center-to-intensity-centroid offset was undertaken. Section 5.4 presents the results of the sensitivity study, in which the parameters of truth model and filter measurement noise variance were altered. Section 5.5 shows the corresponding robustness study results, in which the filter was not informed of parameter changes in the real world. Section 5.6 and 5.7 then present the results from the parameter studies involving the truth model offset distance and pixel proportionality constant.

5.2 Filter Observability Study

Rizzo [14], in his research, discovered an observability-like problem in the filter models used to describe the "pogo" phenomenon he was investigating. He compared the performance of an eight-state benchmark filter (modelling

FLIR plane image position, velocity, acceleration, and atmospheric jitter in both x and y directions) to a ten-state filter (modelling the same eight states plus the two "pogo" states, pogo effect position displacement and velocity) which also included modelling for "pogo" effects. The performance of both filters was measured against a 14-state truth model which also included "pogo" effects modelling (the same 12-state model described in Section 2.2 plus the two "pogo" states). In examining the results, he discovered a performance anomaly, in that the eight-state filter outperformed the ten-state filter. Since the higher order filter had "knowledge" of the "pogo" effects in the truth model and the lower dimensioned filter did not, this was the opposite of the results to be expected. In investigating this anomaly, he performed a stochastic observability test [6] on both the eight- and ten-state filters. The velocity and acceleration states were found to be weakly observable, particularly the acceleration states. Rizzo [14:7-5] recommended that alternate acceleration models be considered in the future, or that the acceleration states be dropped from the filter completely, in order to address this difficulty.

For this research, it was decided [8] to reduce the filter order by dropping acceleration, and possibly velocity states, from the eight-state filter. To determine the final order of the filter, the observability was reexamined. The

stochastic observability condition to be examined is given by the following relationship [6:243]:

$$\alpha \mathbf{I} \leq \sum_{j=i-N+1}^i \Phi^T(t_j, t_i) \mathbf{H}^T(t_j) \mathbf{R}^{-1}(t_j) \mathbf{H}(t_j) \Phi(t_j, t_i) \leq \beta \mathbf{I} \quad (5-1)$$

where the summation term in Equation (5-1) is the stochastic observability Grammian matrix. If there exist positive numbers α and β , and $0 < \alpha < \beta < \infty$, and a positive integer N such that, for all $i \geq N$, the above relationship holds, then the system is said to be stochastically observable. Because of numerical precision problems involved with exponential terms within the Grammian matrix, $N = 13$ and $i = 14$ were used in the test.

The observability Grammian matrix (diagonal terms) for Rizzo's eight-state benchmark filter is:

$$\begin{bmatrix} 3856 & - & - & - & - & - & - & - \\ - & 2341 & - & - & - & - & - & - \\ - & - & 310 & - & - & - & - & - \\ - & - & - & 188 & - & - & - & - \\ - & - & - & - & 11.2 & - & - & - \\ - & - & - & - & - & 6.8 & - & - \\ - & - & - & - & - & - & 244146644 & - \\ - & - & - & - & - & - & - & 148202729 \end{bmatrix}$$

The order of the states in the observability Grammian matrix is: position (x and y), velocity (x and y), acceleration (x and y), and atmospheric jitter (x and y). It is necessary to note that the observability matrix was not a diagonal matrix: for the purpose of clarity and emphasis,

only the diagonal terms are shown. By observation of the size of the diagonal terms, states with potential observability problems can be distinguished by their small magnitude relative to the other diagonal entries. For determination of system model observability, the Grammian matrix eigenvalues must be examined. The eigenvalues for the eight-state filter are:

1673
2756
14.97
24.66
.03037
.0501
148203577
244148042

Of the eight eigenvalues, the third through the sixth are smaller by three to five magnitudes than the next smallest eigenvalues. Here, eigenvalues three and four correspond basically to the velocity states, and five and six to the acceleration states. Particularly the acceleration state eigenvalues, being almost zero, indicate almost complete unobservability. This, in combination with the relatively small diagonal values from the observability matrix, led to the decision to delete the acceleration states from the model. Even though the velocity states were much less observable than either the position or atmospheric

jitter states, the decision was made to keep these states in the model. The need for a filter estimate of the velocity vector orientation angle as a means of aiming the low power laser necessitated this decision. With the deletion of acceleration from the eight-state model, and the remodelling of velocity, the six-state model detailed in Chapter 3 became the basis for the filter used in this research to estimate FLIR plane target parameters.

5.3 Filter Tuning Process

The purpose of this section is to describe the tuning procedure and results obtained during the tuning of the six-state filter for the benign trajectory used for this research. The tuning parameters used in this study are the variances (in both the x and y directions) of the first-order Gauss-Markov representations of the target velocity, and the variances (in the x and y direction) of the atmospheric jitter position processes. This decision was made after conducting an initial tuning study involving the variances and correlation times of both the target velocity and jitter position processes. This study revealed the sensitivity of the filter mainly to changes in the variances. Additionally, in previous research [13,14,18], a value of 0.707 seconds had been shown to be representative for the atmospheric jitter correlation time constant, and the decision [8] was made to remain with this value throughout the

tuning process. A value of 8.5 seconds was used [8] for the correlation time constant of the velocity process, and was also kept constant throughout the tuning process. This value was selected based on the fact that the dynamic maneuvering expected from a ballistic missile in boost phase would be somewhat less than that expected from a large manned bomber (with a correlation time of approximately six seconds).

Table 5.1 lists the variation of the two tuning parameters, the target dynamics velocity and jitter position variances, for the tuning process. For the first tuning run, the dynamics variance was set at 5, and the jitter variance was set at 0.2. The time averaged statistics are listed in Table 5.2 and the performance plots are given in Appendix B, Figures B.1-B.10. The plots in Figure B.1 and B.2 indicate the filter is underestimating the error variances on target position estimates in both the x and y directions. The dynamics state errors in Figures B.2-B.6 also indicate the need for further tuning. The centroid plots, Figures B.7-B.10, are very important. In this research, the need for the filter to provide an accurate estimate of the FLIR image centroid is critical to the aiming of the low power laser and resulting estimation of the missile center of mass (velocity estimation accuracy is also important, in order to establish the estimated orientation angle of Equation (4-1) that indicates the angular orientation of the

center of mass from the intensity centroid). Here, particularly in the plots for the centroid position error after update (Figures B.9-B.10), there is an increasing error over time.

Table 5.1. Tuning Run Parameters

RUN #	$\sigma_x^2, \sigma_y^2 \left(\frac{\text{pixels}^2}{\text{seconds}^2} \right)$	$\sigma_d^2 (\text{pixels}^2)$
1	5	0.2
2	50	0.2
3	200	0.2
4	800	0.8

Table 5.2. Run 1 Temporally Averaged Statistics

Error in Estimate of:	Mean	1 Sigma
$\hat{x}(t_i^-)$	-1.4587	.94001
$\hat{y}(t_i^-)$	2.5274	1.02790
$\hat{x}(t_i^+)$	-1.2958	.90143
$\hat{y}(t_i^+)$	2.2610	.98574
$\hat{x}_c(t_i^-)$	-.0126	.98152
$\hat{y}_c(t_i^-)$	1.4844	.93751
$\hat{x}_c(t_i^+)$	-.1263	.28028
$\hat{y}_c(t_i^+)$.5154	.19054

For the second run, the target dynamics model velocity variance was increased to 50, while the jitter variance was kept at 0.2. The tuning results are presented in Figures

Table 5.3. Run 2 Temporally Averaged Statistics

Error in Estimate of:	Mean	1 Sigma
$\hat{x}(t_i^-)$	-.56178	1.05820
$\hat{y}(t_i^-)$.75109	1.10460
$\hat{x}(t_i^+)$	-.47145	.99714
$\hat{y}(t_i^+)$.61261	1.04780
$\hat{x}_c(t_i^-)$	-.33741	1.00710
$\hat{y}_c(t_i^-)$.44683	.95115
$\hat{x}_c(t_i^+)$	-.12905	.29073
$\hat{y}_c(t_i^+)$.11751	.18595

B.11-B.20 and Table 5.3. Although some improvement in matching the filter-computed error variance to the actual error variance has been made, the improvement is not significant. A significant improvement in the target dynamics position state error and especially in the centroid error has been achieved, as indicated by Figures B.13-B.20. In comparing Figures B.9 and B.10 to B.19 and B.20, note the mean error line slope has been significantly reduced in the x channel. The y channel has also improved, but not to the same degree. This is due to the fact that the R matrix of Equation (3-20) in the measurement model weights the y axis FLIR plane measurements more heavily than the x axis, and thus the filter y axis estimates respond less to changes in the dynamics driving noise strength. The increase in the error over time indicates that filter divergence would eventually become large enough to cause loss of tracking.

However, a target reacquisition algorithm [18] has been previously developed in past work as part of the simulation. If the errors did become large enough, the simulation uses this algorithm in a target acquisition, rather than a target tracking mode. This would prevent total divergence from occurring.

Several interim runs were performed, in which the target dynamics velocity strength was systematically increased while keeping the jitter variance constant. A final value of 200 was used for the target dynamics velocity variance. The results of that run are shown in Figures B.21-B.30 and Table 5.4. As can be seen from Figures B.21 and B.22, changing the target dynamics velocity variance does not significantly affect the match between the filter-computed error variance and the actual error variance. However, the errors in the dynamics states and particularly in the centroid location have been significantly reduced. Note Figures B.29 and B.30. The error in the x-axis centroid location is essentially zero. The y-axis centroid error, while not zero, is less than 0.2 pixels at the end of the simulation.

The next step was to discontinue the tuning via the target dynamics error variance, and to continue the tuning using the jitter variance. When tuning via the jitter variance, a counterproductive result was noted. As the jitter variance was increased, the match between the filter-

Table 5.4. Run 3 Temporally Averaged Statistics

Error in Estimate of:	Mean	1 Sigma
$\hat{x}(t_i^-)$	-.30019	1.2293
$\hat{y}(t_i^-)$.53239	1.1514
$\hat{x}(t_i^+)$	-.23704	1.1340
$\hat{y}(t_i^+)$.43096	1.0550
$\hat{x}_c(t_i^-)$	-.09359	1.0376
$\hat{y}_c(t_i^-)$.30553	.98254
$\hat{x}_c(t_i^+)$	-.01949	.31303
$\hat{y}_c(t_i^+)$.12094	.18187

computed error variance and the actual error variance increased, but the error in the target dynamics position and centroid locations also increased. It was then necessary to increase the target dynamics velocity variances in compensation. This increase in the target dynamics velocity variance then resulted in an increase in the mismatch between the filter-computed error variance and the actual error variance. After several iterations, a final value of 800 was selected for the target dynamics velocity variance and 0.8 for the jitter variance. The final tuning run results are shown in Table 5.5 and Figures B.31-B.40. Note that there is a good match between filter-computed and actual error statistics, as evidence by Figures B.31 and B.32. The tuning to achieve accuracy in locating the centroid location has also been preserved, as shown by the centroid x and y mean errors after update in Table 5.5 and Figures B.39 and

Table 5.5. Run 4 Temporally Averaged Statistics

Error in Estimate of:	Mean	1 Sigma
$\hat{x}(t_i)$	-.22712	1.1871
$\hat{y}(t_i)$.41019	1.1526
$\hat{x}(t_i^-)$	-.21384	1.0945
$\hat{y}(t_i^-)$.31213	1.0663
$\hat{x}_c(t_i)$	-.15671	1.0236
$\hat{y}_c(t_i)$.17855	.95695
$\hat{x}_c(t_i^-)$	-.04210	.21210
$\hat{y}_c(t_i^-)$.00110	.18875

B.40. Comparing the results in Table 5.5 to the prior tuning run results, the tuning process seems to benefit the error means more than the one sigma values. At this point the filter was considered tuned and further tuning was discontinued.

5.4 Mass Center Offset Filter Sensitivity Study

The main thrust of this research is to examine the performance of a filter designed to estimate the offset between the missile hardbody center of mass and the filter computed image centroid, and the effects on this performance of variations in parameters that define the tracking scenario. Before describing the results of these parameter studies, some background material will be presented.

For this work, it was decided to continue using the same size missile used by Rizzo [14]. The missile used in the

simulation had a length of 40 meters and a diameter of 3 meters. As was previously mentioned, it was decided to approximate the shape of the missile in the FLIR plane as a rectangle. With the trajectory used in this work, such that the missile is basically orthogonal to the line of sight, the rectangle dimensions were approximately the same as the missile dimensions.

The next item of consideration was the choice of beamwidth for the low power laser used to generate the "measurement" of the distance between the image centroid and the missile center of mass in the simulation. The desire to choose a beamwidth realistic for the range used in the simulation (approximately 2000 kilometers) versus the need for simplification in the initial simulation of this problem led to a tradeoff study. For ease of implementation of the software simulating the reflection of the laser, it was decided to use a beamwidth less than or equal to the missile diameter. To allow beamwidths wider than the missile diameter would have caused a large increase in the amount of software necessary for the beam simulation. It was also desired to have as large a number of simulated reflections during the simulation as possible. This is a function of the accuracy of estimating the image intensity centroid and target velocity (to establish the line along which to sweep the laser), the true offset between the intensity centroid and missile center of mass, and the laser beamwidth. A

study was then conducted to examine these tradeoffs. Although the details of this study will not be presented, a value of 2.75 meters was finally selected as the beamwidth value at the target location to be used in the study.

The sensitivity study examined the effect of simultaneously changing both filter-assumed measurement noise variance and the truth model measurement noise variance. The variance of the filter discrete-time noise was set at four meters² [8] for the entire study. With no prior knowledge of the physical parameters associated with the "real world" offset, a value equal to ten percent of the missile length was used. Three measurement error levels were examined, representing high, medium, and low levels of accuracy. The measurement error standard deviation levels studied were 0.2, 2, and 20 meters. For this study, two meters is considered the nominal error [8]. The results of the study are presented in Table 5.6 and Figures C.1-C.9. As was previously mentioned in Chapter 4, the error reported in both the time averaged statistics and the performance plots is the error between the truth model center of mass location and the estimated center of mass location which was determined using the filter-estimated offset distance, the estimated velocity vector orientation angle, and the estimated image intensity centroid location. In Table 5.6, the measurement error levels are in meters and the statistics are in pixels.

Table 5.6 Sensitivity Study Time Averaged Statistics

Measurement Noise Standard Deviation	Center of Mass Error Statistic	Mean	1 Sigma
0.2	$\hat{x}_{cm\ error}(t_i^-)$.68248	.20311
	$\hat{x}_{cm\ error}(t_i^+)$.09571	.18694
2.0	$\hat{x}_{cm\ error}(t_i^-)$.74503	.22147
	$\hat{x}_{cm\ error}(t_i^+)$.10714	.14196
20	$\hat{x}_{cm\ error}(t_i^-)$	1.2707	.39839
	$\hat{x}_{cm\ error}(t_i^+)$.19072	.14516

In examining the statistics for the first two measurement precision levels, as well as Figures C.2, C.3, C.5, and C.6, several observations can be made. First, the mean error (particularly after update) changes only approximately ten percent for an order of magnitude change in the measurement precision level. Observing Figures C.2 and C.4, it is apparent that with increasing measurement noise strength, the filter takes longer to learn the underlying dynamics and reach the steady state mean error level, as would be expected. The third measurement precision level had much poorer statistics. In this case, the filter is still learning the underlying dynamics and never does reach the steady state mean error during the simulation time interval. This is well illustrated by Figure C.8. Also note that there is little difference in the standard deviations between the two and twenty meter measurement precision levels. This indicates that increasing the value of measurement noise var-

iance predominantly affects the amount of time the filter needs to estimate the offset, and not the accuracy of that estimate. Also note the effect of using an initial filter covariance of zero, especially in the case of the 20 meter measurement precision level.

5.5 Mass Center Offset Filter Robustness Study

In a robustness study, the truth model is given parameters different from those in the filter, and the performance of the filter analyzed. This analysis indicates the degree of filter robustness when the parameters assumed by the filter models differ from the "real" world as represented by the truth model. In this robustness study, the measurement error level was also the parameter varied. Filters with the three measurement error levels (measurement noise standard deviations of 0.2, 2, and 20 meters) were studied. In each case of filter-assumed measurement precision, the two remaining error levels were consecutively used in the truth model, and the performance of the filter analyzed. As in the sensitivity analysis, the variance of the filter driving noise was held constant at four meters for all cases considered in the robustness study. The results are presented in Table 5.7 and Figures D.1-D.18. The parameter values and statistics from the sensitivity study are included as a reference. The units for Table 5.7 are the same as Table 5.6.

Table 5.7 Robustness Study Time Averaged Statistics

Measurement Noise Standard Deviation		Mass Center Error Statistic	Mean	1 Sigma
Filter	Truth Model			
0.2	0.2	$\hat{x}_{cm\ error}(t_i^-)$.68248	.20311
		$\hat{x}_{cm\ error}(t_i^+)$.09571	.18694
0.2	2.0	$\hat{x}_{cm\ error}(t_i^-)$.67927	.20276
		$\hat{x}_{cm\ error}(t_i^+)$.09551	.19553
0.2	20	$\hat{x}_{cm\ error}(t_i^-)$.78159	.44836
		$\hat{x}_{cm\ error}(t_i^+)$.10935	.25052
2.0	0.2	$\hat{x}_{cm\ error}(t_i^-)$.74923	.22217
		$\hat{x}_{cm\ error}(t_i^+)$.10745	.14231
2.0	2.0	$\hat{x}_{cm\ error}(t_i^-)$.74503	.22147
		$\hat{x}_{cm\ error}(t_i^+)$.10714	.14196
2.0	20	$\hat{x}_{cm\ error}(t_i^-)$.72303	.26899
		$\hat{x}_{cm\ error}(t_i^+)$.10539	.22603
20	0.2	$\hat{x}_{cm\ error}(t_i^-)$	1.21810	.40208
		$\hat{x}_{cm\ error}(t_i^+)$.19252	.14554
20	2.0	$\hat{x}_{cm\ error}(t_i^-)$	1.28010	.40172
		$\hat{x}_{cm\ error}(t_i^+)$.19235	.14487
20	20	$\hat{x}_{cm\ error}(t_i^-)$	1.27070	.39839
		$\hat{x}_{cm\ error}(t_i^+)$.19072	.14516

For the first case, the trend is for decreasing performance with increasing values of measurement noise variance in the truth model. This is to be expected since the mismatch between filter and truth model increases with increasing measurement noise variance. However, the increases in the mean error are only 13 percent for an order of magnitude increase in the truth model noise standard deviation. This is due to the fact that the filter weights

the measurements so heavily that, even with the increased uncertainty in the truth model measurements, the filter is quickly able to learn the value of the offset. Note also in Figures D.5 and D.6 the significant reduction in the standard deviation after update for the case where 20 meters was used in the truth model.

The second case is interesting because it shows the effect of having both larger and smaller measurement noise variances in the truth model as compared to the filter. Here, the mean errors (both before and after update) are smaller when the truth model measurement error level exceeds the filter measurement noise variance, but with higher error standard deviations. This can be seen in both in Table 5.7 and Figures D.8, D.9, D.11, and D.12.

The third case considers the performance of a filter which has low confidence in the measurements it receives. Note that the long transient for the case of the filter with the 20 meter error standard deviation shows clearly the deleterious impact of using zero as the initial value for the covariance. Here the mean error is approximately twice that in case one and two. Particularly note Figures D.14, D.15, D.17, and D.18. Again, similar to the third case considered in the sensitivity study, the filter is still learning the value of the offset state, and does not reach the steady-state value during the simulation. However, the standard deviations in the two variations considered here

are very close to the first part of case two. This situation is similar in that the filter-assumed measurement noise variance was greater than that in the truth model.

5.6 Pixel Constant Study

The next parameter to be investigated is the pixel proportionality constant. The main purpose of this study is to determine the FLIR sensor element resolution necessary for implementation of a tracking scheme involving active illumination of the target. In this study, the variance of the filter discrete-time noise was continued at a value of four meters². Four meters² (corresponding to the nominal error standard deviation of two meters) was used as the measurement noise variance in the mass center offset filter. The same value was also used for the measurement noise variance in the truth model. The performance of the offset filter was examined as the value of the pixel proportionality constant was varied between 7.5, 15, and 30 micro-radians/pixel. The variation involving the 15 micro-radian/pixel value has already been presented in the sensitivity study, but is repeated here to aid in the comparisons. The results are presented in Table 5.8 (in units of pixels) and Figures E.1-E.9.

To compare the results in terms of constant pixel size, the statistics in Table 5.8 for the 7.5 micro-radian/pixel case were determined by multiplying the mean and standard deviation from that analysis by two. In a similar manner,

Table 5.8 Pixel Constant Study Time Averaged Statistics

Pixel Constant	CM Error Statistic	Mean	1 Sigma
7.5	$\hat{x}_{cm\ error}(t_i^-)$	2.57560	1.27740
	$\hat{x}_{cm\ error}(t_i^+)$	1.14648	.34514
15	$\hat{x}_{cm\ error}(t_i^-)$.74503	.22147
	$\hat{x}_{cm\ error}(t_i^+)$.10714	.14196
30	$\hat{x}_{cm\ error}(t_i^-)$.39447	.24665
	$\hat{x}_{cm\ error}(t_i^+)$.01208	.03493

the statistics in Table 5.8 for the 30 micro-radian/pixel case were computed by dividing the mean and standard deviation from that analysis by two. After converting to a constant pixel size (30 meters by 30 meters, for the nominal 15 micro-radian/pixel case at a target range of 2000 kilometers), several observations can be made. First, in observing Table 5.8, the mean center of mass position error decreased with increasing pixel size, both before and after update. The same trend was true for the standard deviations, except in comparing the 15 and 30 micro-radian/pixel preupdate standard deviations. These results seem to be contrary to the expectation of increasing filter performance with increasing sensor resolution (i.e, a smaller pixel constant). However, a different trend is apparent in Figures E.1-E9. Plots E.1 through E.6 appear to echo the trend seen in Table 5.8 when pixel scale factors are considered. Figures E.7-E.9 indicate a much different trend.

Here the actual error is increasing with time as shown in Figure E.7. Figure E.8 echoes this, as the standard deviation about the mean offset value is also increasing with time. The peaks and gaps in Figure E.9 (caused by the fact that the filter may go for extended periods without receiving a measurement update) would seem to indicate that, at this level of resolution, the ability of the six-state filter to provide information about the location of the image centroid and the target velocity orientation angle is seriously degraded. With this degradation, the number of times a reflection occurs (a 10 Monte-Carlo run average of 8.6 reflections for a seven second simulation, with 210 reflections possible) is reduced, and the offset filter performance suffers accordingly.

5.7 Offset Distance Study

The final study conducted examined the mass center offset filter performance as a function of the actual offset distance between the missile center of mass and image center of intensity. The expectation was that, as offset distance was increased, the performance of the filter estimating the offset distance would suffer. This is due to the fact that the error in the six-state filter estimate of the velocity orientation angle used to aim the laser increases linearly with offset distance. As the error increases, there are fewer reflections which can be used to update the filter.

The filter and truth model noise parameters are identical to those in the pixel constant study. The nominal value of the pixel constant, 15 micro-radians/pixel, was also used in the study. The two offset distances considered were 86 and 172 meters. These were selected as multiples of the nominal 43 meter value used for all the other analyses, and because these values would allow both the missile and the FLIR image to be contained in an 8 x 8 pixel field of view.

The time averaged statistics are presented in Table 5.9 and the performance plots in Figures F.1-F.6. In Table 5.9, the offset distance is in meters and the statistics are in pixels. Although not part of this study, the statistics for the nominal 43 meter value are included in Table 5.9 for reference.

The statistics in Table 5.9 confirm the expectation of decreasing filter performance with increasing offset distance. Both the offset mean and standard deviation increase with increasing offset distance. The performance plots also confirm this idea. In comparing Figures F.1-F.3 to F.4-F.6, note that the filter using the 172 meter offset is taking much longer to reach steady state performance. This is due to the fact that there are fewer measurements (a ten Monte-Carlo run average of 23 reflections per 7 second simulation for the 172 meter offset against an average of 28.9 for the 86 meter offset case and 32.6 for the 43 meter

Table 5.9 Offset Distance Study Time Averaged Statistics

Offset Distance	Error Statistic	Mean	1 Sigma
43	$\hat{x}_{cm\ error}(t_i^-)$.75403	.22147
	$\hat{x}_{cm\ error}(t_i^+)$.10714	.14196
86	$\hat{x}_{cm\ error}(t_i^-)$.98793	.24490
	$\hat{x}_{cm\ error}(t_i^+)$.11227	.22204
172	$\hat{x}_{cm\ error}(t_i^-)$	1.61800	.66766
	$\hat{x}_{cm\ error}(t_i^+)$.12636	.29407

offset case) for the filter to learn the state. In examining Figures F.4 and F.5, note the large change in the filter's performance at approximately three seconds. To determine the reason for this, the times at which measurements occurred were examined for all ten Monte-Carlo runs. For two of those runs, only one measurement was received by the filter in the first three seconds. Additionally, for several of the runs, a very small percentage of the total number of measurements in the simulation occurred before three seconds. With only 10 runs, these anomalies have a significant impact on the statistics plotted.

5.8 Summary

This chapter presented the results of this thesis research. The observability analyses and filter tuning process used to develop the six-state FLIR data filter were presented first. Then, using this filter's outputs as the means to produce "measurements" of the low-power laser

returns from the missile hardbody, the studies involving the mass center offset filter were then described. These studies included a sensitivity and robustness analysis of the filter itself, and studies involving variations of the pixel constant and truth model offset distance.

6. Conclusions and Recommendations

6.1 Introduction

This chapter summarizes the conclusions reached in this thesis and recommends topics for further study. Section 6.2 draws conclusions based on the analyses of Chapter 5. Section 6.3 continues with suggestions for continued research in the area of FLIR tracking of ballistic missiles aided by active low power laser illumination.

6.2 Conclusions

Various conclusions have been made in Chapter 5. These conclusions will now be brought together and presented.

6.2.1 Six-State Filter Tuning. Tuning the filter via the target state dynamics driving noise and the atmospheric jitter driving noise proved adequate. The final tuning yielded a filter that could accurately identify the location of the FLIR image centroid. However, the development of the simulation of the laser reflection measurement required an accurate estimate of both the image centroid location and the velocity vector. In estimating velocity, the filter's performance was less than adequate. The initial goal [8] was to be able to aim the laser accurately enough to receive a reflection measurement better than 35 percent of the simulation time. The percentage of measurements actually

received was on the order of 15 percent, much less than anticipated. Comparison of the truth model image centroid and velocity orientation angle to the filter estimates of these parameters showed the errors in the filter-estimated velocity orientation angle to be the reason for the low percentage of reflections received. This problem will be discussed further in Section 6.3.

6.2.2 Offset Filter Sensitivity Study. This study examined the effects of different sensor measurement noise levels on filter performance. The analysis indicated that the steady-state mean error in the offset length is insensitive to measurement noise variance. The standard deviations reported were also relatively independent of measurement noise variance. The measurement noise variance does strongly affect the amount of time the filter takes to reach the steady-state error level. The conclusion from this is that sensor accuracy may be a secondary consideration in system design trade-off studies, for the models used here.

6.2.3 Offset Filter Robustness Study. In a robustness study, the primary area of concern is the filter's performance when the "real world", as represented by the truth model, is different from the filter's internal world model. The parameter used in this study was the measurement noise variance. Three filters, with high, medium, and low assumed measurement noise variances were studied. In each case, the

filter's performance was analyzed when the truth model was given a measurement noise level different from that in the filter. The results indicated that the filter's performance was fairly robust to changes in this truth model parameter. These results lead to the conclusion that single filter performance is adequate and a multiple model adaptive filter algorithm or other form of filter that adapts to this parameter is not necessary.

6.2.4 Pixel Proportionality Constant Study. The results of this study are not conclusive. The general expectation for FLIR tracking systems is that increased sensor resolution should lead to increased tracking accuracy. However, the results did not support this in all respects. The intermediate sensor resolution gave the best filter performance. No immediate explanation was found for this result. Since the six-state filter was tuned using this value, it is unknown whether or not this introduced a bias in the results. No conclusions were reached; this topic will be will addressed further in Section 6.3.

6.2.5 Offset Distance Study. The final study in this research examined the effect of increasing the offset distance between missile hardbody and infrared intensity centroid. The offset distances studied were selected to allow both the FLIR intensity image and the reflections from the missile hardbody to occur within an 8 x 8 pixel field of

view. The results support the conclusion that, as offset distance increases, filter performance decreases; the amount of degradation was quantified.

6.3 Recommendations

The recommendations made here are to suggest possible lines of research to clarify problems uncovered in this research or to expand preliminary investigations started in this work.

6.3.1 Six-State Filter Modeling and Tuning. Based on Rizzo's recommendations [14], a reduced order six-state filter was finally implemented by removing acceleration states from the filter design model. However, Rizzo also recommended remodeling the acceleration states using a constant turn rate instead of a first-order Gauss-Markov model. This suggestion was not implemented in this research. Remodeling the acceleration states, retuning the filter, and then doing an observability analysis, represents an alternative approach to addressing the observability problem. This approach might also yield a filter which better estimates the velocity orientation angle. It cannot be emphasized enough that accurate velocity vector estimation is crucial to the viability of the algorithm in its present form.

The second recommendation is to retune the six-state filter to yield better velocity estimates. The tuning

accomplished in this research paid close attention only to the filter's performance with regard to estimating the FLIR intensity image centroid location. The filter should be retuned for both accurate centroid position and velocity vector estimates. For active illumination of the target to be a viable concept, both the image centroid and the velocity vector must be accurately estimated.

Direct examination of jitter position plots would also benefit the tuning process. In this effort, the jitter position state tuning response could only be examined indirectly by looking at the image centroid plots. By directly examining plots of both dynamics and jitter position states, a clearer understanding of the effect on filter tuning of changing parameters in these two processes could be achieved.

6.3.2 Illumination Modeling Improvement. For this thesis research, a simple geometrical approach was used to model the laser illumination of the target. Many effects were neglected. For future work, a more accurate model is needed. This model should include more accurate representation of the missile's three-dimensional shape. The simulation of the laser reflection itself should include missile shape effects (laser reflecting off cylindrical object rather than flat surface), and the effects of atmospheric distortion in the reflected laser light. Also, the dynamics of sweeping the laser up and down the estimated

velocity vector direction from the intensity centroid should be incorporated. Alternate search patterns, in which the laser is swept both along and perpendicular to the estimated velocity vector in a sinusoidal pattern, should be considered. This would increase the probability of reflection by increasing the search area, as well as reducing the dependence of the algorithm on an accurate velocity vector estimate. The increased accuracy of illumination modeling will significantly enhance the credibility of the simulation and conclusions drawn from it.

6.3.3 Different Initial Filter Parameters. With no previous knowledge of the initial errors involved with pointing a laser at a missile, the initial value for the offset filter mean and covariance were set to zero. As was evident in the sensitivity and robustness studies, this had a significant effect on filter performance. Based on the steady state filter errors found in this research, it is recommended that the analyses be performed again using an initial mean of 0.1 pixels and covariance of .05 pixels² to confirm the results found here.

6.3.4 Pixel Proportionality Constant Filter Tuning. The results of the pixel constant study were inconclusive. To resolve the issue of sensor resolution, the six-state filter should be separately tuned using the two pixel constants studied in Section 5.6. After tuning, comparison of

the performance of the three filters should help resolve this issue.

6.3.5 Mass Center Error Resolution. The error between the filter estimated center of mass and the truth model center of mass used in the analysis was calculated as the scalar length between two coplanar points. To aid in future work, this error should be resolved into a component along the estimated velocity vector, and a component perpendicular to the velocity vector. By doing this, it should be possible to determine the contribution of the offset distance estimate (along velocity vector component) and the estimated velocity vector orientation angle (perpendicular to velocity vector component) to the total error.

Appendix A. Mass Center Measurement Simulation

As presented in Section 2.4.2, the mass center measurement simulation is developed in terms of plane geometry. The projection of the missile hardbody shape onto the two-dimensional FLIR plane is represented by a rectangle. To simulate the reflection of the laser, and the mass center measurement derived from that reflection, the path the laser takes as it is dithered along the velocity vector had to be simulated. It was decided to represent the laser's path as a rectangle in the FLIR plane also. The width of the rectangle was chosen to approximate the laser beamwidth at the target. For this study, a beamwidth of 2.75 meters was used. The length of the rectangle was determined using three times the truth model offset distance between the missile center of mass and the FLIR image centroid. This was done to insure that the rectangle was long enough for intersection with the rectangle representing the missile to occur.

The rectangle representing the laser path is located on the FLIR plane using the filter estimated image centroid location and velocity vector orientation. This is shown in Figure A.1. One end of the rectangle is located coincident with the image centroid location. The coordinates of the opposite end of the laser path rectangle are located using

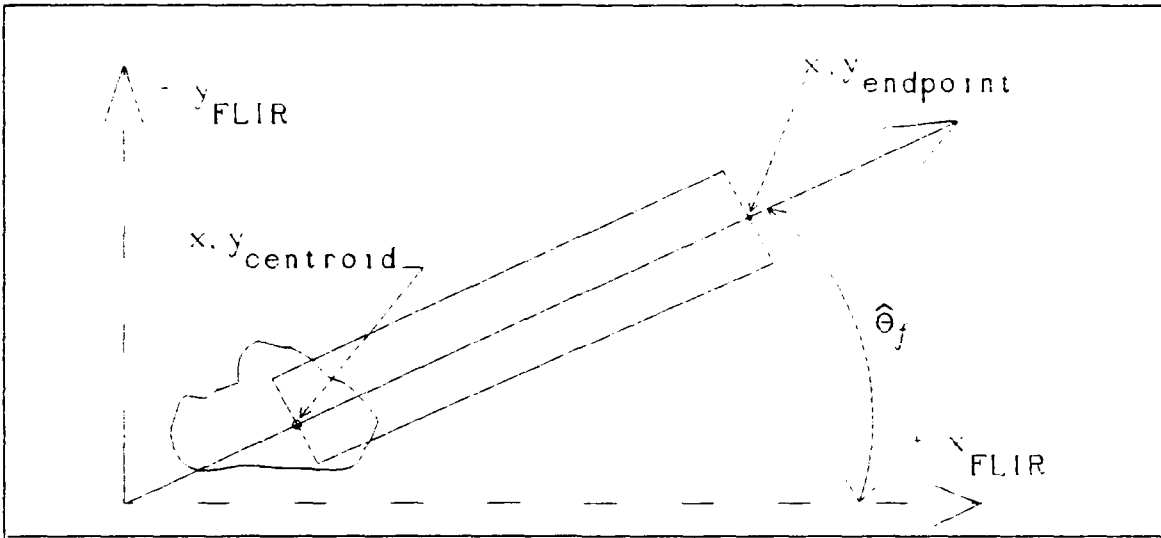


Figure A 1 Laser Beam Simulation

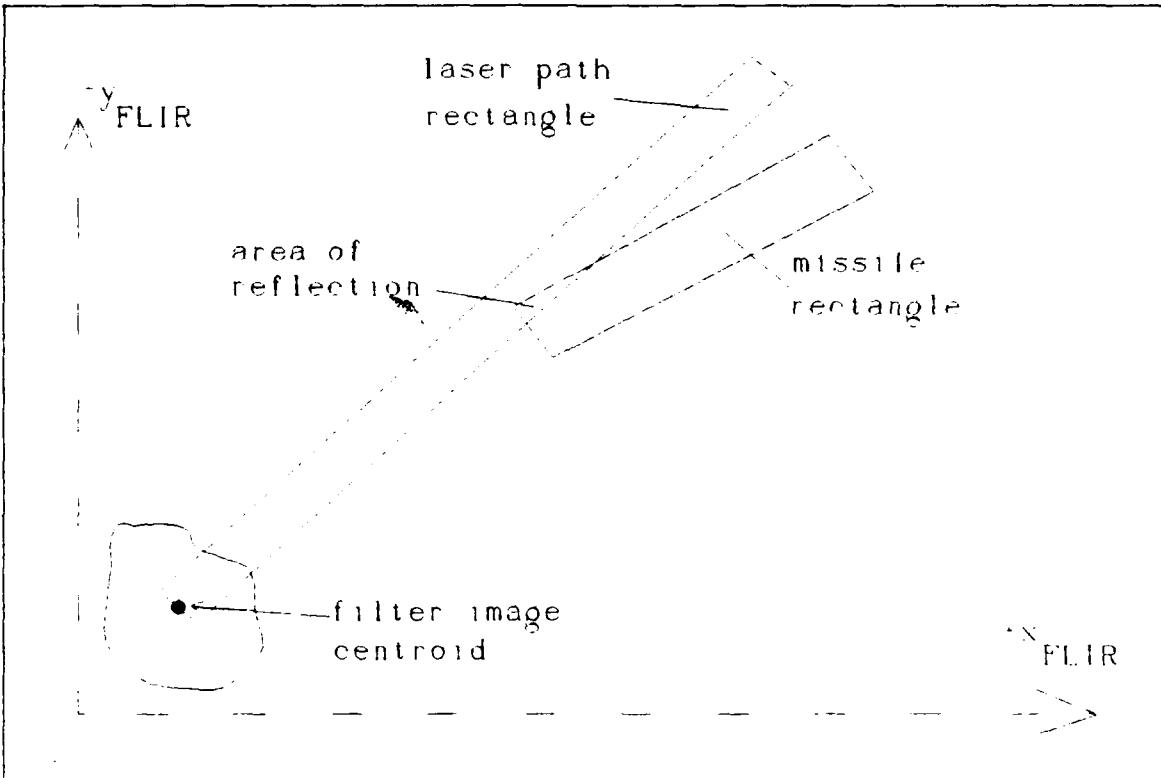


Figure A 2 Reflection Simulation

the filter estimated velocity vector orientation angle. The calculations for the endpoint are as follows:

$$x_{endpoint} = x_{centroid} + length \cos \theta_f \quad (A-1)$$

$$y_{endpoint} = y_{centroid} - length \sin \theta_f \quad (A-2)$$

where:

$x_{endpoint}$, $y_{endpoint}$ = the FLIR plane coordinates of the
rectangle endpoints

$x_{centroid}$, $y_{centroid}$ = the FLIR plane image centroid
coordinates

$length$ = desired rectangle length, in pixels

θ_f = filter estimated velocity vector
orientation angle

Once the endpoints have been determined, the coordinates of the corners of the rectangle are determined by offsetting half the beamwidth distance from the endpoints along a line perpendicular to the velocity vector.

The simulation of the laser reflection and the corresponding center of mass measurement is done in several steps. First, the laser beam striking the missile and reflecting is simulated by determining the area of intersection between the missile rectangle and the rectangle representing the laser beam path, as shown in Figure A.2. This area of intersection is determined using plane geometry. Figure A.3

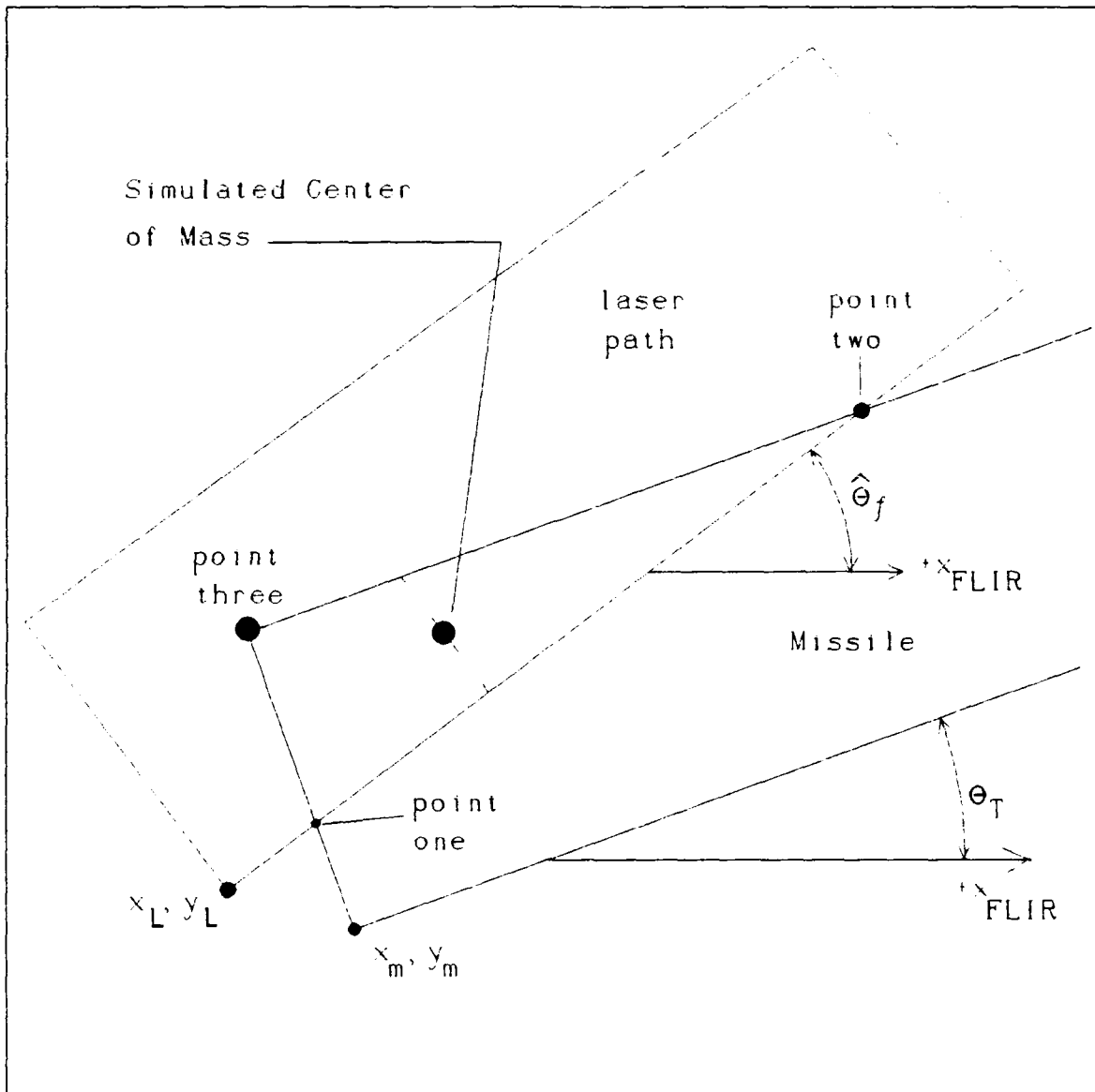


Figure A.3. Center of Mass Measurement Simulation

shows an expanded view of the area of intersection. Note that, for this example, two of the corners of the perimeter of the intersection area are determined by the intersections of line segments representing the outline of the missile and laser path rectangle. The determination of the intersection coordinates is a matter of plane geometry. For example, the determination of the x and y coordinates of point 1 is made as follows:

The slope of the line segment between (x_1, y_1) and point two is m_1 , where $m_1 = \tan \theta_f$; the equation of this line is

$$y = m_1(x - x_1) + y_1 \quad (\text{A-3})$$

Likewise, the slope of the line segment between (x_m, y_m) and point three is m_2 , where $m_2 = -\frac{1}{\tan \theta_f}$; and the equation of this line is

$$y = m_2(x - x_m) + y_m \quad (\text{A-4})$$

Setting Equation (A-3) equal to Equation (A-4) and solving for x yields:

$$x = \frac{m_1 x_m - m_2 x_1 + y_m - y_1}{m_1 - m_2} \quad (\text{A-5})$$

Solving Equation (A-5) and substituting this value into either Equation (A-3) or (A-4) yields the coordinates of point one in Figure A.3. The coordinates for point two, or for any other intersection point, are determined in a similar manner. One area of concern is that Equations (A-3)-(A-5) involve the equations of lines, not line segments.

Therefore, in the simulation, the software checks the value of the x intercept point to determine if it is between the x coordinate of point three and x_4 . If this condition is true, then the line segments do intersect, some portion of the laser beam rectangle falls on the missile rectangle, and reflection occurs. If this condition is not met, then the intersection point occurs beyond the line segment endpoints. In this case, no portion of the laser rectangle and the missile rectangle are in common. This constitutes a "miss", and no reflection occurs.

Assuming reflection has occurred, the next step is to determine the center of mass. Since the entire purpose of using low power laser reflections is to obtain information about the center of mass of the missile, the center of the intersection area is equated to the "measured" center of mass. For the example of Figure A.3, the area defined by points one, two, and three is triangular. Approximating the center of this area is basically approximating the center of a triangle. The center of a triangle would normally be determined by the intersection of three lines, each line running from a corner to the opposite side, and that line bisecting the angle at that corner. This intersection is approximated by first taking a point one third the distance from point one to two along that line segment. At that point, a perpendicular line segment is run to the line segment between points two and three. The center is

approximated by a point halfway along the perpendicular line segment. The distance between this center point and the FLIR image centroid of Figure A.1 becomes the offset length measurement of Equation (2-44). If the area of intersection is rectangular or trapezoidal, then the calculations for the center of the are made accordingly.

Appendix B. Plots for Six-State Filter Tuning

Discussion in Section 5.3

Run #1 Figures B.1-B.10

Run #2 Figures B.11-B.20

Run #3 Figures B.21-B.30

Run #4 Figures B.31-B.40

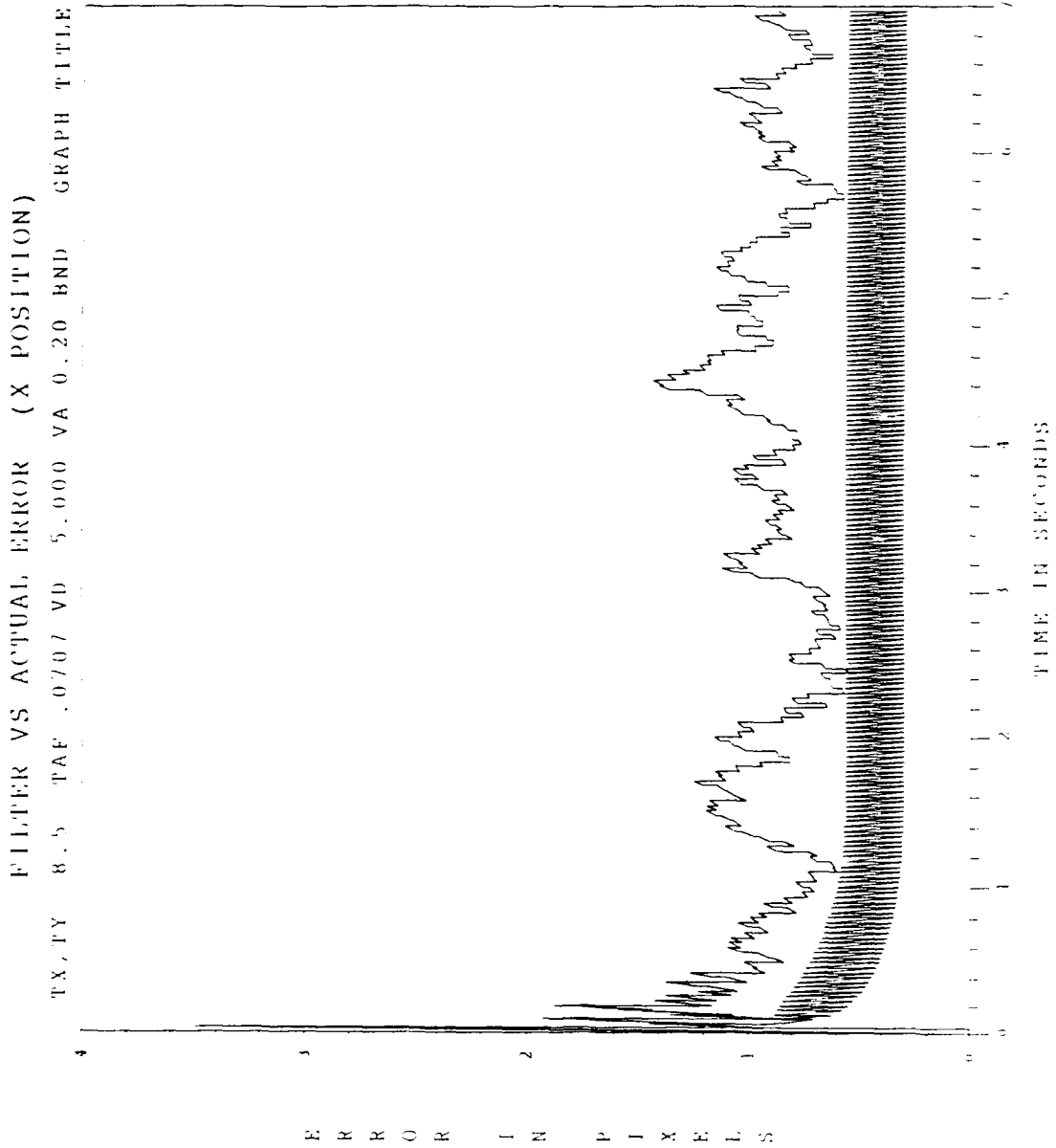


Figure B.1 Tuning Run #1 X-Channel Filter Vs Actual Error

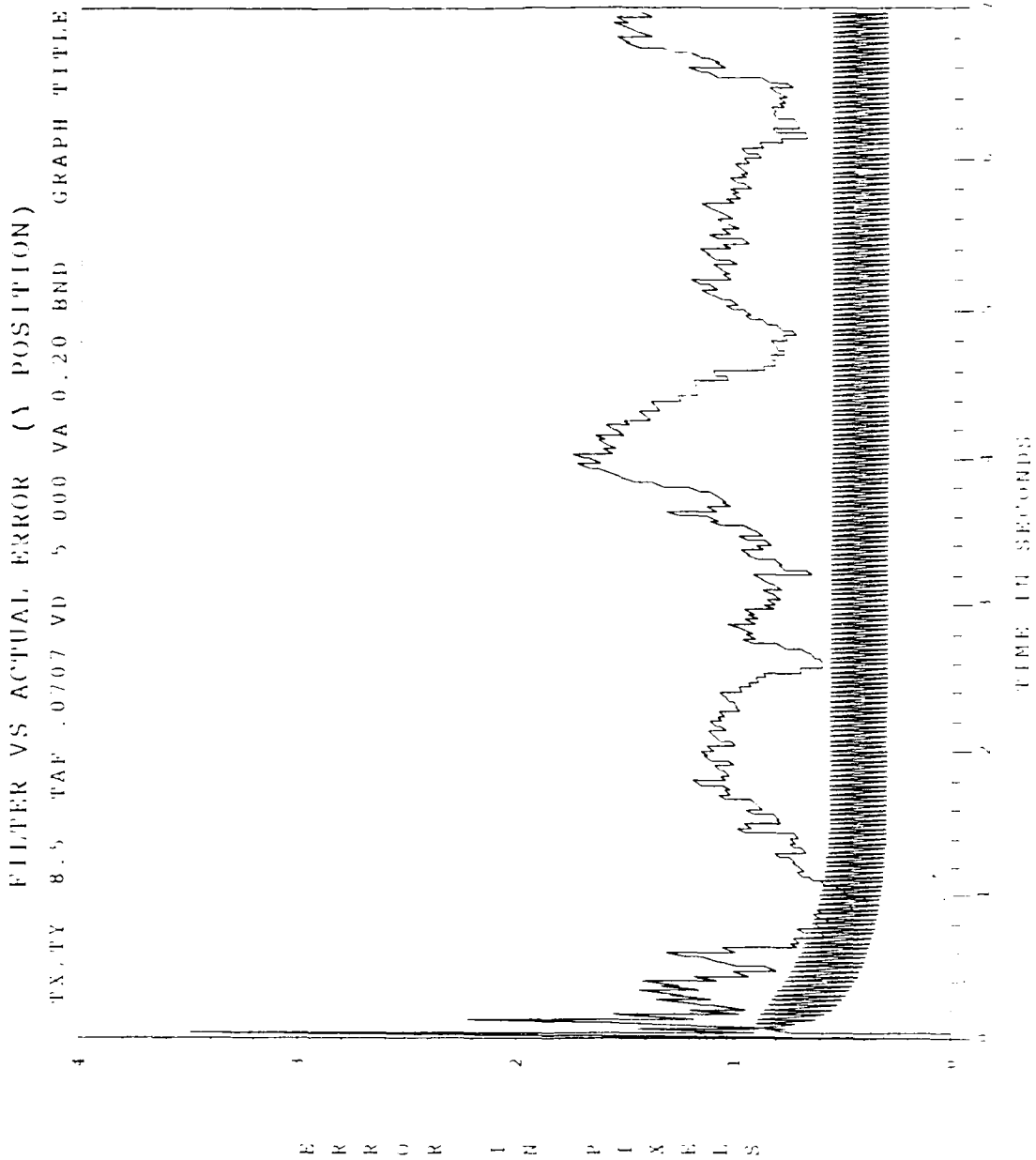


Figure B.2 Tuning Run #1 Y-Channel Filter Vs Actual Error

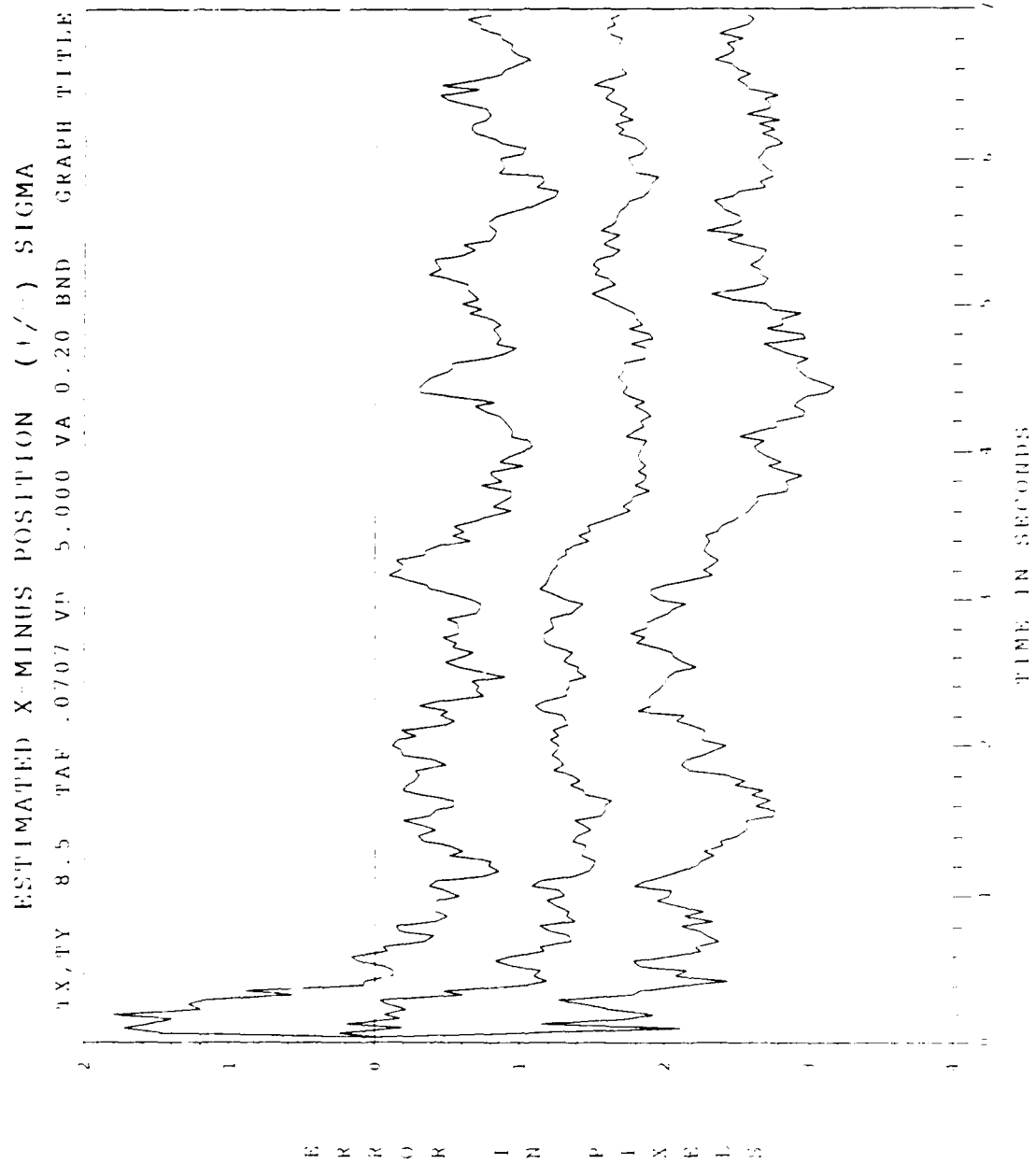


Figure B.3 Tuning Run #1 X-Minus Position Error

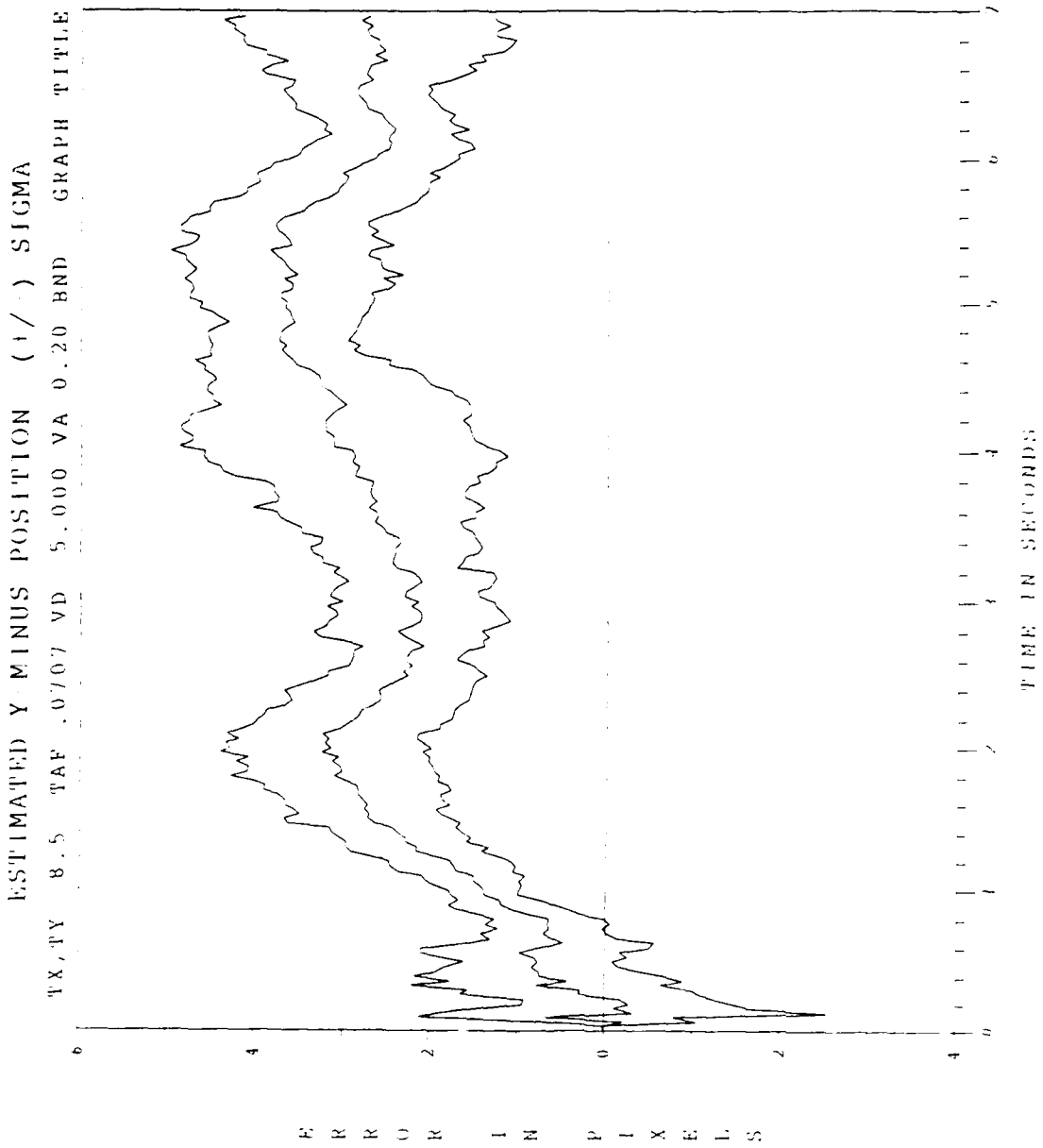


Figure B.4 Tuning Run #1 Y-Minus Position Error

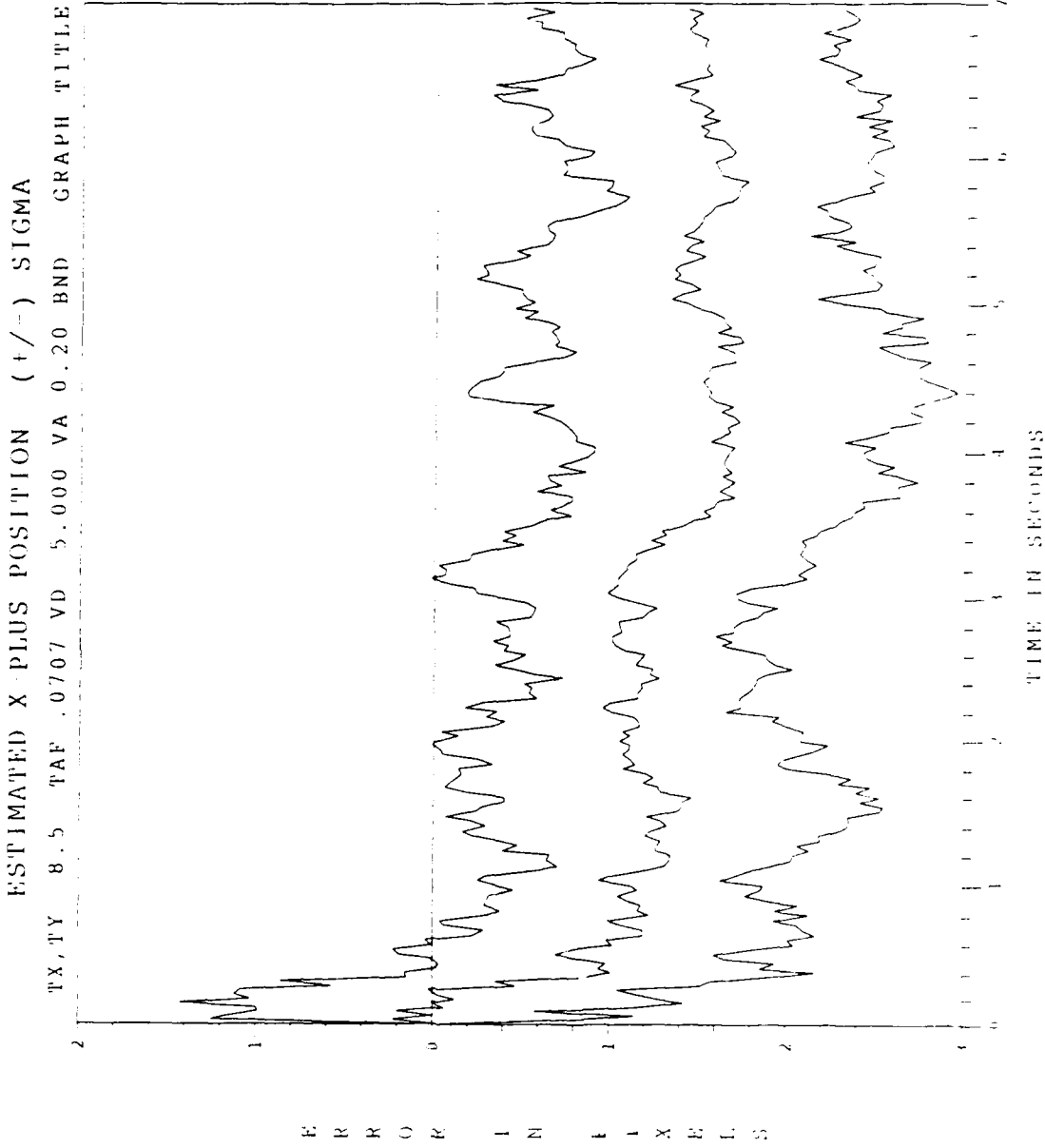


Figure B.5 Tuning Run #1 X-Plus Position Error

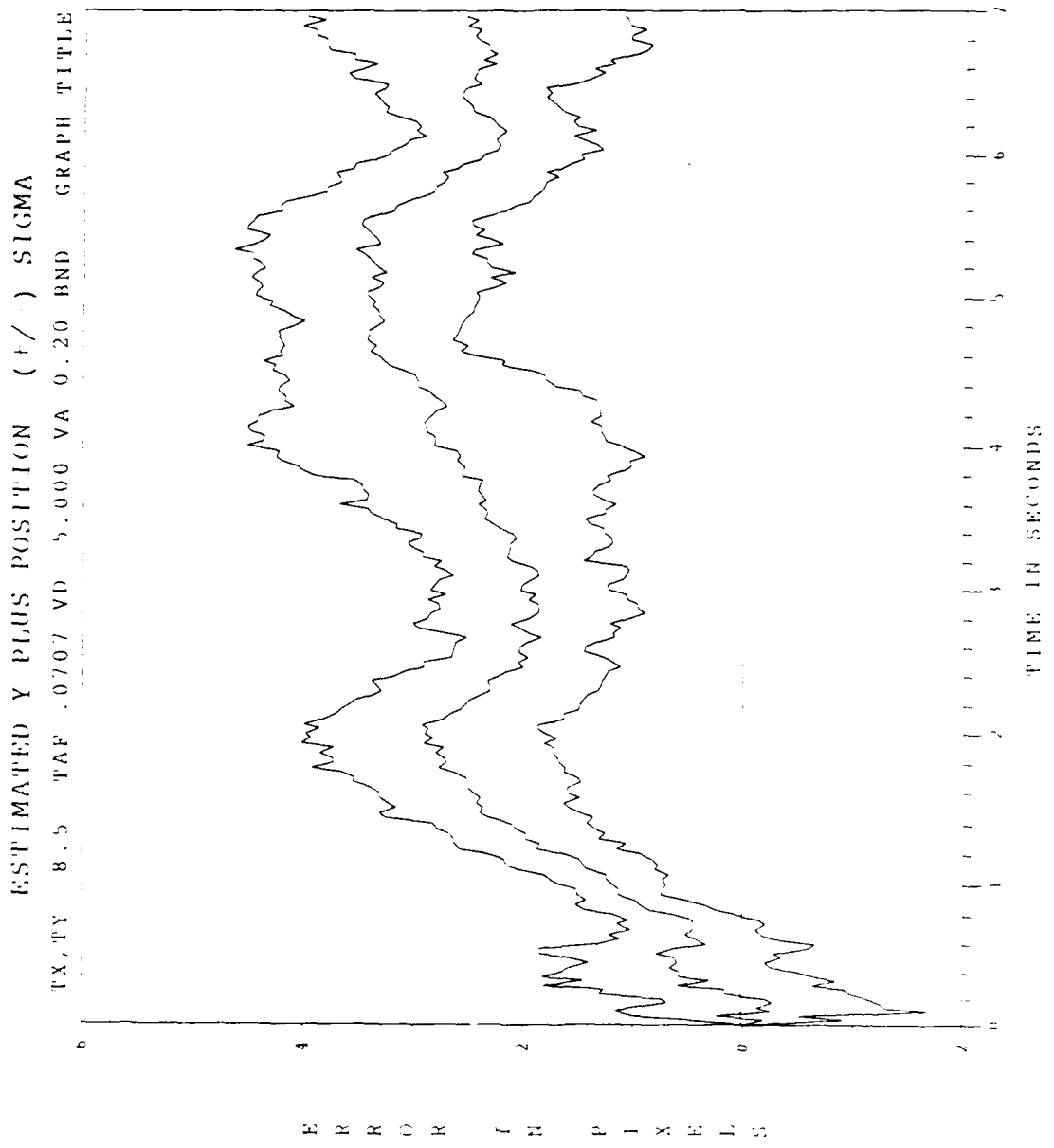


Figure B.6 Tuning Run #1 Y-Plus Position Error

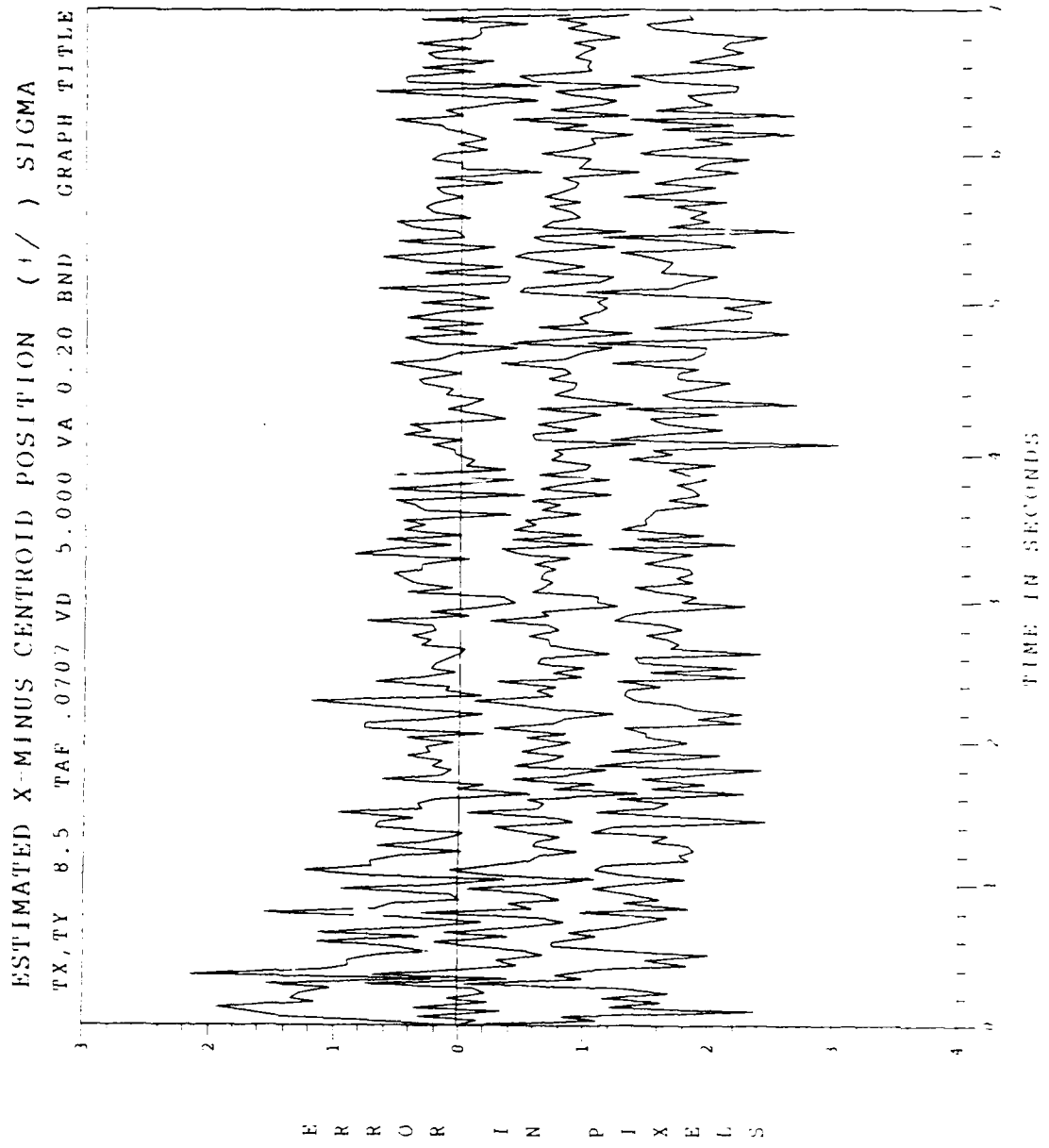


Figure B.7 Tuning Run #1 X-Minus Centroid Position Error

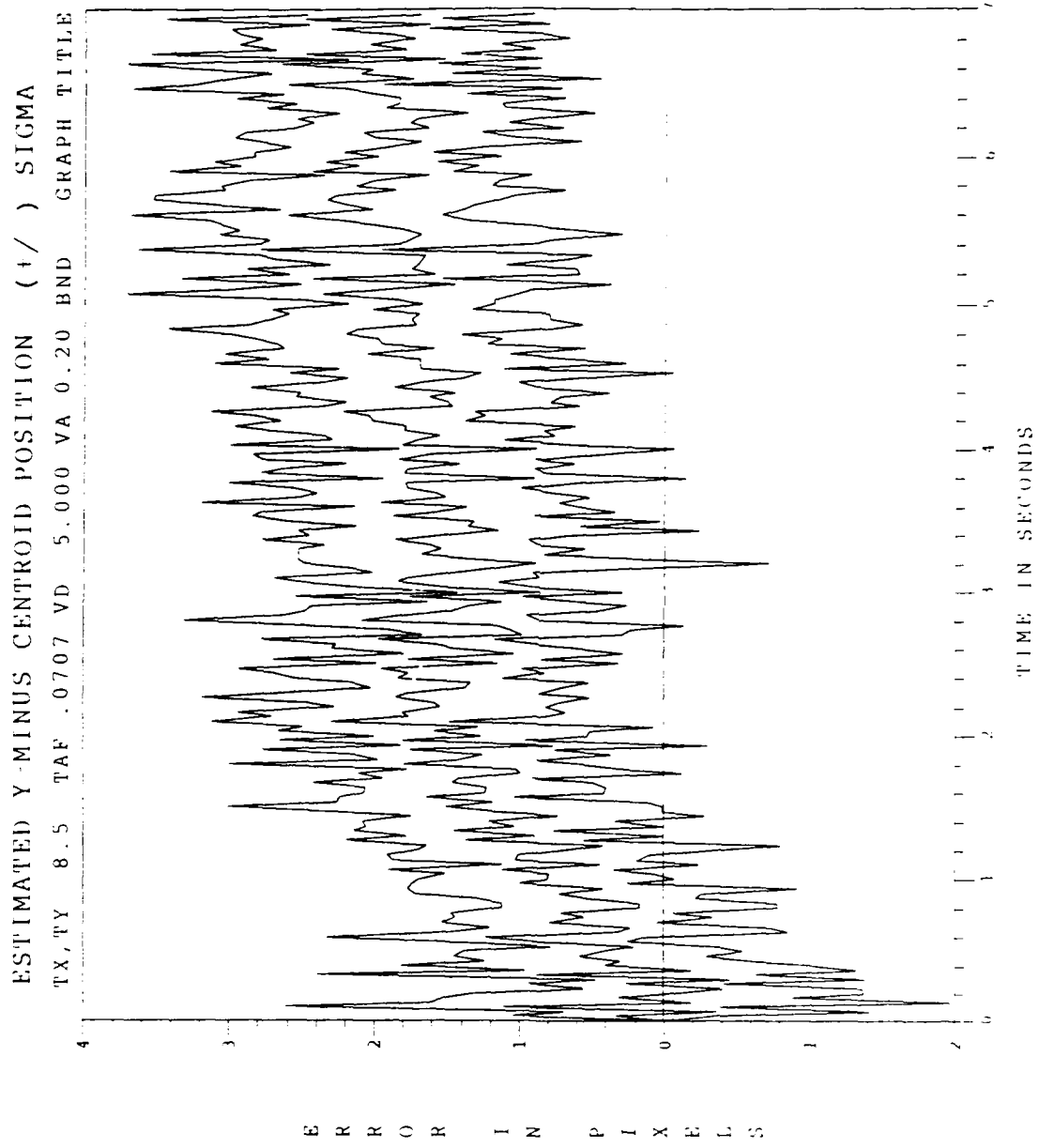


Figure B.8 Tuning Run #1 Y-Minus Centroid Position Error

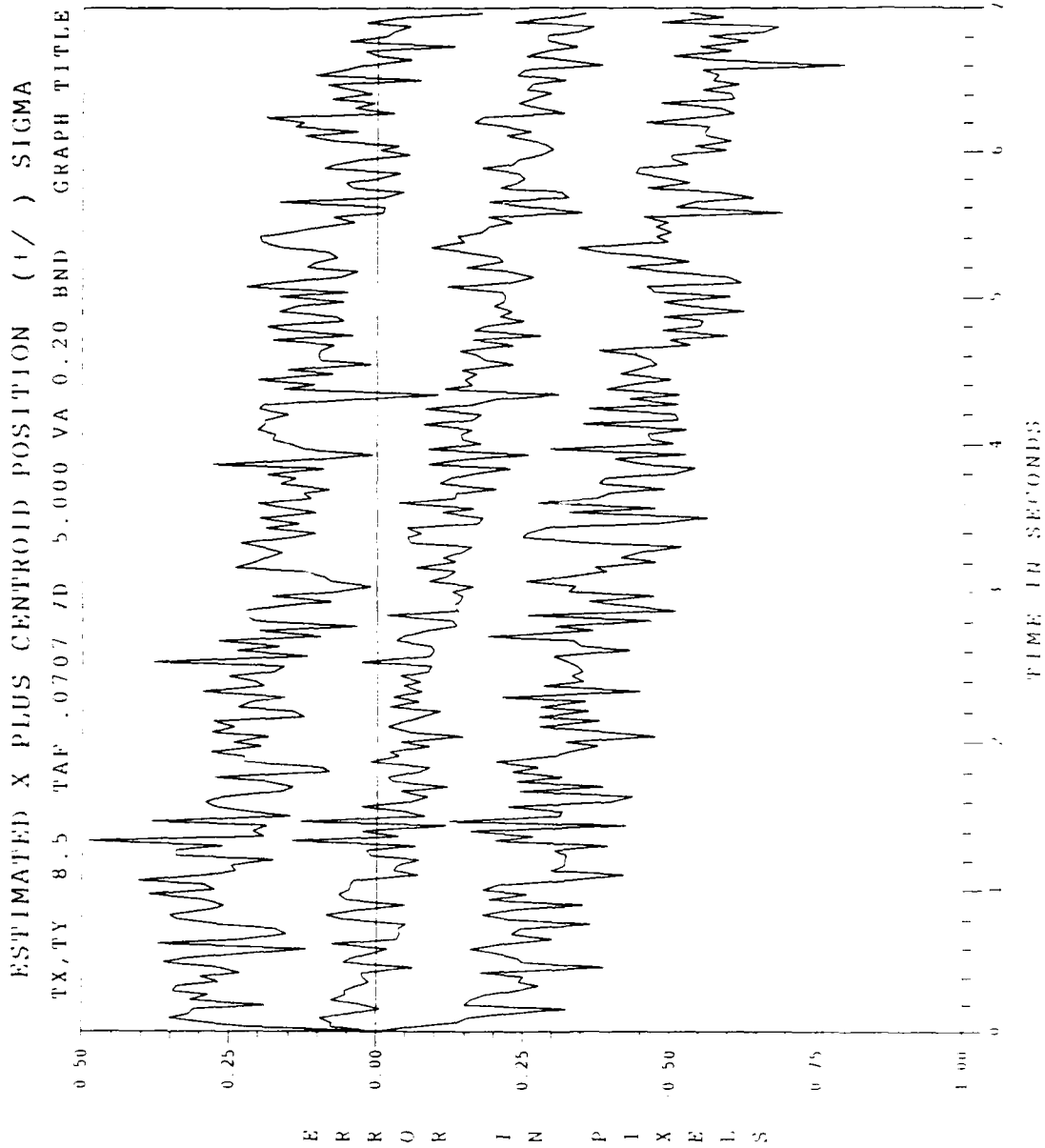


Figure B.9 Tuning Run #1 X-Plus Centroid Position Error

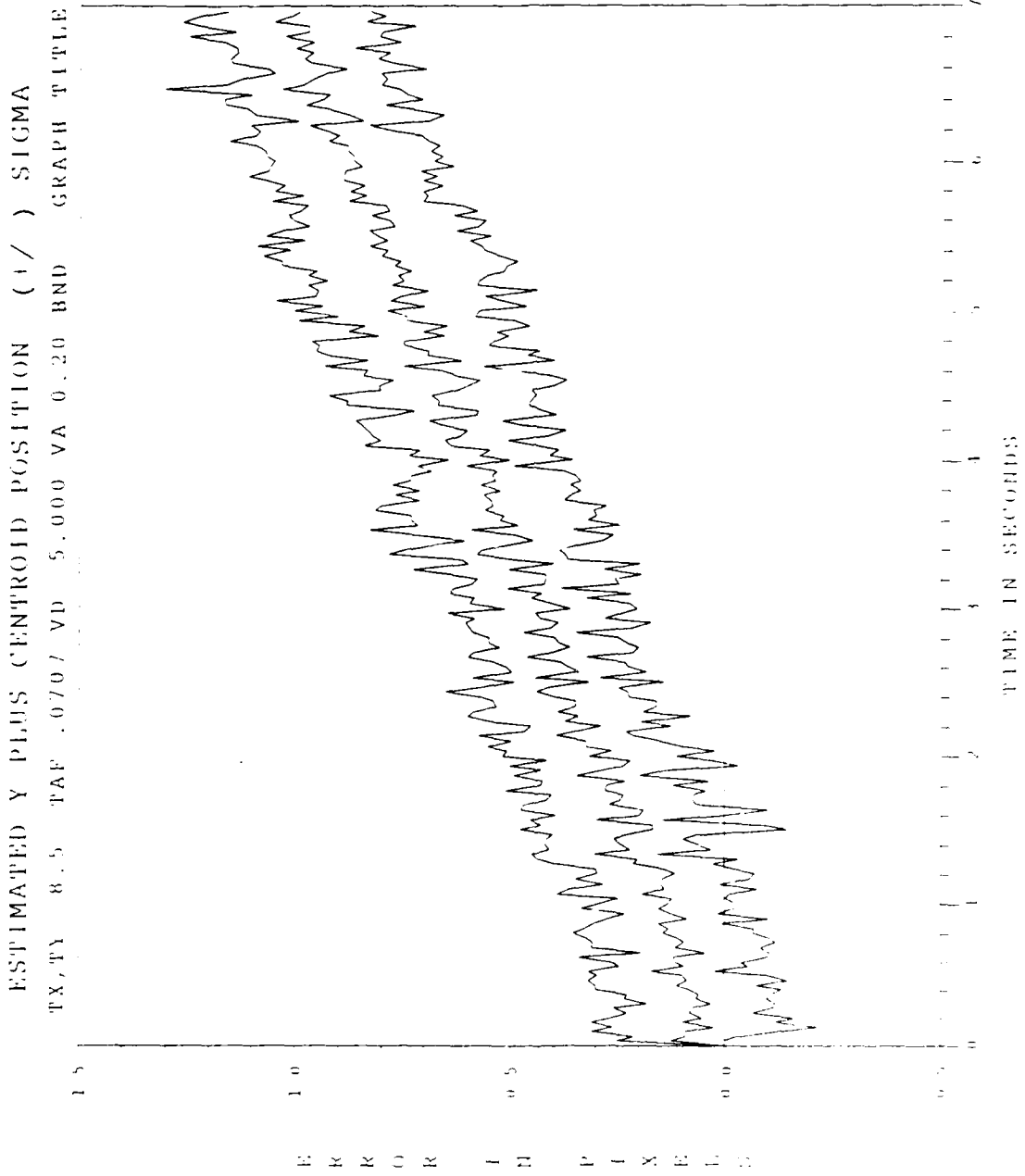


Figure B.10 Tuning Run #1 Y-Plus Centroid Position Error

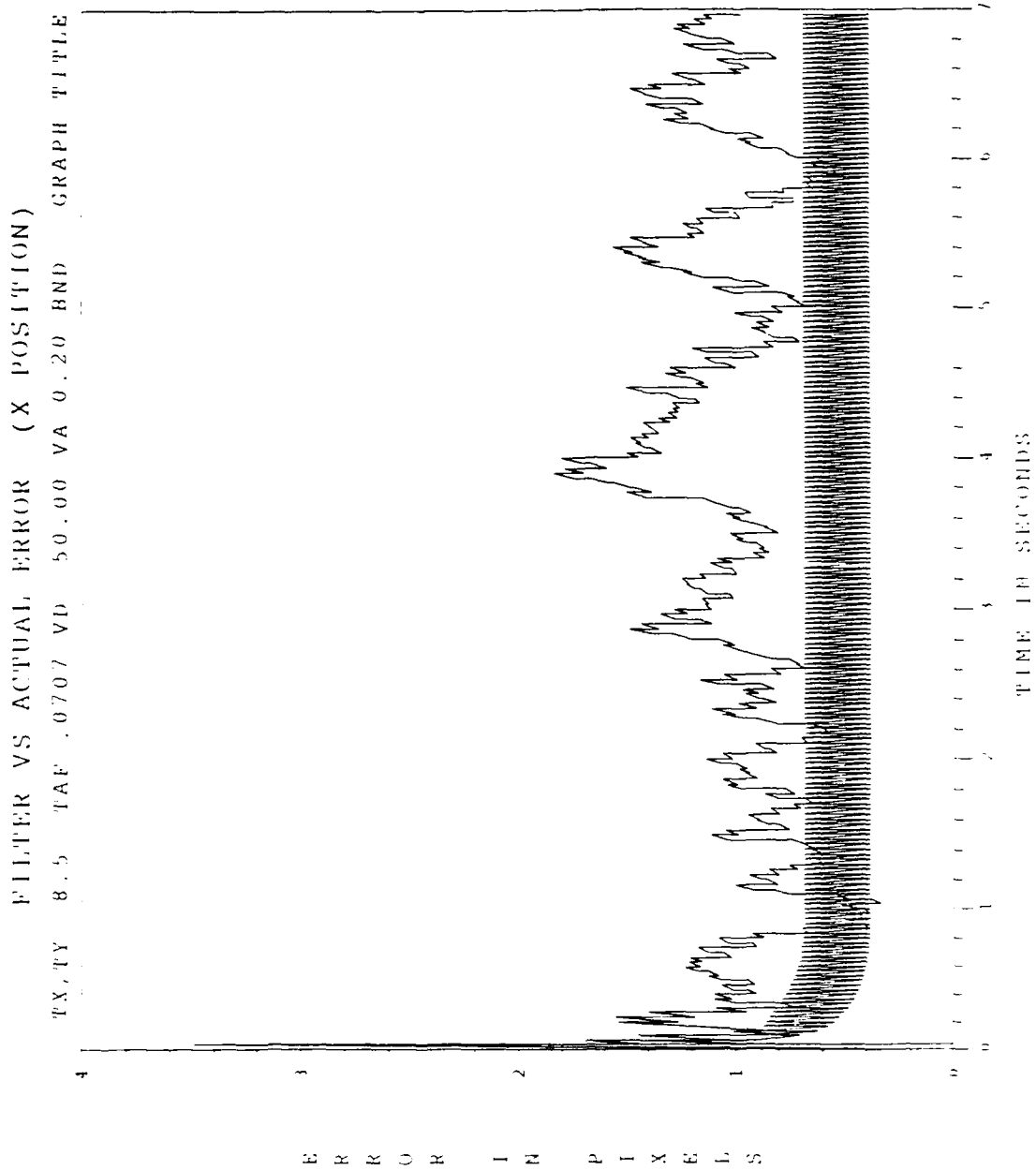


Figure B.11 Tuning Run #2 X-Channel Filter Vs Actual Error

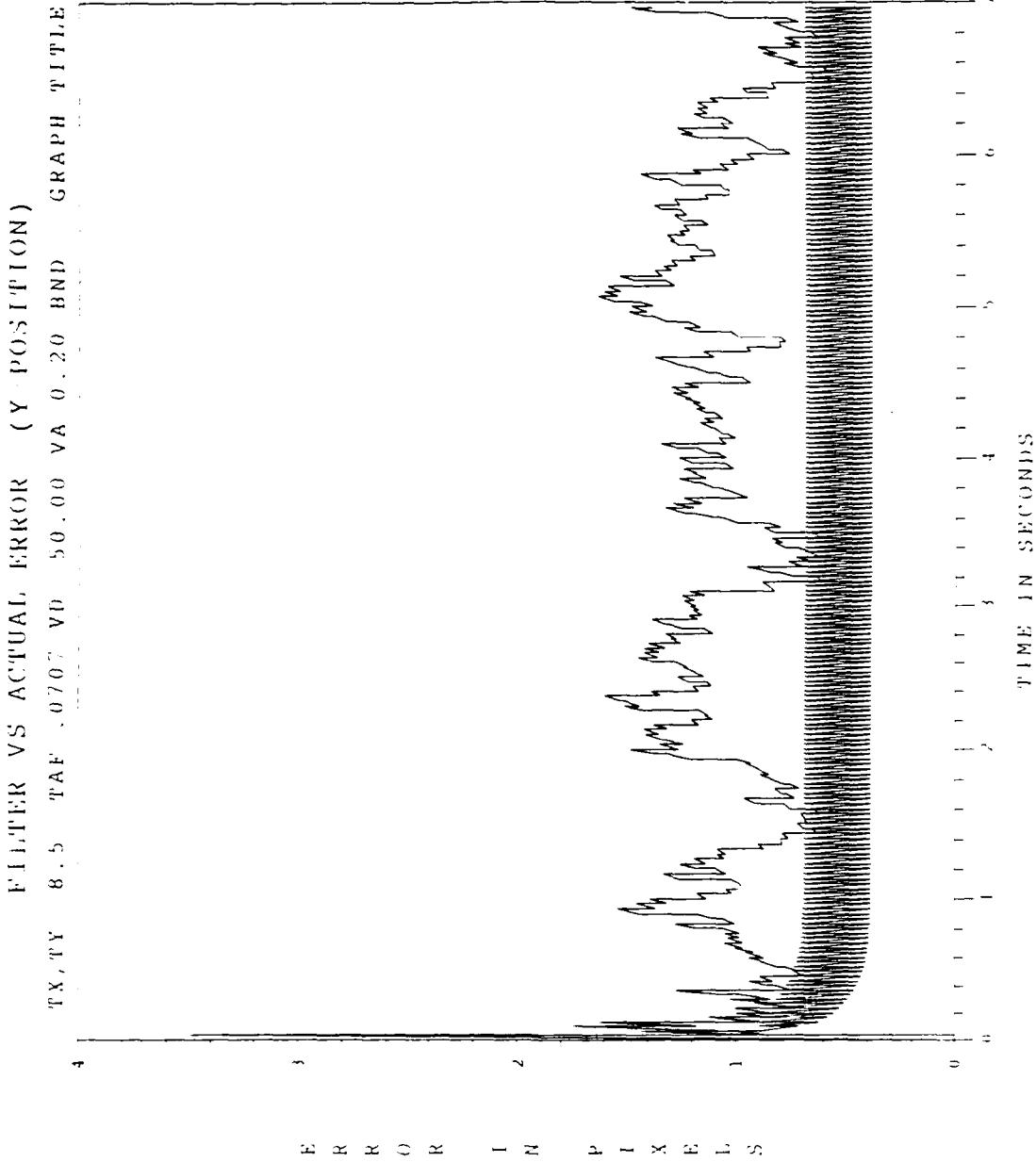


Figure B.12 Tuning Run #2 Y-Channel Filter Vs Actual Error

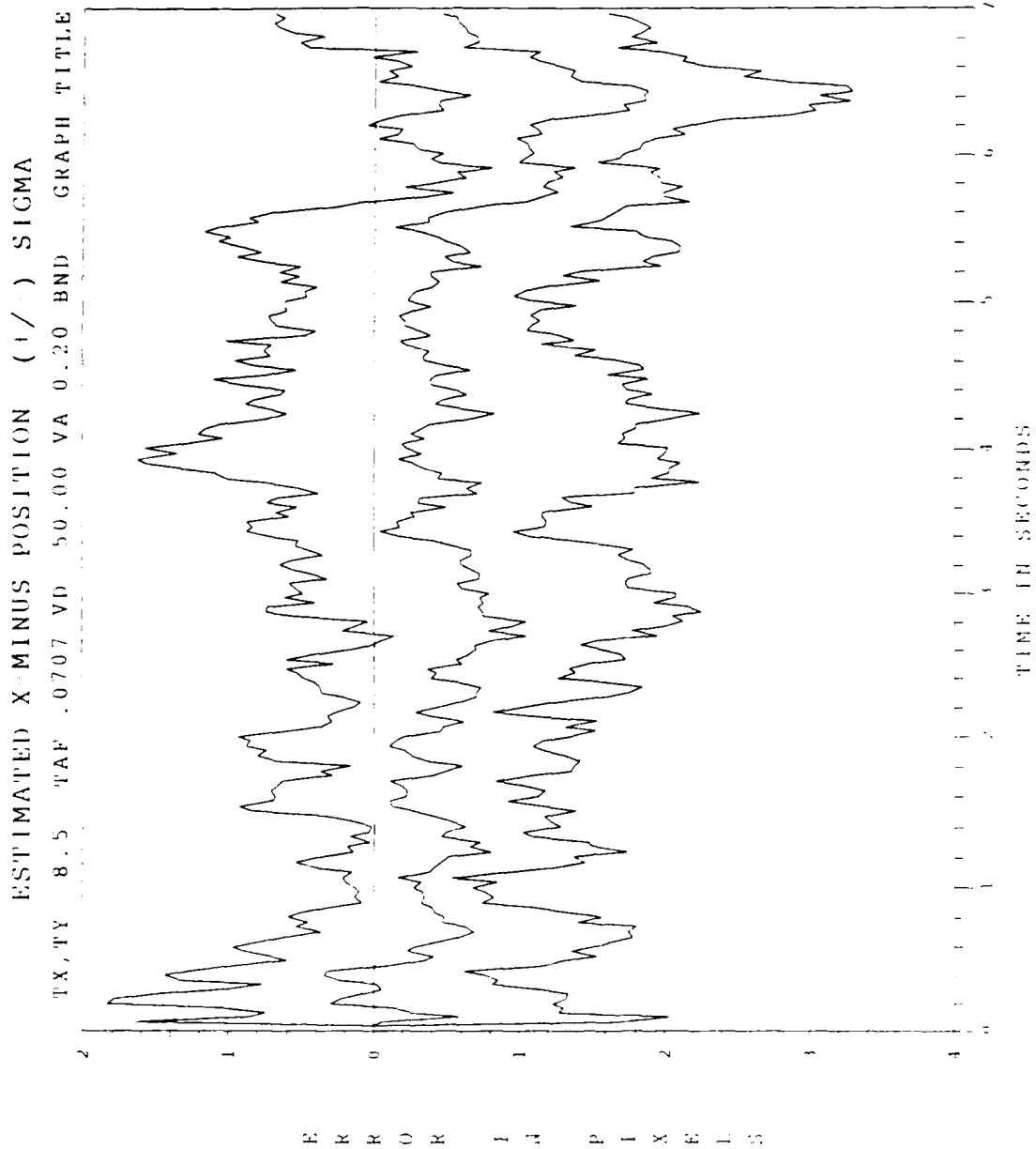


Figure B.13 Tuning Run #2 X-Minus Position Error

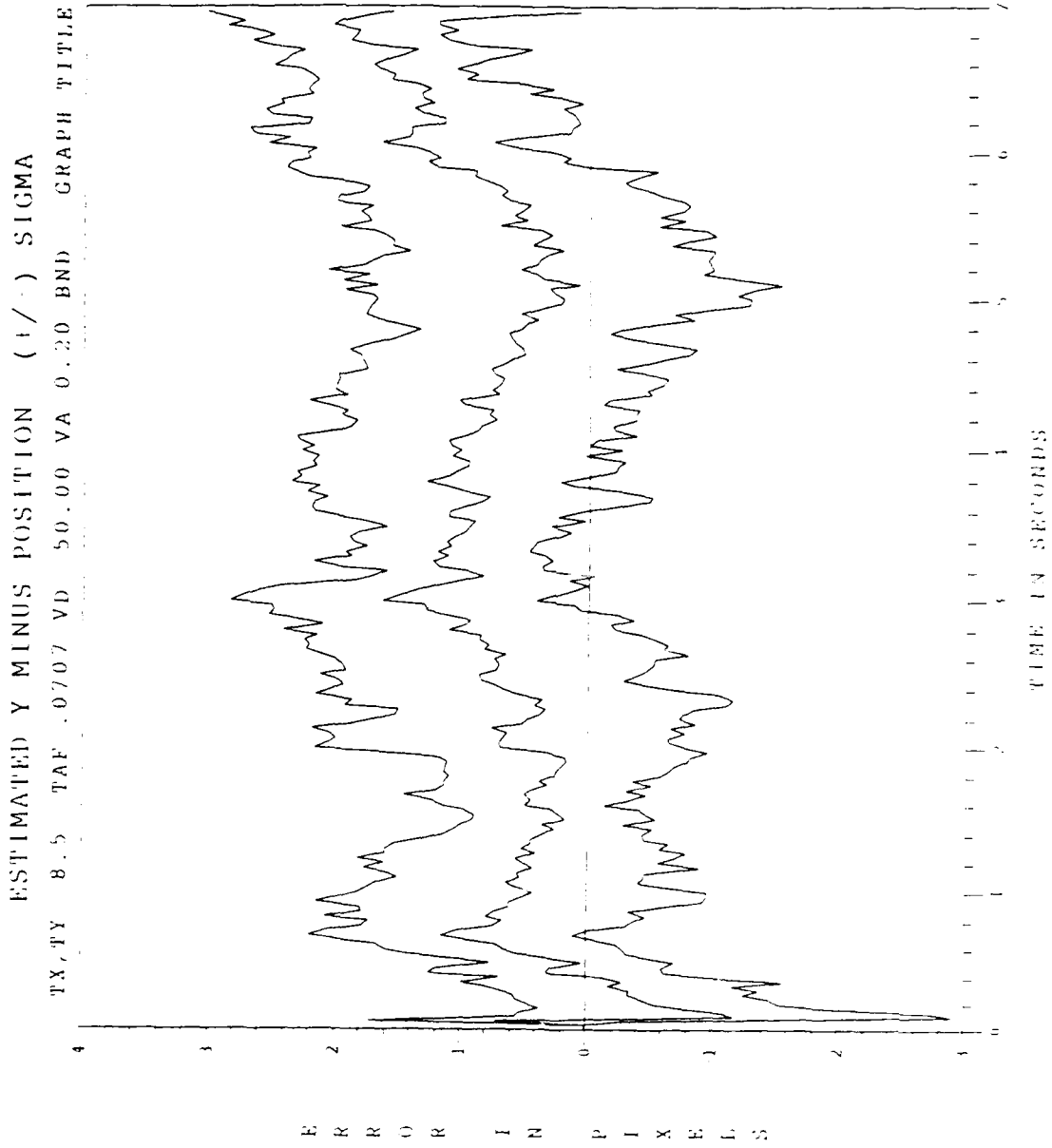


Figure B.14 Tuning Run #2 Y-Minus Position Error

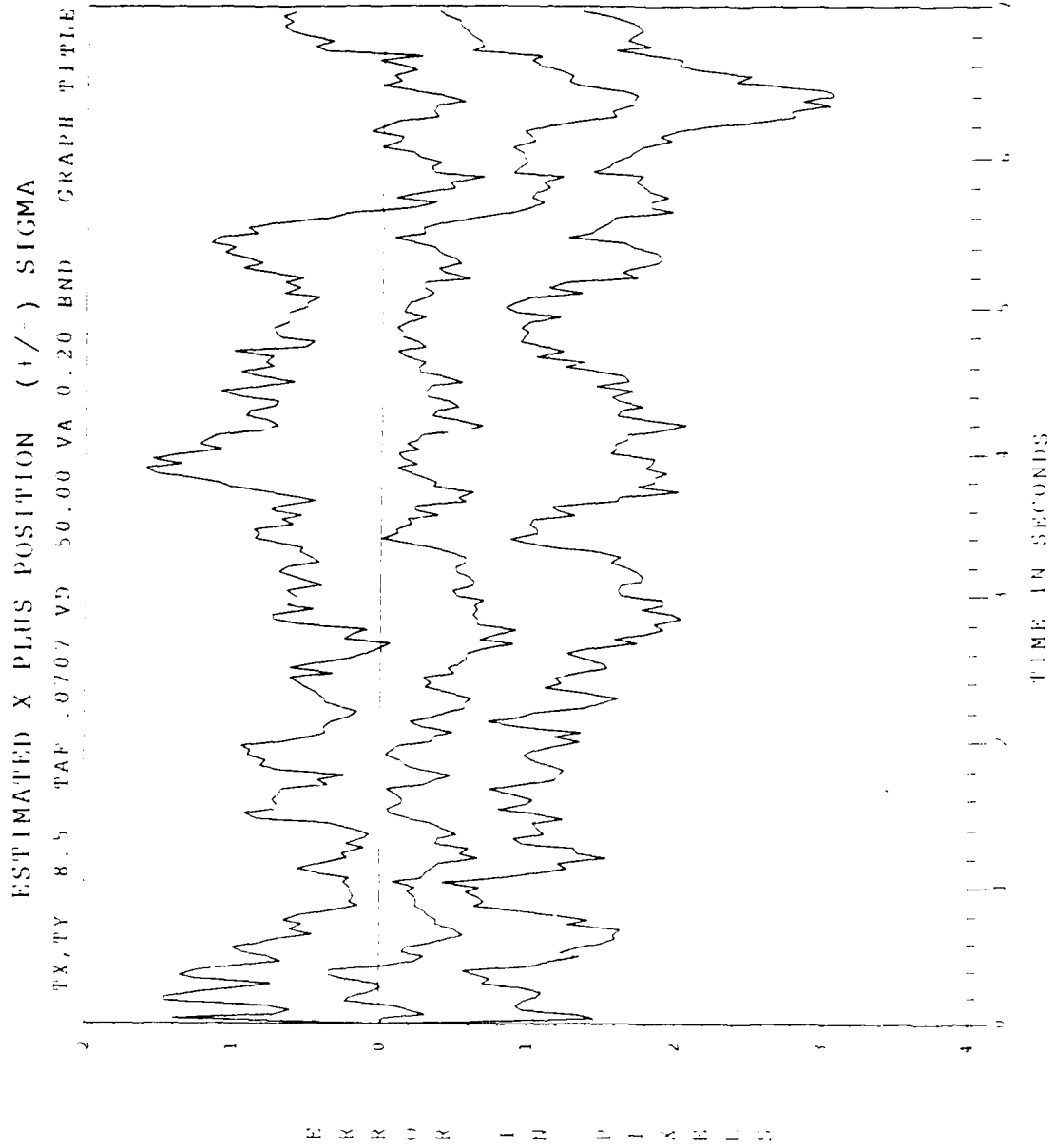


Figure B.15 Tuning Run #2 X-Plus Position Error

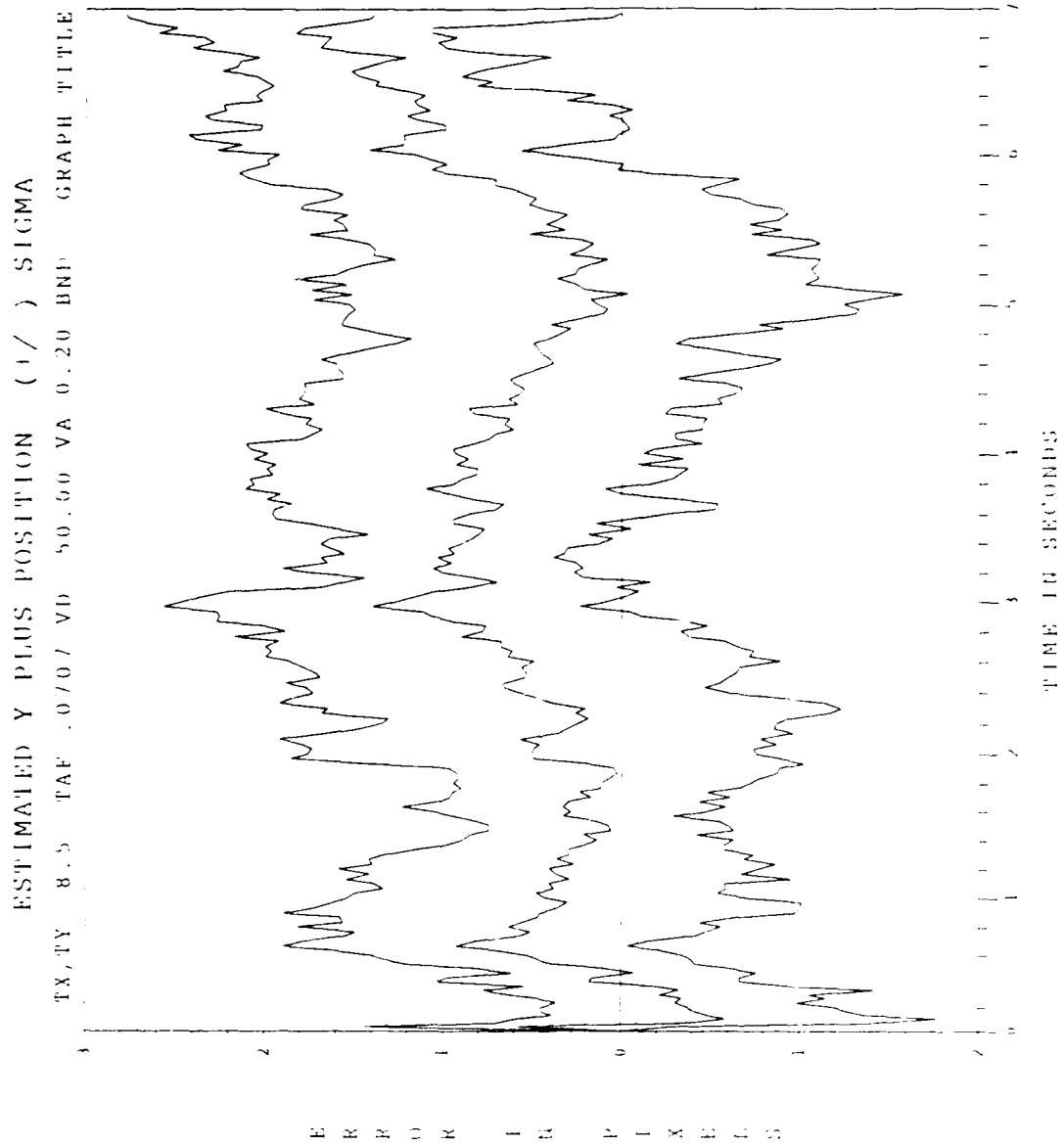


Figure B.16 Tuning Run #2 Y-Plus Position Error

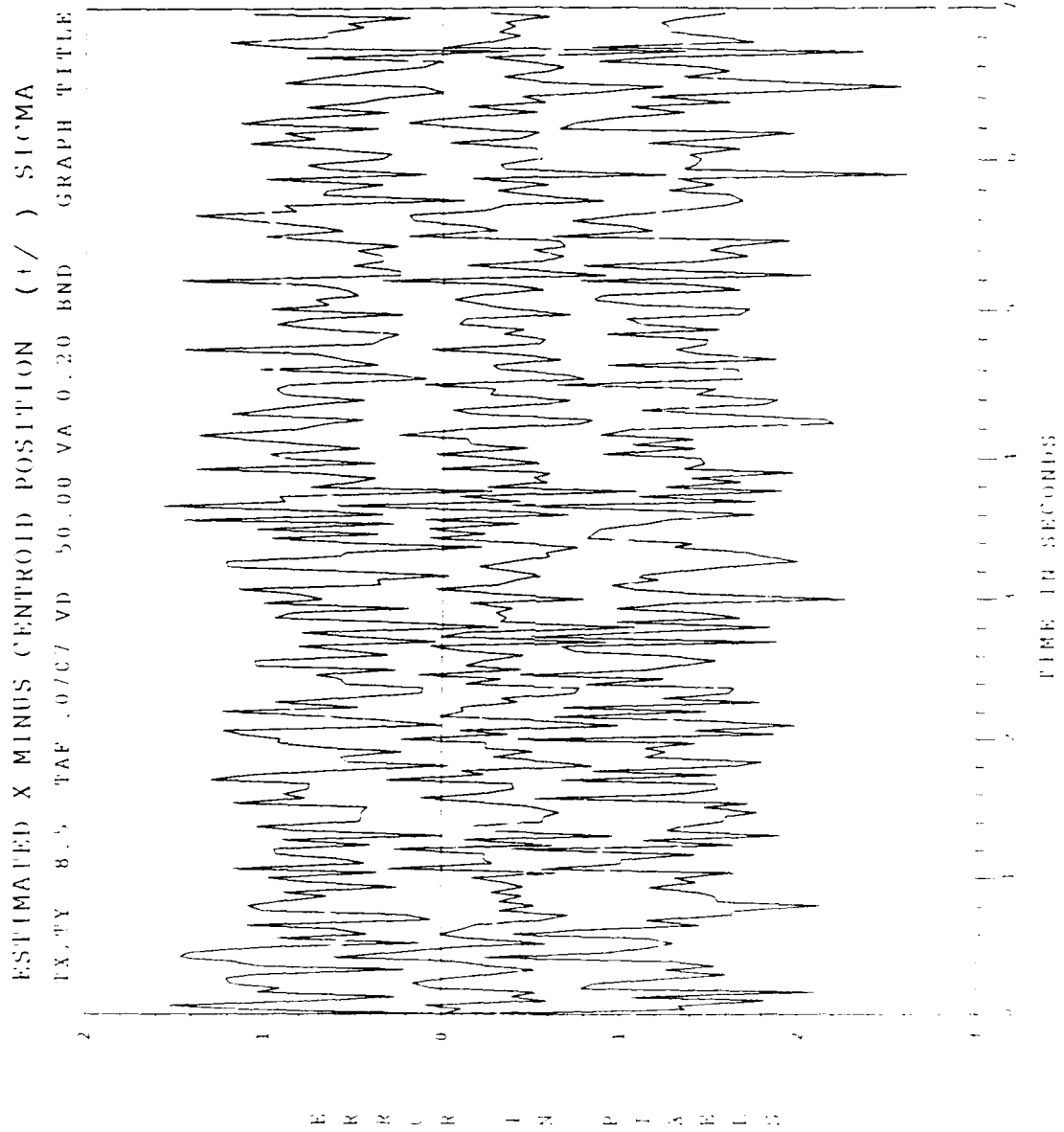


Figure B.17 Tuning Run #2 X-Minus Centroid Position Error

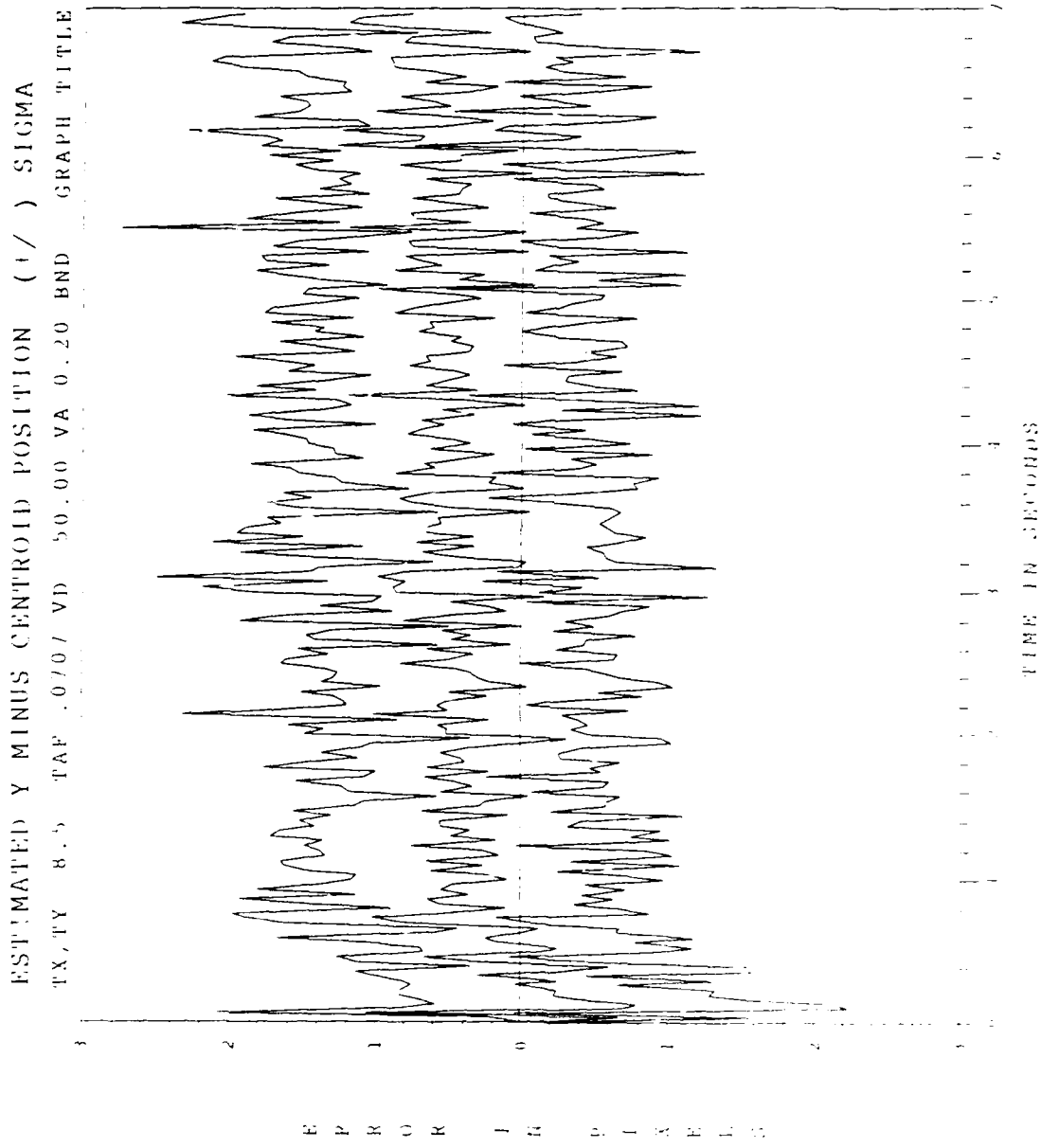


Figure B.18 Tuning Run #2 Y-Minus Centroid Position Error

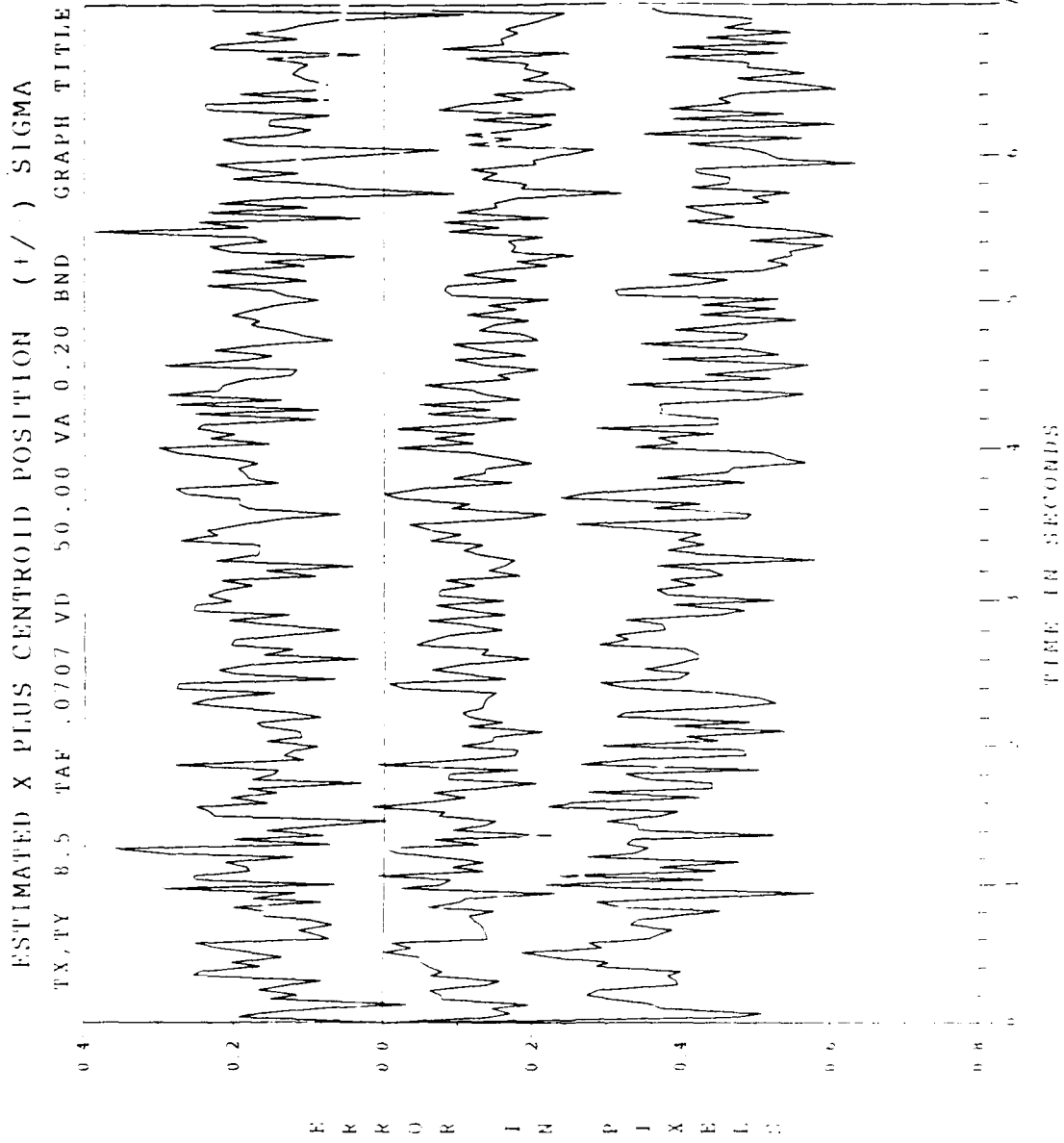


Figure B.19 Tuning Run #2 X-Plus Centroid Position Error

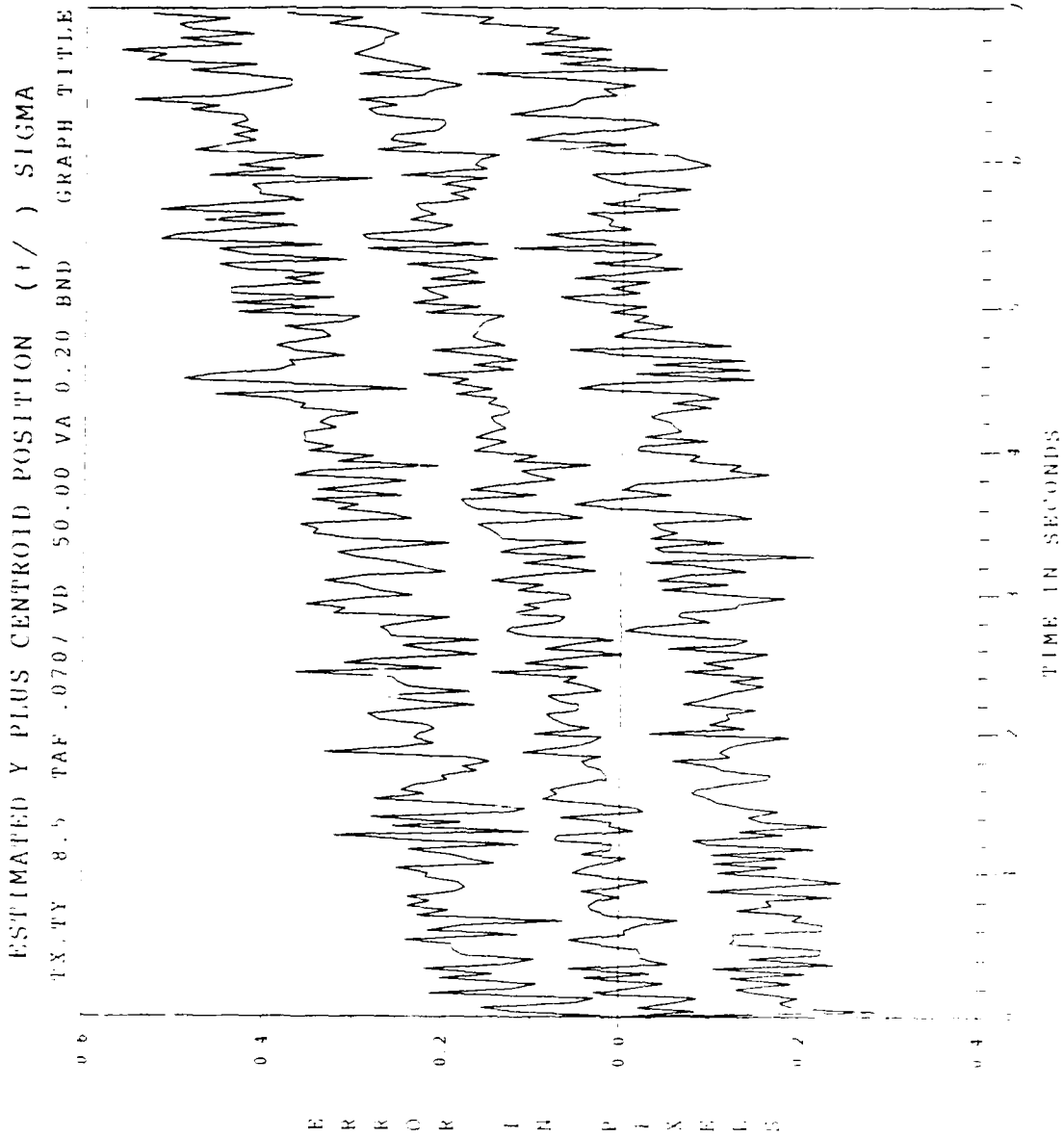


Figure B.20 Tuning Run #2 Y-Plus Centroid Position Error

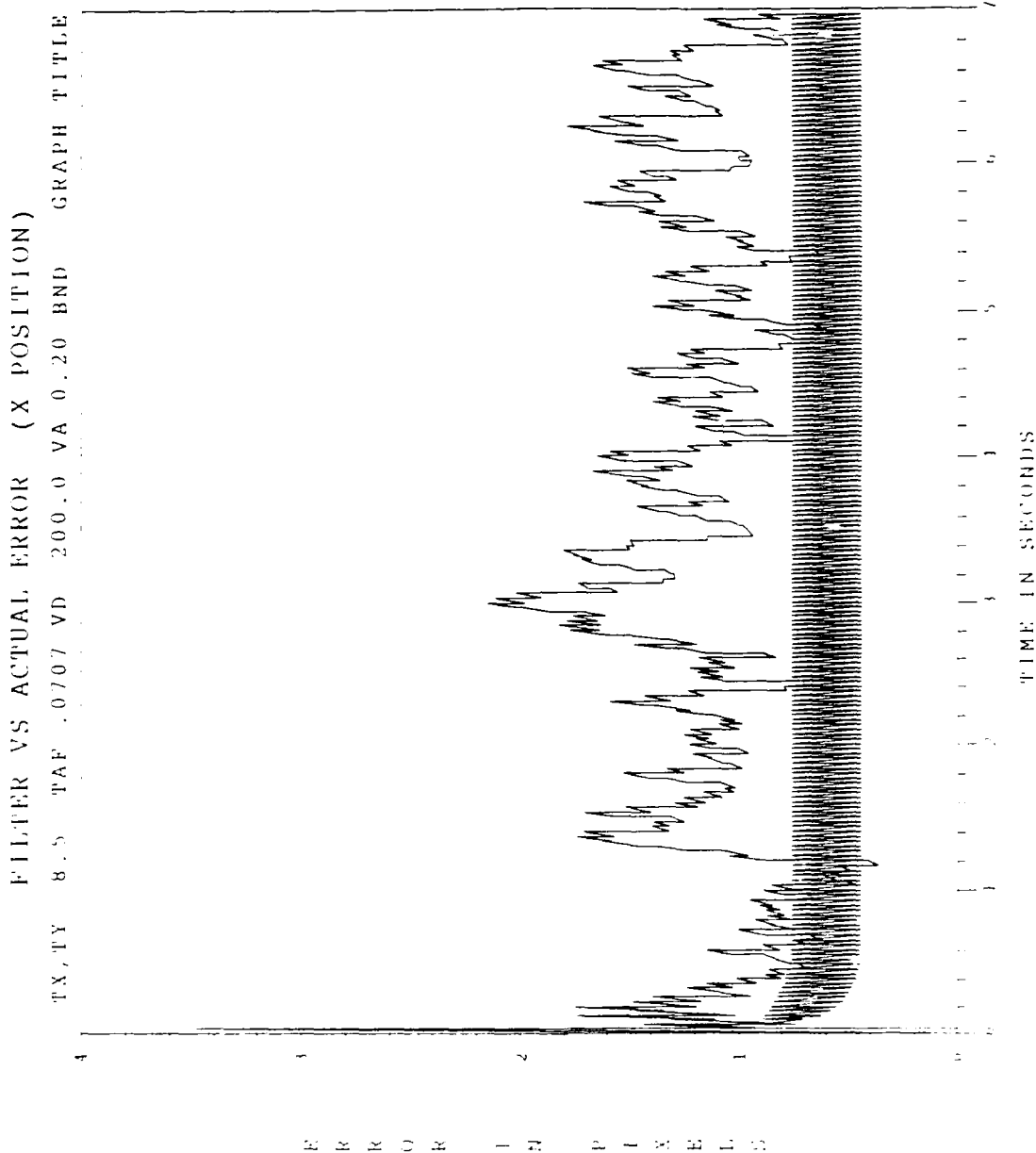


Figure B.21 Tuning Run #3 X-Channel Filter Vs Actual Error

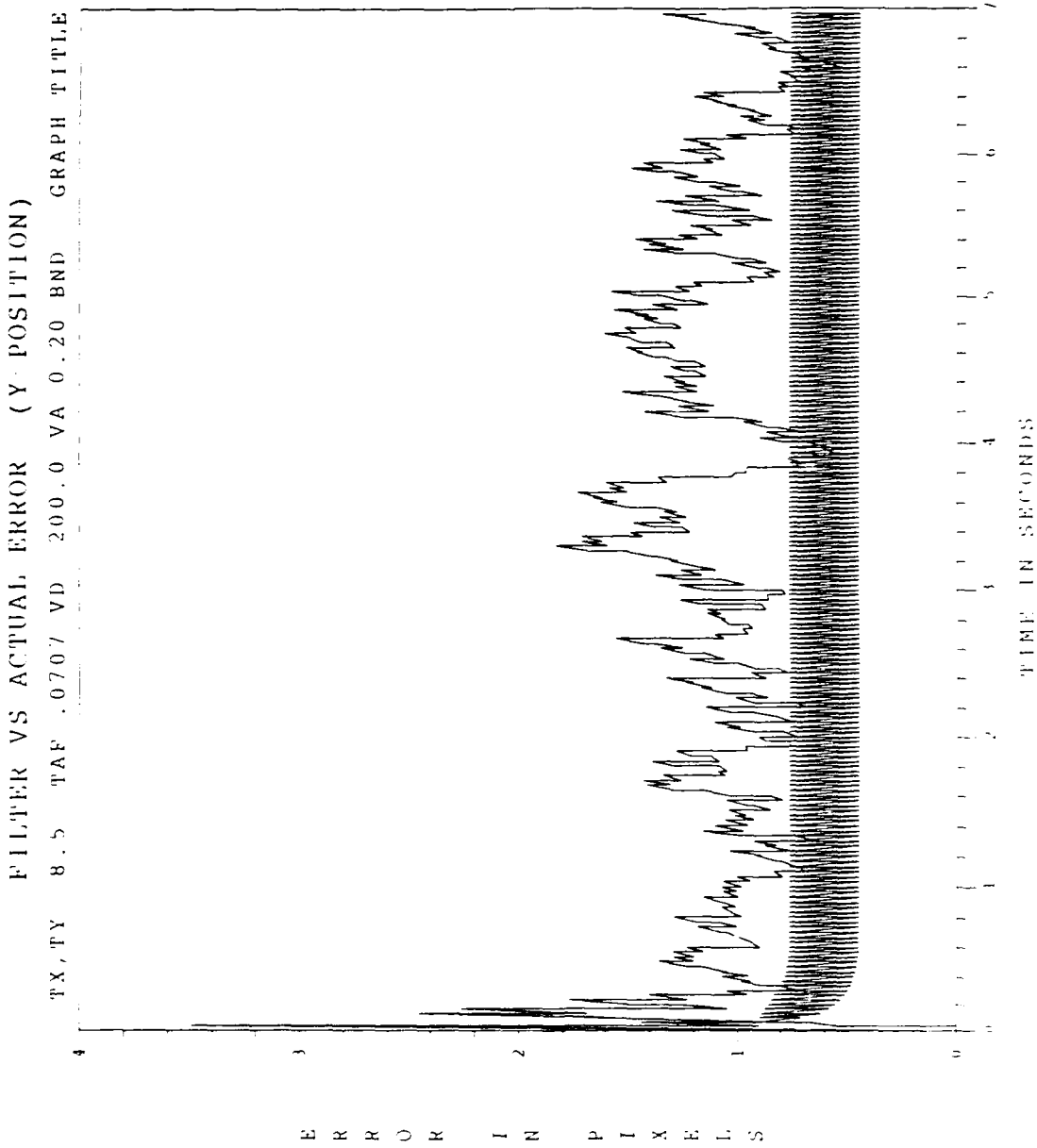


Figure B.22 Tuning Run #3 Y-Channel Filter Vs Actual Error

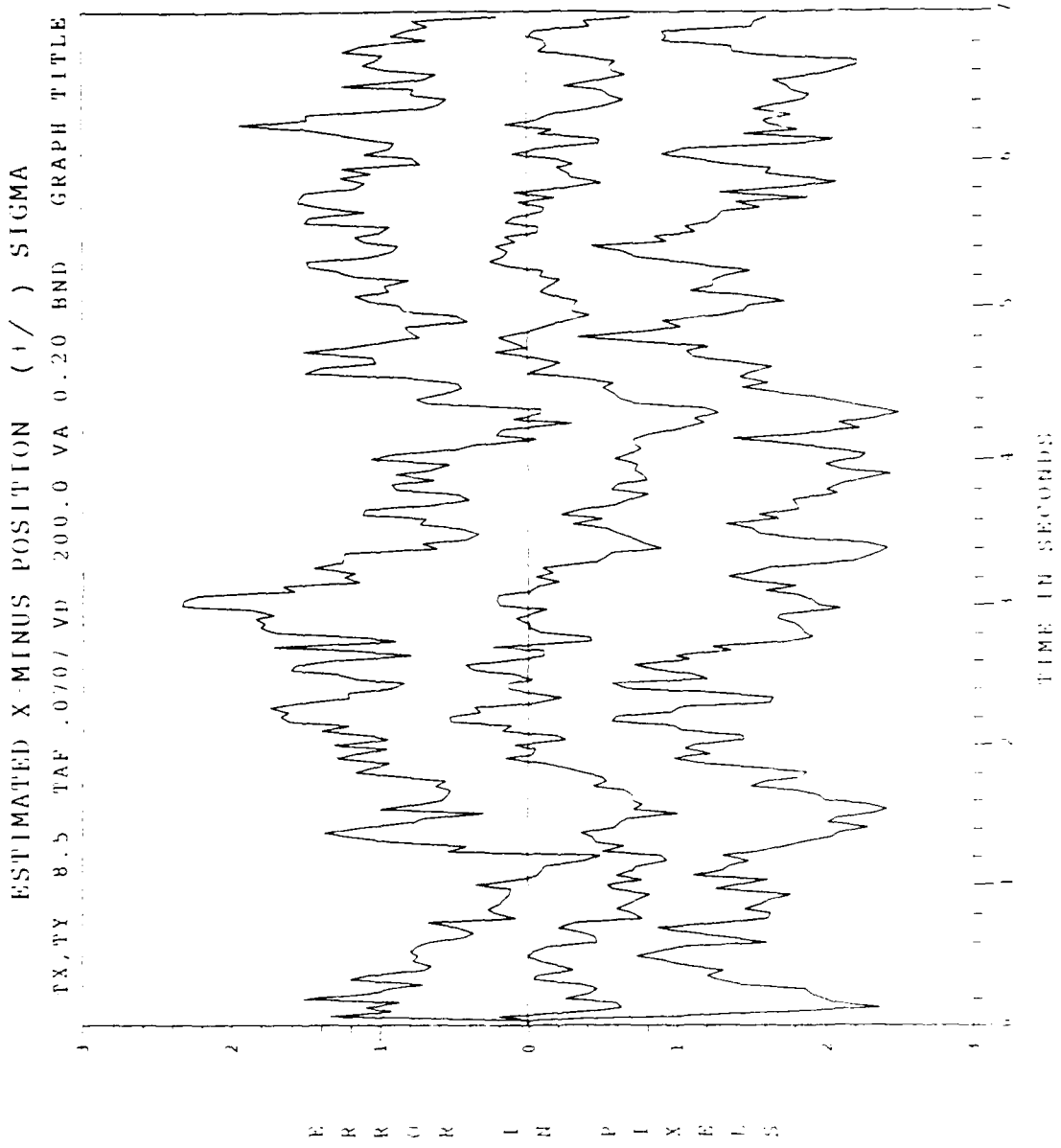


Figure B.23 Tuning Run #3 X-Minus Position Error

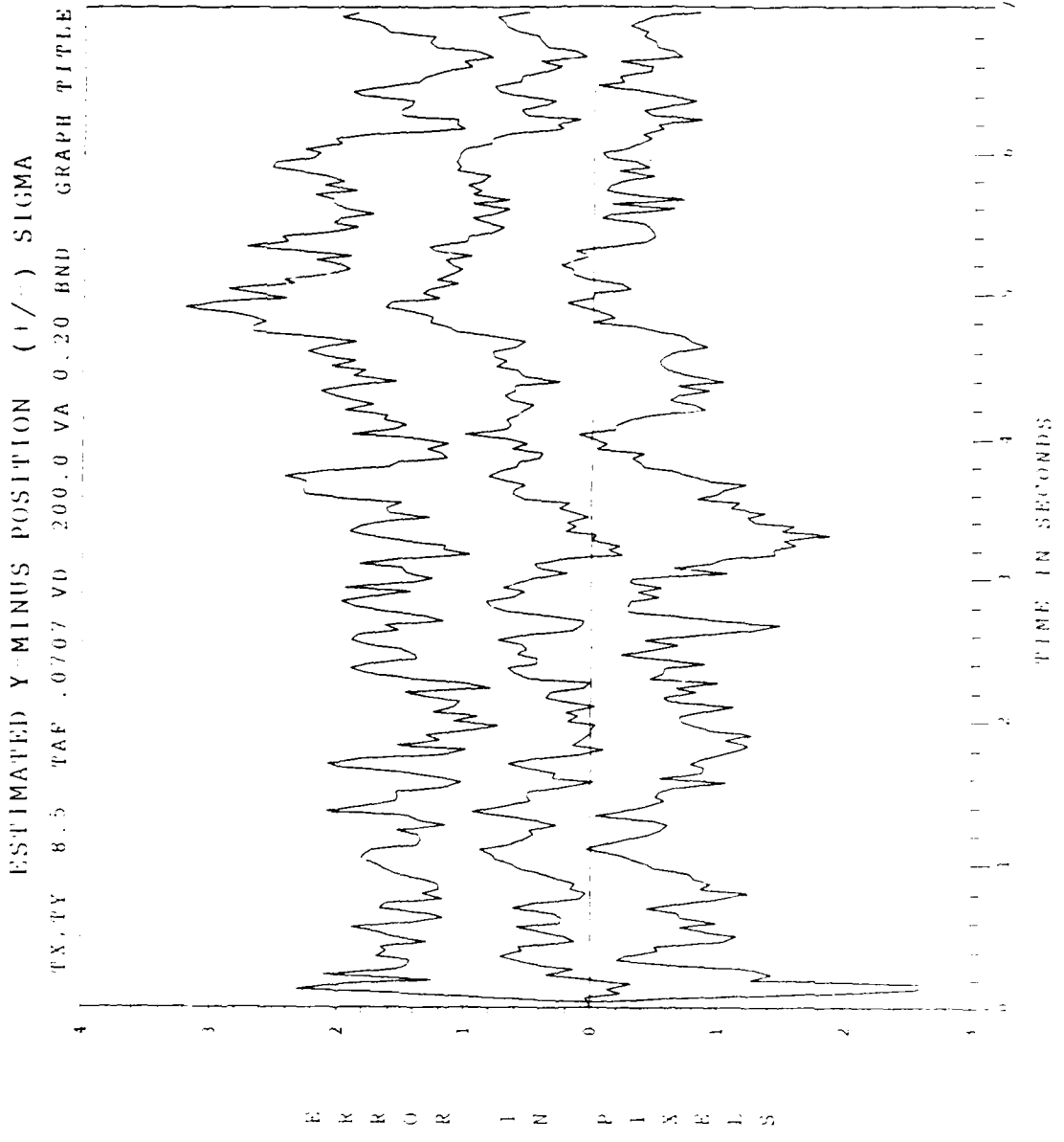


Figure B.24 Tuning Run #3 Y-Minus Position Error

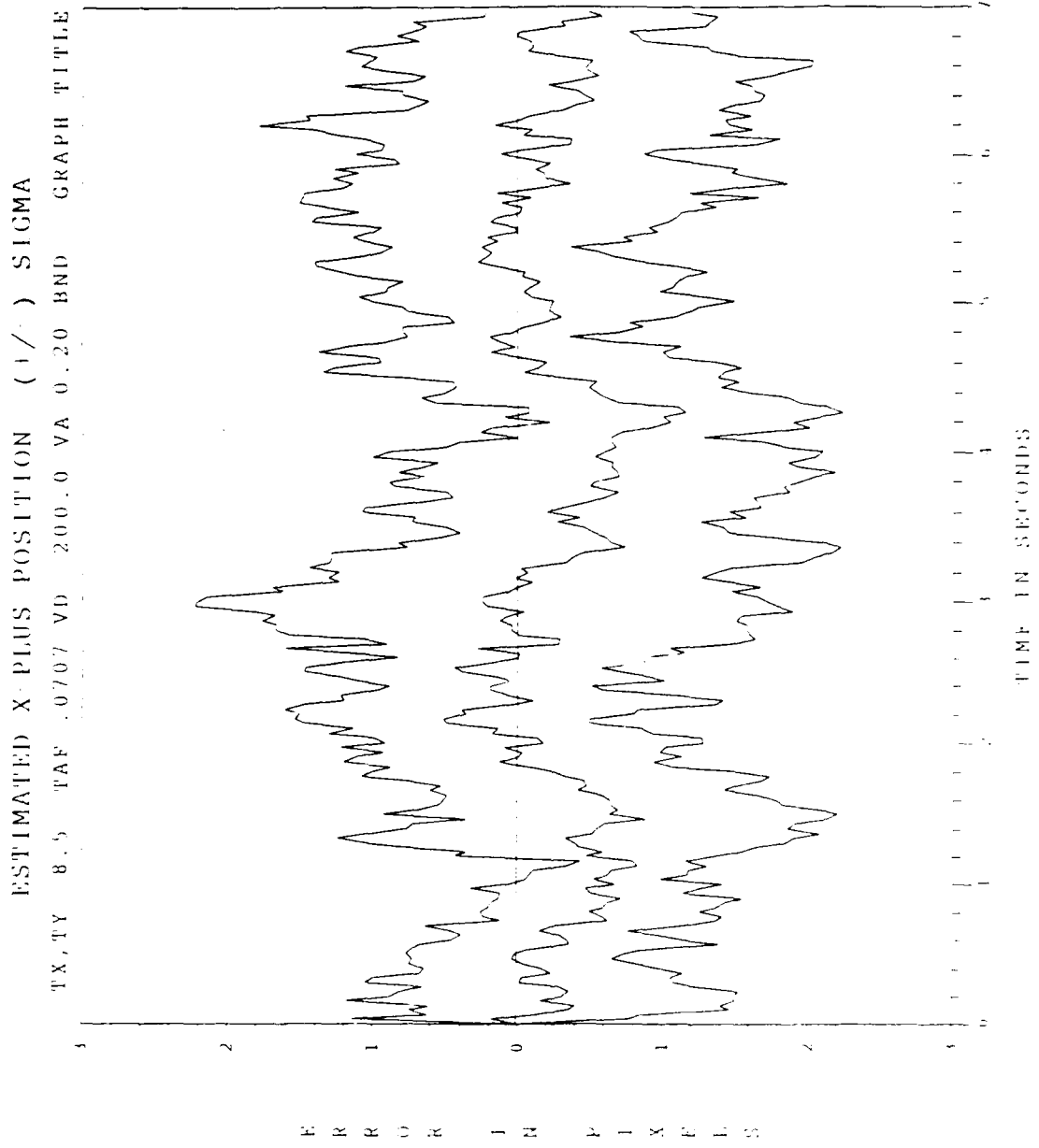


Figure B.25 Tuning Run #3 X-Plus Position Error

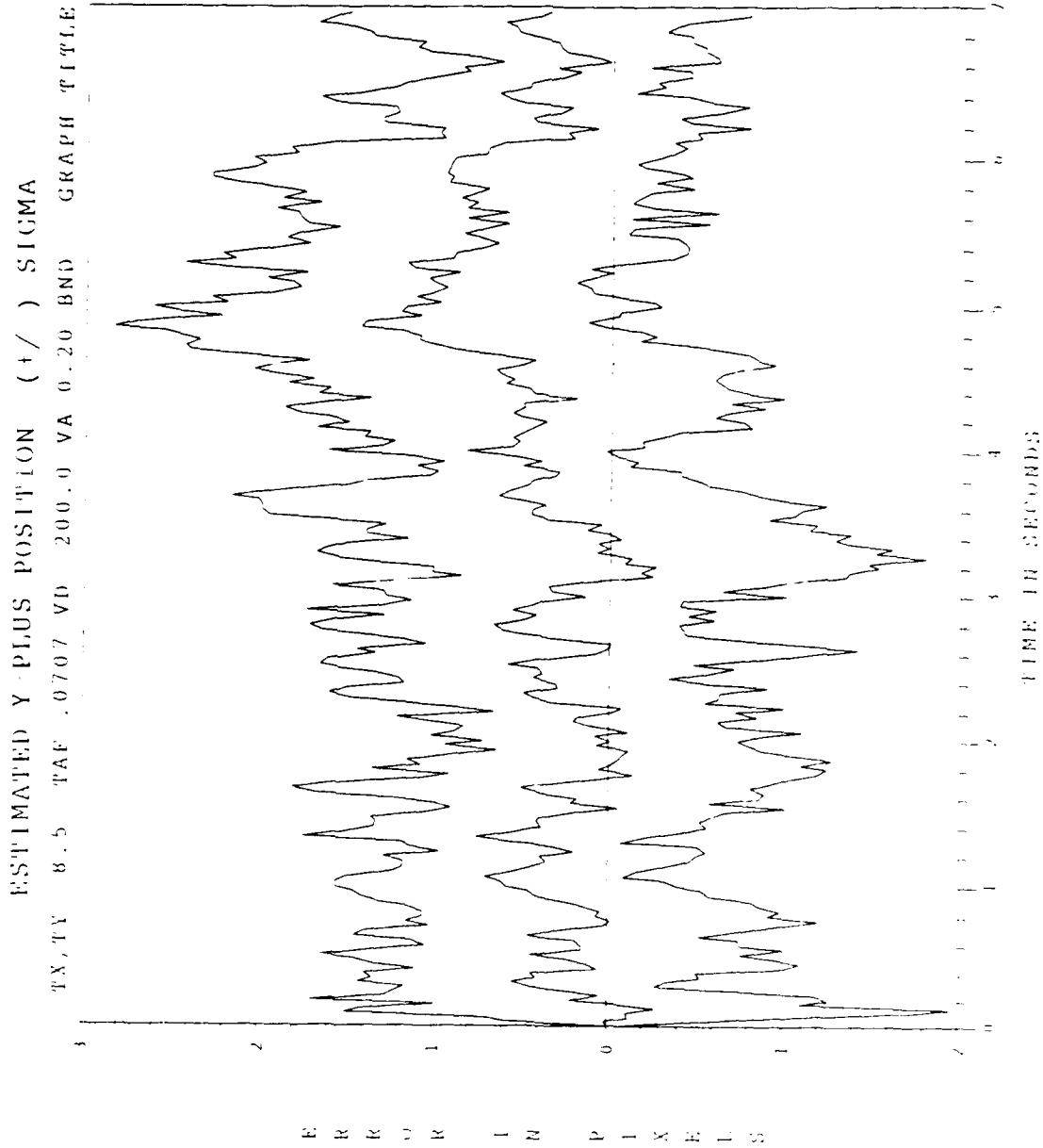


Figure B.26 Tuning Run #3 Y-Plus Position Error

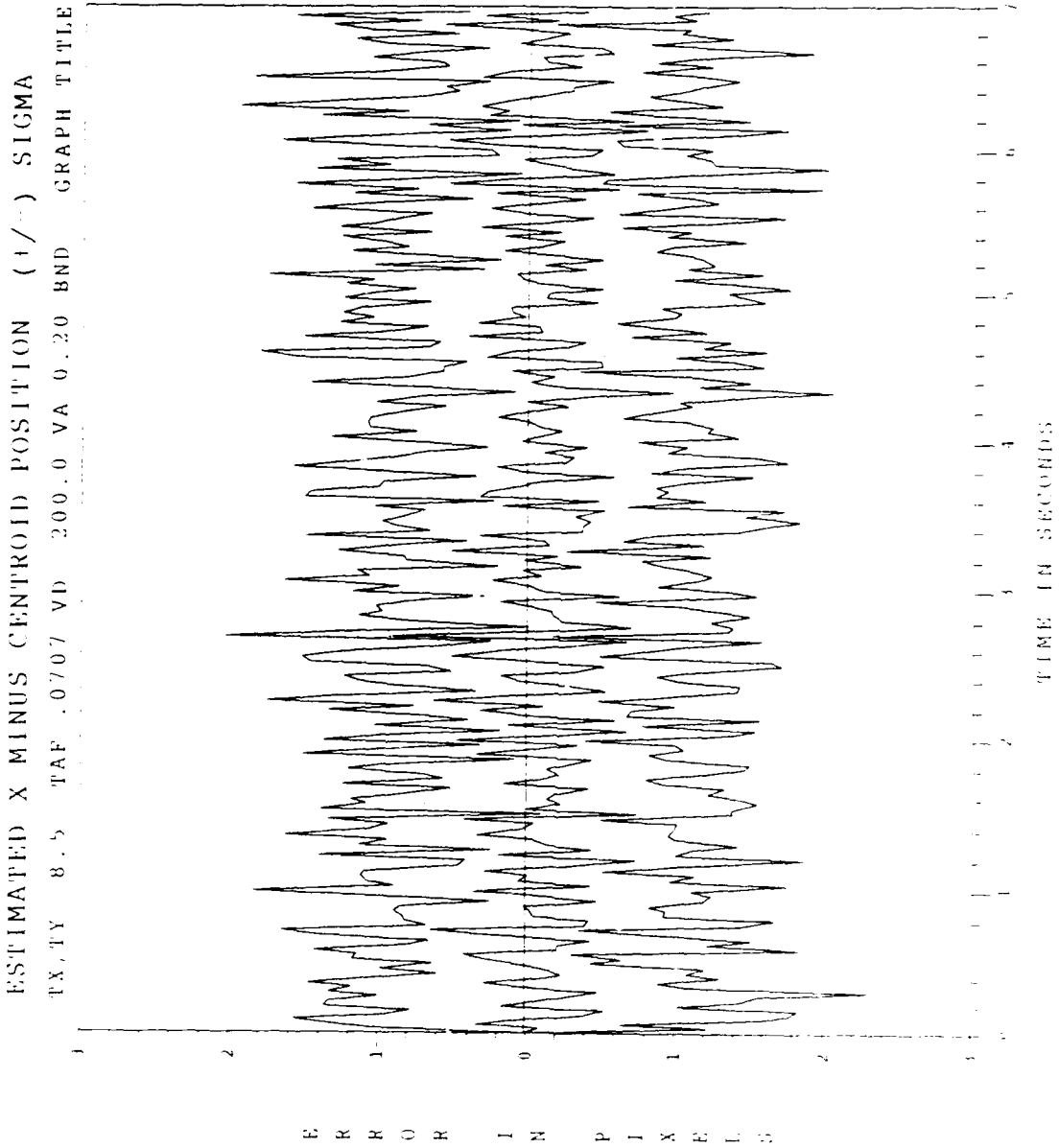


Figure B.27 Tuning Run #3 X-Minus Centroid Position Error

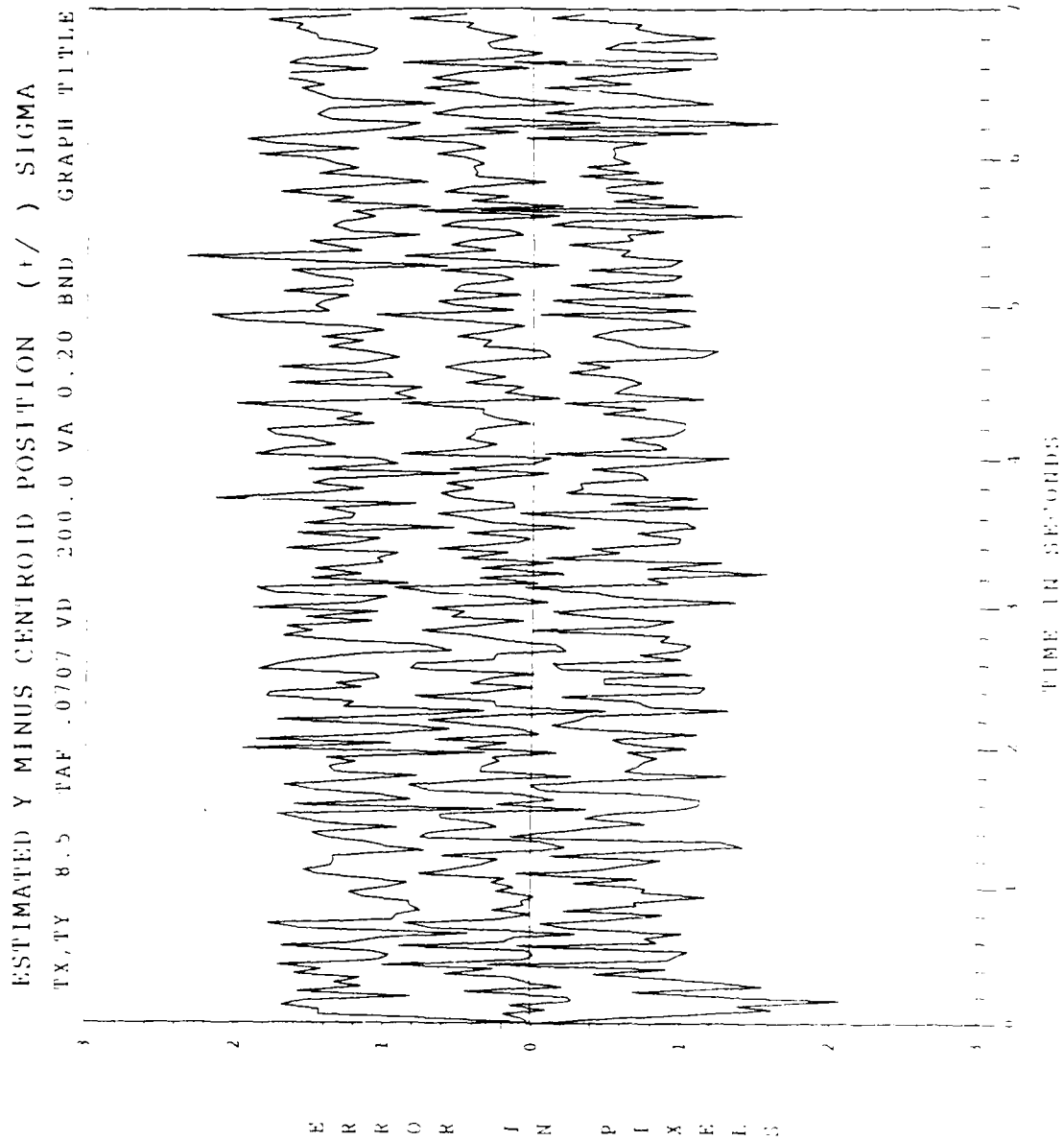


Figure B.23 Tuning Run #3 Y-Minus Centroid Position Error

ESTIMATED X PLUS CENTROID POSITION (1 /) SIGMA

PX.TY 8.5 TAF .0707 VD 200.0 VA 0.20 BND GRAPH TITLE

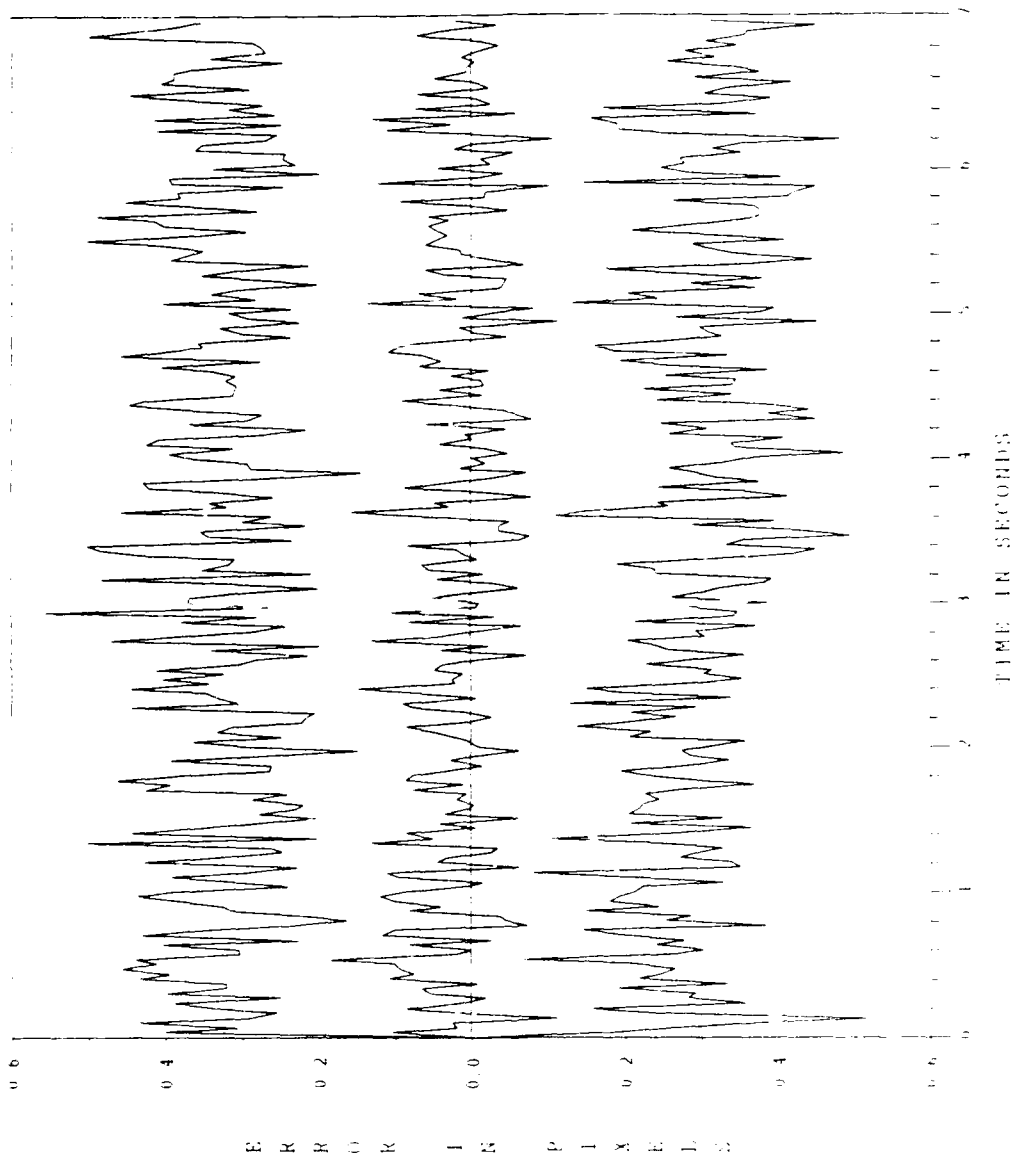


Figure B.29 Tuning Run #3 X-Plus Centroid Position Error

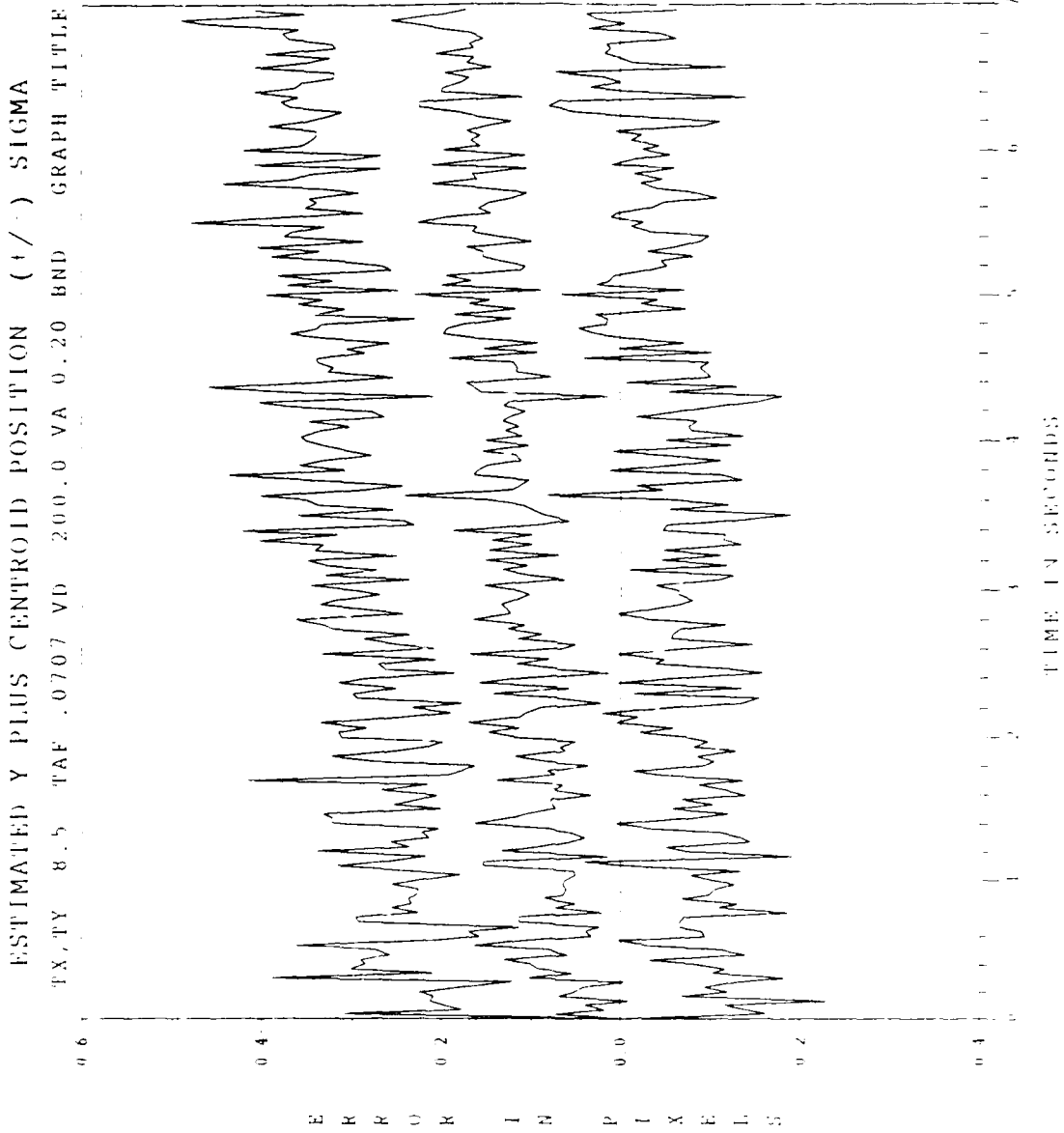


Figure B.30 Tuning Run #3 Y-Plus Centroid Position Error

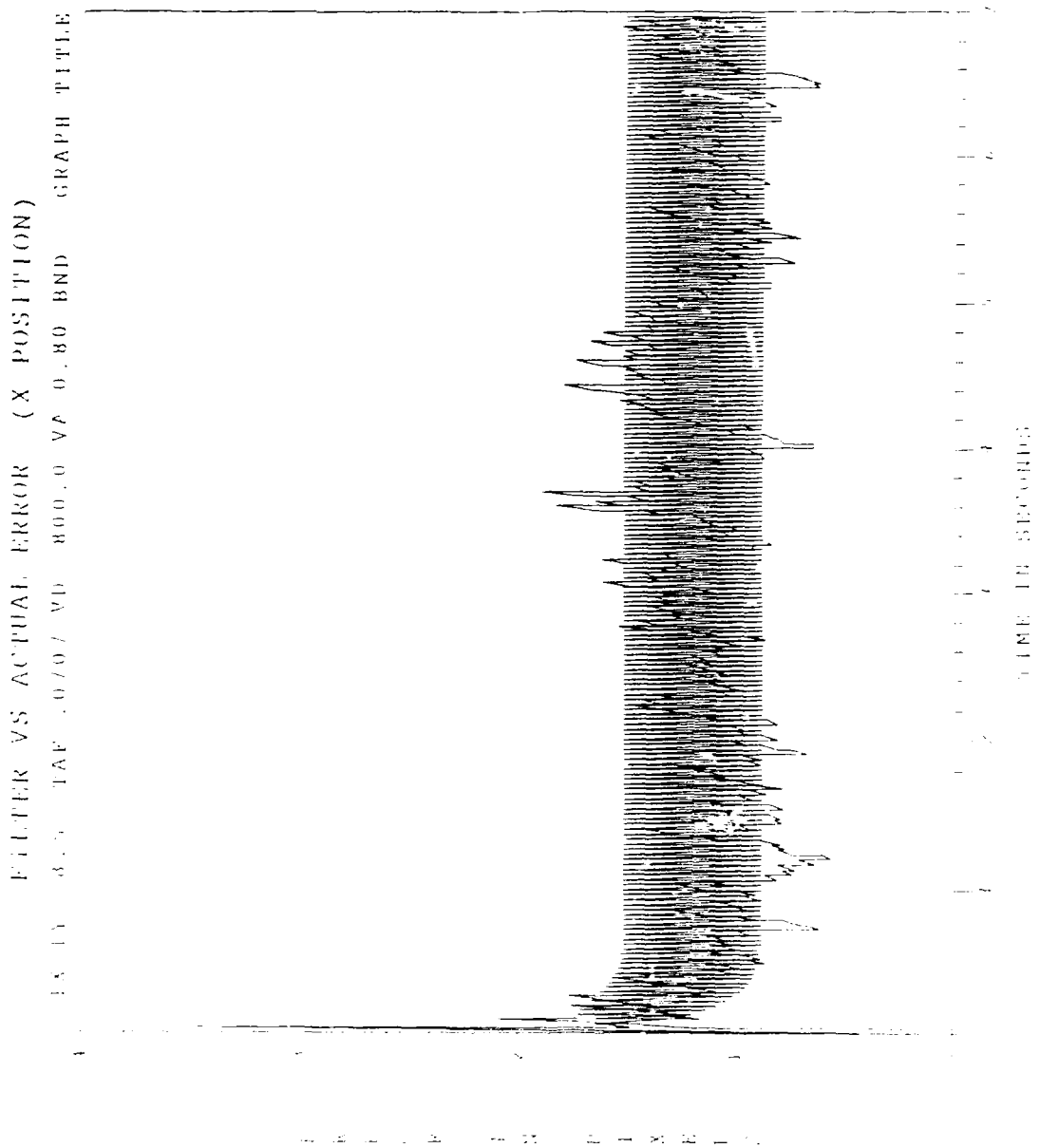


Figure B.11 Tuning Run #4 N-Channel Filter Vs Actual Error

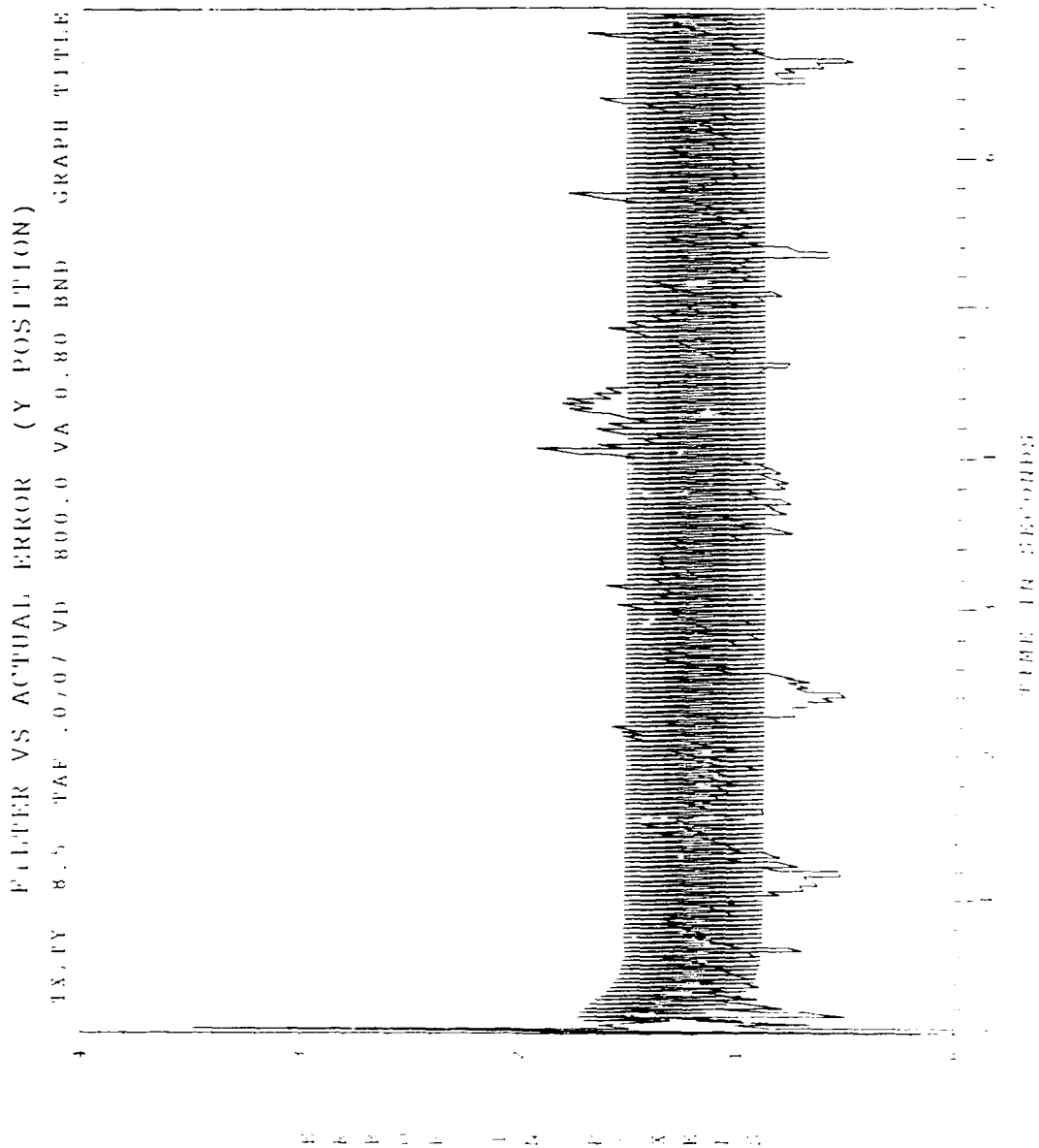


Figure B.32 Tuning Run #4 Y-Channel Filter Vs Actual Error

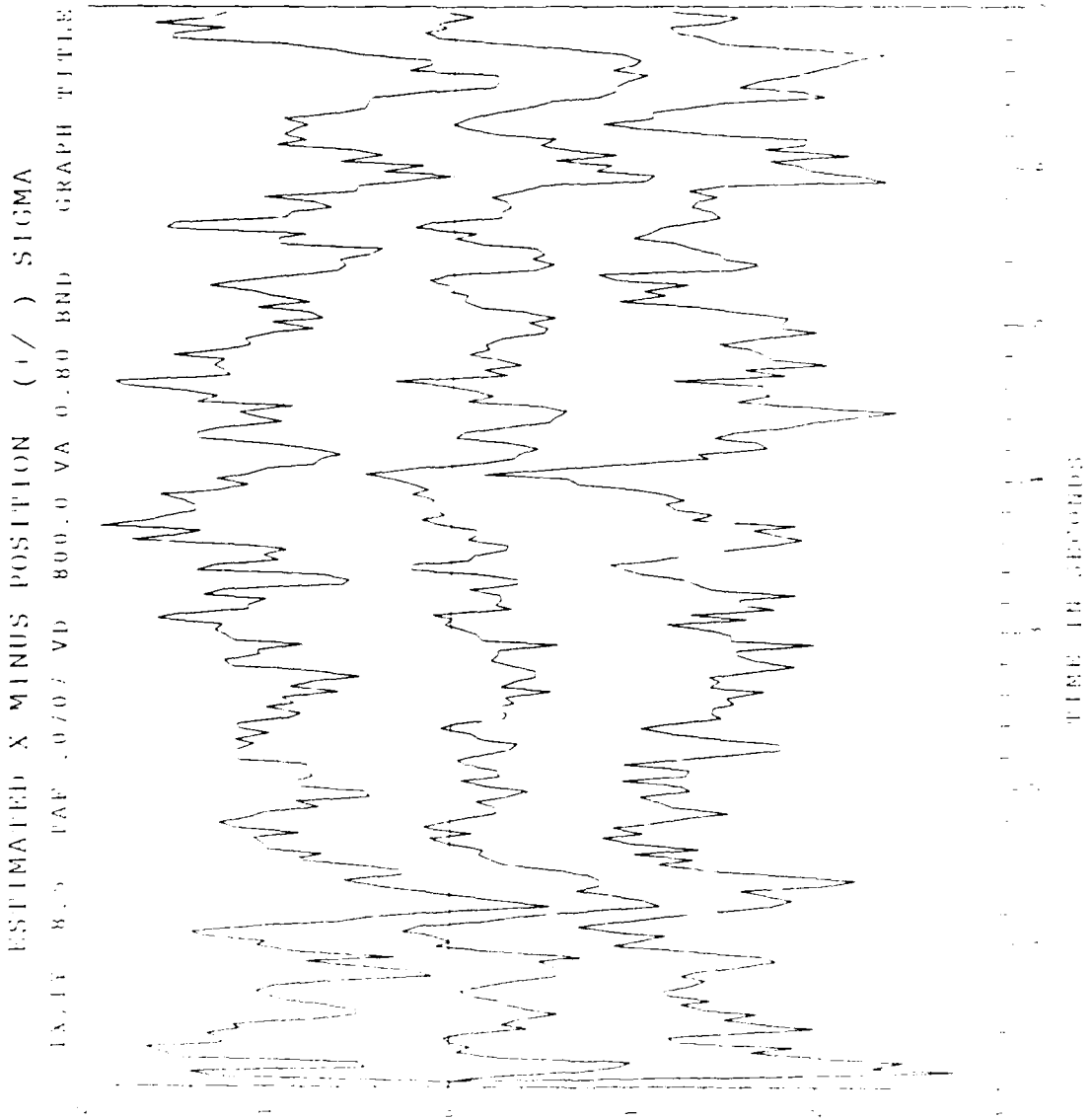


Figure B.33 Tuning Run #4 X-Minus Position Error

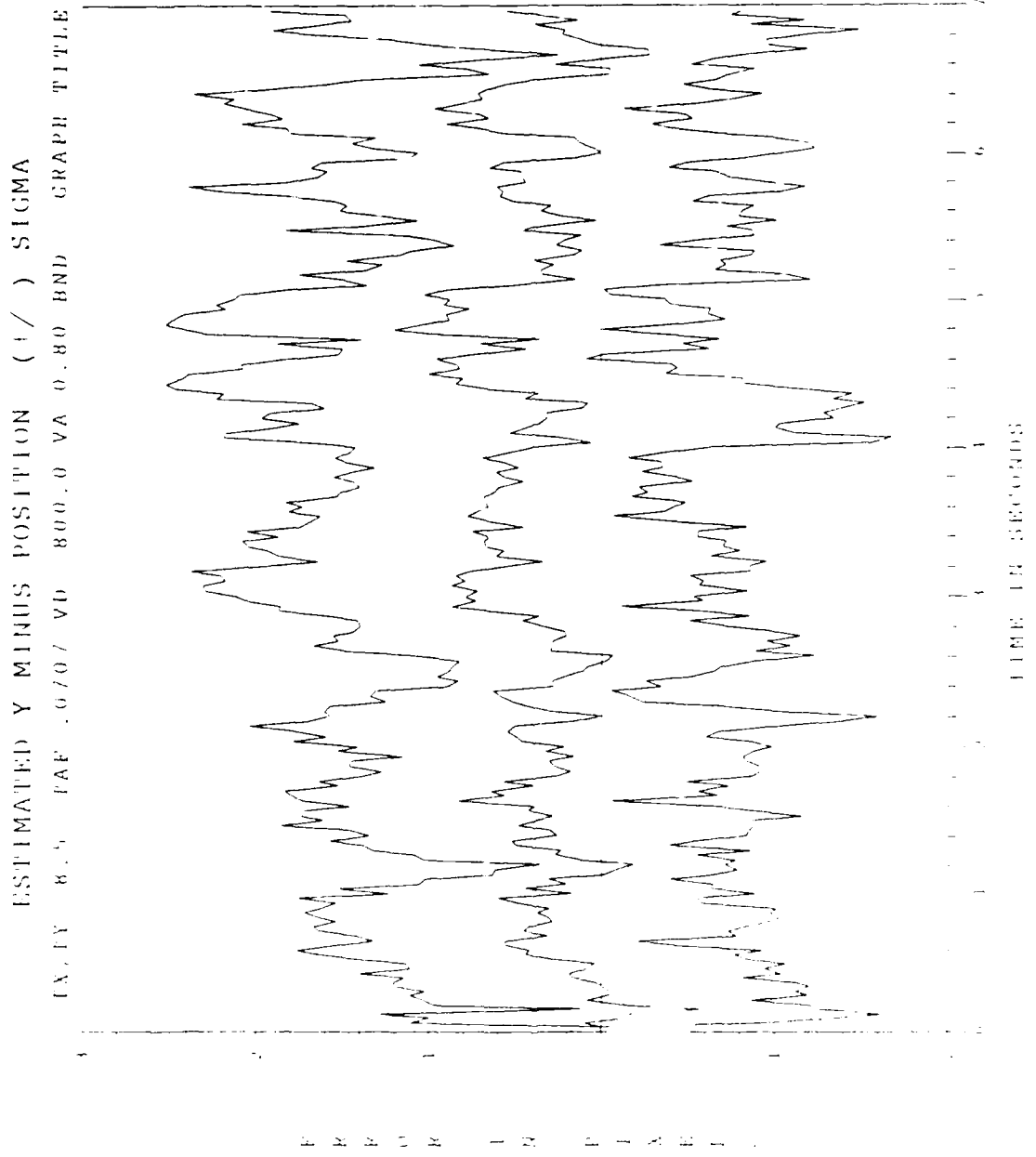


Figure B.34 Tuning Run #4 Y-Minus Position Error

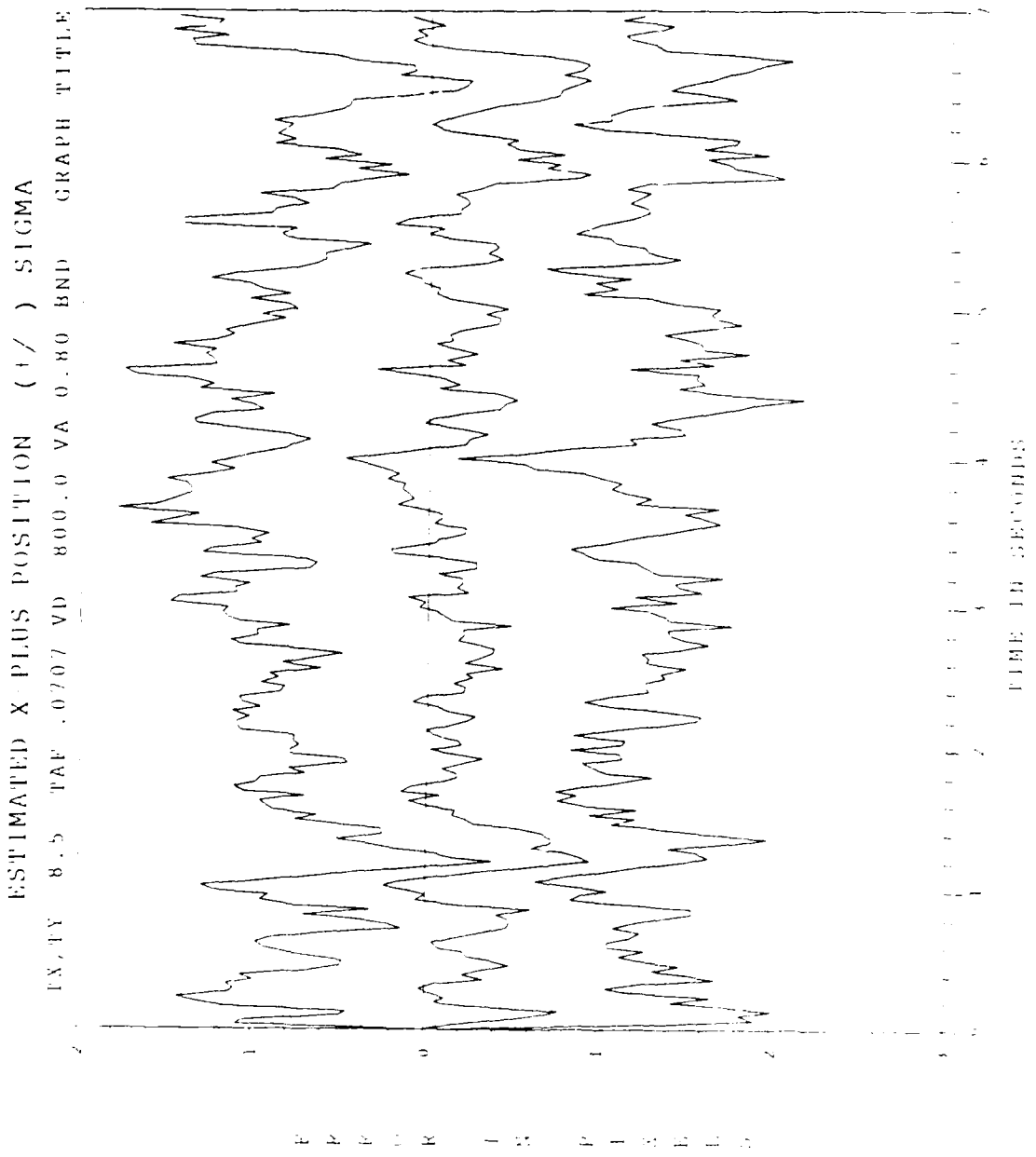


Figure B.35 Tuning Run #4 X-Plus Position Error

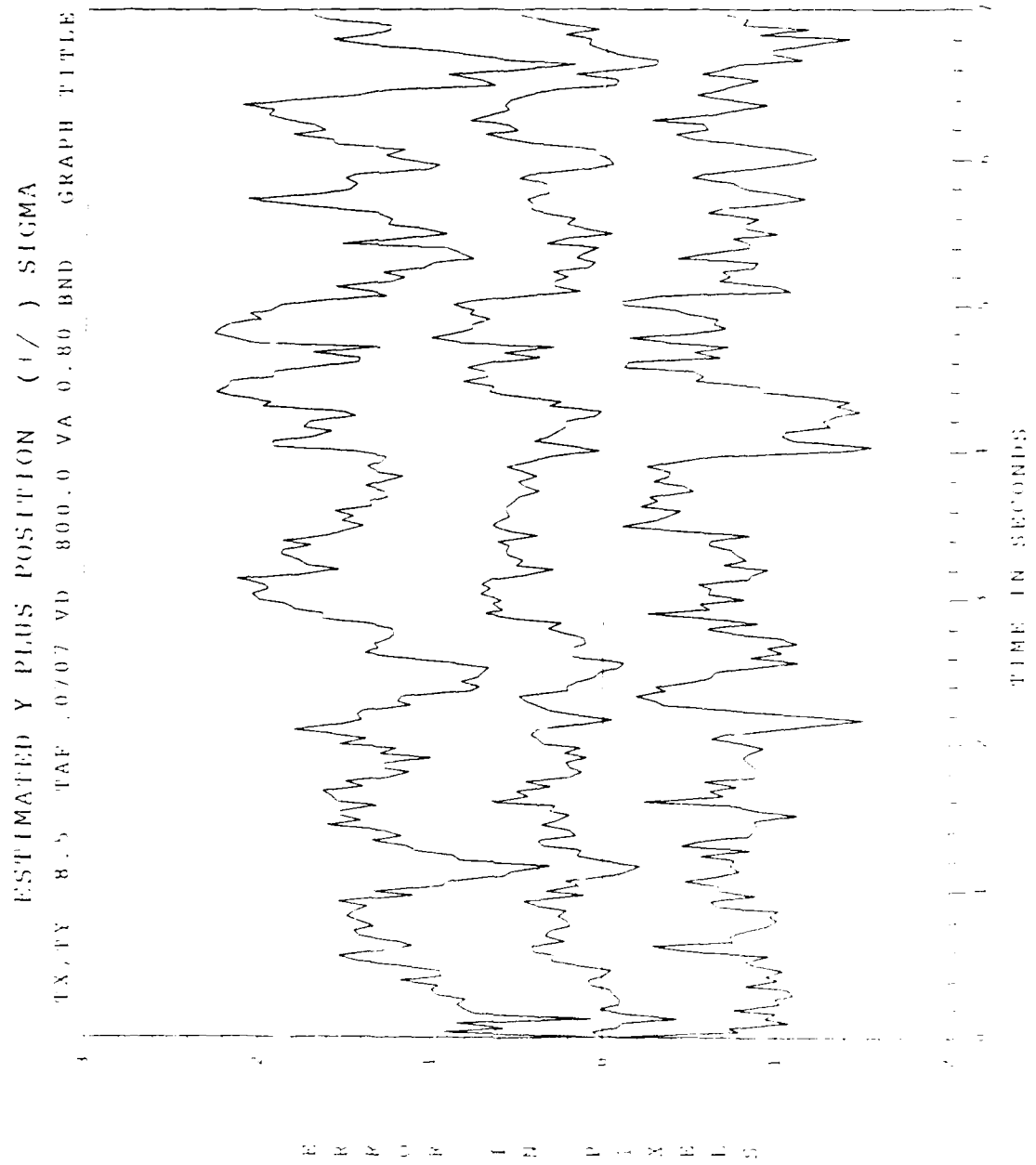


Figure B.36 Tuning Run #4 Y-Plus Position Error

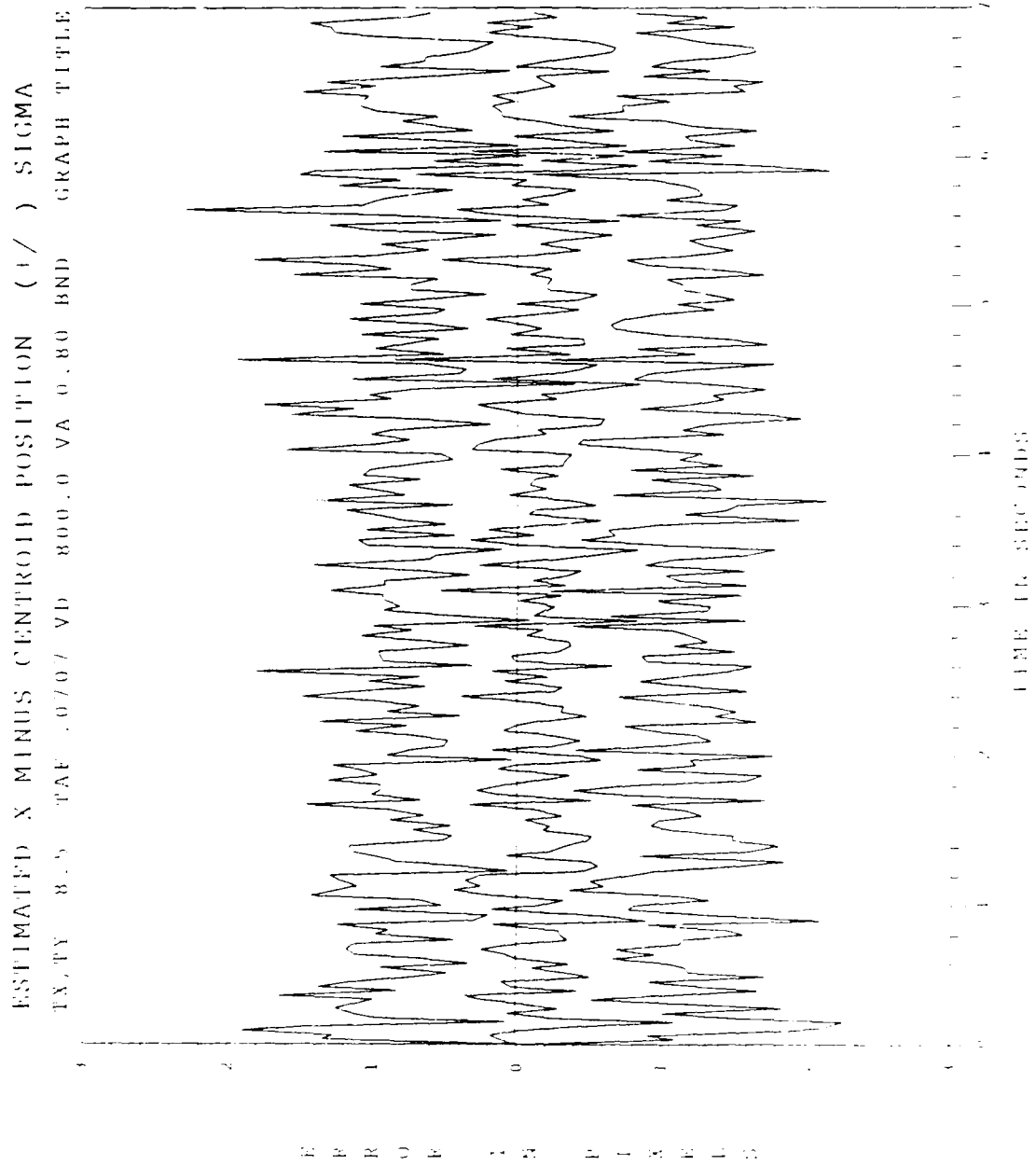


Figure B.37 Tuning Run #4 X-Minus Centroid Position Error

ESTIMATED Y MINUS CENTROID POSITION (1 /) SIGMA

TX, TY 8.5 1AF .0707 VD 800.0 VA 0.80 BND GRAPH TITLE

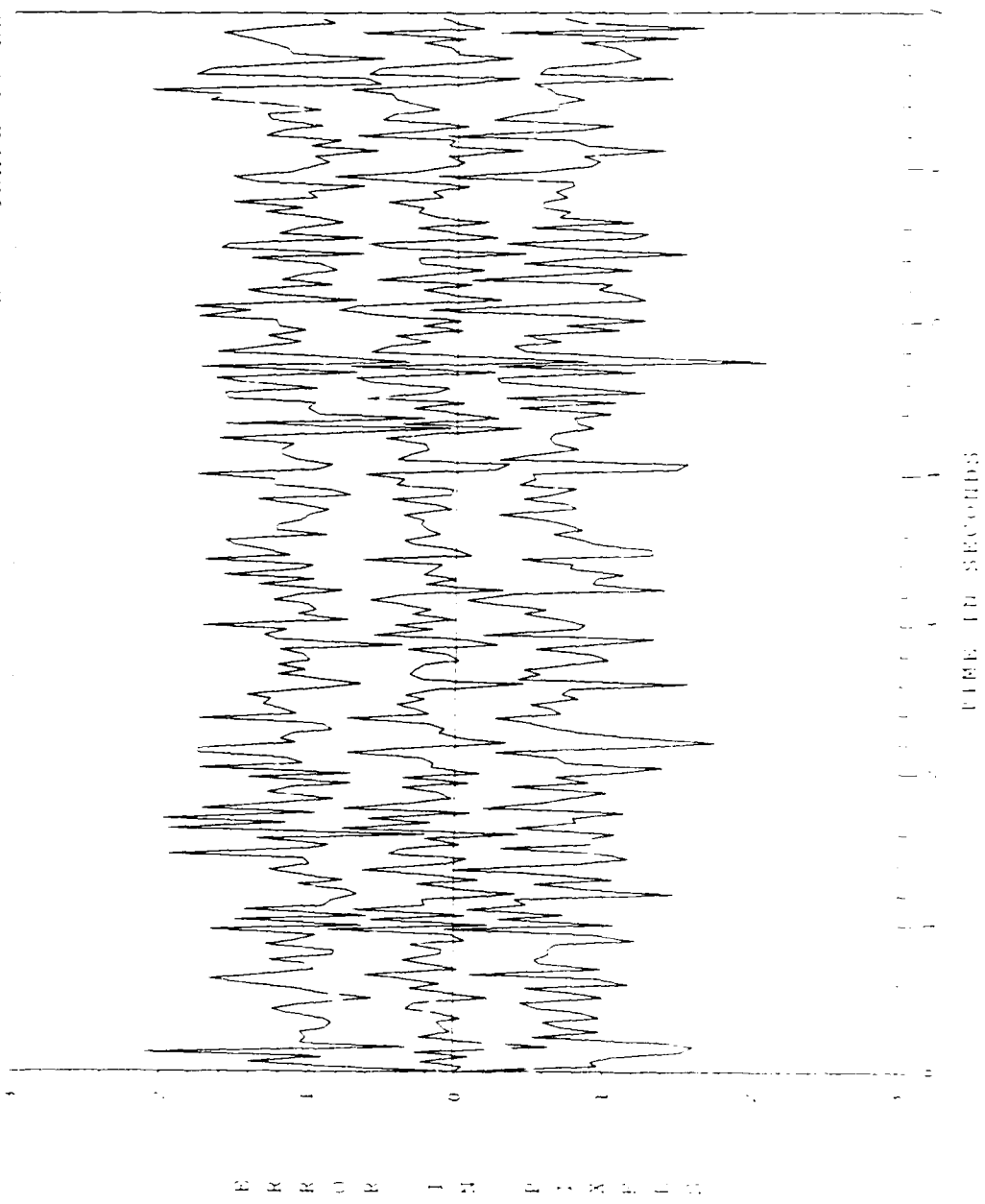


Figure B.38 Tuning Run #4 Y-Minus Centroid Position Error

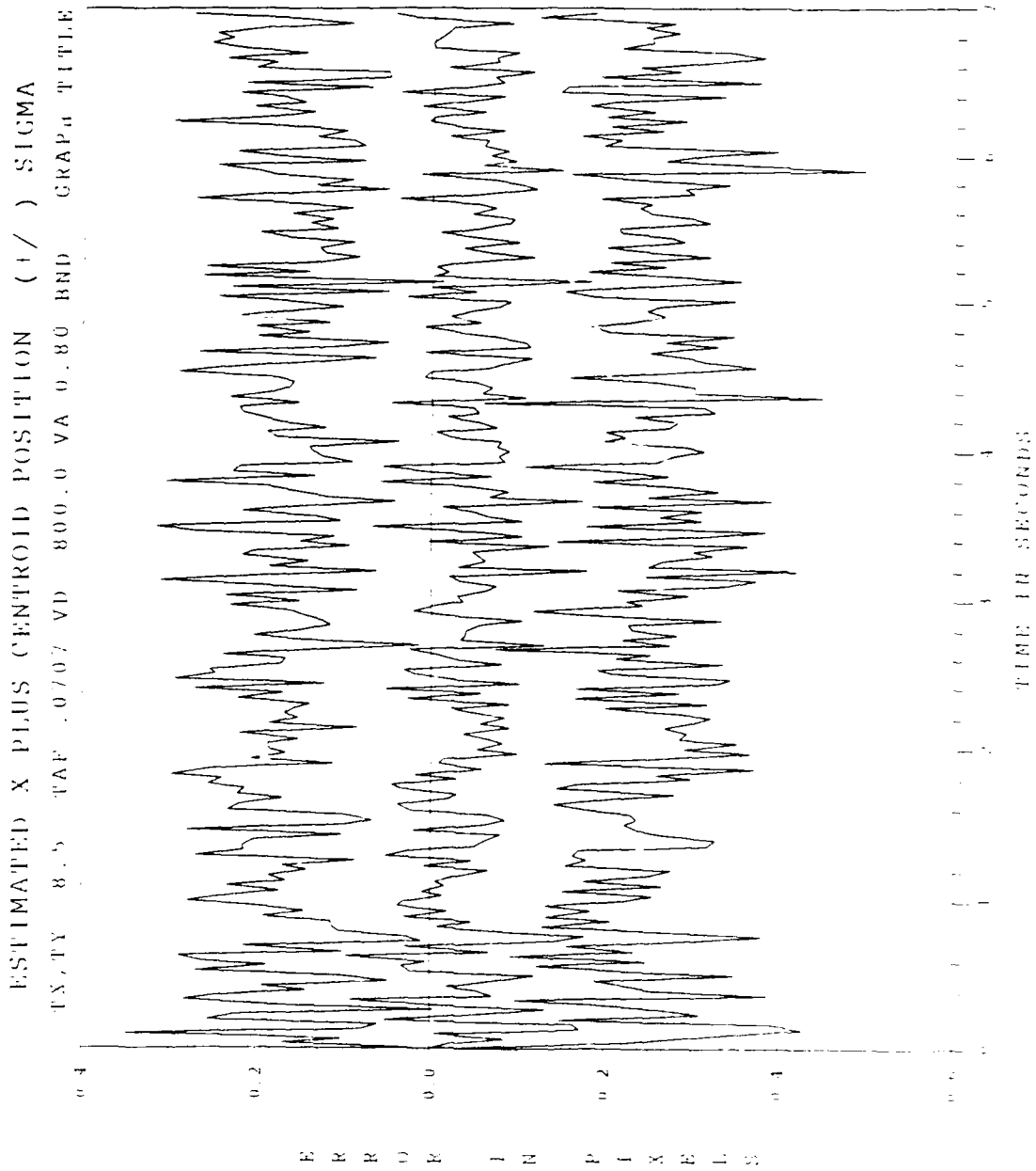


Figure B.39 Tuning Run #4 X-Plus Centroid Position Error

ESTIMATED Y PLUS CENTROID POSITION (1 /) SIGMA

EX, TY 8.5 TAF .0707 VD 800.0 VA 0.80 BND GRAPH TITLE

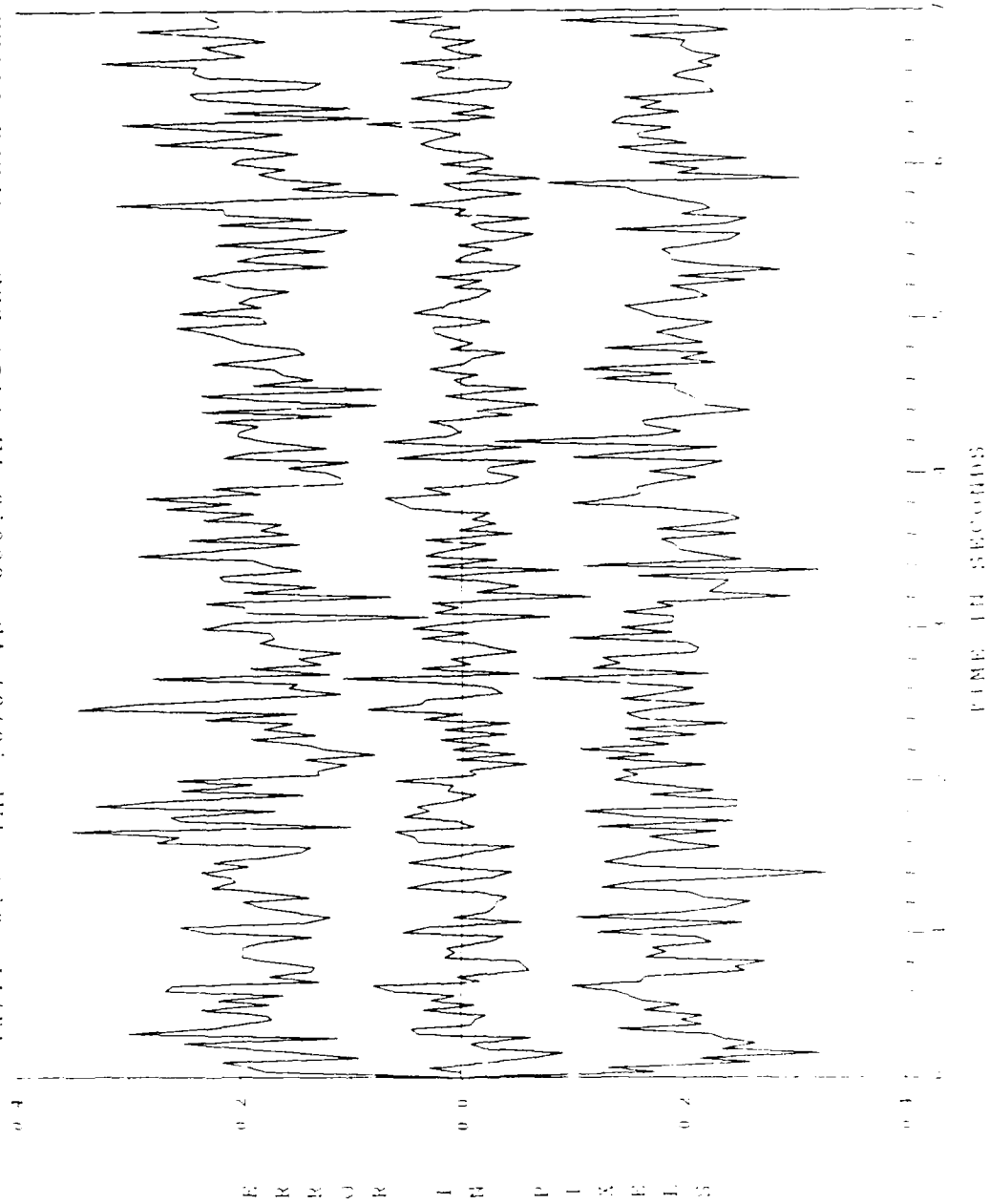


Figure B.40 Tuning Run #4 Y-Plus Centroid Position Error

Appendix C. Plots for Sensitivity Study

Discussion in Section 5.4

Error Level .2 meters Figures C.1-C.3

Error Level 2 meters Figures C.4-C.6

Error Level 20 meters Figures C.7-C.9

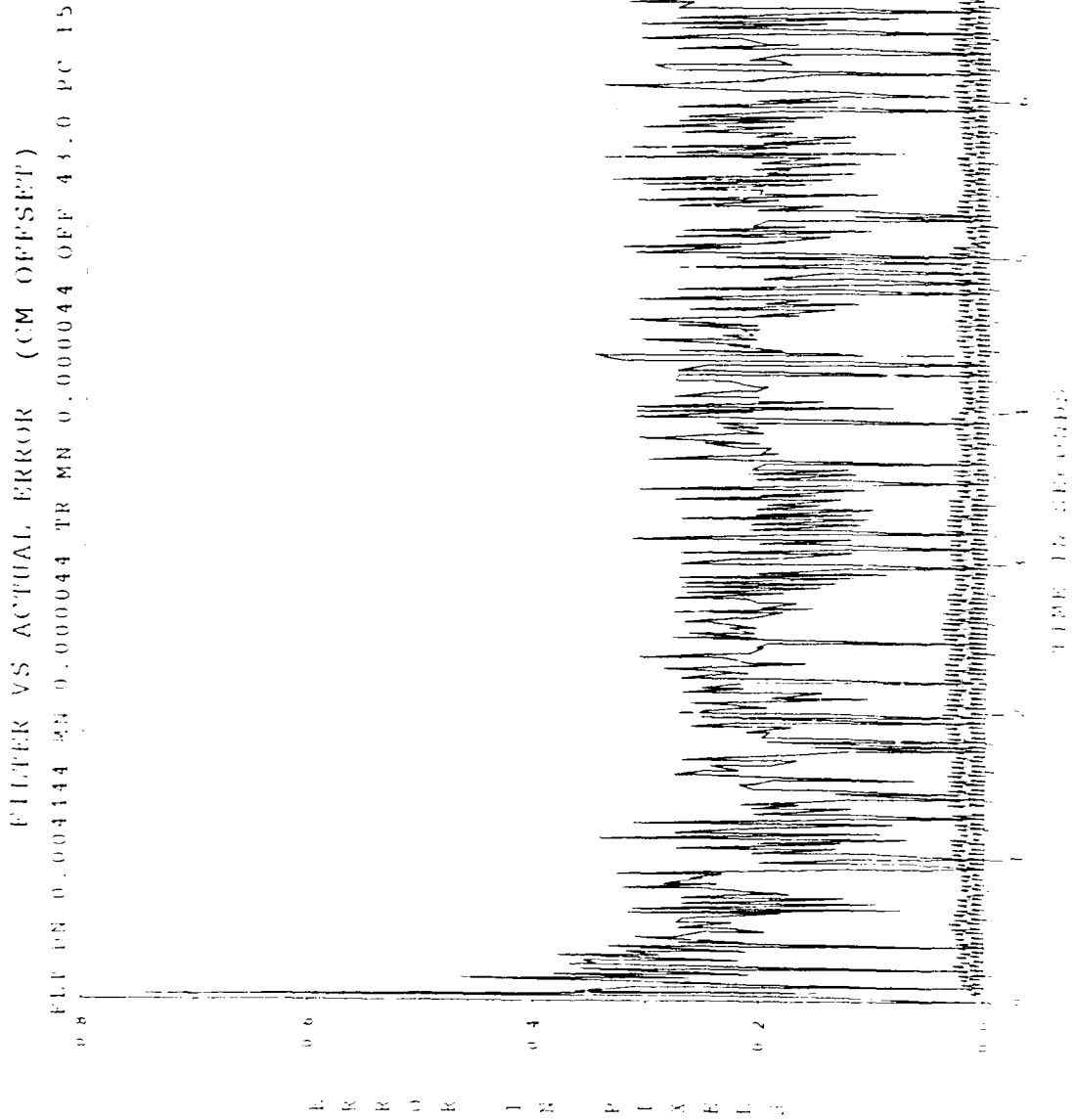


Figure C.1 .2 Meter Error Offset Filter Vs Actual Error

ESTIMATED OFFSET MINUS POSITION (+ /) SIGMA

ELL DN 0 004444 NN 0.000044 TR IN 0.000044 OFF 43.0 PC 15

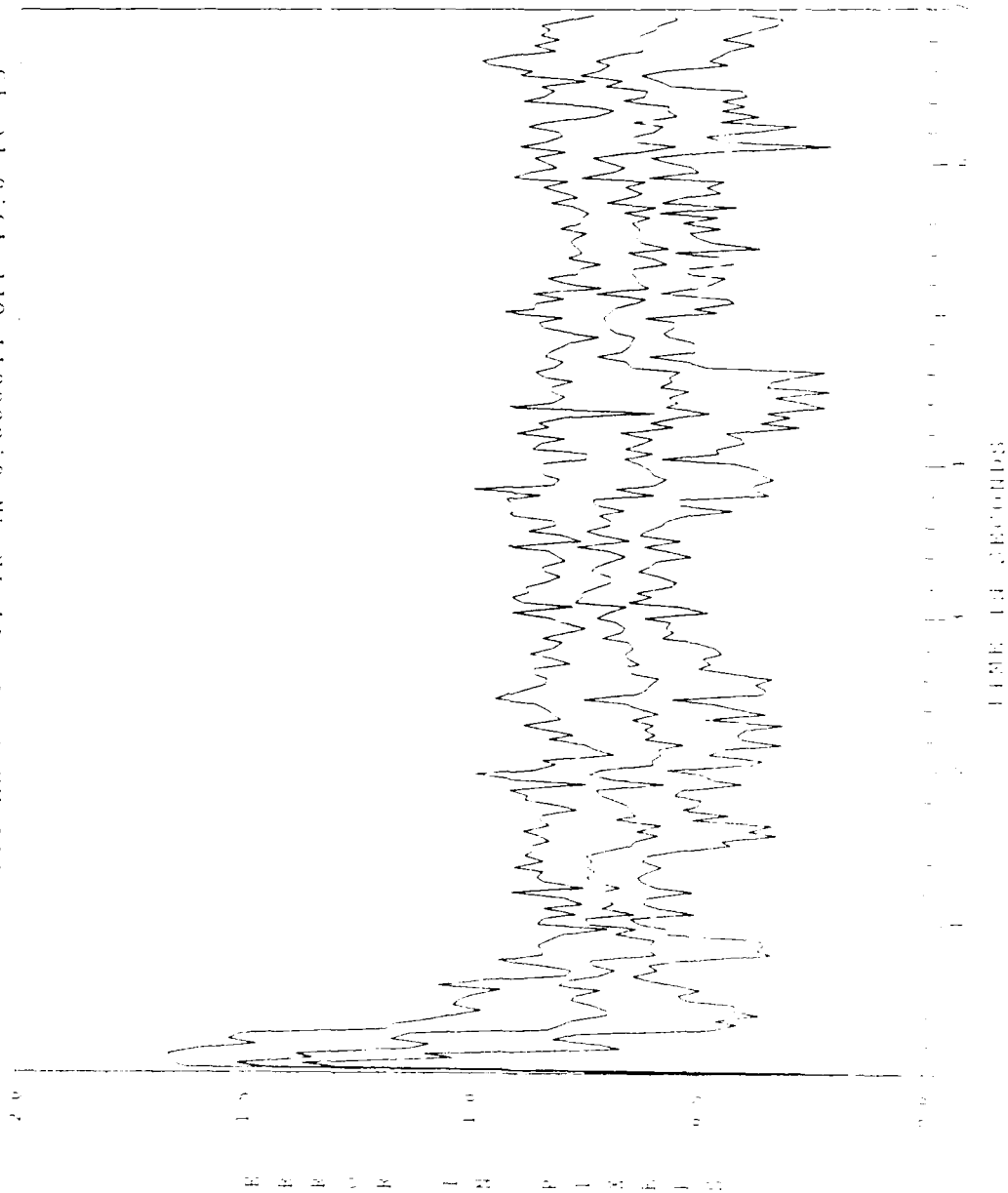


Figure C.2 .2 Meter Error Offset-Minus Error

ESTIMATED OFFSET PLUS POSITION (1/) SIGMA

111 08 0.004444 NN 0.000044 TR MN 0.000044 OFF 43.0 PC 15

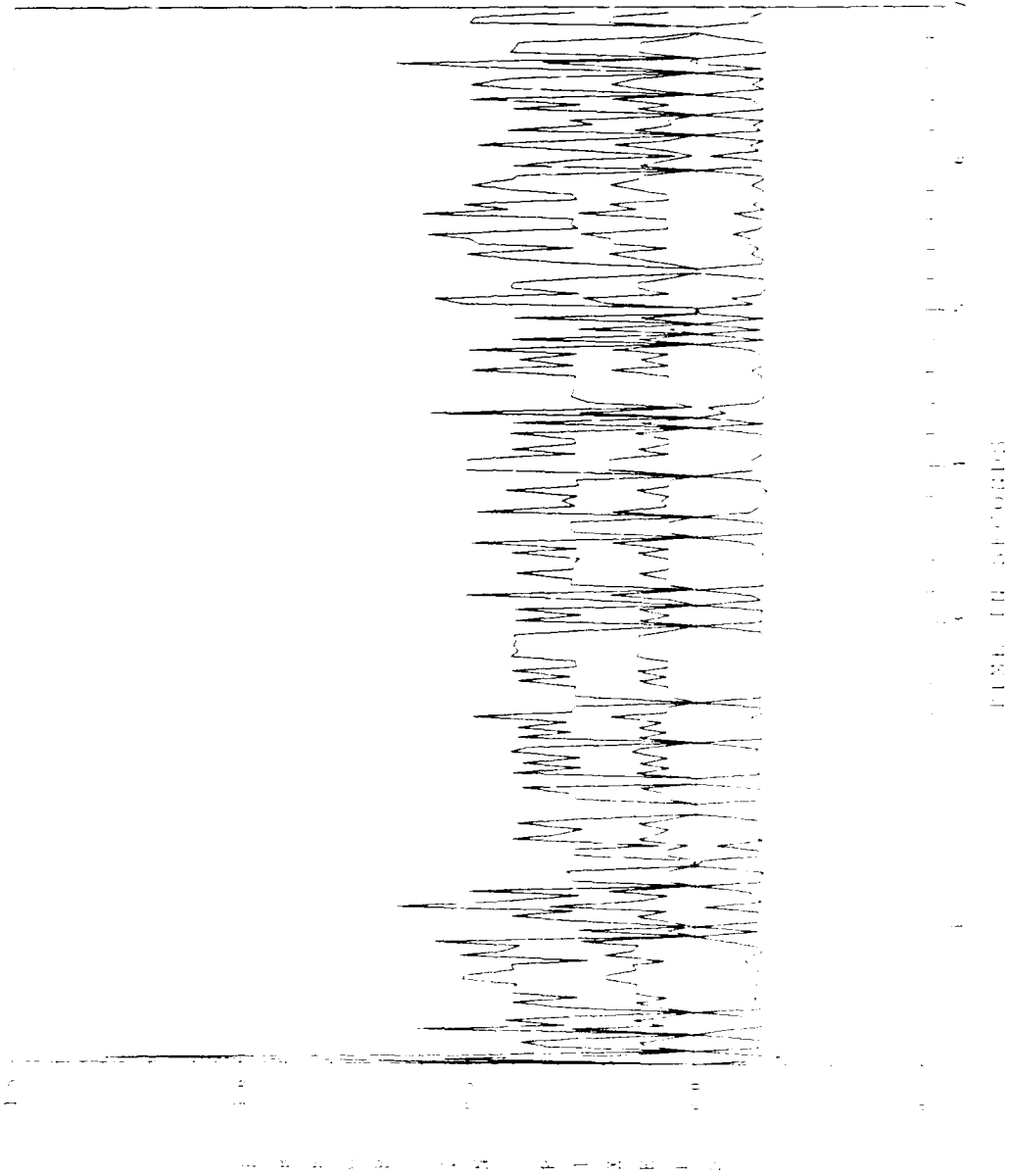


Figure C. 1.2 Meter Error Offset-Plus Error

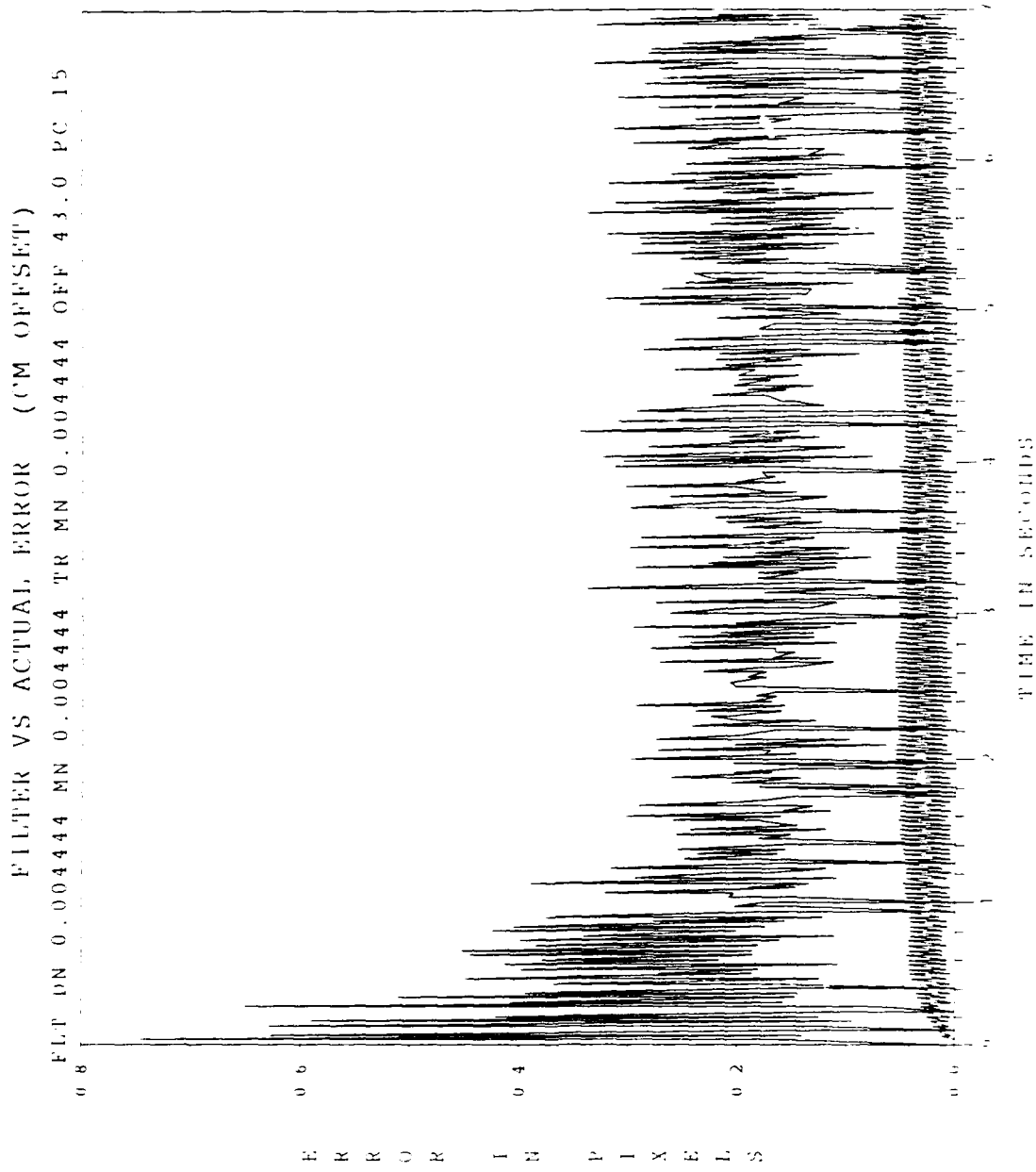


Figure C.4 2 Meter Error Offset Filter Vs Actual Error

ESTIMATED OFFSET-MINUS POSITION (+ / -) SIGMA
FLT DN 0.004444 MN 0.004444 TR MN 0.004444 OFF 43.0 PC 15

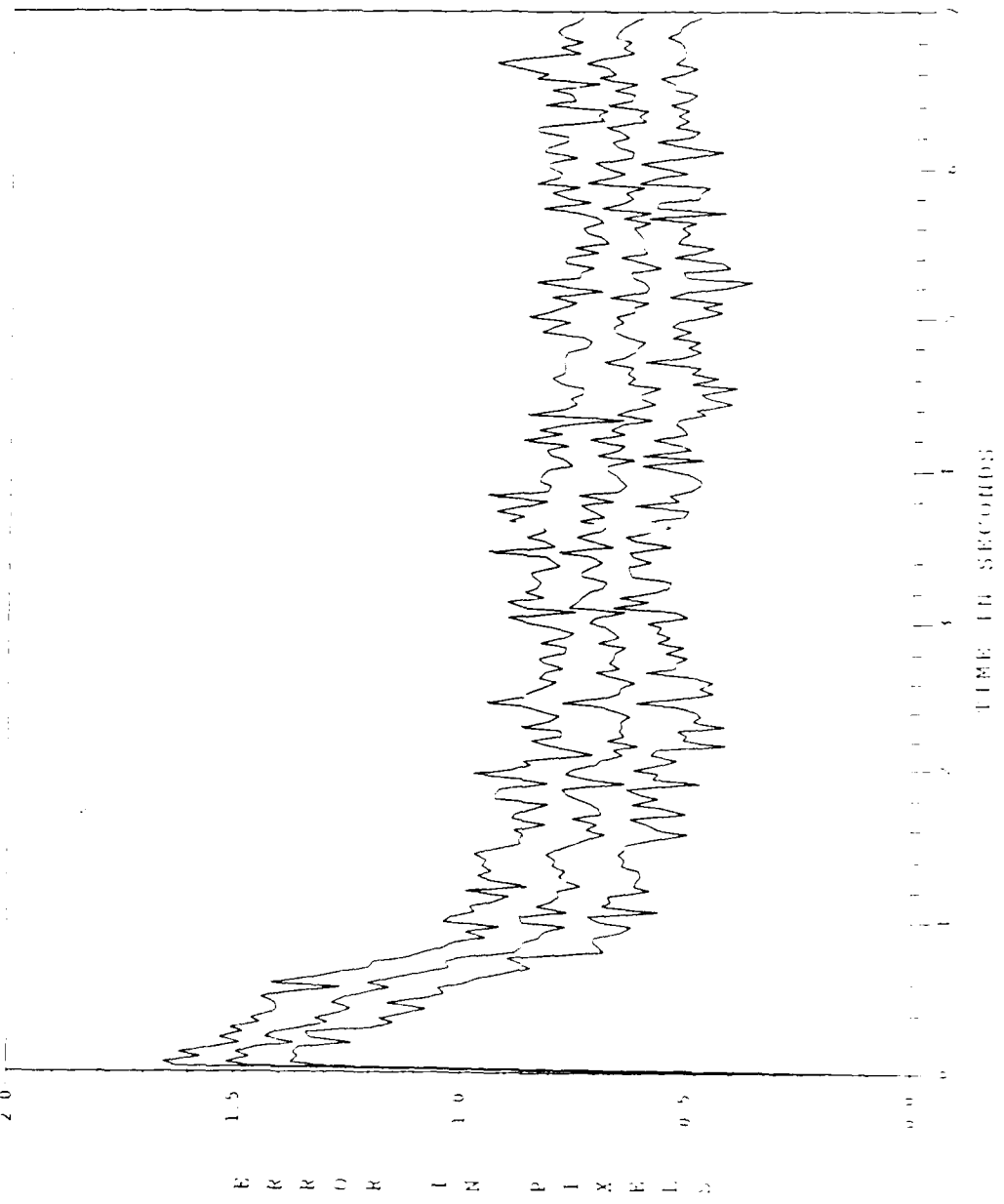


Figure C.5 2 Meter Error Offset-Minus Error

ESTIMATED OFFSET PLUS POSITION (1/) SIGMA

FLT DN 0.004444 MN 0.004444 TR MN 0.004444 OFF 43.0 PC 15

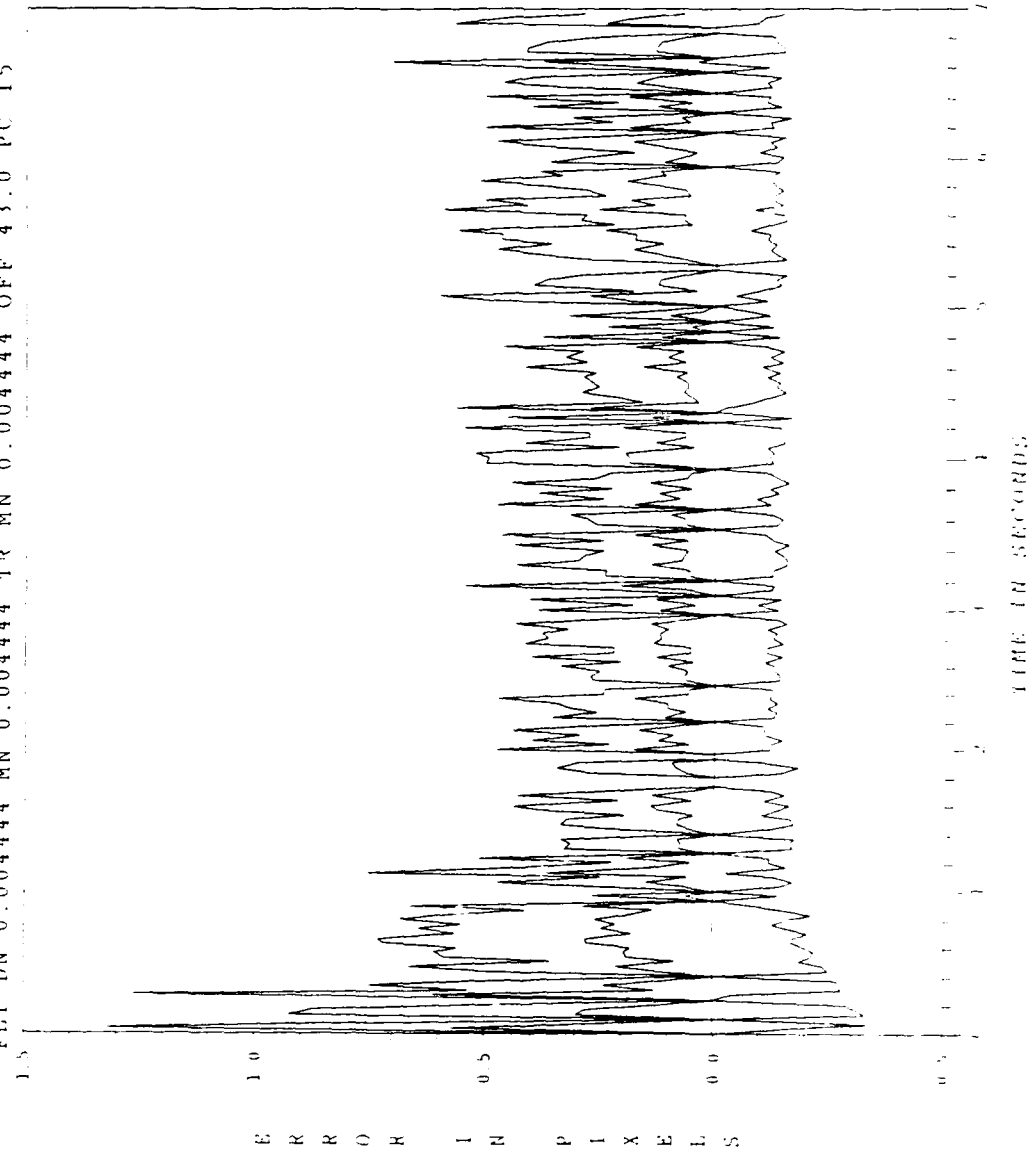


Figure C.6 2 Meter Error Offset-Plus Error

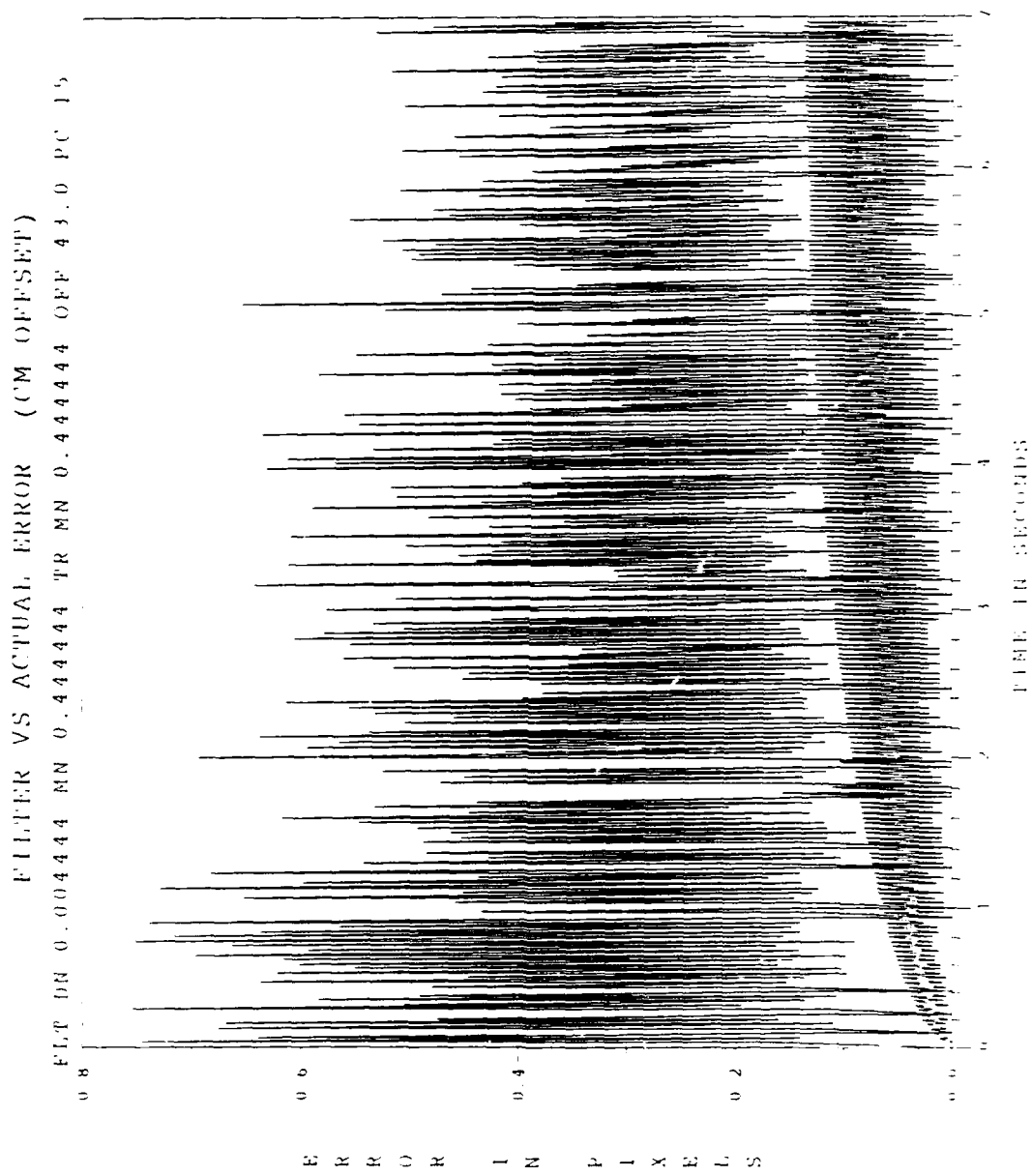


Figure C.7 20 Meter Error Offset Filter Vs Actual Error

ESTIMATED OFFSET MINUS POSITION (1 /) SIGMA

FLT DN 0.004444 MN 0.444444 TR MN 0.444444 OFF 43.0 PC 15

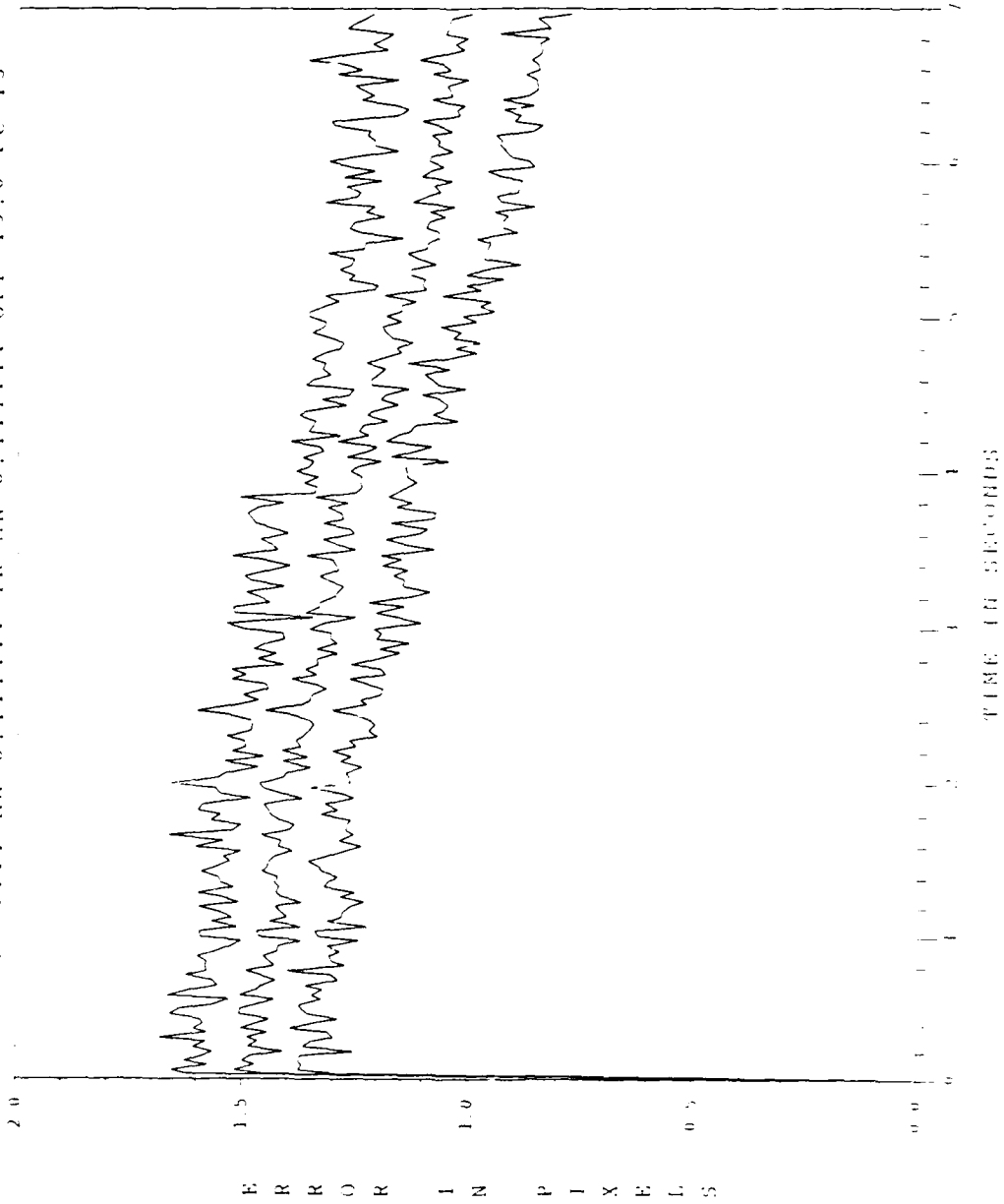


Figure C.8 20 Meter Error Offset-Minus Error

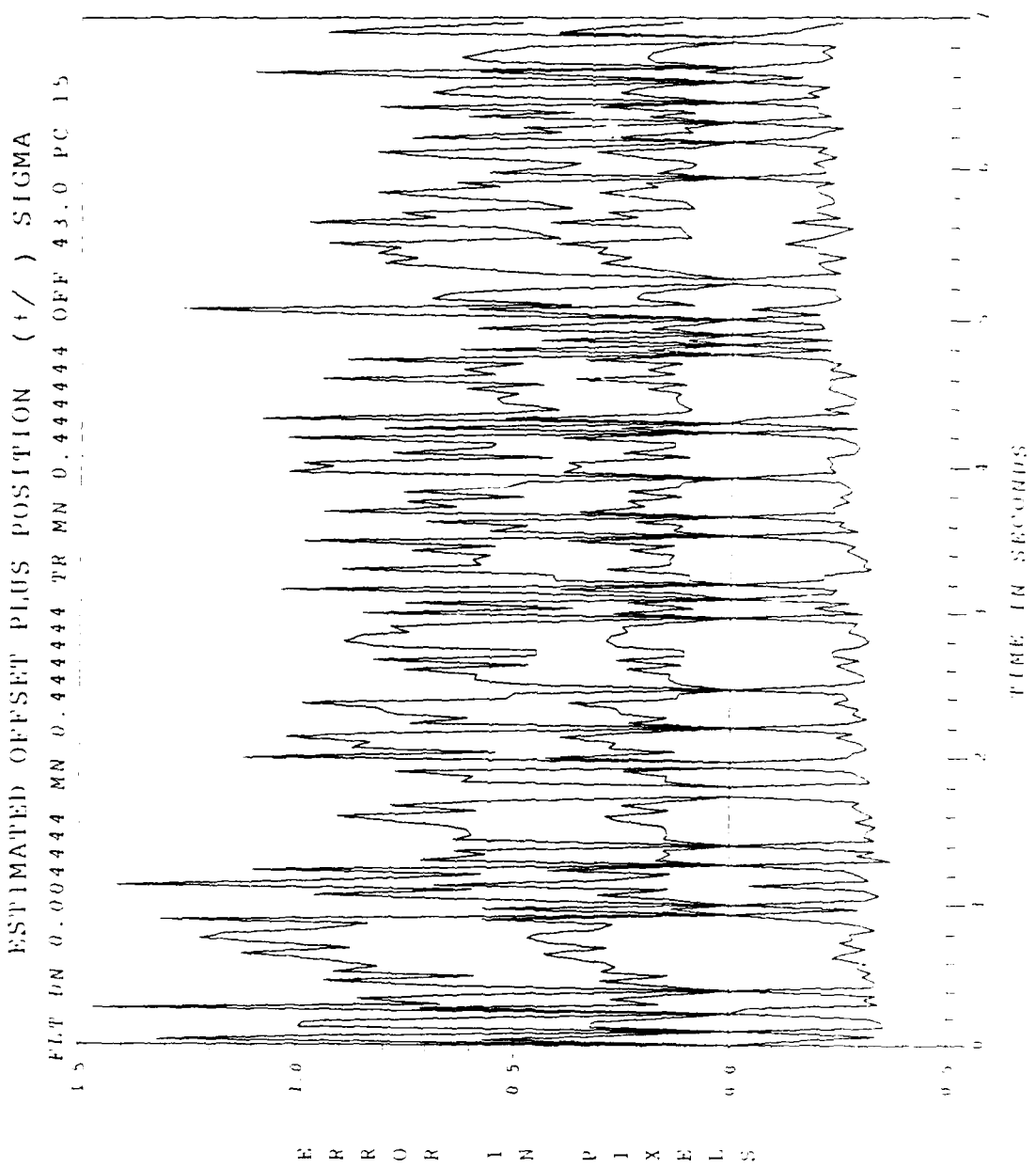


Figure C.9 20 Meter Error Offset-Plus Error

Appendix D. Plots for Robustness Study

Discussion in Section 5.5

Filter Error .2 meters, Truth Model Error 2 meters

Figures D.1-D.3

Filter Error .2 meters, Truth Model Error 20 meters

Figures D.4-D.6

Filter Error 2 meters, Truth Model Error .2 meters

Figures D.7-D.9

Filter Error 2 meters, Truth Model Error 20 meters

Figures D.10-D.12

Filter Error 20 meters, Truth Model Error .2 meters

Figures D.13-D.15

Filter Error 20 meters, Truth Model Error 2 meters

Figures D.16-D.18

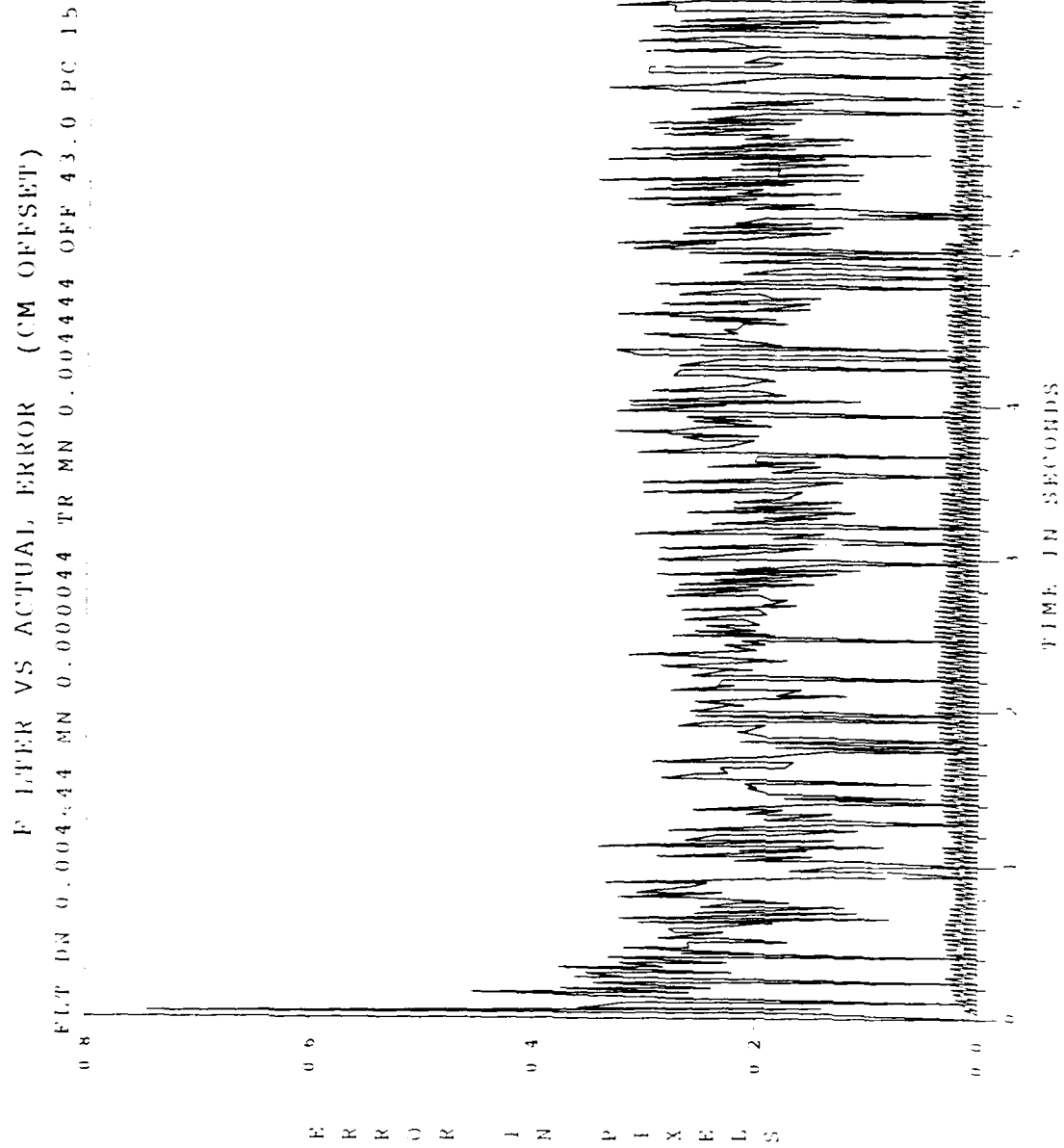


Figure D.1 Offset Filter Vs Actual Error

ESTIMATED OFFSET MINUS POSITION (/) SIGMA
OFF DN 0.004444 HR 0.000044 TP MR 0.004444 OFF 43.0 PC 15

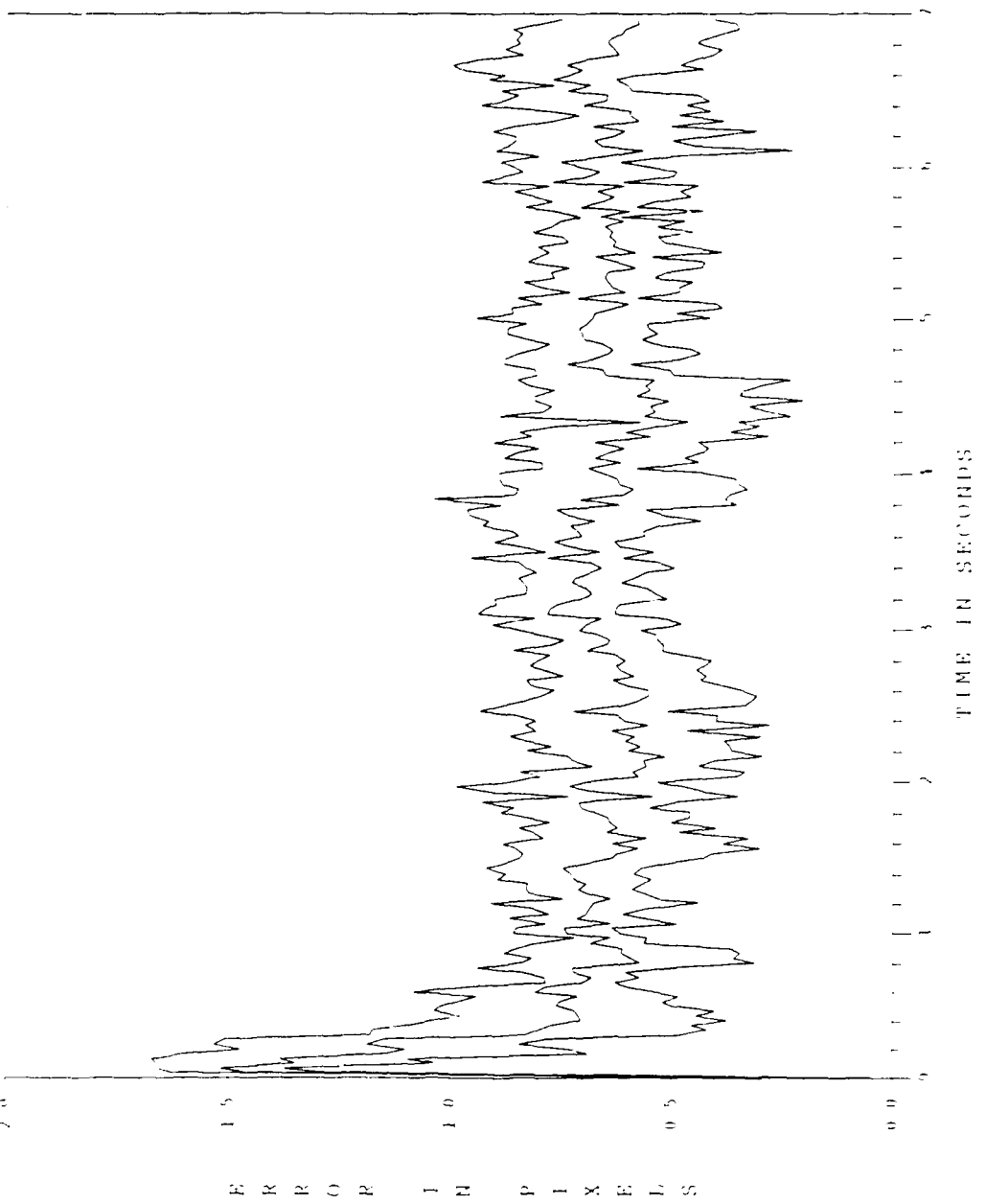


Figure D.2 Offset Minus Error

ESTIMATED OFFSET PLUS POSITION (1/) SIGMA

FLT DN 0.004444 MN 0.000044 TR MN 0.004444 OFF 43.0 PC 15

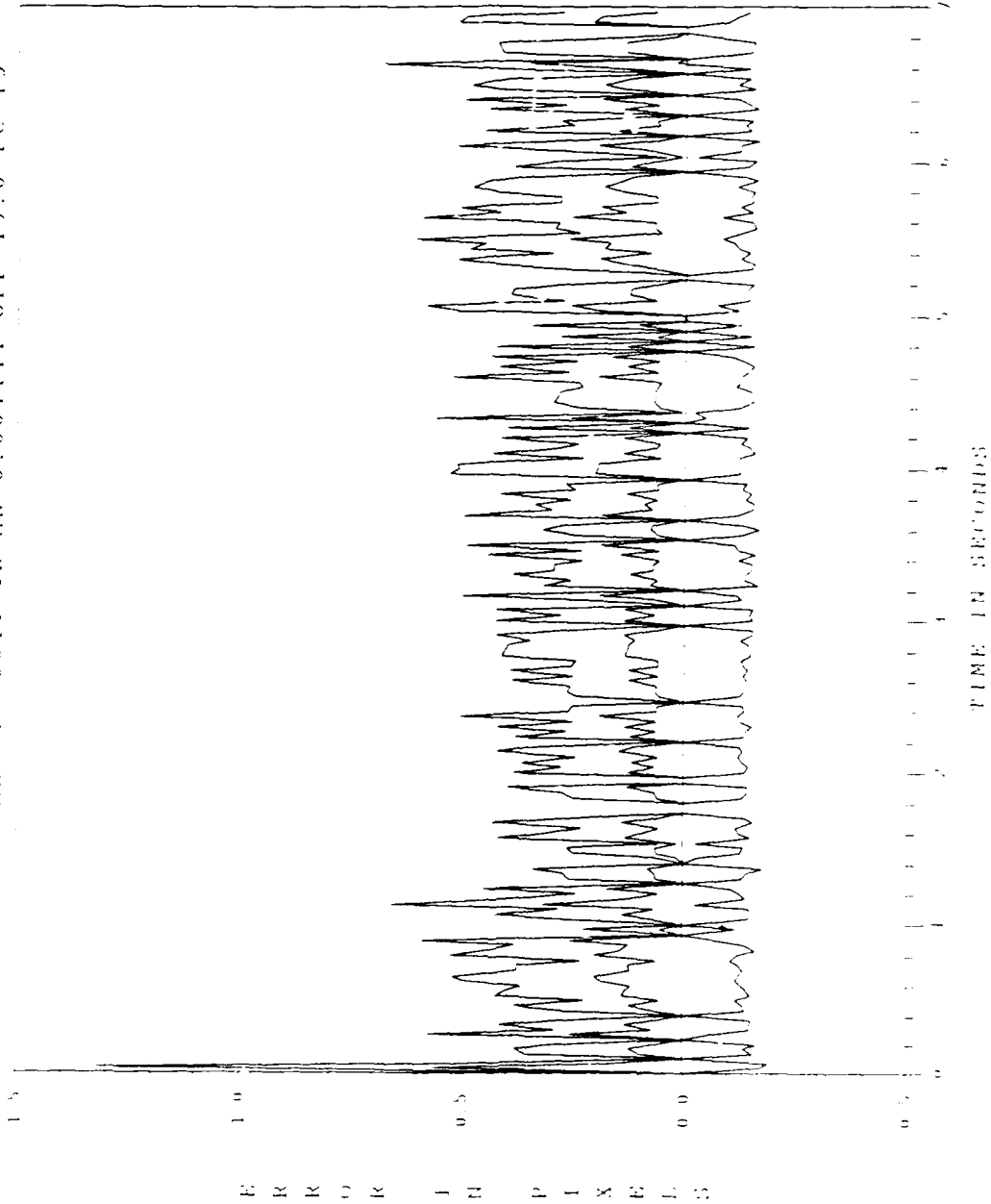


Figure D.3 Offset Plus Error

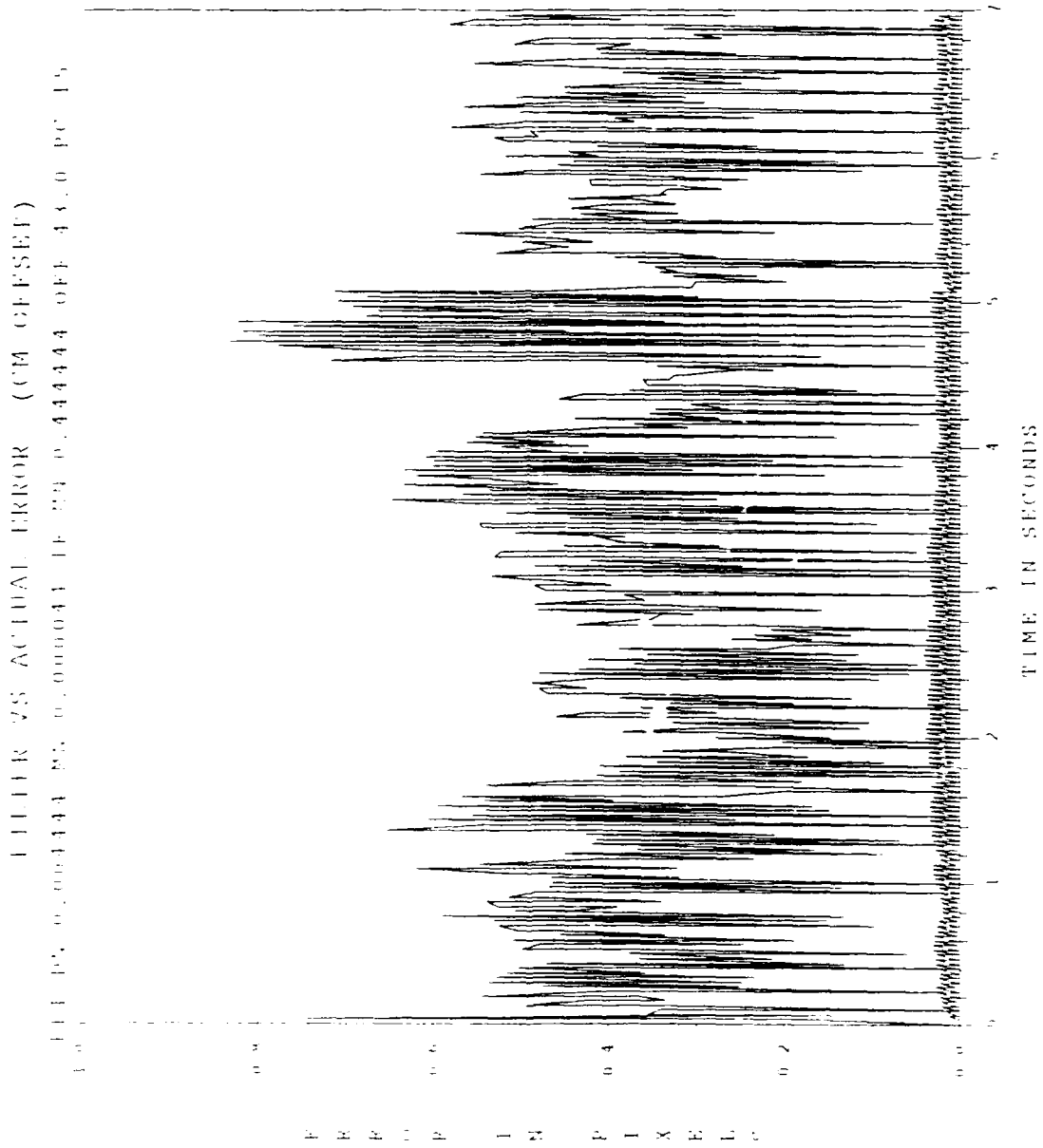


Figure D.4 Offset Filter Vs Actual Error

ESTIMATED OFFSET MINUS POSITION (σ) SIGMA

FLT BN 0.004444 ME 0.000044 TR MN 0.444444 OFF 43.0 PC 15

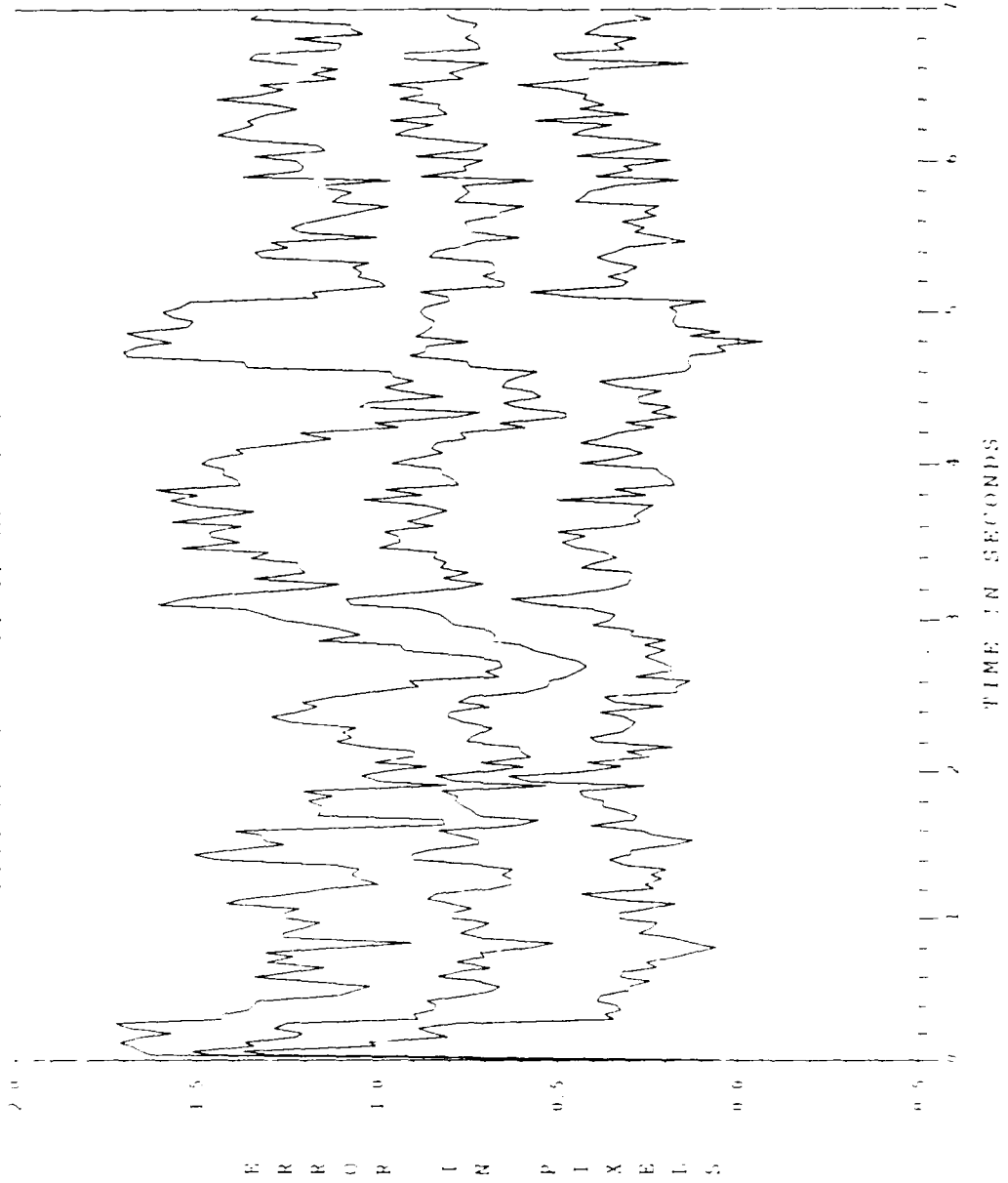


Figure D.5 Offset Minus Error

ESTIMATED OFFSET PLUS POSITION (1 /) SIGMA

FILE NO 0.004444 MH 0.000044 IR MH 0.444444 OFF 43.0 PC 15

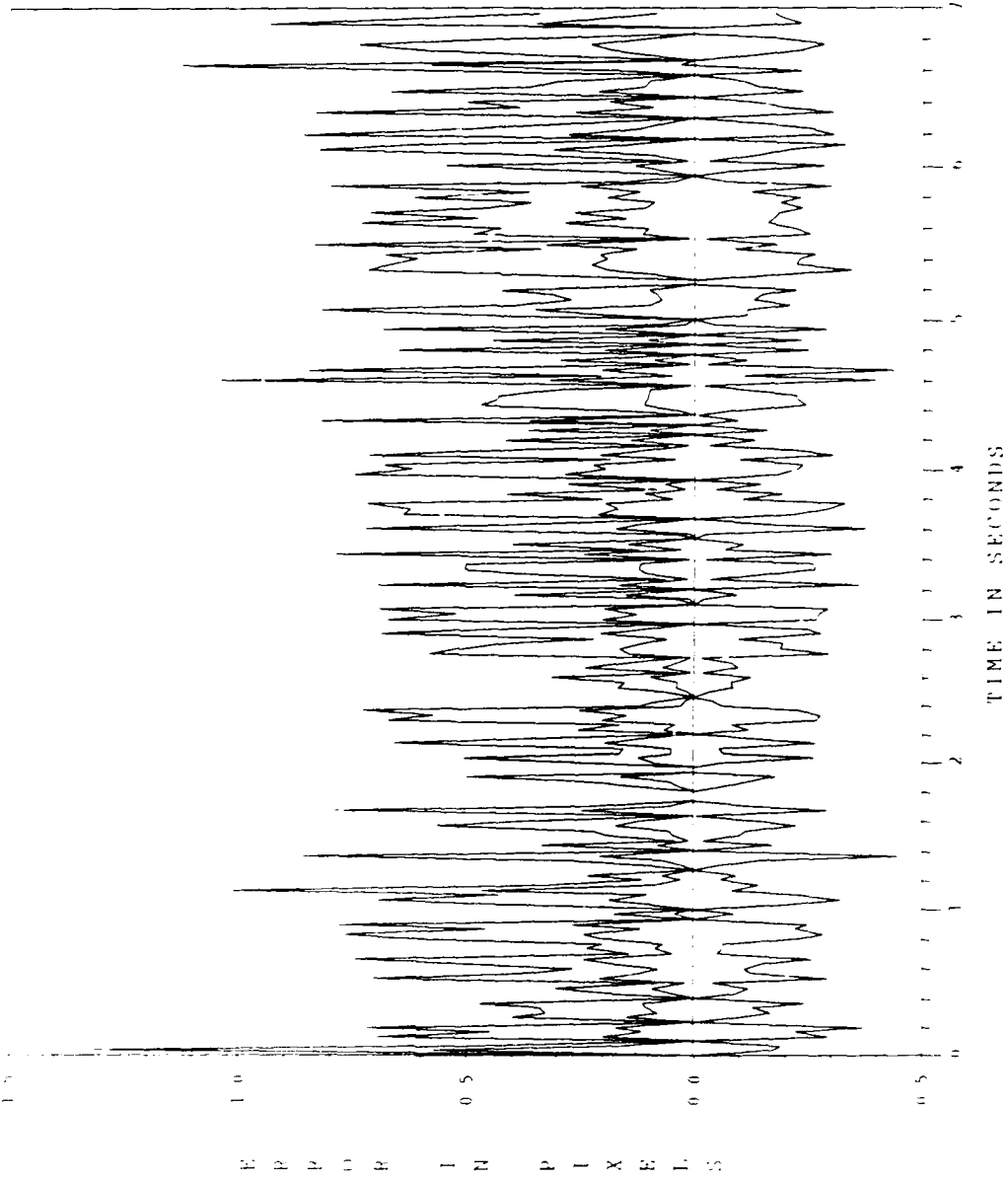


Figure D.6 Offset Plus Error

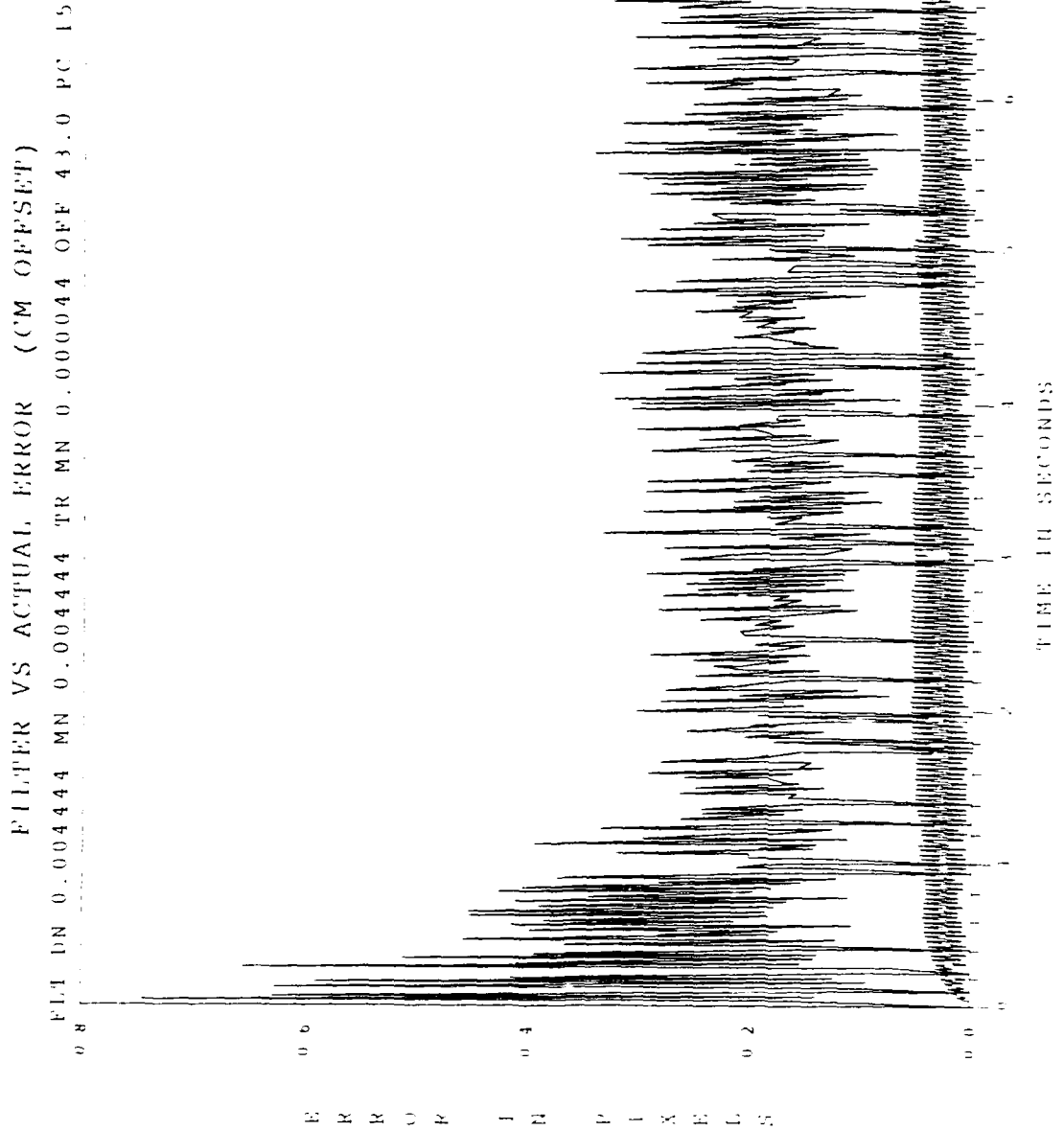


Figure D.7 Offset Filter Vs Actual Error

ESTIMATED OFFSET MINUS POSITION (+ /) SIGMA

FLT DN 0.004444 MN 0.004444 TR MN 0.000044 OFF 43.0 PC 15

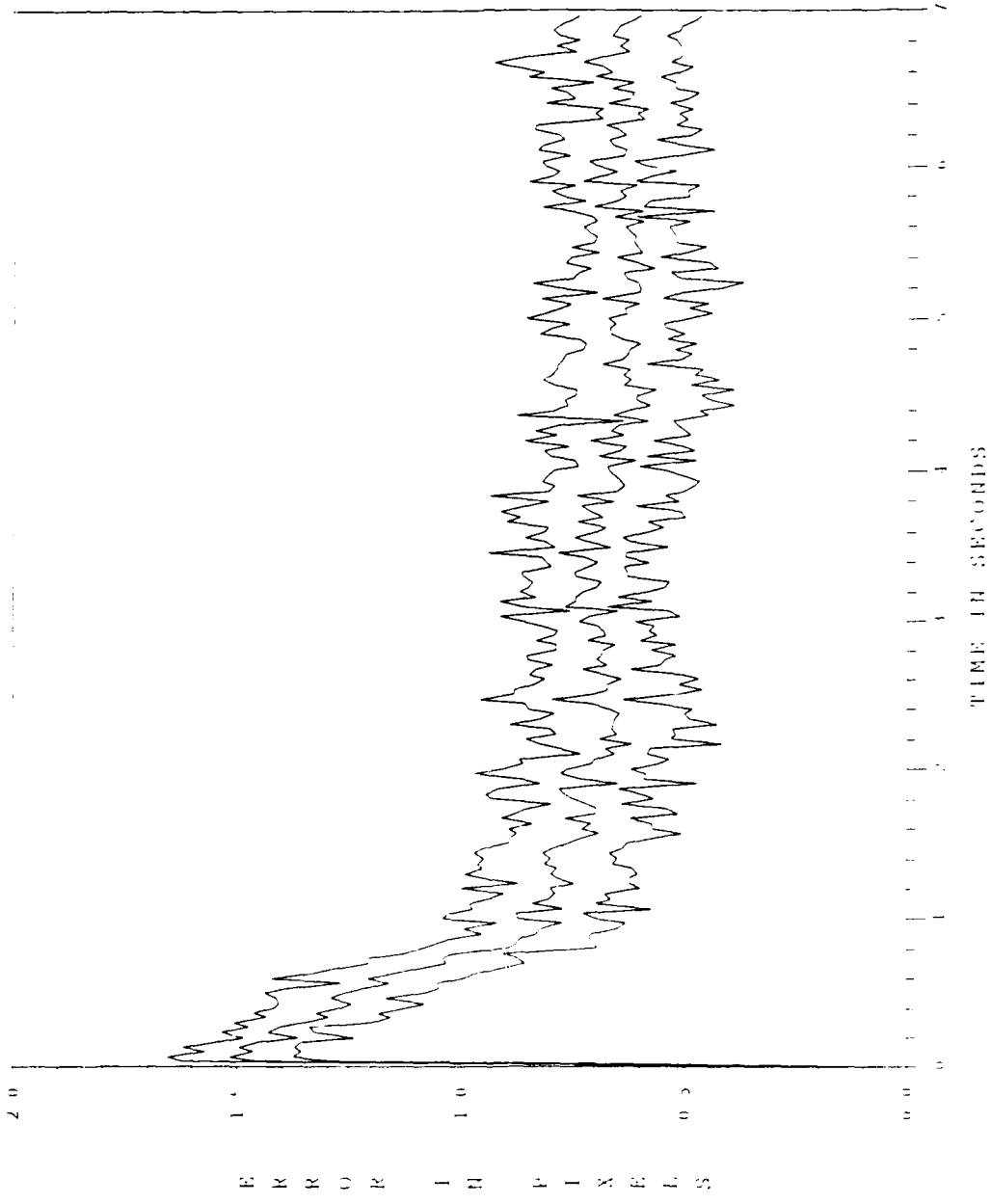


Figure D.8 Offset Minus Error

ESTIMATED OFFSET PLUS POSITION (1 /) SIGMA

FLT DN 0.004444 MN 0.004444 TR MN 0.000044 OFF 43.0 PC 15

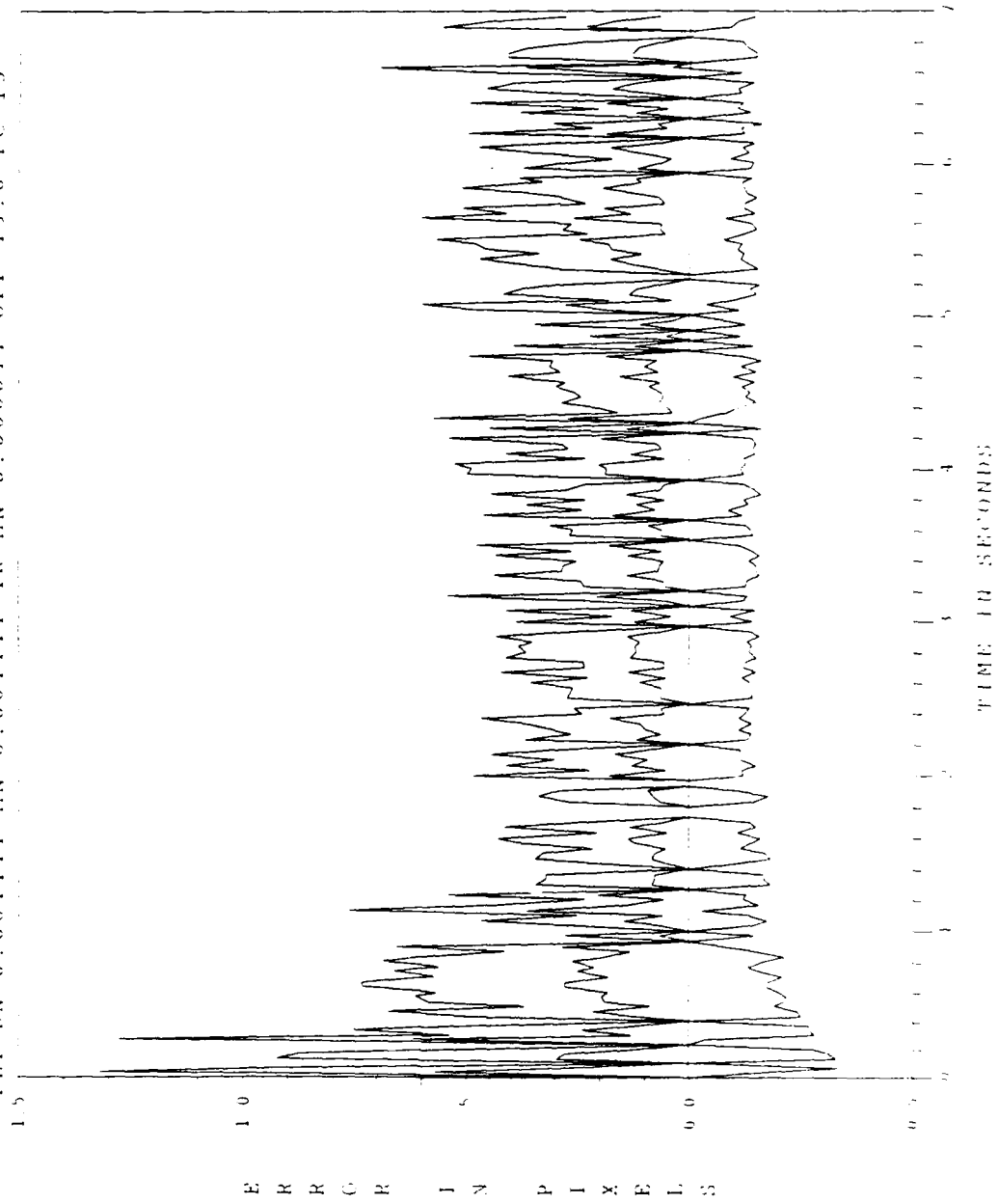


Figure D.9 Offset Plus Error

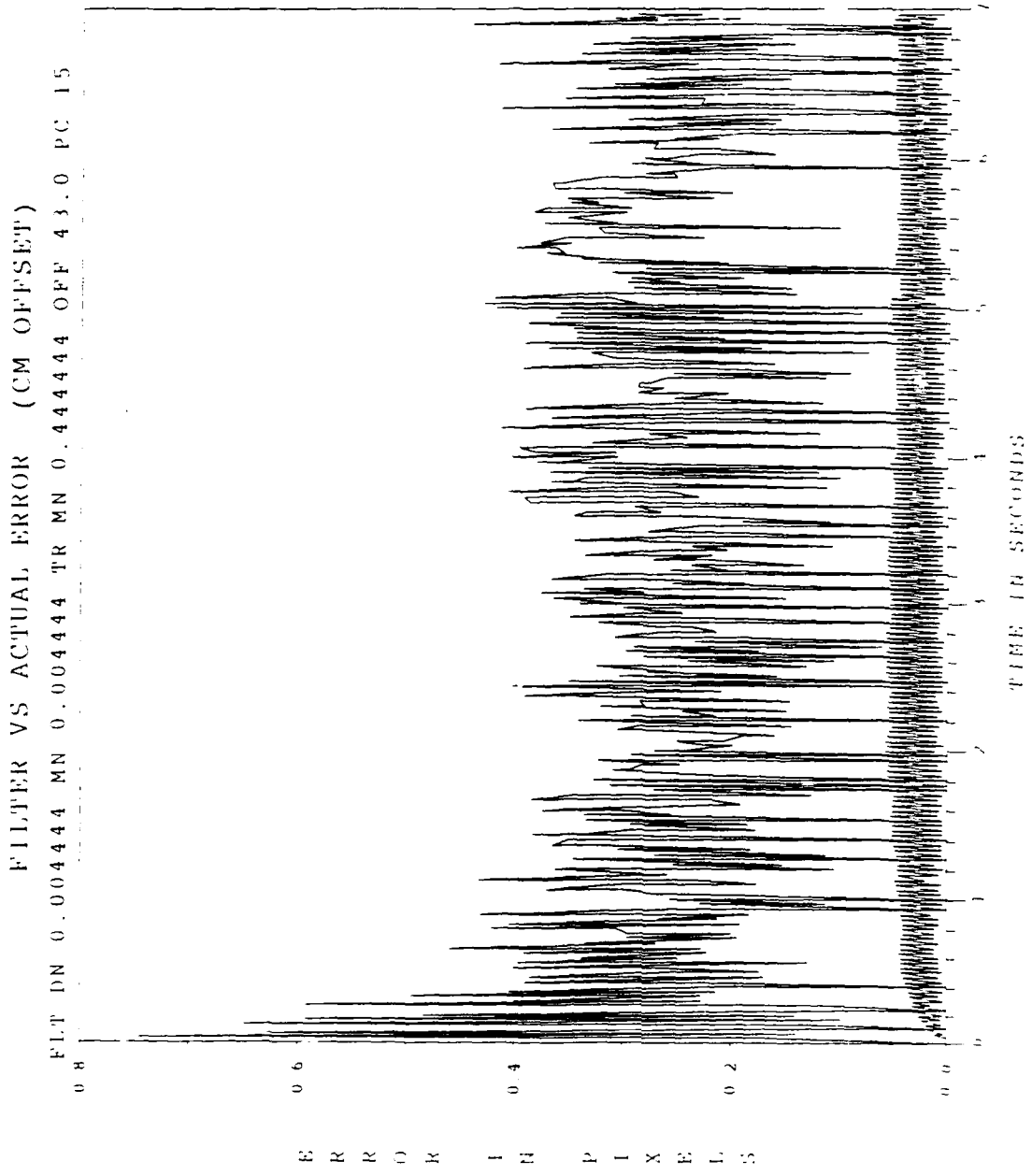


Figure D.10 Offset Filter Vs Actual Error

ESTIMATED OFFSET MINUS POSITION (1/σ) SIGMA

FLT DN 0.004444 MN 0.004444 TR MN 0.444444 OFF 43.0 PC 15

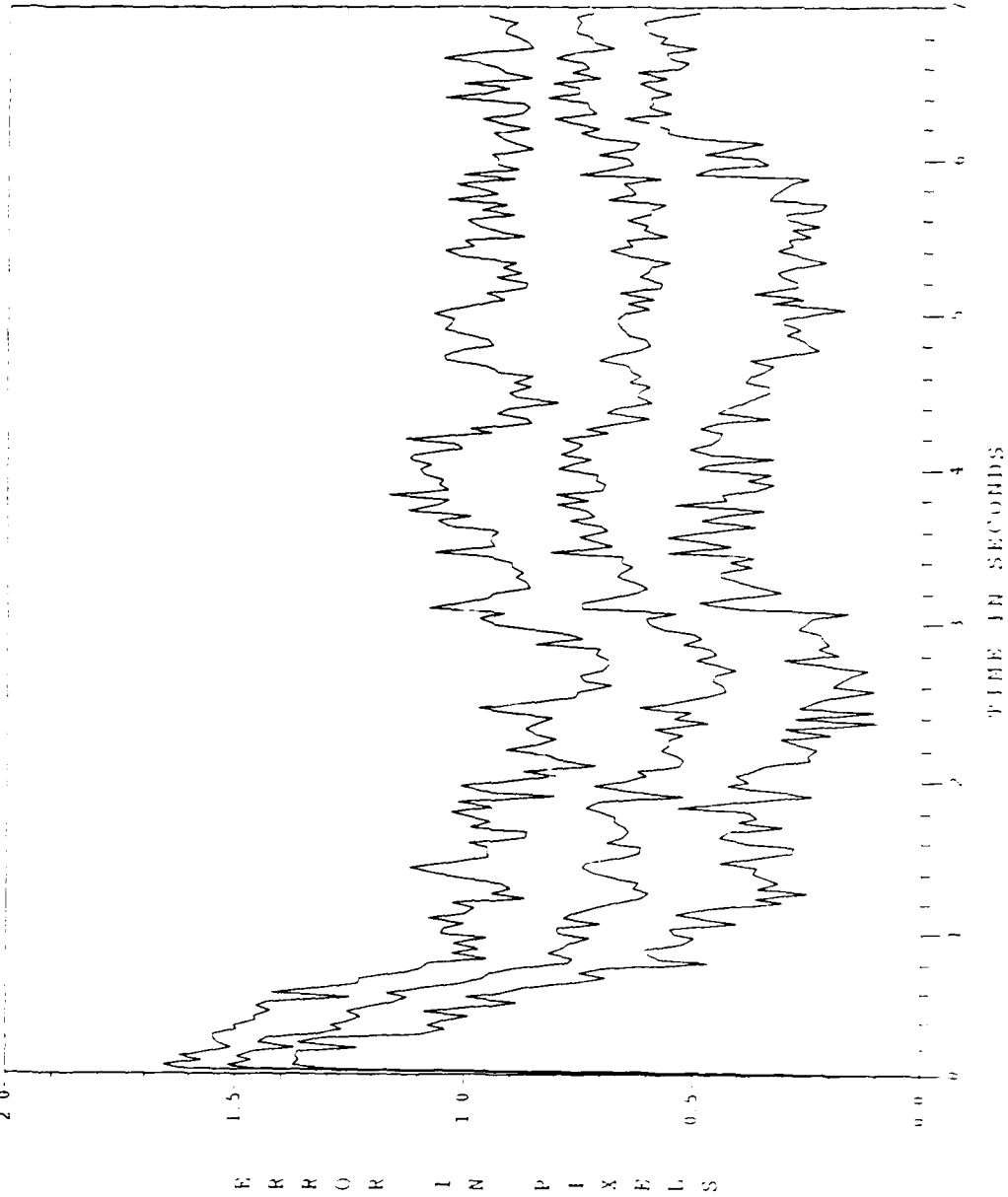


Figure D.11 Offset Minus Error

ESTIMATED OFFSET-PLUS POSITION (1 /) SIGMA

FLT DN 0.004444 MN 0.004444 TR MN 0.444444 OFF 43.0 PC 15

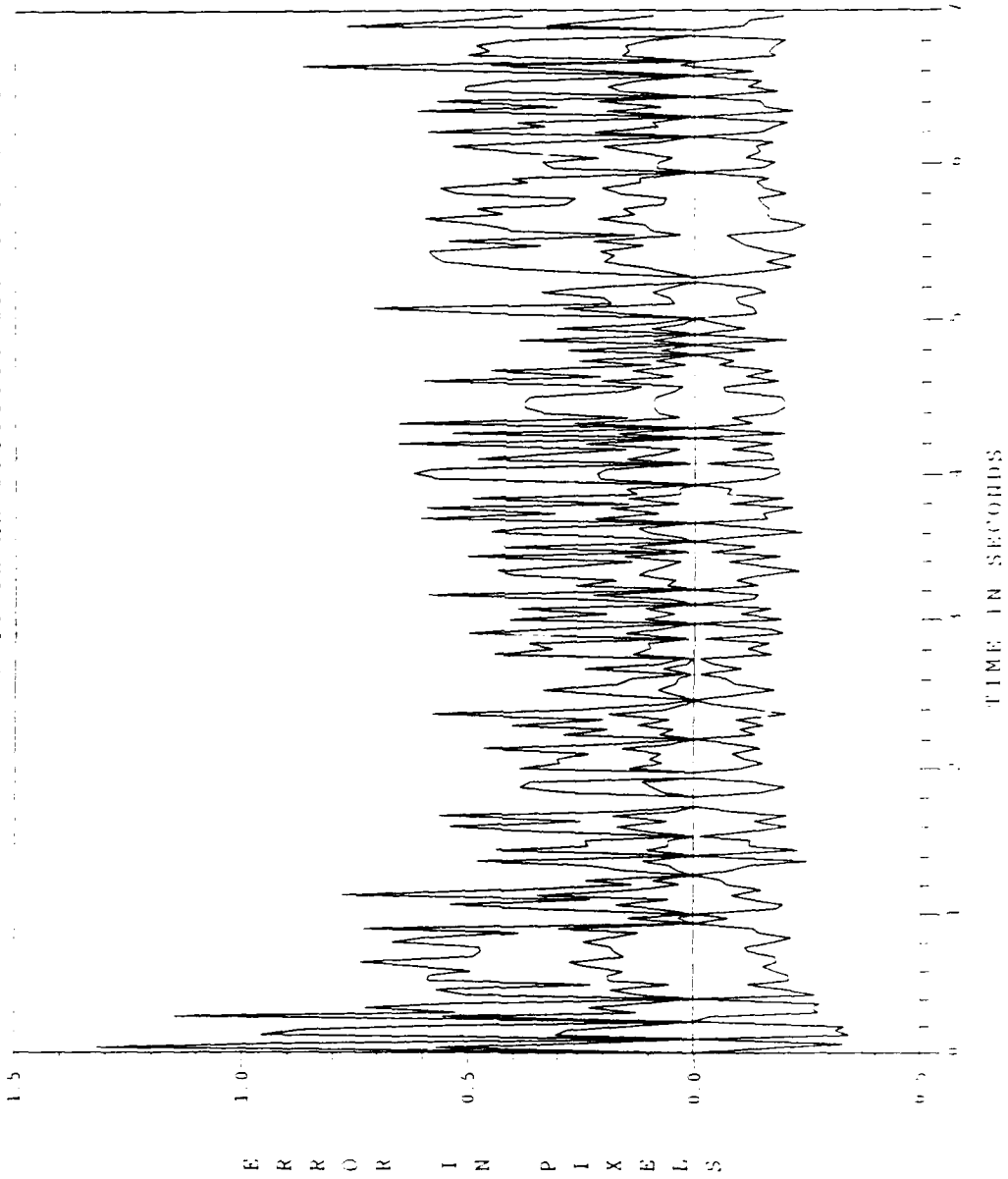


Figure D.12 Offset Plus Error

FILTER VS ACTUAL ERROR (CM OFFSET)

FLT DN 0.004444 MN 0.444444 TR MN 0.000044 OFF 43.0 PC 15

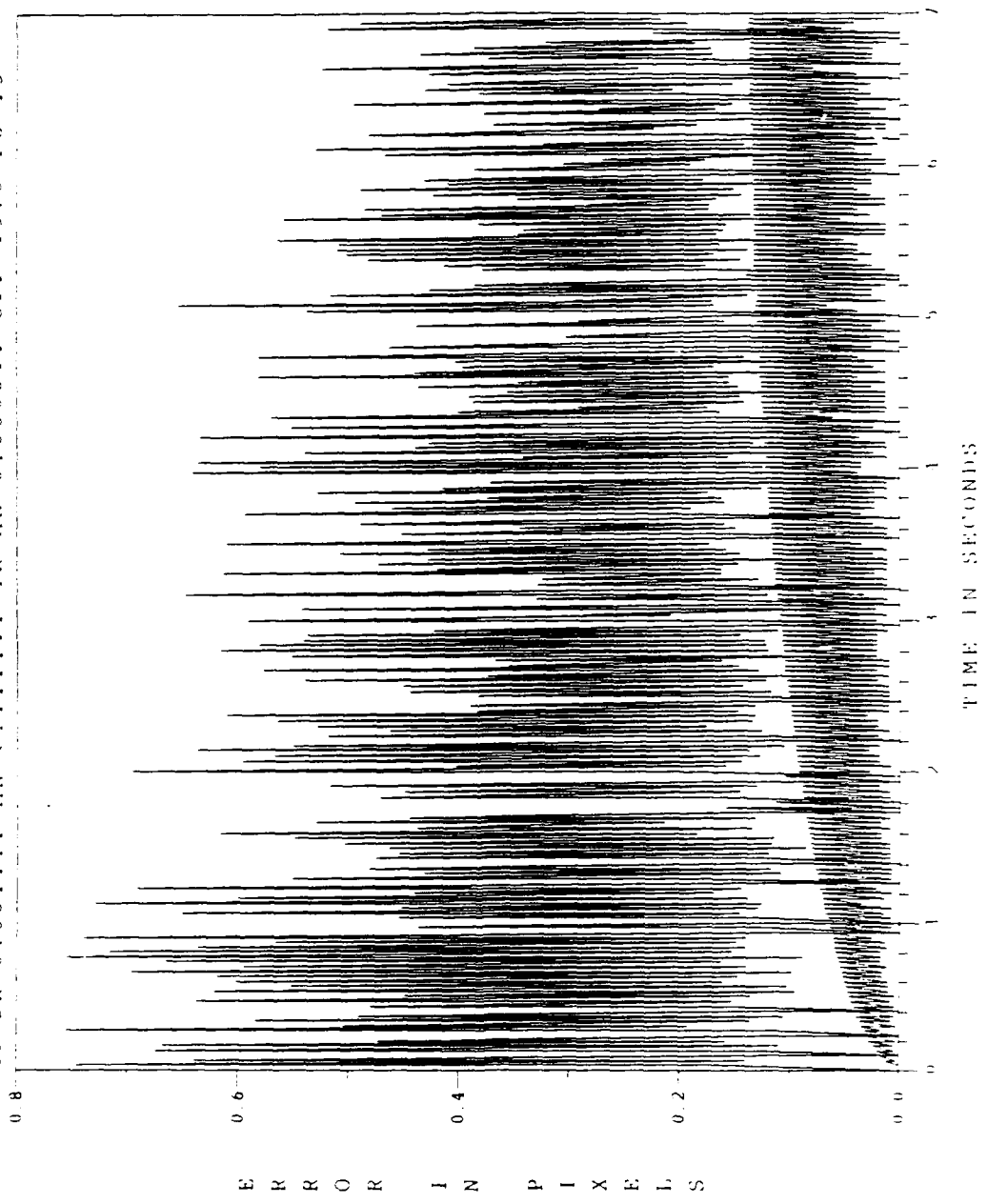


Figure D.13 Offset Filter Vs Actual Error

ESTIMATED OFFSET MINUS POSITION (1 /) SIGMA

FLT DN 0.004444 MN 0.444444 TR MN 0.000044 OFF 43.0 PC 15

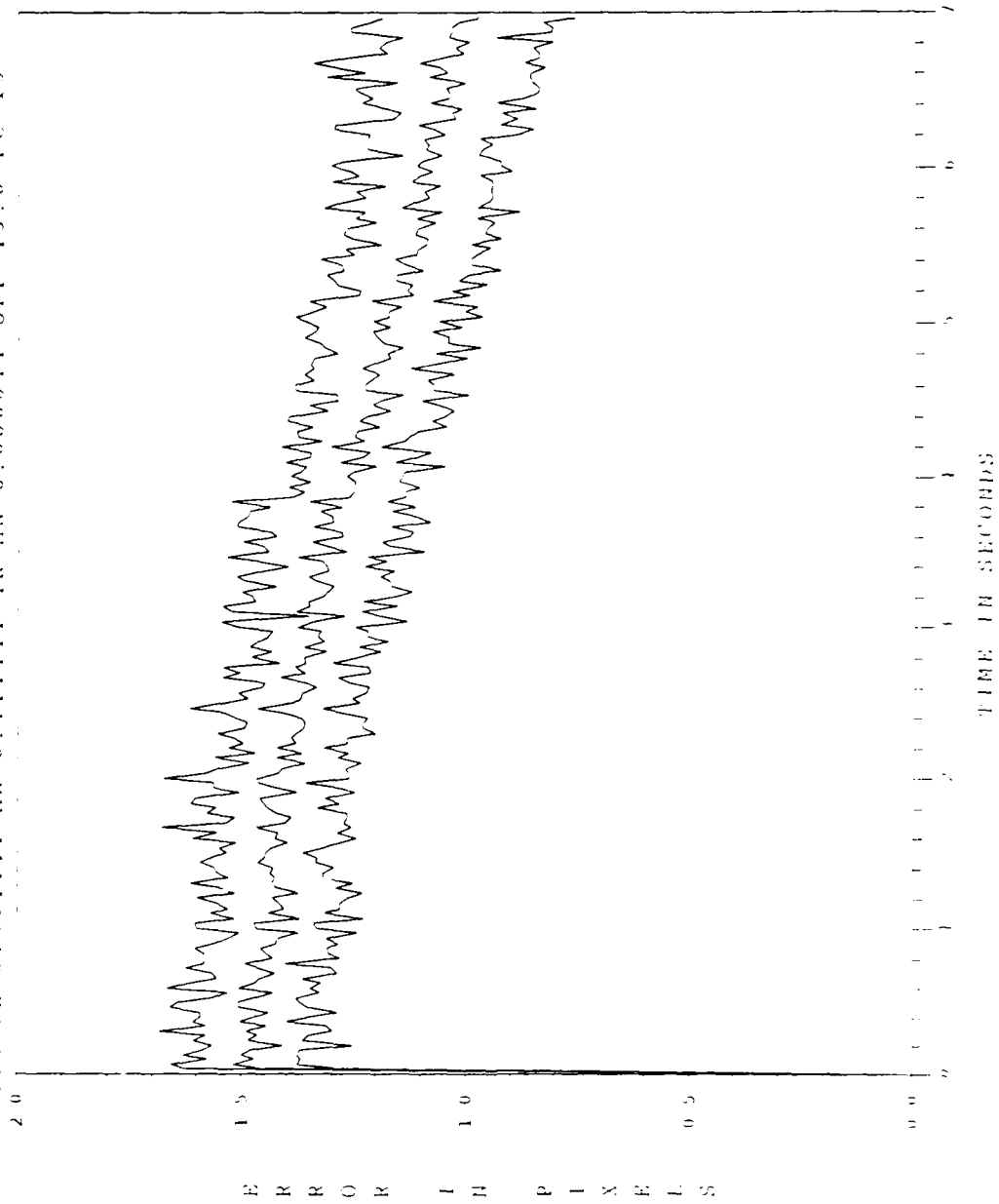


Figure D.14 Offset Minus Error

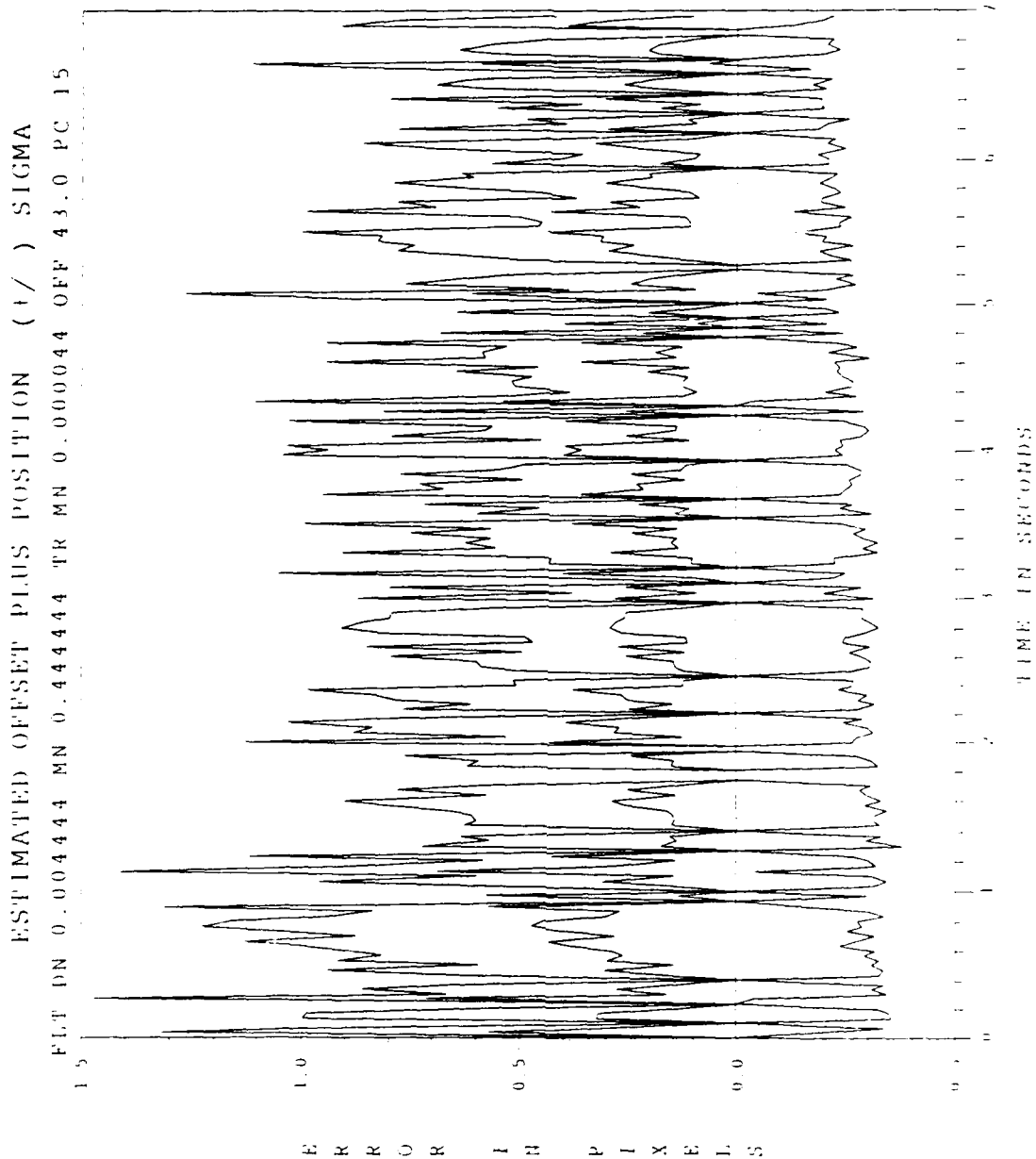


Figure D.15 Offset Plus Error

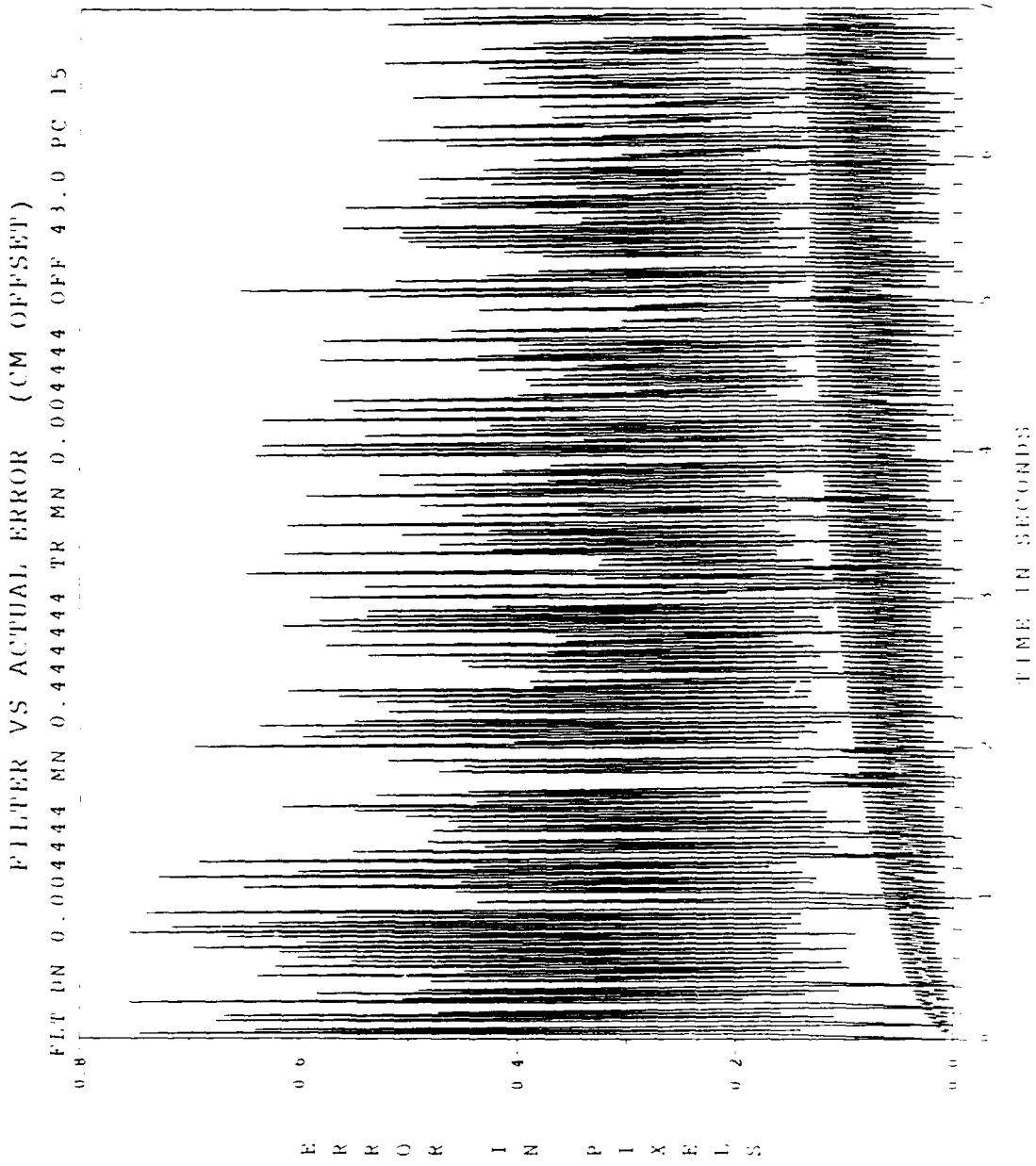


Figure D.16 Offset Filter Vs Actual Error

ESTIMATED OFFSET MINUS POSITION (1 /) SIGMA
FLT DN 0.004444 MN 0.444444 TR MN 0.004444 OFF 43.0 PC 15

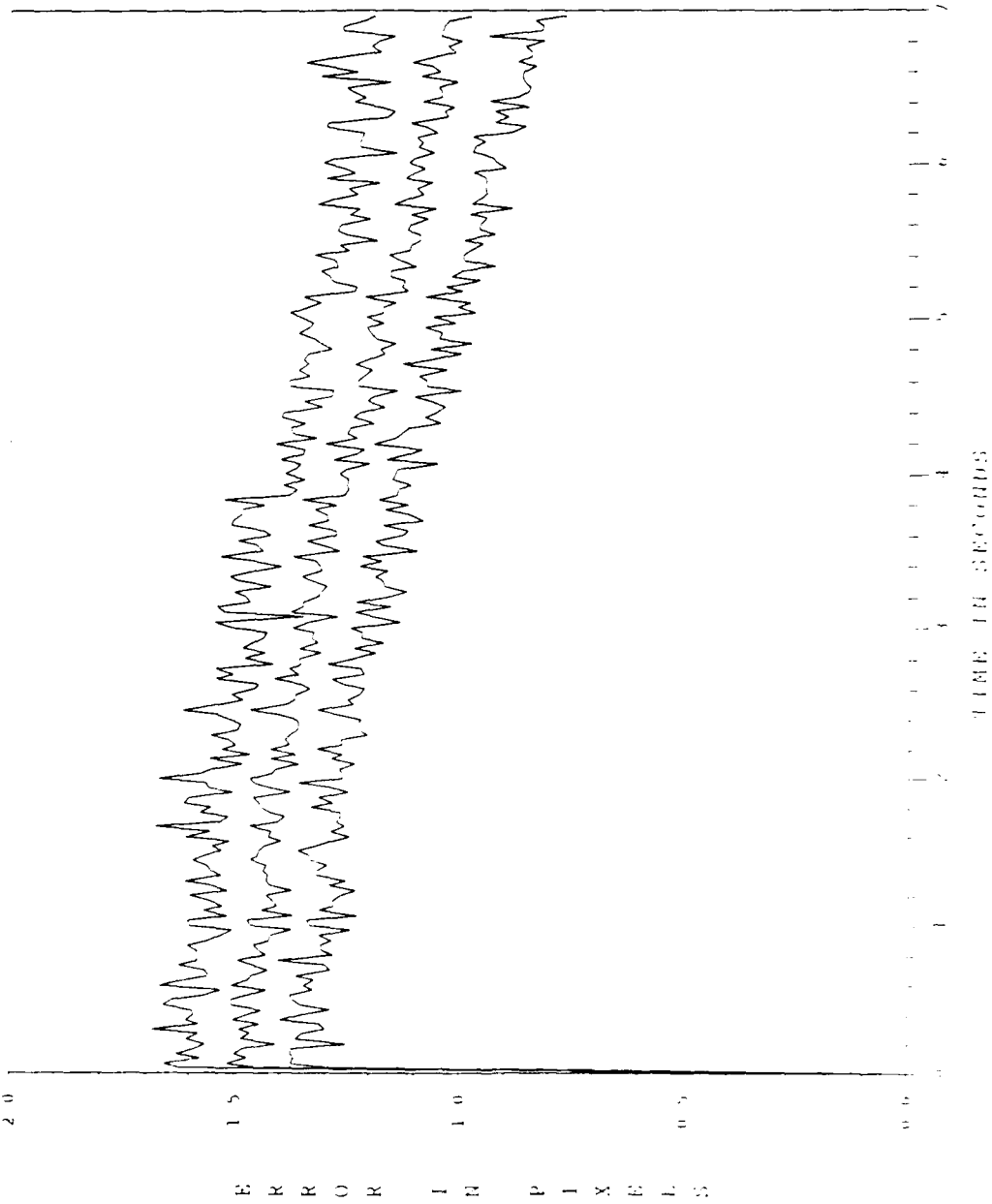


Figure D.17 Offset Minus Error

ESTIMATED OFFSET PLUS POSITION (+) SIGMA

FLT DN 0.004444 MN 0.444444 TR MN 0.004444 OFF 43.0 PC 15

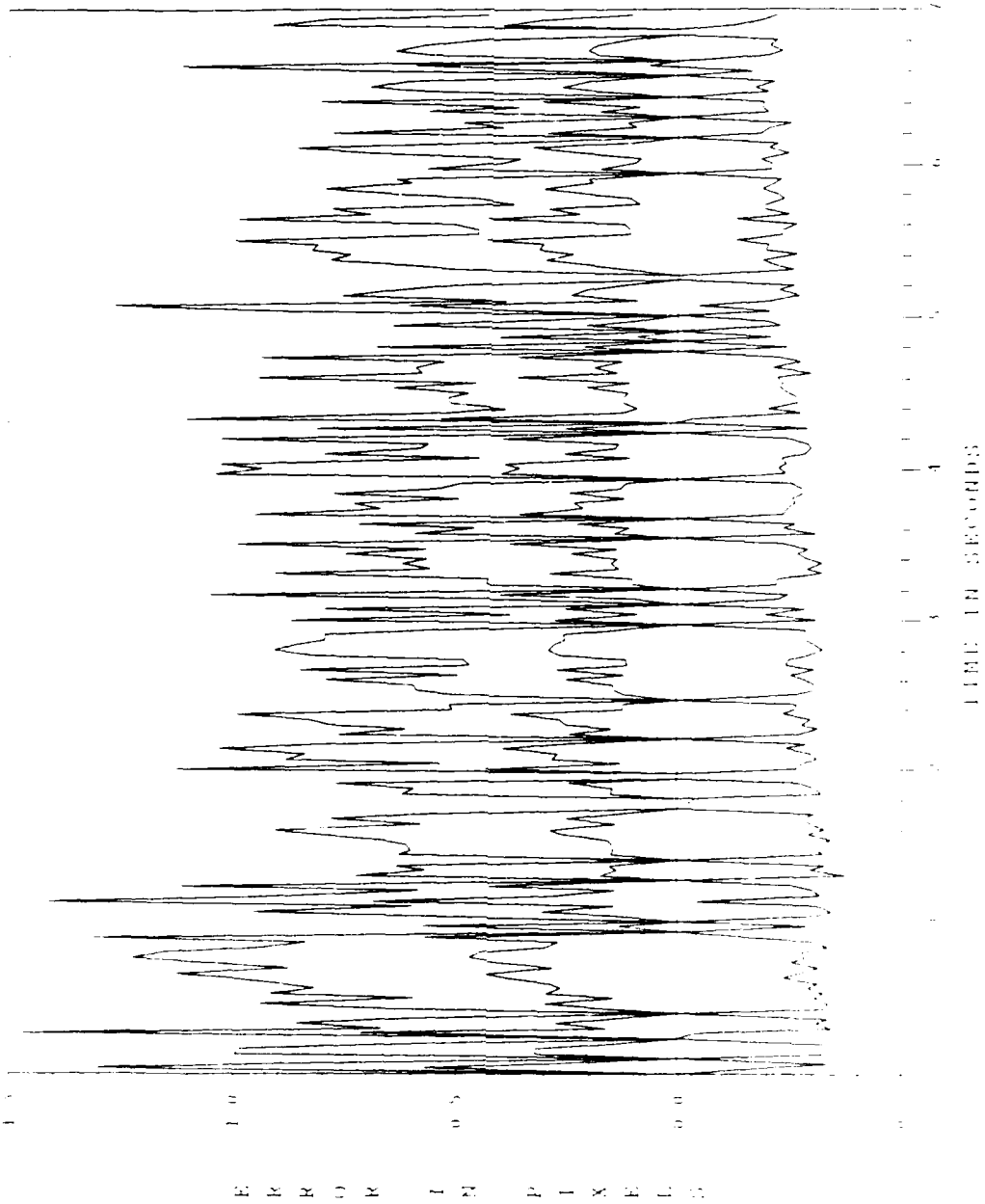


Figure D.13 Offset Plus Error

Appendix E. Plots for Pixel Constant Study

Discussion in Section 5.6

Pixel Constant (Micro-radians/Pixel)

7.5 Figures E.1-E.3

15 Figures E.4-E.6

30 Figures E.7-E.9

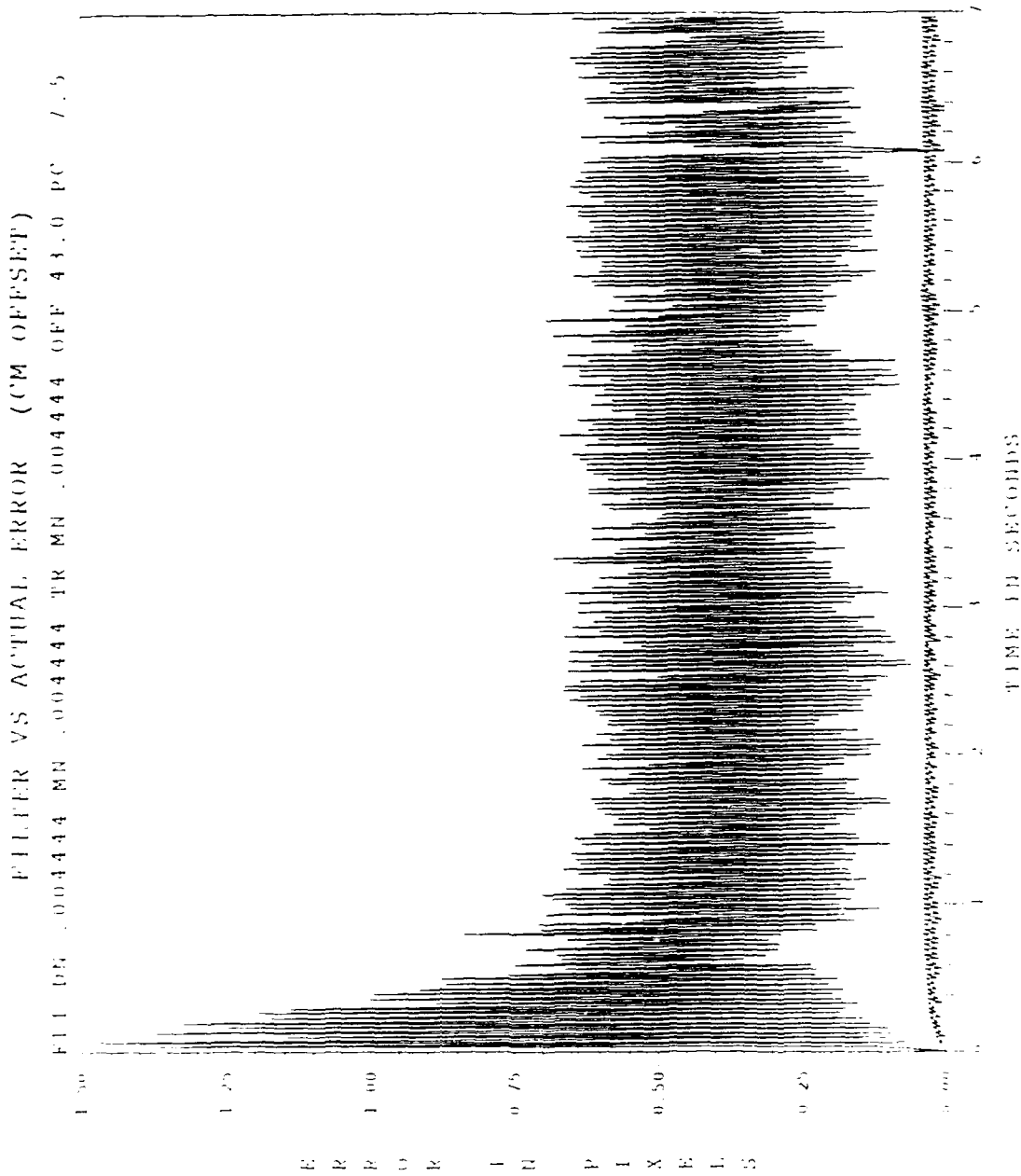


Figure E.1 PC 7.5 Offset Filter Vs Actual Error

ESTIMATED OFFSET MINUS POSITION (1/) SIGMA
FLT ON .004444 MN .004444 TR MN .004444 OFF 43.0 PC 7.5

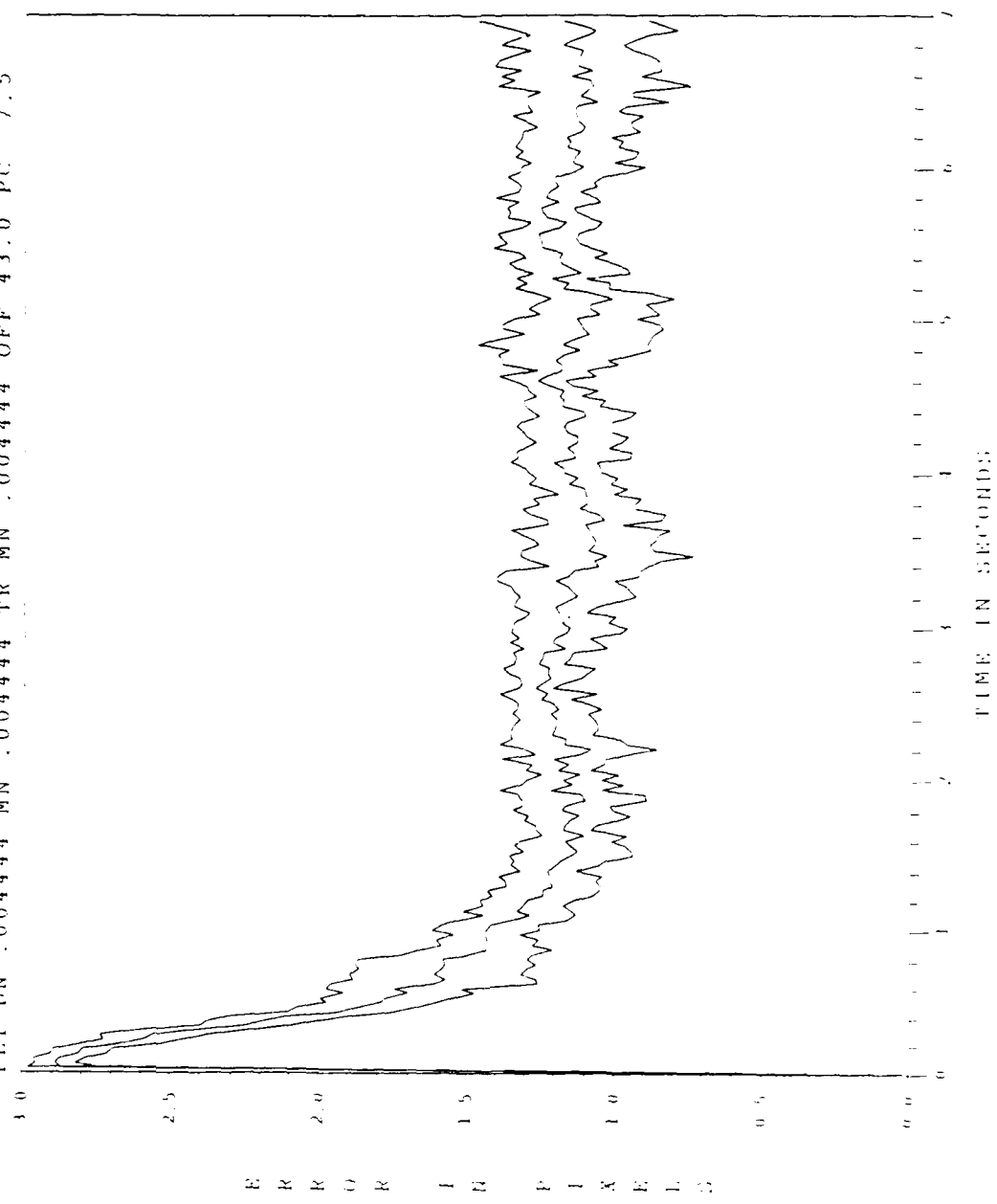


Figure E.2 PC 7.5 Offset Minus Error

ESTIMATED OFFSET PLUS POSITION (1 /) SIGMA

FLT IN .004444 MN .004444 TR MN .004444 OFF 43.0 PC 7.5

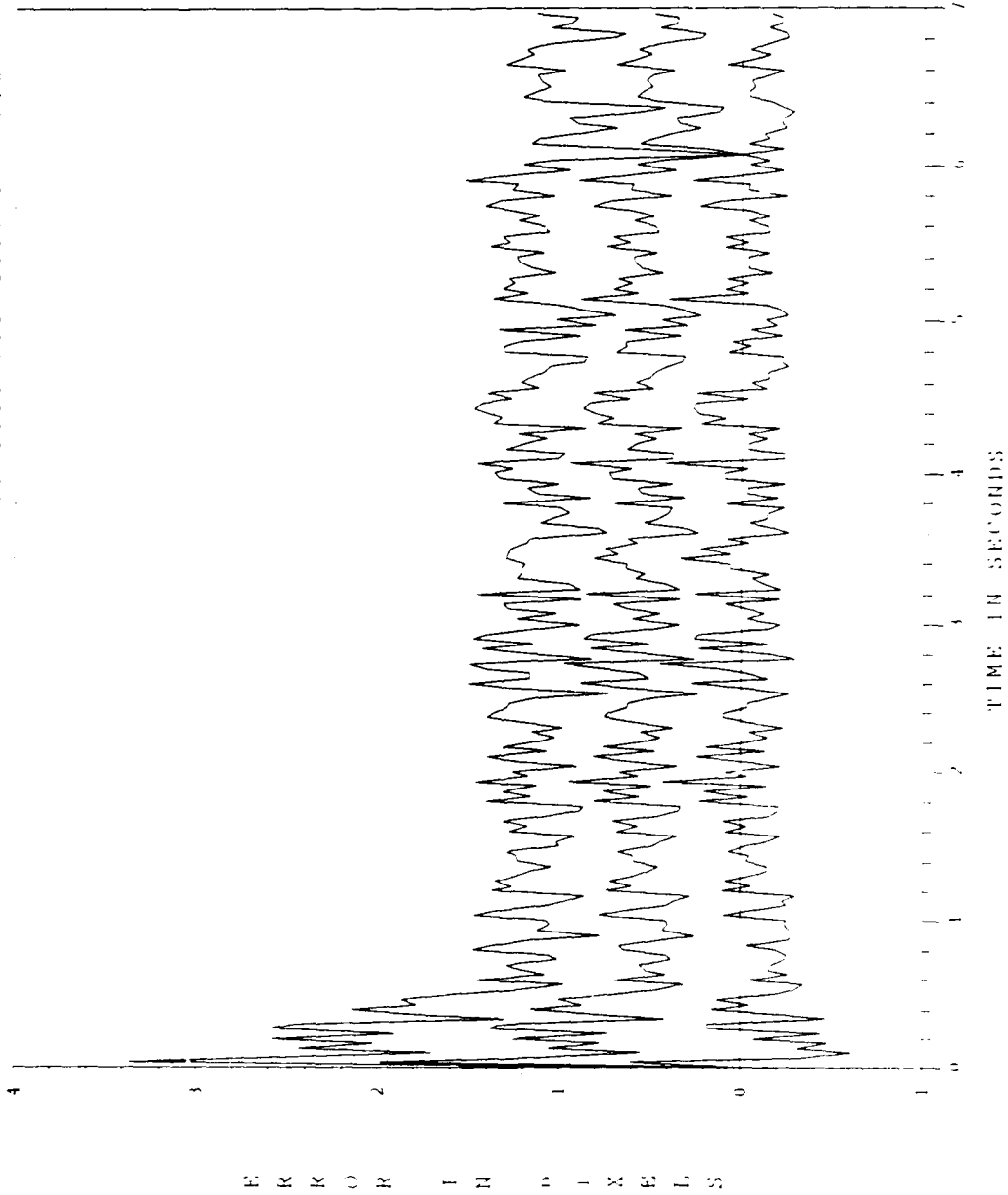


Figure E.3 PC 7.5 Offset Plus Error

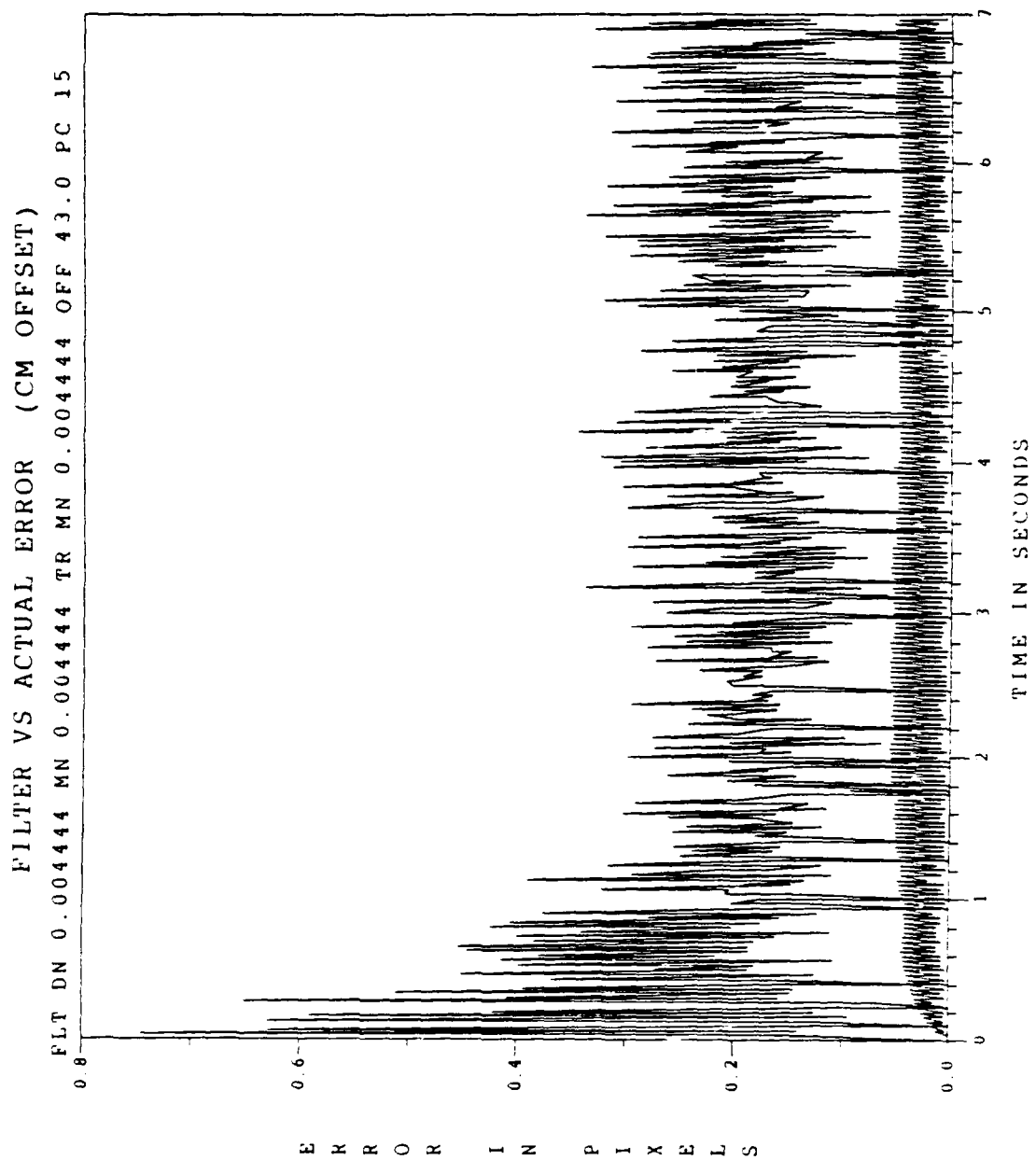


Figure E.4 PC 15 Offset Filter Vs Actual Error

ESTIMATED OFFSET-MINUS POSITION (+/-) SIGMA

FLT DN 0.004444 MN 0.004444 TR MN 0.004444 OFF 43.0 PC 15

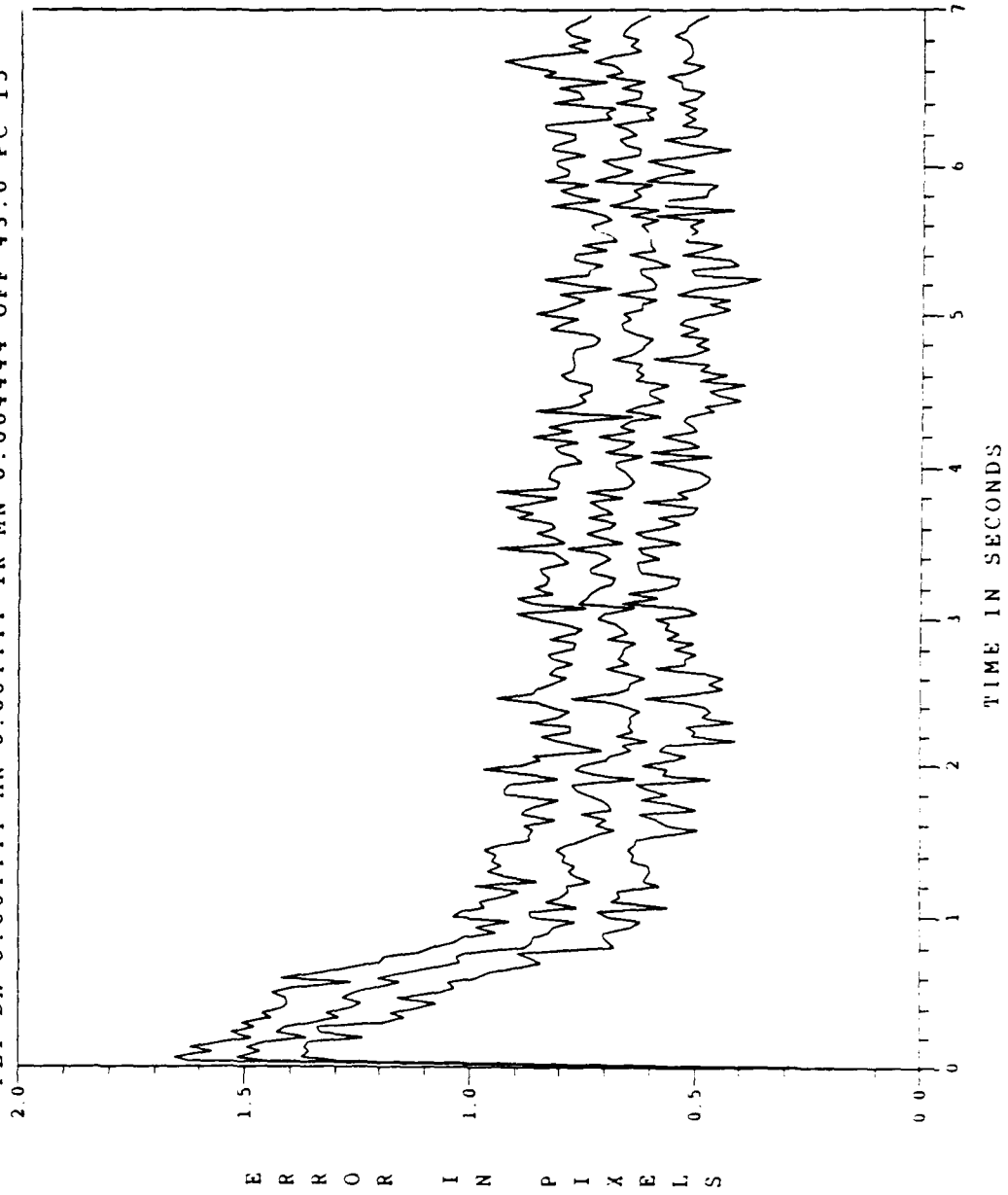


Figure E.5 PC 15 Offset Minus Error

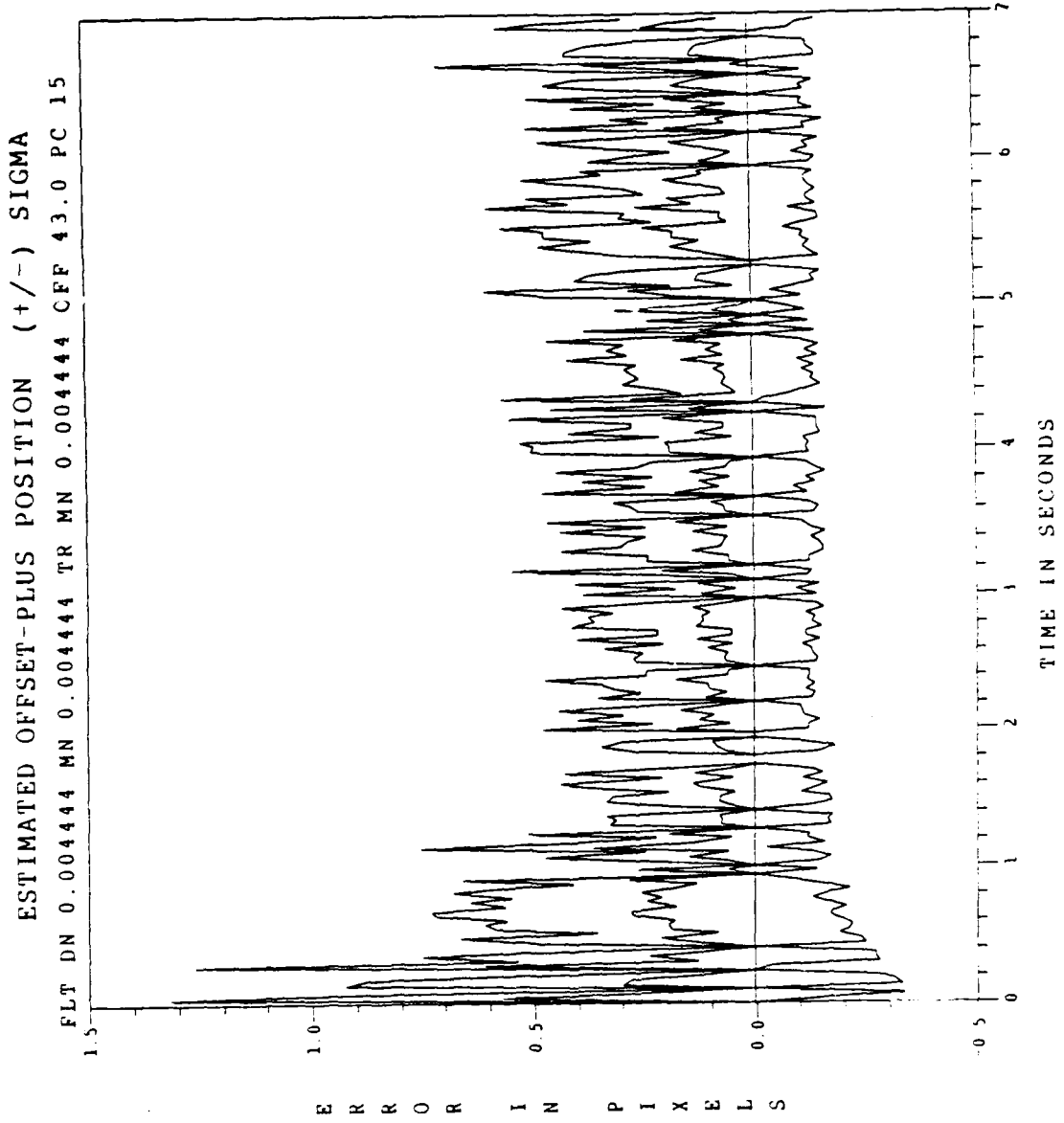


Figure E.6 PC 15 Offset Plus Error

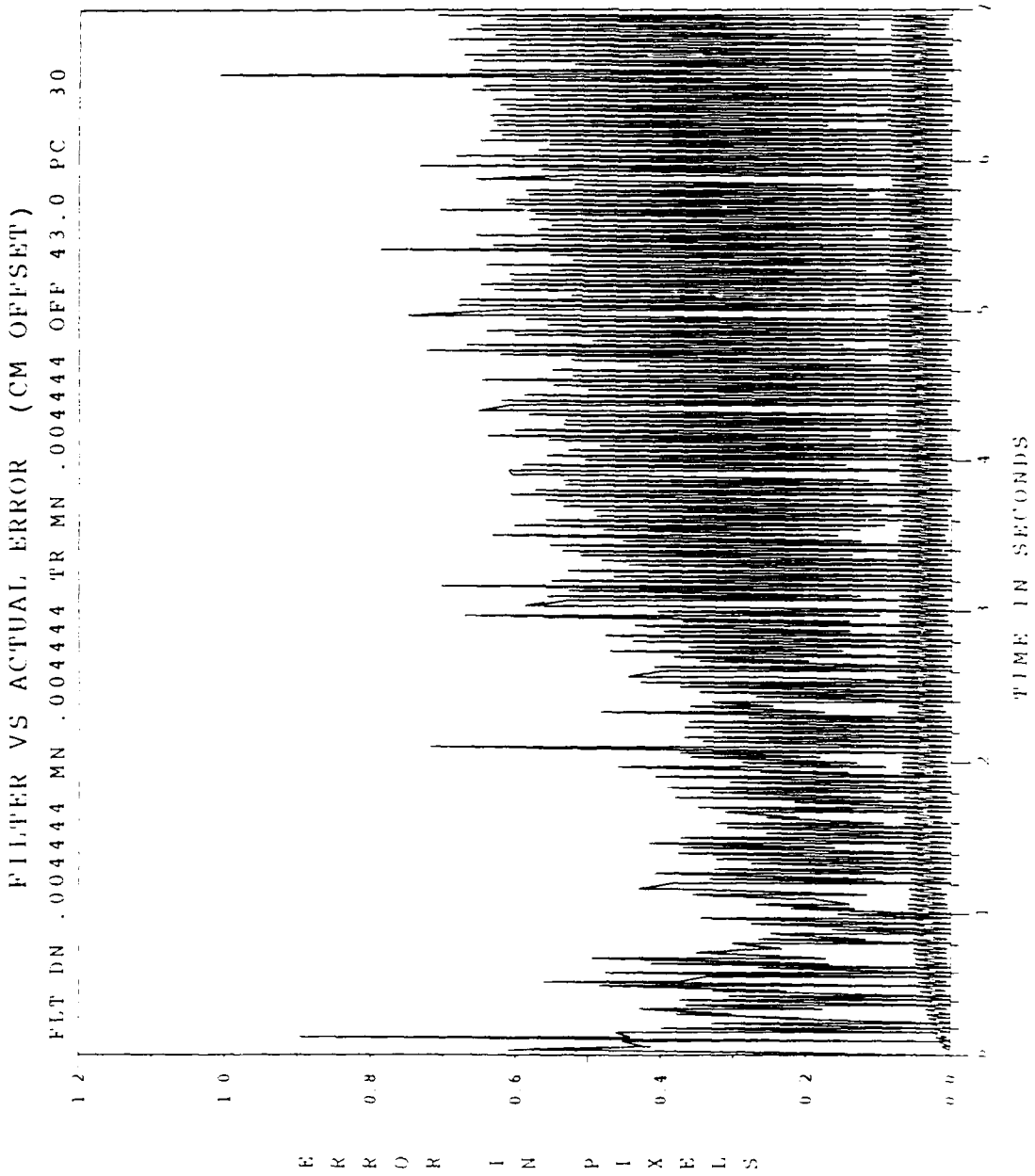


Figure E.7 PC 30 Offset Filter Vs Actual Error

ESTIMATED OFFSET MINUS POSITION (1 /) SIGMA

FLT DN .004444 MN .004444 TR MN .004444 OFF 43.0 PC 30

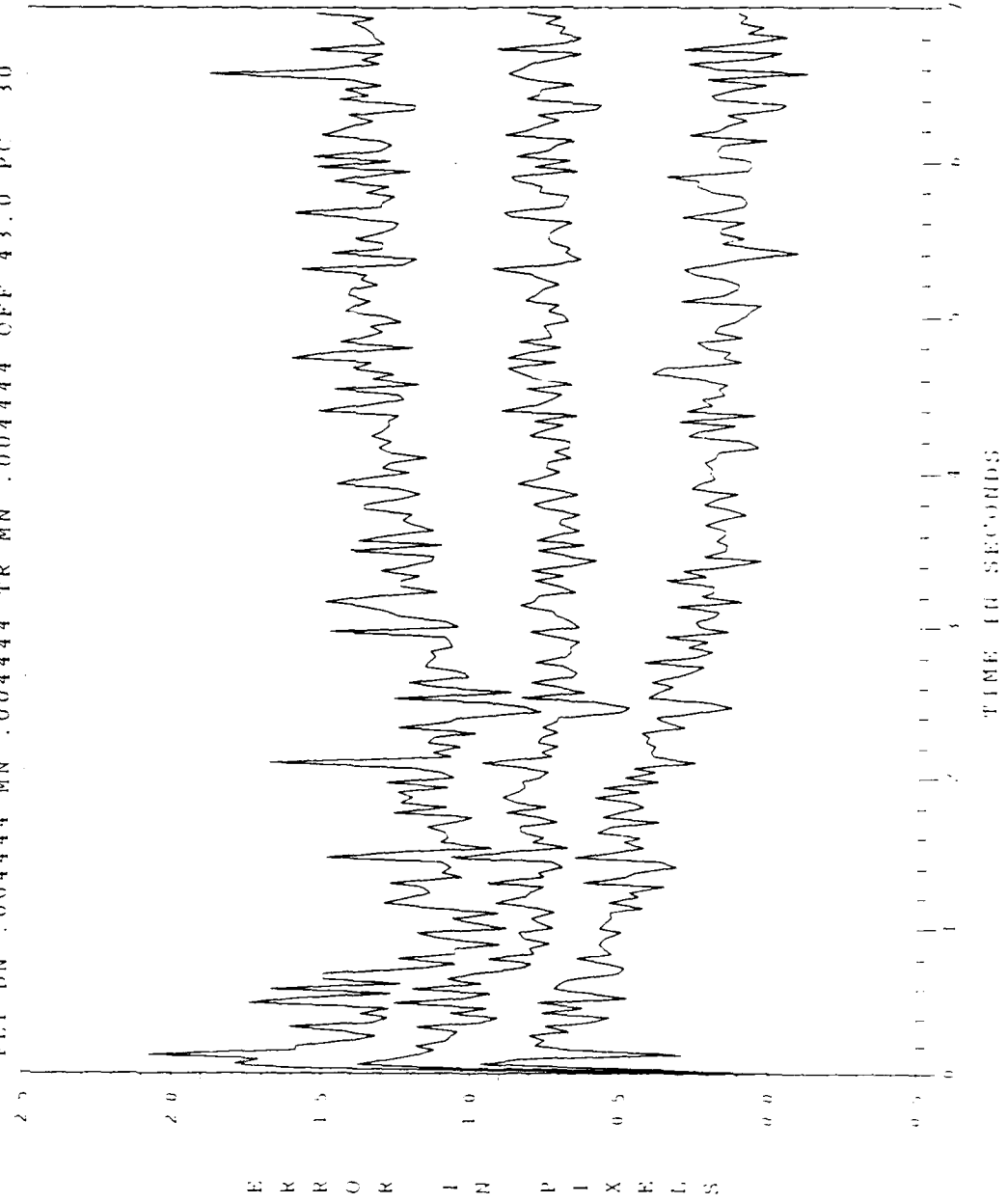


Figure E.8 PC 30 Offset Minus Error

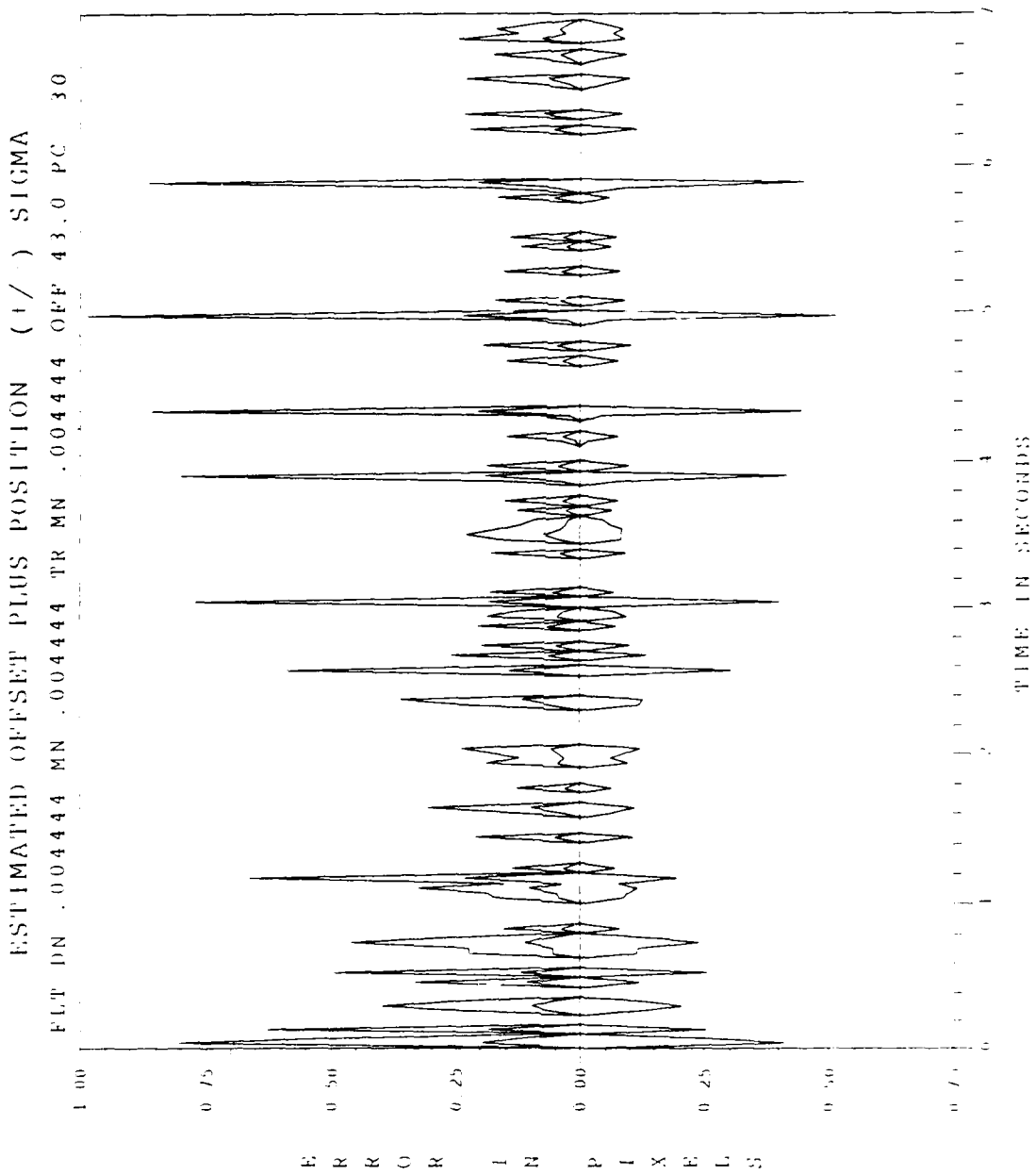


Figure E.9 PC 30 Offset Plus Error

Appendix F. Plots for Offset Distance Study

Discussion in Section 5.7

Offset Distance (Meters)

86 Figures F.1-F.3

172 Figures F.4-F.6

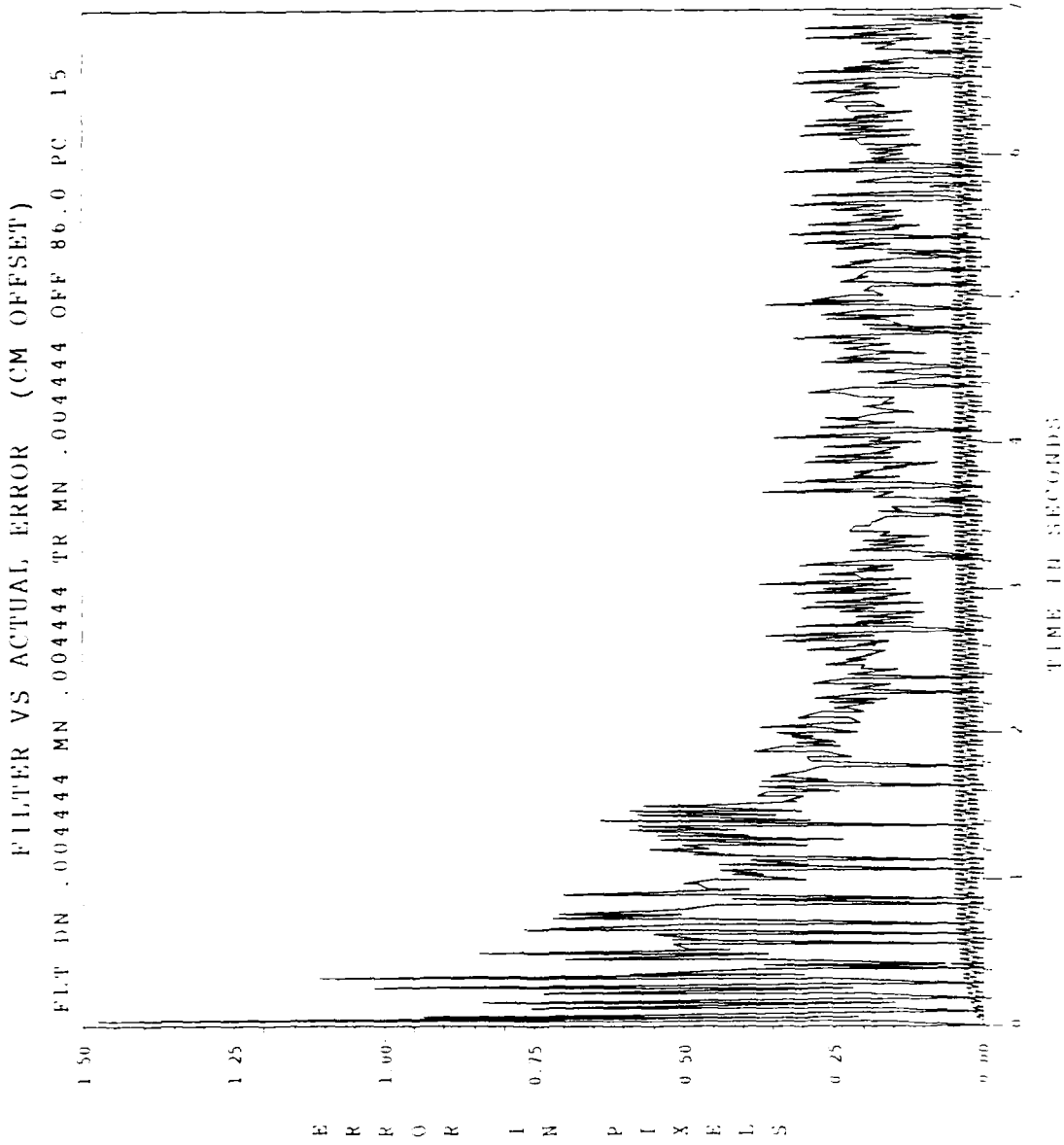


Figure F.1 Offset 86m Offset Filter Vs Actual Error

ESTIMATED OFFSET-MINUS POSITION (+ /) SIGMA
FLT DN .004444 MN .004444 TR MN .004444 OFF 86.0 PC 15

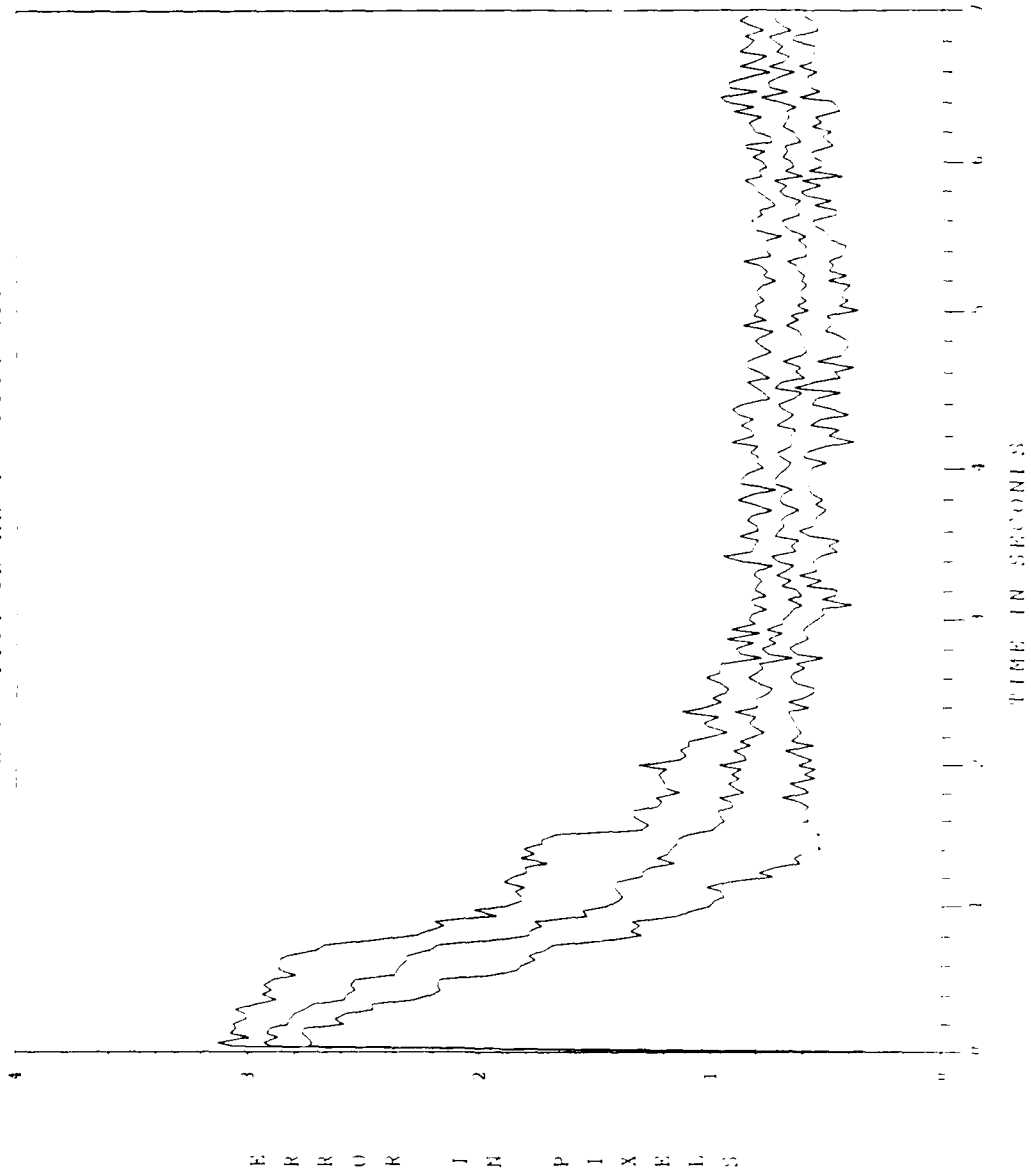


Figure F.2 Offset 86m Offset Minus Error

ESTIMATED OFFSET PLUS POSITION (1/) SIGMA

FLT DN .004444 MN .004444 TR MN .004444 OFF 86.0 PC 15

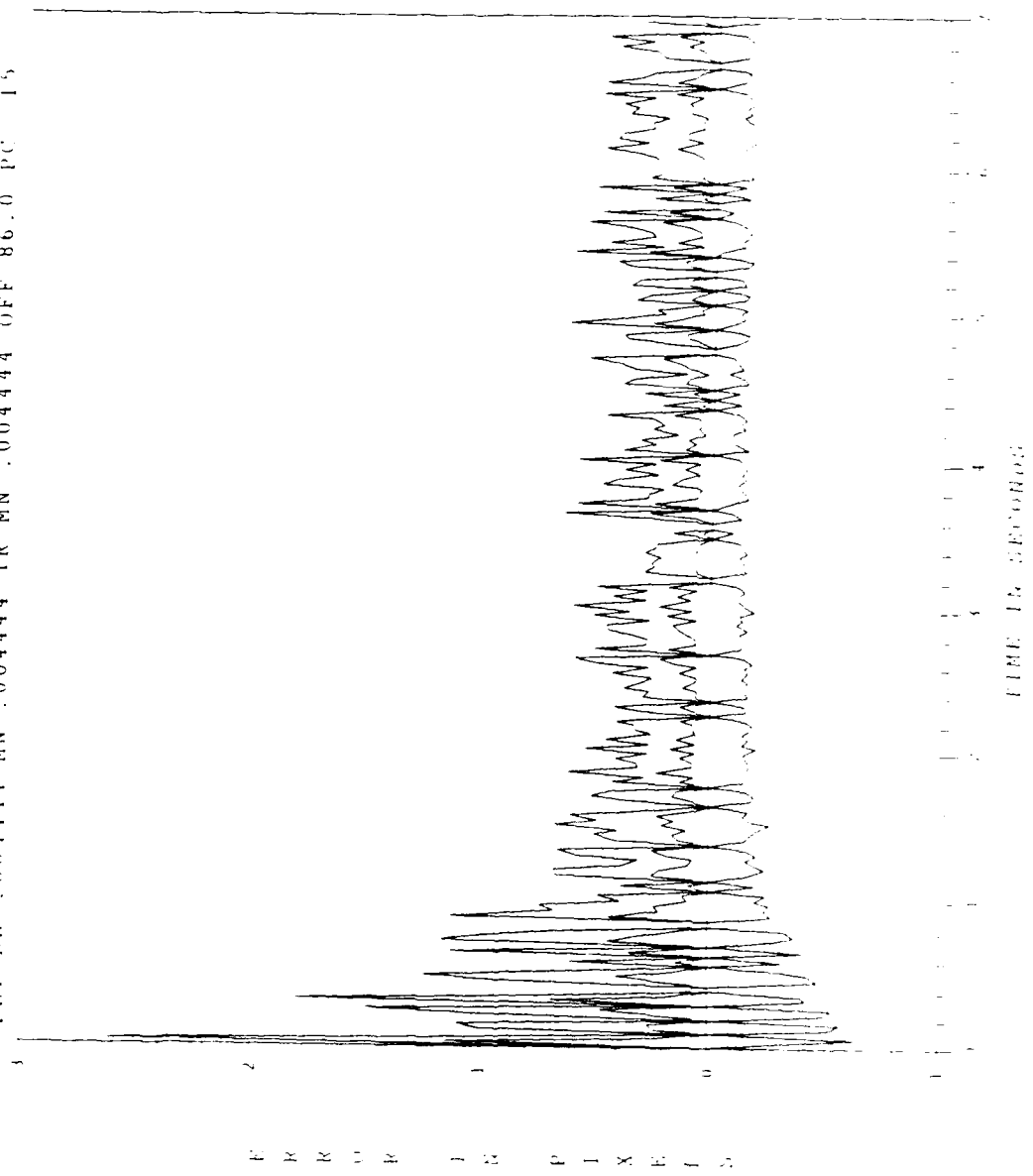


Figure F.3 Offset 86m Offset Plus Error

FILTER VS ACTUAL ERROR (CM OFFSET)

FLC 00 .004444 ME .004444 TR MN .004444 OFF 172 PC 15

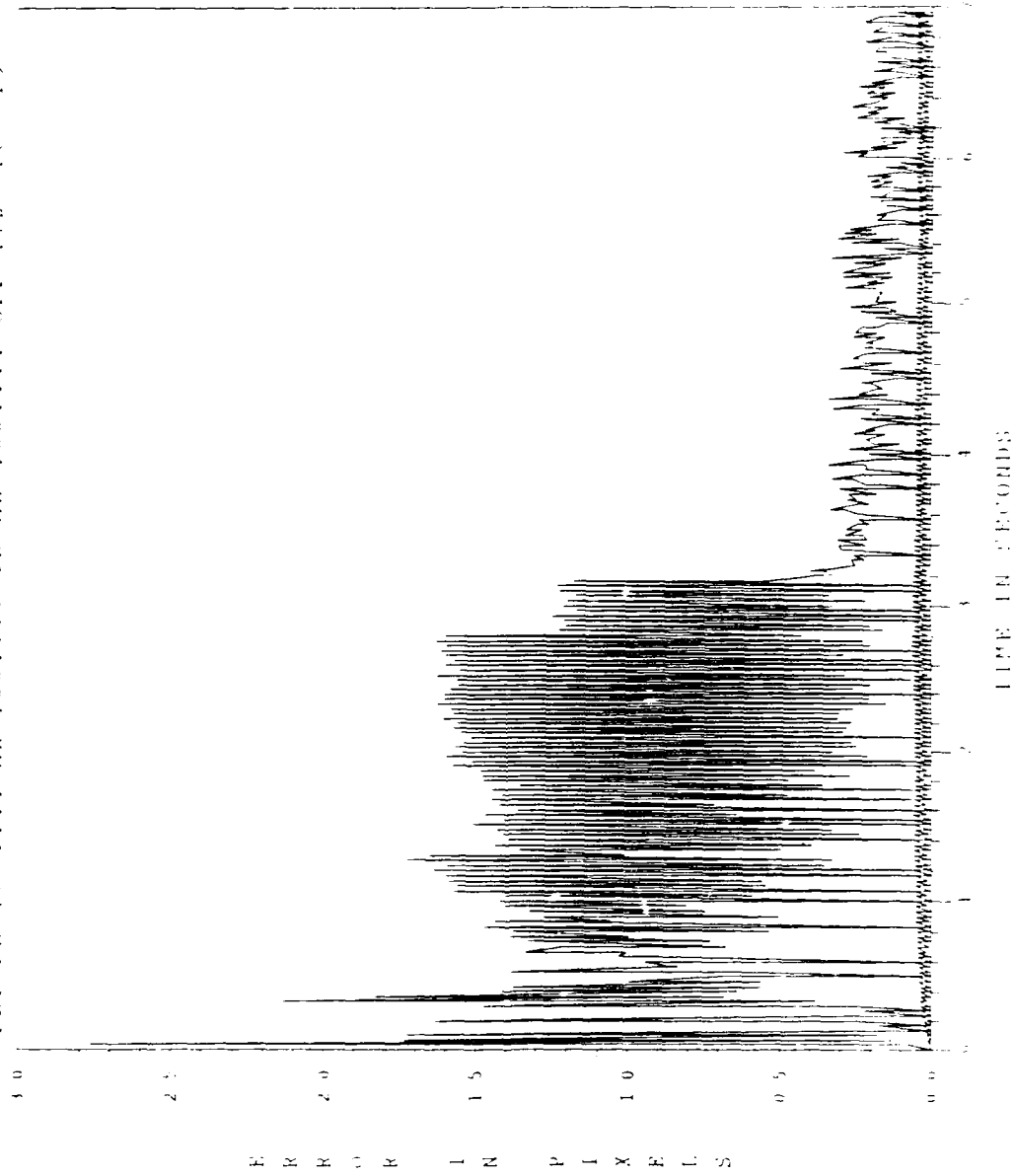


Figure F.4 Offset 172m Offset Filter Vs Actual Error

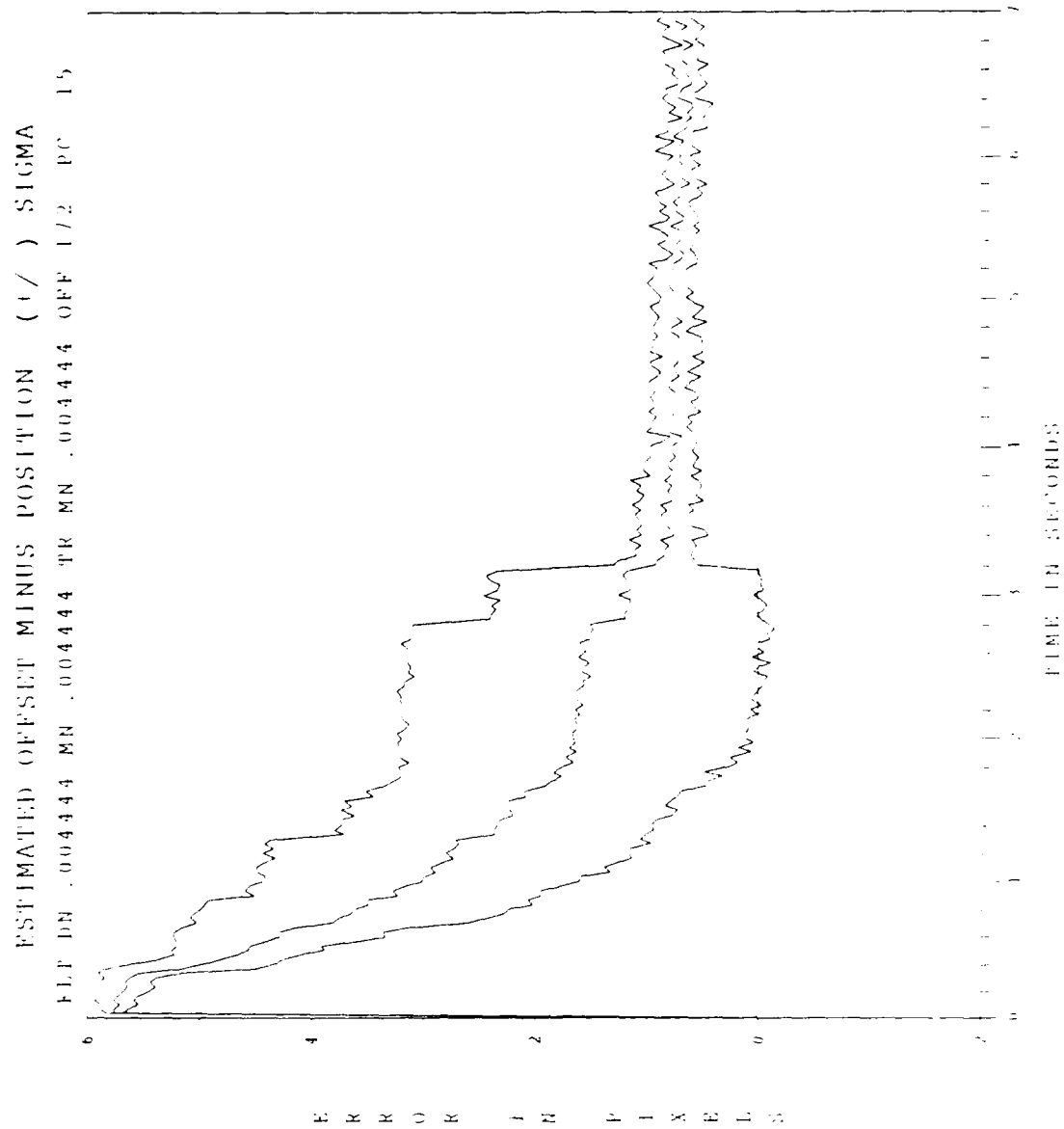


Figure F.5 Offset 172m Offset Minus Error

ESTIMATED OFFSET PLUS POSITION (1/) SIGMA
FLT DN .004444 MN .004444 TR MN .004444 OFF 172 PC 15

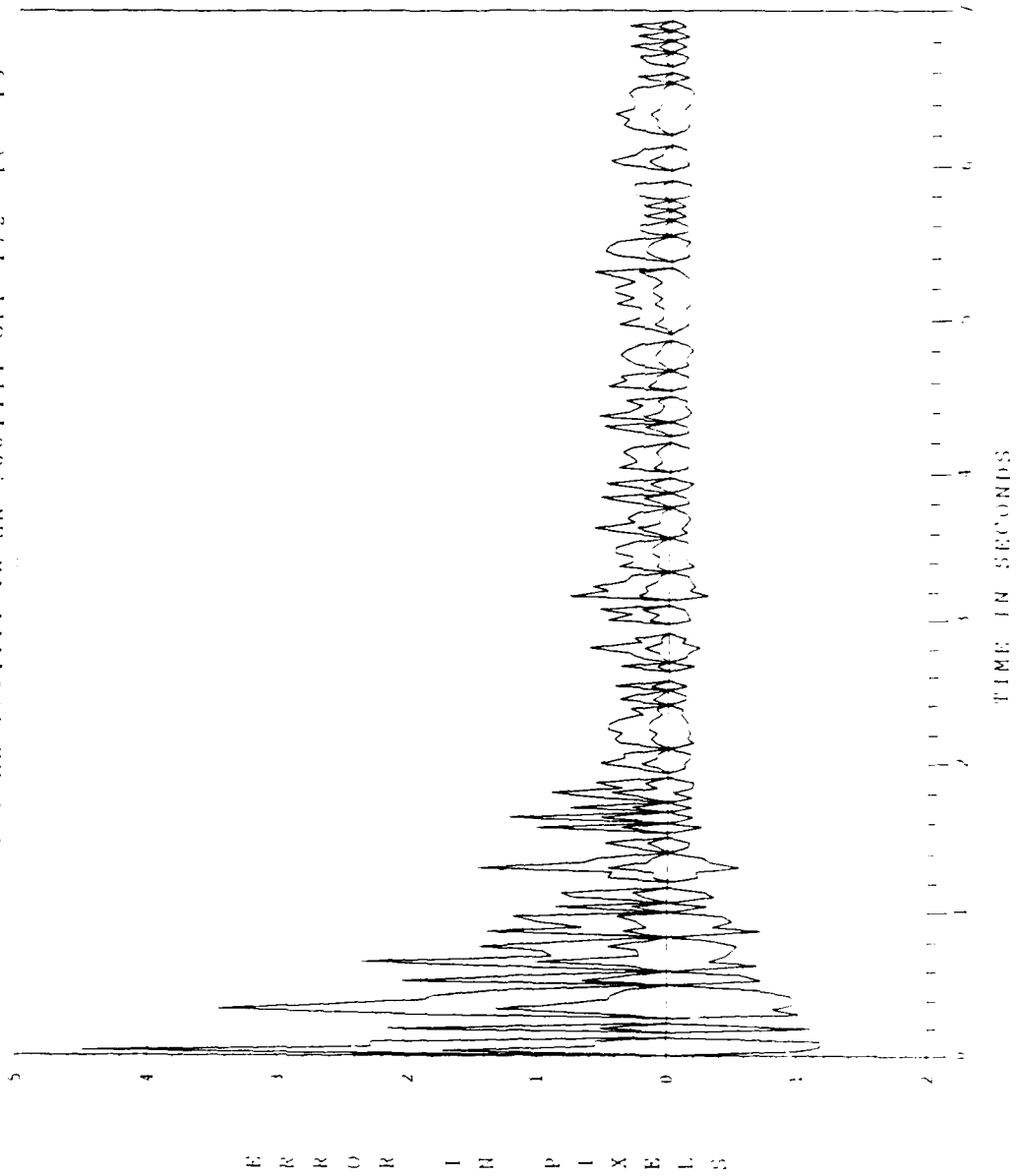


Figure F.6 Offset 172m Offset Plus Error

Bibliography

1. Flynn, Patrick M. Alternative Dynamics Models and Multiple Model Filtering for a Short Range Tracker. MS Thesis, School of Engineering, Air Force Institute of Technology (AU), Wright-Patterson AFB OH, December 1981
2. Harnly, Douglas A., and Robert L. Jensen. An Adaptive Distributed-Measurement Extended Kalman Filter for a Short Range Tracker. MS Thesis, School of Engineering, Air Force Institute of Technology (AU), Wright-Patterson AFB OH, December 1982
3. Kozemchak, Mark R. Enhanced Image Tracking: Analysis of Two Acceleration Models in Tracking Multiple Model Hot-Spot Images. MS Thesis, School of Engineering, Air Force Institute of Technology (AU), Wright-Patterson AFB OH, December 1982
4. Leeney, Thomas L. A Multiple Mode Adaptive Tracking Algorithm Against Airborne Targets. MS Thesis, School of Engineering, Air Force Institute of Technology (AU), Wright-Patterson AFB OH, December 1987
5. Loving, Phyllis A. Bayesian VS MAP Multiple Model Adaptive Estimation for Field of View Expansion in Tracking Airborne Targets. MS Thesis, School of Engineering, Air Force Institute of Technology (AU), Wright-Patterson AFB OH, March 1985
6. Maybeck, Peter S. Stochastic Models, Estimation and Control, Volume I. New York: Academic Press, 1979
7. _____. Stochastic Models, Estimation and Control, Volume II. New York: Academic Press 1982
8. _____. Professor of Electrical Engineering. Personal Interviews. Air Force Institute of Technology (AU), School of Engineering, Wright-Patterson AFB OH, January 1989 through December 1989
9. _____ and S. K. Rogers. " Adaptive Tracking of Multiple Hot-Spot Target IR Images," IEEE Transactions on Automatic Control, Vol. AC-28, No. 10. 937-943, October 1983
10. Mercier, Daniel E. An Extended Kalman Filter for use in a Shared Aperture Medium Range Tracker. MS Thesis, School of Engineering, Air Force Institute of Technology (AU), Wright-Patterson AFB OH, December 1978

11. Millner, Paul P. Enhanced Tracking of Airborne Targets Using a Correlator/Kalman Filter. MS Thesis, School of Engineering, Air Force Institute of Technology (AU), Wright-Patterson AFB OH, December 1982
12. Netzer, Allan S. Characteristics of Bayesian Multiple Model Adaptive Estimation for Tracking Airborne Targets. MS Thesis, School of Engineering, Air Force Institute of Technology (AU), Wright-Patterson AFB OH, December 1985
13. Norton, John E. Multiple Model Adaptive Tracking of Airborne Targets. MS Thesis, School of Engineering, Air Force Institute of Technology (AU), Wright-Patterson AFB OH, December 1988
14. Rizzo, David R. Enhanced Tracking of Ballistic Targets Using Forward Looking Infrared Measurements. MS Thesis, School of Engineering, Air Force Institute of Technology (AU), Wright -Patterson AFB OH, March 1989
15. Rogers, Steven K. Enhanced Tracking of Airborne Targets Using Forward Looking Infrared Measurements. MS Thesis, School of Engineering, Air Force Institute of Technology (AU), Wright-Patterson AFB OH, December 1981
16. Singletery, James. Adaptive Laser Pointing and Tracking Problem. MS Thesis, Air Force Institute of Technology (AU), Wright-Patterson AFB OH, December 1980
17. Suizu, Robert I. Enhanced Tracking of Airborne Targets Using Multiple Model Filter Techniques for Adaptive Field of View Expansion. MS Thesis, School of Engineering, Air Force Institute of Technology (AU), Wright-Patterson AFB OH, December 1983
18. Tobin, David M. A Multiple Model Adaptive Tracking Algorithm for a High Energy Laser Weapon System. MS Thesis, School of Engineering, Air Force Institute of Technology (AU), Wright-Patterson AFB OH, December 1986

Vita

Captain Claude W. Eden [REDACTED]
[REDACTED]
[REDACTED]

[REDACTED] he attended Morehead State University, Morehead Kentucky. In May 1975, Capt Eden was awarded a Bachelor of Science degree in Animal Science. He continued with graduate studies at North Carolina State University at Raleigh, and was awarded a Master of Science degree in Quantitative Genetics in December 1977. In August, 1981, he entered the United States Air Force Officer Training School, Lackland Air Force Base, Texas, receiving his commission in December of that same year. His first assignment was to the Air Force Institute of Technology (AFIT), where he was enrolled in the Undergraduate Electrical Engineering Conversion program at Auburn University, Auburn, Alabama. Upon graduating in December 1983, Capt Eden was assigned to the Warner Robins Air Logistics Center, and spent the next four and a half years working as a radar engineer. Captain Eden was assigned to AFIT in May 1988 to pursue a Master's degree in Electrical Engineering.

[REDACTED] [REDACTED]

REPORT DOCUMENTATION PAGE				Form Approved OMB No. 0704-0188		
1a. REPORT SECURITY CLASSIFICATION UNCLASSIFIED			1b. RESTRICTIVE MARKINGS			
2a. SECURITY CLASSIFICATION AUTHORITY			3. DISTRIBUTION/AVAILABILITY OF REPORT Approved for public release; distribution unlimited			
2b. DECLASSIFICATION/DOWNGRADING SCHEDULE						
4. PERFORMING ORGANIZATION REPORT NUMBER(S) AFIT/GE/ENG/89D-11			5. MONITORING ORGANIZATION REPORT NUMBER(S)			
6a. NAME OF PERFORMING ORGANIZATION School of Engineering		6b. OFFICE SYMBOL (If applicable) AFIT/ENG	7a. NAME OF MONITORING ORGANIZATION			
6c. ADDRESS (City, State, and ZIP Code) Air Force Institute of Technology Wright Patterson AFB, OH 45433-6585			7b. ADDRESS (City, State, and ZIP Code)			
8a. NAME OF FUNDING/SPONSORING ORGANIZATION Air Force Weapons Laboratory		8b. OFFICE SYMBOL (If applicable)	9. PROCUREMENT INSTRUMENT IDENTIFICATION NUMBER			
8c. ADDRESS (City, State, and ZIP Code) Kirtland AFB, NM 87117			10. SOURCE OF FUNDING NUMBERS			
			PROGRAM ELEMENT NO.	PROJECT NO.	TASK NO.	WORK UNIT ACCESSION NO.
11. TITLE (Include Security Classification) ENHANCED TRACKING OF BALLISTIC TARGETS USING FORWARD LOOKING INFRARED MEASUREMENTS WITH ACTIVE TARGET ILLUMINATION; (UNCLASSIFIED)						
12. PERSONAL AUTHOR(S) Capt Claude W. Eden						
13a. TYPE OF REPORT MS Thesis		13b. TIME COVERED FROM _____ TO _____		14. DATE OF REPORT (Year, Month, Day) 1989 December	15. PAGE COUNT 235	
16. SUPPLEMENTARY NOTATION						
17. COSATI CODES			18. SUBJECT TERMS (Continue on reverse if necessary and identify by block number) Kalman filter, Tracking, Ballistic Missile, FLIR, Laser Illumination			
FIELD	GROUP	SUB-GROUP				
17	5					
19. ABSTRACT (Continue on reverse if necessary and identify by block number) Thesis Chairman: Dr. Peter S. Maybeck Abstract: (on back of this form)						
20. DISTRIBUTION/AVAILABILITY OF ABSTRACT <input checked="" type="checkbox"/> UNCLASSIFIED/UNLIMITED <input type="checkbox"/> SAME AS RPT <input type="checkbox"/> DTIC USERS			21. ABSTRACT SECURITY CLASSIFICATION UNCLASSIFIED			
22a. NAME OF RESPONSIBLE INDIVIDUAL Dr. Peter S. Maybeck			22b. TELEPHONE (Include Area Code) 513-255-3576		22c. OFFICE SYMBOL AFIT/ENG	

The purpose of this line of research has been to develop an algorithm to track airborne targets using forward looking infrared (FLIR) measurements, as a means of aiming a high energy laser.

Past research has concentrated on the use of passively acquired measurements, i.e. measurements of the target's thermal intensity functions (hotspots) from an array of infrared detector elements. This research deviated from this by considering active illumination of the target by a low power laser. The measurement of the reflected laser light would then give information about the hardbody location, and presumably an aiming point for the high power laser.

Specifically, this thesis investigated a ballistic missile in boost phase of flight. Measurements of the missile exhaust plume thermal intensity from an array of infrared detector elements were used by an enhanced correlator/linear Kalman filter to produce estimates of the FLIR image centroid location and velocity. These estimates were then used to simulate the aiming of a low power laser at the missile. The "pseudo-measurement" output of an optical sensor receiving the reflections from the missile hardbody was then used by a second Kalman filter to estimate the location of the missile.

This thesis effort involved sensitivity and robustness studies of the measurement noise variance in the filter which estimates the missile location. These studies indicated the filter's relative insensitivity to changes in the measurement noise variance; this parameter only affected the transient time for the filter to reach the steady state value of the missile location. Other parameter studies involved variation of offset distance between missile and exhaust plume, and variation of infrared sensor resolution. The first study indicated decreased filter performance in locating the missile with increased offset distance. The results from the second study were inconclusive and require further work.